VOLUME 81 MAY 19, 1977 NUMBER 10

JPCHAx

# THE JOURNAL OF PHYSICAL CHEMISTRY

PUBLISHED BIWEEKLY BY THE AMERICAN CHEMICAL SOCIETY

THE JOURNAL OF

# PHYSICAL CHEMISTRY



*Published by the*
**AMERICAN CHEMICAL SOCIETY**
**BOOKS AND JOURNALS DIVISION**

D. H. Michael Bowen, Director

Marjorie Laflin, Assistant to the Director

Editorial Department: Charles R. Bertsch, Head; Marianne C. Brogan, Associate Head; Celia B. McFarland, Joseph E. Yurvati, Assistant Editors

Magazine and Production Department: Bacil Guiley, Head

Research and Development Department: Seldon W. Terrant, Head

Advertising Office: Centcom, Ltd., 25 Sylvan Road South, Westport, Conn. 06880.



Published biweekly by the American Chemical Society at 20th and Northampton Sts., Easton, Pennsylvania 18042. Second class postage paid at Washington, D.C. and at additional mailing offices.

### Editorial Information

**Instructions for authors** are printed in the first issue of each volume. Please conform to these instructions when submitting manuscripts.

**Manuscripts for publication** should be submitted to *The Journal of Physical Chemistry,* Department of Chemistry, University of Minnesota, Minneapolis, Minn. 55455. Correspondence regarding **accepted papers and proofs** should be directed to the Editorial Department at the ACS Easton address.

**Page charges** of $60.00 per page may be paid for papers published in this journal. Ability to pay does not affect acceptance or scheduling of papers.

**Bulk reprints or photocopies** of individual articles are available. For information write to Business Operations, Books and Journals Division at the ACS Washington address.

Requests for **permission to reprint** should be directed to Permissions, Books and Journals Division at the ACS Washington address. The American Chemical Society and its Editors assume no responsibility for the statements and opinions advanced by contributors.

### Subscription and Business Information

1977 Subscription rates—including surface postage

| | U.S. | PUAS | Canada, Foreign |
|---|---|---|---|
| Member | $24.00 | $33.00 | $34.00 |
| Nonmember | 96.00 | 105.00 | 106.00 |
| Supplementary material | 15.00 | 19.00 | 20.00 |

**Air mail and air freight** rates are available from Membership & Subscription Services, at the ACS Columbus address.

**New and renewal subscriptions** should be sent with payment to the Office of the Controller at the ACS Washington address. **Changes of address** must include both old and new addresses with ZIP code and a recent mailing label. Send all address changes to the ACS Columbus address. Please allow six weeks for change to become effective. **Claims for missing numbers** will not be allowed if loss was due to failure of notice of change of address to be received in the time specified: if claim is dated (a) North America—more than 90 days beyond issue date, (b) all other foreign—more than 1 year beyond issue date; or if the reason given is "missing from files". Hard copy claims are handled at the ACS Columbus address.

**Microfiche subscriptions** are available at the same rates but are mailed first class to U.S. subscribers, air mail to the rest of the world. Direct all inquiries to Special Issues Sales, at the ACS Washington address or call (202) 872-4554. **Single issues** in hard copy and/or microfiche are available from Special Issues Sales at the ACS Washington address. Current year $4.75. Back issue rates available from Special Issues Sales. **Back volumes** are available in hard copy and/or microform. Write to Special Issues Sales at the ACS Washington address for further information. **Microfilm** editions of ACS periodical publications are available from volume 1 to the present. For further information, contact Special Issues Sales at the ACS Washington address. **Supplementary material** mentioned in the journal appears in the microfilm edition. Single copies may be ordered directly from Business Operations, Books and Journals Division, at the ACS Washington address.

| | U.S. | PUAS, Canada | Other Foreign |
|---|---|---|---|
| Microfiche | $2.50 | $3.00 | $3.50 |
| Photocopy | | | |
| 1–7 pages | 4.00 | 5.50 | 7.00 |
| 8–20 pages | 5.00 | 6.50 | 8.00 |

Orders over 20 pages are available only on microfiche, 4 × 6 in., 24X, negative, silver halide. Orders must state photocopy or microfiche if both are available. Full bibliographic citation including names of all authors and prepayment are required. Prices are subject to change.

American Chemical Society
1155 16th Street, N.W.
Washington, D.C. 20036
(202) 872-4600

Member & Subscription Services
American Chemical Society
P.O. Box 3337
Columbus, Ohio 43210
(314) 421-7230

Editorial Department
American Chemical Society
20th and Northampton Sts.
Easton, Pennsylvania 18042
(215) 258-9111

**Notice to Authors last printed in the issue of January 13, 1977**

THE JOURNAL OF

# PHYSICAL CHEMISTRY

*Volume 81, Number 10 May 19, 1977*

JPCHAx 81(10) 937–1030 (1977)

ISSN 0022-3654



## COMMUNICATIONS TO THE EDITOR

■ Supplementary and/or miniprint material for this paper is available separately (consult the masthead page for ordering information); it will also appear following the paper in the microfilm edition of this journal.

* In papers with more than one author, the asterisk indicates the name of the author to whom inquiries about the paper should be addressed.

## AUTHOR INDEX

THE JOURNAL OF
PHYSICAL CHEMISTRY



VOLUME 81, NUMBER 10 MAY 19, 1977

# Radiolytic Chain Decomposition of Peroxomonophosphoric and Peroxomonosulfuric Acids[1]

**P. Maruthamuthu and P. Neta***

*Radiation Laboratory, University of Notre Dame, Notre Dame, Indiana 46556* *(Received January 5, 1977)*

*Publication costs assisted by the U.S. Energy Research and Development Administration*

Radiolytic studies of peroxomonophosphoric acid, $H_3PO_5$, and peroxomonosulfuric acid, $H_2SO_5$, have been carried out over a wide pH range. Unlike the corresponding peroxodiacids, $H_4P_2O_8$ and $H_2S_2O_8$, the peroxomono acids undergo radiolytic chain decomposition, with $G$ values increasing from about 6 to 60 in going from pH 1 to 12.6. Sharp rises in $G$ values appear at pH values near the $pK_a$ of the hydroperoxy proton (highest $pK_a$). The mechanism suggested for these chain reactions involves successive oxidation and reduction of the parent compounds by radicals produced in the preceding step. Pulse radiolysis experiments showed that the reaction of $e_{aq}^-$ with peroxomonophosphate ($k = 4.4 \times 10^8$ $M^{-1}$ $s^{-1}$ at pH 7) produces OH radicals twice as frequently as $\dot{H}PO_4^-$ radicals. Previous results with peroxomonosulfate showed a factor of 4 for similar reactions. The rate constant for reaction of OH radicals with peroxomonophosphate at pH 7 was found to be $4.3 \times 10^7$ $M^{-1}$ $s^{-1}$, and with peroxomonosulfate $1.7 \times 10^7$ $M^{-1}$ $s^{-1}$ at pH 7 and $2.1 \times 10^9$ $M^{-1}$ $s^{-1}$ at pH 11. The reactions of OH are suggested to be the chain initiation step and possibly responsible for the main chain propagation as well.

## Introduction

Peroxomonophosphoric acid, $H_3PO_5$ (PMP), and peroxomonosulfuric acid, $H_2SO_5$ (PMS), can be considered as substituted hydrogen peroxide in which one of the hydrogens is replaced by an oxyanion group of phosphorus or sulfur. They are more powerful oxidizing agents than the corresponding peroxodi acids ($H_4P_2O_8$ or $H_2S_2O_8$) but they may act sometimes as reducing agents similar to $H_2O_2$. Hart[2] has used mixtures of $H_2S_2O_8$, $H_2SO_5$, and $H_2O_2$ in the radiolytic decomposition of formic acid and has concluded that peroxomonosulfuric acid was more reactive in this chain decomposition than peroxodisulfuric acid. Pulse radiolytic studies[3] showed that the reaction of $e_{aq}^-$ with PMS may take two different courses:

$$HSO_5^- + e_{aq}^- \rightarrow \dot{SO}_4^- + OH^- \quad (1a)$$

$$HSO_5^- + e_{aq}^- \rightarrow SO_4^{2-} + \dot{O}H \quad (1b)$$

to produce OH radicals four times more frequently than $\dot{SO}_4^-$ radicals. Moreover, PMS was found to react with OH relatively rapidly while peroxodisulfate does not react with OH.[3]

Thermal reactions of these compounds showed[4,5] a marked dependence upon pH and it was inferred that the rate of spontaneous decomposition was maximum when the pH was equal to the $pK_a$ of the respective acid. As part of a program of studies of various secondary oxidants it was felt desirable to carry out radiolytic studies of these peracids to extend the information from the thermal studies. Unlike $S_2O_8^{2-}$ and $P_2O_8^{4-}$ or their protonated forms, PMS and PMP were found to undergo radiolytic chain decomposition. This chain reaction is a result of their ability to be both reduced and oxidized. The mechanism of the chain reaction is discussed in this report.

## Experimental Section

*Reagents.* (1) *Peroxomonophosphoric Acid.* The preparation consists of essentially two stages: (a) conversion of $K_4P_2O_8$ into $Li_4P_2O_8 \cdot 4H_2O$ and (b) acid hydrolysis of $Li_4P_2O_8 \cdot 4H_2O$. (a) $K_4P_2O_8$, donated by the FMC Corporation, was purified to greater than 99.5% by

converting into $Li_4P_2O_8 \cdot 4H_2O$ and recrystallizing from methanol–water mixture, as described previously.[6,7] Extra care was taken to remove even a trace amount of methanol used for recrystallization. The purity of the salt, $Li_4P_2O_8 \cdot 4H_2O$, was determined by iodometric analysis as well as by reaction with $Fe^{2+}$. In the latter case the solution was treated with a known excess concentration of $Fe^{2+}$ in 1 N $H_2SO_4$ and the unused $Fe^{2+}$ was titrated with $Ce^{4+}$ using ferroin indicator. (b) The method of Edwards and co-workers[8] to prepare $H_3PO_5$ by acid hydrolysis of $Li_4P_2O_8 \cdot 4H_2O$ was slightly modified so that $H_2O_2$-free peroxomonophosphoric acid was obtained. A solution containing 0.03 M $Li_4P_2O_8 \cdot 4H_2O$ and 0.6 M $HClO_4$ was slowly heated to a final temperature of 50 °C with occasional stirring such that the increment in temperature is 5 °C per 20 min. The solution was then cooled in an ice bath and neutralized with NaOH to pH 4–5. It was then kept in a refrigerator and used within a few days. Analysis of this solution by reaction with $Fe^{2+}$ (in 1 N $H_2SO_4$) and estimation of $Fe^{3+}$ formed spectrophotometrically at 304 nm using an $\epsilon$ of 2174 $M^{-1}$ $cm^{-1}$, as well as iodometric titration in acetate buffer, showed that the hydrolysis was complete >99%. Tests carried out with $KMnO_4$[9] showed that the solution contained no free $H_2O_2$ ($\leq 10^{-6}$ M), and the concentration of $H_3PO_5$ was found to be constant for more than a month.

(2) *Peroxomonosulfate.* Peroxomonosulfate, in the form of a triple salt ($2KHSO_5 \cdot KHSO_4 \cdot K_2SO_4$) was donated by DuPont Chemical Co. Analysis of this sample as in the case of PMP showed that it was 96% pure. Test with $KMnO_4$ showed the absence of free $H_2O_2$ ($\leq 10^{-6}$ M). Attempts to further purify this compound proved futile and so this sample was used as such. From the method of preparation of this compound, it is assumed that $KHSO_4$ or $K_2SO_4$ or both might account for the 4% difference between the formula and the analysis results.

Other chemicals such as $HClO_4$, NaOH, $NaH_2PO_4$, $Na_2HPO_4$, and $Na_2B_4O_7 \cdot 10H_2O$ were Baker Analyzed Reagents.

*Solution Preparation.* Quadruply distilled water was used for the preparation of all solutions for $\gamma$ irradiation. For the pulse radiolysis experiments reagent grade water from a Millipore Milli-Q system (passed through five cartridges: filter, reverse osmosis, charcoal, and two ion exchange) was found to be satisfactory, i.e., $t_{1/2}$ for the decay of $e_{aq}^-$ in 0.01 M methanol solution at pH 11 was ~40 μs. PMP or PMS at concentration of 3.5–10 mM were used for the experiments. The pH in the region of 1–4 was adjusted with dilute $HClO_4$. Sodium phosphates and tetraborate were used as buffers to maintain the pH 5–10. In the case of PMS it was always necessary to use 4 to 6 mM of buffers since the product of the decomposition ($HSO_4^-$) is a stronger acid than the reactant ($HSO_5^-$). NaOH was used to maintained pH >10.

*Irradiation.* Solutions were bubbled with nitrogen to remove oxygen or were saturated with $N_2O$. $\gamma$ irradiations were carried out at room temperature using $^{60}Co$ $\gamma$ source with dose rate of $4.8 \times 10^{17}$ eV $g^{-1}$ $min^{-1}$. After irradiation, the samples were analyzed for the concentration of PMP or PMS decomposed. Since both these acids react immediately with $Fe^{2+}$ (in 1 N $H_2SO_4$), $Fe^{3+}$ formed was measured spectrophotometrically at 304 nm using the molar extinction coefficient of 2174 $M^{-1}$ $cm^{-1}$. The values of $G$(–PMP) or $G$(–PMS) were calculated from the slope of the plot of OD vs. irradiation time. This plot was in most cases linear up to ~40% decomposition.

Hydrogen peroxide produced by the radiolysis also reacts with $Fe^{2+}$. In order to estimate the contribution of $H_2O_2$ analyses were also carried with iodide at pH 4.5 using acetate buffer. Under these conditions PMP and PMS oxidize $I^-$ rapidly but $H_2O_2$ does not. The difference between the results of the two analytical methods was found to be very small. An attempt to determine $H_2O_2$ by $KMnO_4$ also showed that the yield of $H_2O_2$ is very small. It appears that most of the hydrogen peroxide produced in the spurs is destroyed, possibly by reaction with $\dot{SO}_4^-$ or $H_2\dot{PO}_4$. In any case, the maximum yield of hydrogen peroxide amounts to only ~10% of the lowest yield measured in the present experiments and its contribution is neglected in the discussion of our results.

Solutions for determination of $G(O_2)$ were evacuated on a vacuum line and after irradiation were opened on the line and the $O_2$ quantities were measured by volume–pressure measurement after being transferred by a Toepler pump. The gas contents were verified by mass-spectrometric analysis and corrected wherever necessary.

The spectrophotometric pulse radiolysis experiments were performed using an ARCO LP-7 linear accelerator with the optical detection apparatus interfaced with the computerized system described previously.[10,11] Electron pulses were of 5 or 10 ns duration and produced 1–10 μM of radicals as determined by thiocyanate dosimetry.

*Thermal Reactions.* Both these acids, under the present experimental conditions, do not undergo thermal decomposition up to pH 8. The thermal decomposition amounted to ~10% in the pH range 9–12 and blank experiments were always carried out and corrections applied. It was not possible to carry out experiments at higher pH since PMS at pH >12 and PMP at pH >12.6 exhibited a high degree of spontaneous decomposition under our experimental condition.

Peroxomonophosphoric acid does not undergo hydrolysis to produce $H_2O_2$ down to pH 0.[5] Tests carried out with each sample of PMP and PMS before irradiation showed the absence of $H_2O_2$.

## Results and Discussion

The $G$ value for decomposition of peroxomonosulfuric acid $G$(–PMS) ranged from 10 at pH 1 to 60 at pH 12, and $G$(–PMP) ranged from 6 at pH 1 to 60 at pH 12.6. It is clear that both of these compounds undergo radiolytic chain decomposition. The initiation steps are the reactions of $e_{aq}^-$ (1a and 1b) and of OH

$$HSO_5^- + \dot{O}H \rightarrow \dot{SO}_5^- + H_2O \qquad (2)$$

In this reaction the OH radical abstracts hydrogen from the –OOH group, similar to the reaction of OH with $H_2O_2$[12] and a peroxy radical $\dot{O}OSO_3^-$ is produced. At higher pH values, where this group dissociates, the reaction may be an electron transfer:

$$SO_5^{2-} + \dot{O}H \rightarrow \dot{SO}_5^- + OH^- \qquad (3)$$

When $\dot{O}H$ dissociates into $\dot{O}^-$ (p$K$ = 11.9) a reaction similar to (3) is expected to take place to produce $\dot{SO}_5^-$, possibly at a slightly lower rate owing to electrostatic repulsion between the reactants. Hydrogen atoms may either reduce the peroxomono acid in a reaction similar to 1 or abstract H as in reaction 2. The $\dot{SO}_5^-$ radical may be stable as such or may hydrolyze to give $\dot{O}_2^-$ as is the case with some organic peroxy radicals:[13]

$$\dot{SO}_5^- + H_2O \overset{?}{\rightarrow} SO_4^{2-} + \dot{O}_2^- + 2H^+ \qquad (4)$$

In any case, $\dot{SO}_5^-$ or its product $\dot{O}_2^-$ may act as a reductant toward the parent molecule and propagate the chain, e.g.

$$HSO_5^- + \dot{SO}_5^- + H_2O \begin{cases} \nearrow \dot{SO}_4^- + SO_4^{2-} + O_2 + H_3O^+ & (5a) \\ \searrow \dot{O}H + 2SO_4^{2-} + O_2 + 2H^+ & (5b) \end{cases}$$

or similar reactions with $\dot{O}_2^-$ to produce the same radical species and oxygen. The propagation cycle is completed when $\dot{O}H$ or $\dot{SO}_4^-$ produced by reaction 5, similarly with those produced by reaction 1, react with the parent compound to produce $\dot{SO}_5^-$ as exemplified in reactions 2 and 6.

$$HSO_5^- + \dot{SO}_4^- \rightarrow \dot{SO}_5^- + HSO_4^- \quad (6)$$

In order to verify the mechanism, steady-state and pulse radiolysis experiments were carried out under various conditions. Rate constants for the initiation steps were measured by pulse radiolysis. The rate constant for reaction of $e_{aq}^-$ with PMP was measured by following the rate of decay of the $e_{aq}^-$ absorption in the presence of varying concentrations of PMP. A plot of the pseudo-first-order decay rates vs. the PMP concentration gave a good straight line from which $k = 4.4 \times 10^8$ $M^{-1}$ $s^{-1}$ was calculated for the reaction of $e_{aq}^-$ with $HPO_5^{2-}$ at pH 7. The rate constant for $H_2PO_5^-$ could not be measured because it exists only in acidic solution[5] where $e_{aq}^-$ will rapidly react with $H^+$. It is expected, however, to be somewhat higher than the value observed at pH 7. The rate for the fully dissociated form $PO_5^{3-}$ is expected to be lower because of the multiple negative charge, but could not be experimentally measured owing to the instability of PMP at high pH. The rate constant for $e_{aq}^-$ reaction with $HSO_5^-$ was reported[3] to be $8.4 \times 10^9$ $M^{-1}$ $s^{-1}$. All of these $e_{aq}^-$ rate constants are sufficiently fast to suggest that reactions 1a and 1b for both PMS and PMP would be quantitative under the $\gamma$ radiolysis experimental conditions.

The distribution between reactions 1a and 1b was reported[3] for PMS to be 1:4. Consequently 80% of the $e_{aq}^-$ are converted into OH by reaction 1b and the OH then reacts with PMS. The ratio between reactions 1a and 1b for PMP was determined in the present study by comparing the absorption spectra observed in pulse radiolysis experiments with PMP and PDP (peroxodiphosphate). The reaction of $e_{aq}^-$ with PDP gives a quantitative yield of $\dot{HPO}_4^-$ (at pH 7), the spectrum of which was determined by several investigators.[14-16] We have repeated these experiments and observed an identical spectrum. The reaction of $e_{aq}^-$ with PMP at pH 7 yielded a transient with a similar spectrum but only one third of the absorbance. It is concluded, therefore, that the distribution between reactions 1a and 1b is 1:2. Again, PMP converts $e_{aq}^-$ into OH with a high efficiency, though not as high as PMS. It appears that OH is the main initiator of the chain reactions.

Experiments with $N_2O$ saturated solutions gave very similar $G$ values as with deoxygenated solutions, except for the case of PMP in alkaline pH where somewhat higher values were observed. This finding suggests that the OH radical is an important initiator of the chain. The lack of large differences between the yields with $N_2$ and $N_2O$ saturated solutions is a result of the conversion of most $e_{aq}^-$ into OH by reaction 1b. In fact, when reaction 1b is four times more efficient than 1a, as is the case with PMS,[3] no measurable effect of $N_2O$ was found. With PMP, when the parallel reaction 1b is only twice more efficient than 1a, higher yields were observed under $N_2O$. These results indicate that the reaction of OH with the solutes is necessary for the chain reaction. No chain reaction is observed with the peroxodi acids, which do not react with OH.

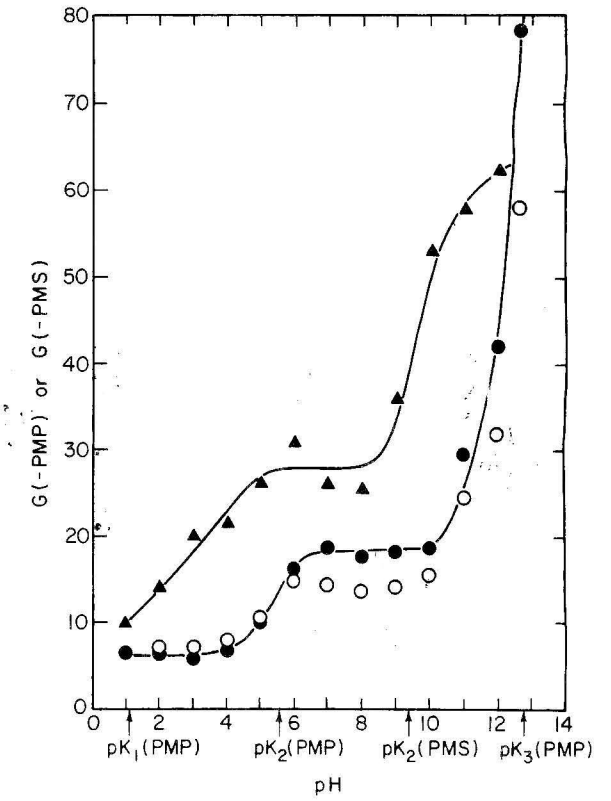


**Figure 1.** Effect of pH on the radiolytic decomposition of peroxomonophosphoric and peroxomonosulfuric acids. Solutions contained 3.5 mM PMP (●, $N_2O$ saturated; ○, deoxygenated) or PMS (▲, $N_2O$ saturated).

The rate constants for OH radical reactions were measured by competition with *p*-nitrobenzoic acid as described previously.[17] The value for $HPO_5^{2-}$ at pH 7 was found to be $4.3 \times 10^7$ $M^{-1}$ $s^{-1}$ and for $HSO_5^-$ at pH 7, $1.7 \times 10^7$ $M^{-1}$ $s^{-1}$. However, at pH 11 the rate constant for OH + $SO_5^{2-}$ was much higher, $2.1 \times 10^9$ $M^{-1}$ $s^{-1}$. The value of $2.9 \times 10^8$ reported previously[3] for OH + $HSO_5^-$ appears to contain contributions from both OH + $SO_5^{2-}$ and OH + $HSO_5^-$ reactions as it was measured by competition with carbonate ion. The rates for $HSO_5^-$ and $HPO_5^{2-}$ are comparable with the value of $4.5 \times 10^7$ $M^{-1}$ $s^{-1}$ for $H_2O_2$,[12] which suggests a similar mechanism, i.e., in all cases the OH radical abstracts hydrogen from the –OCH group. The much higher value found for $SO_5^{2-}$ indicates a change in mechanism from reaction 2 to reaction 3, with the electron transfer being much faster than the H abstraction. The large difference observed in the rate constant for OH + PMS between pH 7 and 11 may be part of the cause for the change in $G$(–PMS) with pH (see Figure 1).

The reaction of OH with PMS was previously[3] suggested to produce $\dot{SO}_5^-$. This radical was observed in pulse radiolysis experiments by its weak UV absorption.[3] It was also observed by ESR in irradiated potassium peroxodisulfate in the solid state.[18,19] In the present work the radical $\dot{PO}_5^{2-}$ produced by the reaction of OH with PMP was monitored by pulse radiolysis and found to have a weak absorption in the UV ($\epsilon_{260}$ 500, $\epsilon_{300}$ 250, $\epsilon_{350}$ 150, and $\epsilon_{400}$ 100 $M^{-1}$ $cm^{-1}$) somewhat similar to that assigned to $\dot{SO}_5^-$. The absorptions of $\dot{SO}_5^-$ and $\dot{PO}_5^{2-}$ are not sufficiently intense to allow meaningful monitoring of the kinetics of formation or decay of these radicals. However, the absorptions appear to be broader than that of $\dot{O}_2^-$[20] so that rapid hydrolysis of $\dot{SO}_5^-$ or $\dot{PO}_5^{2-}$ into $\dot{O}_2^-$ (reaction 4) can be ruled out. Slow hydrolysis may take place and play a part in the mechanism of the chain reaction. It should be noted that a reaction similar to 4 takes place

with the parent compounds, i.e., they hydrolyze to $H_2O_2$, but only in strongly acidic solutions.[5]

The propagation of the chain reaction may or may not involve $O_2^-$ radicals. In order to check whether $O_2^-$ is capable of propagating this chain reaction a few experiments were carried out in oxygen saturated solutions under such conditions that all $e_{aq}^-$ react with $O_2$ to produce $O_2^-$. The $G$ values were found to be only slightly (~15%) lower than those in the absence of oxygen. This fact indicates that if $O_2^-$ is produced by reaction 4 the chain decomposition may propagate efficiently, although it does not exclude the direct reaction of $SO_5^-$ as shown in reactions 5.

Oxygen should be produced in reactions 5 or their analogues involving $O_2^-$ instead of $SO_5^-$, with a yield approximately half that of the decomposition of the parent compounds. A few experiments with PMS at pH 3 and with PMP at pH 7 showed that $O_2$ is indeed produced in the expected yields.

The effect of pH on the decomposition rate is shown in Figure 1. Increases in the $G$ values appear at several pH regions which appear to be related to the $pK_a$ values of PMP and PMS (shown on the abscissa). The steepest increase appears at the pH region where the last portion dissociates (from the -OOH group). One of the propagation steps must, therefore, become accelerated upon dissociation of the parent compound. It is unlikely that the accelerated propagation is related to the conversion of $SO_4^-$ or $PO_4^{2-}$ to OH radicals by reaction with $OH^-$

$$SO_4^- + OH^- \rightarrow SO_4^{2-} + OH \quad (7)$$

since this process will not explain the changes observed in acid solutions. Moreover, the rate constant for reaction 7 was reported to be $8.3 \times 10^7$ $M^{-1}$ $s^{-1}$ [21] while the corresponding value for $PO_4^{2-}$ was measured in the present work and found to be $6.2 \times 10^5$ $M^{-1}$ $s^{-1}$. It should be also noted that most oxidizing radicals produced by the reduction of PMS or PMP in reactions 1 or 5 may be OH radicals so that further conversion as in reaction 7 is unimportant. The large increase in the rate constant of OH radical reaction with PMS upon dissociation, owing to a change in mechanism from reactions 2 to 3, is probably the main reason for the pH effect on the $G$ values. The reactions of OH are the main initiation step and may be also one of the main propagation steps. The alternate propagation by $SO_4^-$ or $PO_4^{2-}$, as in reaction 6, may also have pH dependent rate constants. An attempt was made to measure the rate constant for reaction 6. The $SO_4^-$ or $HPO_4^-$ were produced by reaction of $S_2O_8^{2-}$ or $HP_2O_8^{3-}$ with hydrated electrons and the rate of decay of their absorptions at 450 and 520 nm, respectively, was followed in the presence of increasing concentrations of peroxomono acids. In both cases it was found that the rate constant for reaction 6 was $<10^5$ $M^{-1}$ $s^{-1}$ so that the pH dependence could not be examined. However, as mentioned above, reaction 2 is probably far more important in these systems than reaction 6.

All the propagation steps involve the reaction of a radical with the parent compound, either to reduce or oxidize it. It is not surprising, therefore, that an increase in concentration from $3.5 \times 10^{-3}$ to $6 \times 10^{-3}$ M at pH 6 caused an increase in $G$(-PMS) from 31 to 45 and $G$(-PMP) from 15 to 22.

## Summary and Conclusions

The rate constant for the reaction of $e_{aq}^-$ with $HSO_5^-$ is $8.4 \times 10^9$ $M^{-1}$ $s^{-1}$ [3] and with $HPO_5^{2-}$ is $4.4 \times 10^8$ $M^{-1}$ $s^{-1}$. The rates for reaction with $SO_5^{2-}$ and $PO_5^{3-}$ are probably lower than those for the corresponding protonated forms. The reaction of $e_{aq}^-$ with PMS yields OH four times more frequently than it yields $SO_4^-$.[3] In the case of PMP the ratio is only 2:1. The OH radical reacts with $HSO_5^-$ with a rate constant of $1.7 \times 10^7$ $M^{-1}$ $s^{-1}$ and with $HPO_5^{2-}$, $4.3 \times 10^7$ $M^{-1}$ $s^{-1}$, to abstract hydrogen from the -OOH group and produce $SO_5^-$ or $PO_5^{2-}$, respectively. When the parent compound is fully dissociated the reaction with OH is much faster, $k = 2.1 \times 10^9$ $M^{-1}$ $s^{-1}$ for $SO_5^{2-}$, and proceeds by electron transfer. The $SO_5^-$ and $PO_5^{2-}$ radicals appear to be able to reduce their parent compounds, or to produce a radical ($O_2^-$) which reduces their parent compound, forming again an oxidizing species and thus propagating a chain reaction. The $G$ values for decomposition of PMS or PMP in irradiated aqueous solutions were found to be very high, especially at high pH, indicating an efficient chain reaction. The OH radical is the main initiator and propagator of the chain. The suggested mechanism involves oxidation of PMS or PMP, mainly by OH, to produce $SO_5^-$ or $PO_5^{2-}$, which then reduce their parent compounds to produce mainly OH.

## References and Notes

(1) The research described herein was supported by the Division of Physical Research of the U.S. Energy Research and Development Administration. This is Radiation Laboratory Document No. NDRL-1726.
(2) E. J. Hart, *J. Am. Chem. Soc.*, **83**, 567 (1961).
(3) W. Roebke, M. Renz, and A. Henglein, *Int. J. Radiat. Phys. Chem.*, 1, 39 (1969).
(4) D. L. Ball and J. O. Edwards, *J. Am. Chem. Soc.*, **78**, 1125 (1956).
(5) I. I. Creaser and J. O. Edwards, *Top. Phosphorus Chem.*, 7, 379 (1972).
(6) T. Chulski, Ph.D. Thesis, Michigan State University, 1953.
(7) P. Maruthamuthu, Ph.D. Thesis, Madras University, 1974.
(8) E. Koubek, M. L. Haggett, C. J. Battaglia, K. M. Ibne-Rasa, H. Y. Pyun, and J. O. Edwards, *J. Am. Chem. Soc.*, **85**, 2263 (1963).
(9) G. Mamantov, J. H. Burns, J. R. Hall, and D. B. Lake, *Inorg. Chem.*, **3**, 1043 (1964).
(10) L. K. Patterson and J. Lilie, *Int. J. Radiat. Phys. Chem.*, **6**, 129 (1974).
(11) R. H. Schuler, P. Neta, H. Zemel, and R. W. Fessenden, *J. Am. Chem. Soc.*, **98**, 3825 (1976).
(12) H. A. Schwarz, *J. Phys. Chem.*, **66**, 255 (1962).
(13) See, e.g., Y. Ilan, J. Rabani, and A. Henglein, *J. Phys. Chem.*, **80**, 1558 (1976).
(14) J. R. Huber and E. Hayon, *J. Phys. Chem.*, **72**, 3820 (1968).
(15) E. D. Black and E. Hayon, *J. Phys. Chem.*, **74**, 3199 (1970).
(16) G. Levey and E. J. Hart, *J. Phys. Chem.*, **79**, 1642 (1975).
(17) P. Neta and L. M. Dorfman, *Adv. Chem. Ser.*, **No. 81**, 222 (1968).
(18) S. B. Barnes and M. C. R. Symons, *J. Chem. Soc. A*, 66 (1966).
(19) M. C. R. Symons and S. B. Barnes, *J. Chem. Soc. A*, 2000 (1970).
(20) D. Behar, G. Czapski, J. Rabani, L. M. Dorfman, and H. A. Schwarz, *J. Phys. Chem.*, **74**, 3209 (1970).
(21) J. L. Redpath and R. L. Willson, *Int. J. Radiat. Biol.*, **27**, 389 (1975).

# Inhibition of Positronium Formation and Reactions of Positronium Atoms in Solutions

**Hans J. Ache,* Ralph E. Wild, and Lawrence J. Bartal**

*Department of Chemistry, Virginia Polytechnic Institute and State University, Blacksburg, Virginia 24061* *(Received October 25, 1976)*

The interactions of positrons with inorganic compounds in aqueous solutions are discussed in terms of the "modified Ore gap" model and the "spur reaction" model.

## Introduction

In contrast to the negatively charged electron whose importance in the various aspects of radiation chemistry has been early and widely acknowledged, the role of the positron, its reactions,[1-8] and the contribution it can make to radiation chemistry have only very recently been recognized.

Thus in the following a few aspects of the interactions of the positron and its possible interrelationship with electron interactions and in turn with radiation chemistry shall be demonstrated by a reexamination of some of our previously reported experimental results[5-8] on the positronium (Ps) formation process in terms of the spur reaction model.[9-14]

## Experimental Section

A description of the experimental procedures, the assessment of the rate constants, as well as the actual experimental results can be found in the previous papers.[5-8]

## Results and Discussion

Positrons are most commonly emitted as a result of the radioactive decay of a neutron deficient nuclide. They lose their high kinetic energy in collisions with the surrounding matter until they reach thermal or near thermal energies at which point the cross section for mass annihilation with an electron assumes a maximum value.

A certain fraction of these positrons, however, may enter the bound state of the positronium (Ps) which could be formed in two ground states either in the triplet or ortho state, with parallel spin orientation and an intrinsic average annihilation lifetime of $1.4 \times 10^{-7}$ s, or in the singlet or para state with antiparallel spin orientation, which has an intrinsic average lifetime of $1.25 \times 10^{-10}$ s.

Two basic models, the Ore gap model and the spur reaction mode,[9-13] have been invoked to describe the Ps formation process. More recently a modified spur reaction model has been suggested.[14]

In the previous papers[5-8] we have interpreted our experimental results in terms of the (modified) Ore gap model of Ps formation.[3-8] It postulates that positrons generated in the radioactive decay of certain nuclides are slowing down from higher energies and pass through an energy gap in which they can abstract an electron and form Ps ($e^+e^-$).

It was assumed that the energetic o-Ps, which is formed in the Ore gap with kinetic energies varying between 6.8 eV and thermal energies, has, as any other "hot" atom, two alternatives, namely, it may undergo chemical reactions while still hot, followed by a rapid annihilation of the positron in the resulting reaction products, or lose its excess kinetic energy in moderating collisions, becoming a thermalized Ps atom and reacting as such.

The thermalization time of Ps is sufficiently long so that the presence and the reactions of the thermalized Ps which lead to subsequent rapid annihilation of the positron can be recognized by the appearance of a second (long-lived) component in the time spectra, and the changes of the average lifetime, $\tau_2$, associated with this component.

On the other hand, "hot" reactions between solute and Ps atom have to take place shortly after the birth of the Ps before it becomes thermalized. Thus, the lifetime of the positrons incorporated in positronium atoms taking part in "hot" reactions will become indistinguishable from that of the free positrons or p-Ps, i.e., it will drop out of the second component and appear as a part of the short-lived component. The only observable evidence for the occurrence of such a hot reaction is then a reduction of the number of Ps atoms reaching thermal energies. Since this number is related to the intensity, $I_2$, of the second component in the time spectra, hot reaction can be detected by a decrease of $I_2$.

By using this approach it was found that in aqueous solutions of inorganic ions where the rate constant for the reaction between Ps and solute remains close or below the detectable limit ($10^7$ $M^{-1}$ $s^{-1}$), i.e., where reactions of thermal Ps are extremely slow, $I_2$ eventually assumes a lower limit (or saturation value), $I_2^{satd} \neq 0$, which is characteristic for each individual compound.[5]

This result was interpreted by assuming that $(I_2^0 - I_2^{satd})/I_2^0$ represents the fraction of all Ps atoms formed which have sufficient energy to overcome the reaction barrier ($I_2^0$ is the intensity in pure solvent).

By correlating the $I_2^{satd}$ in the various systems to the free-energy changes involved in the reduction of the inorganic ion ($A_{aq}^{n+} + e \rightarrow A^{(n-1)+}$) the redox potential of the Ps atom was roughly approximated.[15]

If one wants to interpret the experimental results in terms of the spur reaction model[9-14] which postulates that Ps is formed as a result of a spur reaction between the positron and a secondary electron in the positron spur, one would have to consider the competition between positron and electron combination and the reaction of the electron with the scavenger (inorganic ions) in the spur created by the positron.

Qualitatively one can expect that the presence of compounds which can effectively react with the electrons formed in the spur will reduce the probability of Ps formation via recombination of an electron with the positron. Since the number of (thermalized) Ps atoms formed is related to $I_2$, the intensity of the long-lived component in the positron lifetime spectra (vide supra), a decrease in Ps formation will again be indicated by a simultaneous reduction of $I_2$.

A quantitative approach to assess the Ps yield as a function of scavenger concentration would have to make certain assumptions about the competition between positrons and scavenger for the available electrons.

If one assumes that the Ps yield resulting from the electron–positron combination in the positron spur can be compared with the electron–ion recombination in the electron spur one can invoke the familiar concepts from

radiation chemistry,[11] where by using a simple competitive kinetic model a function F(M) has been derived which describes the removal of free electrons by the scavenger at moderate scavenger concentration [M]:[16,17]

$$F(M) = k[M]/(1 + k[M]) \quad (1a)$$

($k$ is the scavenging constant).

Thus in analogy with the approach used by Hamill[16,17] and several other authors for a simple competition for dry or solvated electrons in a solution one could derive the following correlation between the o-Ps formation probability $P$ at a given solute concentration [M], if the o-Ps formation probability in the pure solvent is $P^0$:[11]

$$P = P^0\left(1 - \frac{K[M]}{1 + K[M]}\right) \quad (1b)$$

or

$$P = P^0/(1 + K[M]) \quad (1c)$$

where $K$ is now the rate constant for inhibition of o-Ps formation.

If the solute is also capable of undergoing chemical reaction with *thermal* o-Ps (rate constant $K_1$) and if the thermal o-Ps annihilation with solvent is $\lambda_p$, and furthermore the annihilation rate of the free positrons in solution is $\lambda_F$, then the following expression can be obtained which correlates the intensity $I_2$ with the Ps formation probability $P$:[18]

$$I_2 = {}^3/_4 P(1 + K_1[M]/(\lambda_F - \lambda_P - K_1[M])) \quad (2)$$

In a pure solvent (intensity $I_2^0$)

$$I_2^0 = {}^3/_4 P^0 \quad (3)$$

Substitution of eq 2 and 3 into eq 1 results:[19]

$$I_2 = \frac{I_2^0(\lambda_F - \lambda_P)}{\lambda_F - \lambda_P + ((\lambda_F - \lambda_P)K - K_1)[M] - KK_1[M]^2} \quad (4)$$

In water:

$$\lambda_{F_{est}} = 2.50 \times 10^9\ s^{-1} \qquad I_2 = 28\%$$
$$\lambda_{P_{obsd}} = 0.54 \times 10^9\ s^{-1}$$

$K_1$ can be obtained from the well-know correlation between the lifetime $\tau_2$ of the long-lived component in the positron lifetime spectra and the solute concentration. In dilute solutions:

$$1/\tau_2 \equiv \lambda_2 = \lambda_P + K_1[M] \quad (5)$$

Thus by determining $I_2$ at various solute concentrations [M], the rate constant $K$ for inhibition of Ps formation can be derived.

If the solute is only weakly reacting with thermal o-Ps, i.e., $K_1 < 10^8\ s^{-1}$, and in the case of relatively small solute concentrations, i.e., [M] < 1 M, $K_1[M]$ and $K_1K[M]^2$ can be considered as insignificant compared with $(\lambda_F - \lambda_P)$ and $(\lambda_F - \lambda_P)K[M]$, respectively, and eq 4 can be simplified and rewritten to give

$$(I_2^0/I_2) - 1 = K[M] \quad (6)$$

Plots of this function for various aqueous solutions containing solutes which exhibit only a weak reactivity toward thermal Ps are shown in Figure 1. (Data taken from ref 5–8.)

The $K$ values assessed from these plots are summarized in Table I which also includes for comparison the known

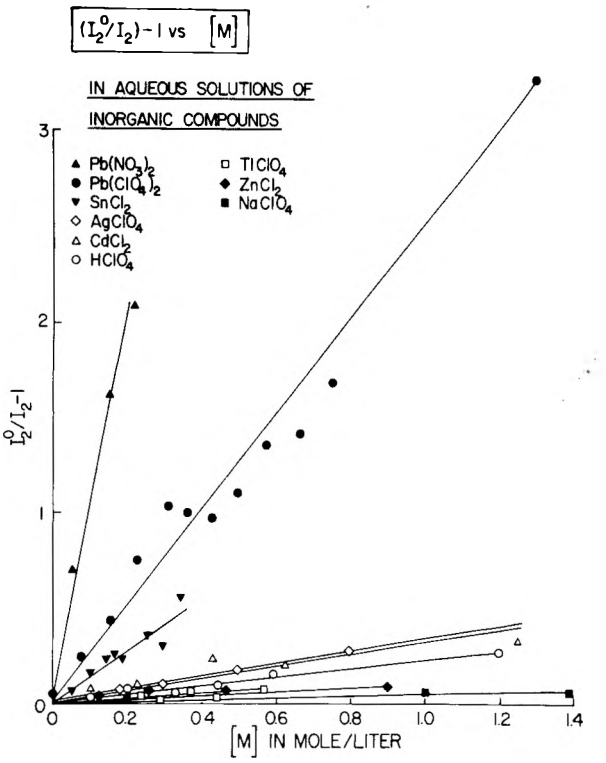


**Figure 1.** Plot of $(I_2/I_2^0) - 1$ vs. [M] in aqueous solutions of organic compounds: ▲, $Pb(NO_3)_2$; ▼, $SnCl_2$; △, $CdCl_2$; □, $TlClO_4$; ■, $NaClO_4$; ●, $Pb(ClO_4)_2$; ◇, $AgClO_4$; O, $HClO_4$; ◆, $ZnCl_2$.

TABLE I: Positronium Inhibition Constants, $K$, Rate Constants, $K(e_{aq}^-)$, and $C_{37}$ Values for the Reaction of a Variety of Inorganic Ions in Solution with Solvated Electrons and Dry Electrons, Respectively

| Ion | $K$, $M^{-1}$ | $K(e_{aq}^-)$, $10^{10}\ M^{-1}\ s^{-1}$ | Ref | $C_{37}$,[a] mol $dm^{-3}$ |
|---|---|---|---|---|
| $Pb^{2+}$ | 2.5 | 3.9 | 25 | |
| $Sn^{2+}$ | 1.2 | 0.34 | 25 | |
| $Cd^{2+}$ | 0.37 | 3.5 | 21 | 0.35 ± 0.05 |
| $Ag^+$ | 0.35 | 3.2 | 25 | |
| $H^+$ | 0.22 | 1.2 | 21 | >10 |
| $Tl^+$ | 0.10 | 3.7 | 25 | |
| $Zn^{2+}$ | 0.10 | 0.12 | 21 | 8 ± 1 |
| $Na^+$ | <0.05 | <0.00001 | 25 | |
| $NO_3^-$ | 3.5 | 2.0 | 21 | 0.45 ± 0.05 |

[a] Reference 21.

rate constants for the reactions of these ions with hydrated electrons.

No apparent correlation seems to exist between the inhibition constants $K$ and the reported rate constants for the reactions of hydrated electrons (Table I) with these compounds, which makes an interpretation of the observed inhibition in terms of a competition for solvated electrons between positron and scavenger, i.e., the inorganic ions, rather unlikely.

Another possibility would involve the combination of dry electrons and positrons, in which case scavenger and positron compete for the dry electrons. Unfortunately very little is known about the rate constants for dry electron reactions so that no satisfactory comparison can be made.[20] In the few cases for which the relative activities of the dry electrons toward the scavenger have been determined, e.g., in the form of $C_{37}$ values as reported by Lam and Hunt,[21] no correlation between $K$ and $C_{37}$ can be found (Table I). However, one has to keep in mind that the $C_{37}$ values are still very uncertain[20] and therefore do not allow any final conclusions as to the participation of dry electrons in the Ps formation process.

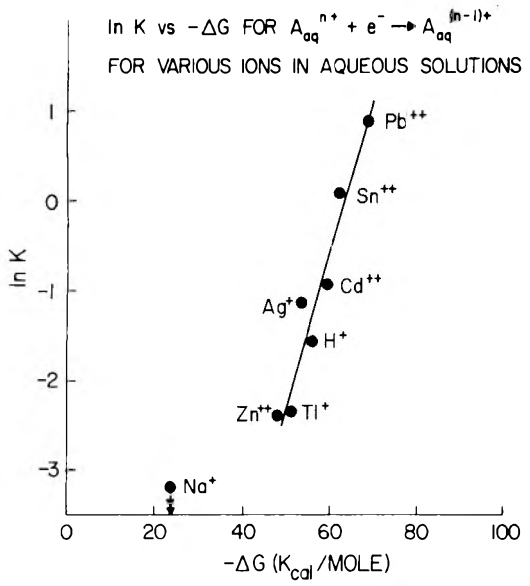


**Figure 2.** ln $K$ vs. $-\Delta G$ for $A_{aq}^{n+} + e^- \rightarrow A_{aq}^{(n-1)+}$ for various ions in aqueous solutions.

If, however, these $C_{37}$ values should prove to be correct, it would most likely preclude dry electrons from being considered as precursors of the Ps and other explanations such as the one suggested by Eldrup et al.[11] would have to be invoked if one wants to explain the results within the framework of the spur model.

On the other hand, Byakov[22] presented some evidence for the participation of dry electrons in Ps formation when he studied the nature of the precursors of radiolytic molecular hydrogen in water and compared the observed yields of radiolytic $H_2$ in the presence of scavengers with the Ps yields in similar solutions. On the basis of his results he suggested that both $H_2$ and Ps have nonsolvated electrons as common precursors.[22]

In Figure 2 the inhibition constants $K$ are plotted on a logarithmic scale as a function of $-\Delta G°$, the free energy for the one electron transfer process.

$\Delta G°$ has been obtained either directly from the known standard redox potentials or calculated by using Baxendale's method.[7,15,23] In the case of $Ag^+|Ag^0$, $Tl^+|Tl^0$, etc. the standard redox potentials were used and corrections made for the sublimation energy which does not become available in these reactions because of the small number of atoms involved.

The correlation between the inhibition constants $K$ and free energy for the one electron transfer process (Figure 2) is interesting. It could be interpreted by assuming that the energy maximum of the cross section curve for electron attachment to the scavenger ions coincides with the free energy change involved in the process:

$$A_{aq}^{+} + e_{dry}^{-} \rightarrow A_{aq}^{(n-1)+} \qquad (7)$$

or as previously suggested for the case of $Cd^{2+}$[11] to the fact that only "dry" electrons with energies above a certain threshold can be scavenged by these ions.

The higher the energy threshold the less electrons are available which fulfill this minimum energy requirement for reaction 7 and therefore less electrons will be scavenged.

This explanation, however, closely resembles certain features of the Ore model[1] and it will be difficult to distinguish the results of the scavenging of dry or kinetically excited electrons from the results of a similar attachment of kinetically excited positrons or Ps atoms to the scavenger.

In the latter case one could argue that the cross section curve for nondissociative or dissociative attachment of kinetically excited positrons or Ps atoms to these inorganic ions, resulting among others in Ps complex formation[24] or electron transfer, shows certain energy maxima which again coincide with the $-\Delta G$ values for the electron transfer, assumptions which are an essential part of the modified Ore model.[7,8]

Thus, in summary, it can be said that the reevaluation of our experimental data seems to exclude Ps formation in aqueous solution via recombination of *positrons* with hydrated electrons. It can, however, not distinguish between Ps formation via positron- (dry) electron combination (spur model) or Ps formation in the Ore gap.

Such a decision will have to wait until more reliable data on the rate constants of dry electrons with these scavengers become available which allow a conclusive comparison with the Ps inhibition constants.

If this comparison should suggest that dry electrons are the precursors of Ps the Ps inhibition studies could in turn provide a convenient tool to study the reactions of dry electrons with chemical compounds.

*Acknowledgment.* Work supported in part by the U.S. Energy Research and Development Agency.

## References and Notes

(1) For general references, see (a) J. Green and J. Lee, "Positronium Chemistry", Academic Press, New York, N.Y., 1964; (b) V. I. Goldanskii, *At. Energy Rev.*, **6**, 3 (1968); (c) J. D. McGervey in "Positron Annihilation", A. T. Stewart and L. O. Roellig, Ed., Academic Press, New York, N.Y., 1967, p 143; (d) J. A. Merrigan, S. J. Tao, and J. H. Green, "Physical Methods of Chemistry", Vol. 1, Part III. D A. Weissberger and B. W. Rossiter, Ed., Wiley, New York, N.Y., 1972; (e) H. J. Ache, *Angew. Chem., Int. Ed. Engl.*, **11**, 179 (1972); (f) J. H. Green, *MTP Int. Rev. Sci., Radiochem.*, **8**, 251 (1972); (g) V. I. Goldanskii and V. G. Virsov, *Annu. Rev. Phys. Chem.*, **22**, 209 (1971).
(2) J. E. Jackson and J. D. McGervey, *J. Chem. Phys.*, **38**, 300 (1963).
(3) S. J. Tao and J. H. Green, *J. Chem. Soc. A*, 408 (1968).
(4) S. J. Tao and J. H. Green, *J. Phys. Chem.*, **73**, 882 (1969).
(5) L. J. Bartal, J. B. Nicholas, and H. J. Ache, *J. Phys. Chem.*, **76** 1124 (1972).
(6) L. J. Bartal and H. J. Ache, *Radiochim. Acta*, **17**, 205 (1972).
(7) L. J. Bartal and H. J. Ache, *Radiochim. Acta*, **19**, 49 (1973).
(8) H. J. Ache in "Hot Atom Chemistry Status Report", IAEA, Vienna, 1975, pp 81/105.
(9) O. E. Mogensen, *J. Chem. Phys.*, **60**, 998 (1974).
(10) P. Jansen, M. Eldrup, O. E. Mogensen, and P. Pagsberg, *Chem. Phys.*, **6**, 265 (1974).
(11) M. Eldrup, V. P. Shantarovich, and O. E. Mogensen, *Chem. Phys.*, **11**, 129 (1975).
(12) P. Jansen, M. Eldrup, B. Skytte Jensen, and O. E. Mogensen, *Chem. Phys.*, **10**, 303 (1975).
(13) O. E. Mogensen, *Appl. Phys.*, **6**, 315 (1975).
(14) S. J. Tao, *Appl. Phys.*, **10**, 67 (1976).
(15) L. J. Bartal and H. J. Ache, *J. Inorg. Nucl. Chem.*, **36**, 922 (1974).
(16) W. H. Hamill, *J. Phys. Chem.*, **73**, 1341 (1969).
(17) T. Sawai and W. H. Hamill, *J. Phys. Chem.*, **74**, 3914 (1970).
(18) This equation is identical with the formula used by A. G. Maddock et al.[19] to interpret their experimental results on Ps inhibition by halo acetates. For a derivation of eq 2 see: T. L. Williams and H. J. Ache, *J. Chem. Phys.*, **50**, 4493 (1969); H. Horstman, *J. Inorg. Nucl. Chem.*, **27**, 1191 (1965).
(19) A. G. Maddock, J. Ch. Abbee, and A. Haessler, *Chem. Phys.*, **17**, 343 (1976).
(20) For a review on dry electrons see, e.g., G. Czapski and E. Peled, *Proc. Int. Congr. Radiat. Res., 5th*, 356 *ff* (1975).
(21) K. Y. Lam and J. W. Hung, *Int. J. Radiat. Phys. Chem.*, **7**, 317 (1975).
(22) V. M. Byakov, *Int. J. Radiat. Chem.*, **8**, 283 (1976).
(23) J. H. Baxendale and R. S. Dixon, *Z. Phys. Chem.*, **43**, 161 (1964).
(24) See, e.g., W. J. Madia, A. L. Nichols, and H. J. Ache, *J. Am. Chem. Soc.*, **97**, 5041 (1975).
(25) M. Anbar and P. Neta, *Int. J. Appl. Radiat. Isotopes*, **18**, 493 (1967).

# An Equilibrium and Kinetic Investigation of Salt–Cycloamylose Complexes

**R. P. Rohrbach, L. J. Rodriguez, Edward M. Eyring,***

*Department of Chemistry, University of Utah, Salt Lake City, Utah 84112*

**and J. F. Wojcik**

*Chemistry Department, Villanova University, Villanova, Pennsylvania 19085* *(Received December 8, 1976)*

*Publication costs assisted by the Office of Naval Research and the Air Force Office of Scientific Research*

The equilibrium constants and rate constants for the formation of inclusion complexes of cycloheptaamylose with small inorganic anions were measured by a spectrophotometric technique and an ultrasonic relaxation technique, respectively. The stability of the complexes of anions with cycloheptaamylose decreased in the order $ClO_4^- > I^- > SCN^- > Br^- > NO_3^- > Cl^-$. Comparison is made between the equilibrium constants and the interaction of free anions with the solvent. Periodate and $ClO_4^-$ exhibited a complexation rate constant 30 times greater than the remainder of the anions. A concentration independent relaxation was observed for aqueous cyclohexaamylose in the uncomplexed state. No like behavior was observed for cycloheptaamylose. A conformational change in the cycloheptaamylose may be the rate-determining step in the complexation of the more slowly reacting anions.

## Introduction

The cycloamyloses (cyclodextrins) are capable of forming inclusion complexes with a wide variety of guests ranging from hydrophobic to ionic character.[1-3] The mode of ionic complexation is the least studied and understood facet of cycloamylose chemistry. Recently, equilibrium constants for cyclohexaamylose, sometimes denoted by $\alpha$-CD, with various inorganic salts were measured.[4] The complexes were determined to be anionic, and a correlation was observed between the logarithm of the measured equilibrium constant and the "structure breaking" properties of the free anions.

Explanations for the driving force for complexation have been as diverse as the guests which are complexed. Complexation has been attributed to hydrophobic interactions, hydrogen bonding, and nonspecific van der Waals forces.[1] Saenger and co-workers have postulated a driving force arising from the relaxation of the conformational strain in the cyclohexaamylose brought about by complexation.[5] Crystallographic evidence suggests that the cyclohexaamylose in the complexed state with both hydrophobic and ionic guests is in a slightly different conformation than in the uncomplexed state.[5-8]

In the present study of the mode of ionic complexation with cycloamylose, the kinetics, and equilibrium constants of complexation were measured for cycloheptaamylose ($\beta$-CD) and various inorganic salts. The kinetics of an apparent conformational change in pure aqueous cycloheptaamylose and cyclohexaamylose were also studied by means of an ultrasonic absorption relaxation technique.

## Experimental Section

All solutions were prepared using deionized, redistilled water. Cyclohexaamylose and cycloheptaamylose were purchased from Sigma Chemicals and Aldrich Chemicals, respectively. Both cycloamyloses were purified by literature methods.[9] All inorganic salts used were reagent grade sodium salts.

The equilibrium constants for the various salt–cycloheptaamylose systems were measured with a Cary 14 recording UV–vis spectrophotometer equipped with a thermostated cell compartment kept at 25.0 ± 0.1 °C. Equilibrium constants for the various salt–cycloamylose complexes were measured by a spectral competitive inhibition technique.[2] A 4-nitrophenylazo-2′-hydroxy-6′-sulfonaphthalene dye was used in this study and was prepared by standard azo dye coupling procedures.[10]

All spectroscopic measurements were made at 510 nm which corresponds to the largest difference in extinction coefficient between the free and complexed forms of the azo dye. Solutions were 0.1 M in salt and $2.0 \times 10^{-5}$ M in azo dye while the cycloheptaamylose concentration varied from 0 to $10^{-2}$ M. All equilibrium constants were determined at pH 5.7 and an ionic strength $I = 0.1$ M. At least seven solutions varying in cycloheptaamylose concentration were used in obtaining the equilibrium constant for each anion. The equilibrium constant for the dye–cycloheptaamylose system was measured in the same manner as above but with $Na_2SO_4$, a salt which does not complex, establishing the $I = 0.1$ M.[2]

The ultrasonic absorption kinetic measurements were made at a temperature of 25.0 ± 0.1 °C over the frequency range of 15–205 MHz using a laser acousto-optical technique.[11]

## Results

Spectrophotometric titrations were made with 4-nitrophenylazo-2′-hydroxy-6′-sulfonaphthalene and cycloheptaamylose in the presence of the sodium salts of $ClO_4^-$, $I^-$, $SCN^-$, $Br^-$, $NO_3^-$, $Cl^-$, and $SO_4^{2-}$, respectively. The equilibrium constant for the dye interacting with cycloheptaamylose was measured in the absence of added electrolyte and also with $I = 0.1$ M ($Na_2SO_4$). The two measured equilibrium constants were the same within experimental error. The following equation describes the interaction of such hydrophobic guests with cycloheptaamylose:

$$CD + In \overset{K_D}{\rightleftharpoons} CD{\cdot}In \qquad (1)$$

Here In, CD, and CD·In represent the free dye, free cycloheptaamylose, and complexed form of cycloheptaamylose, respectively. In Figure 1, curve A represents the data obtained by plotting the change in absorbance, $\Delta A$, vs. the cycloheptaamylose concentration. In all cases the dye concentration was constant at $2.0 \times 10^{-5}$ M and the cycloheptaamylose varied from 0 to $10^{-2}$ M. The data were plotted using the Hildebrand–Benesi relation.[12] The

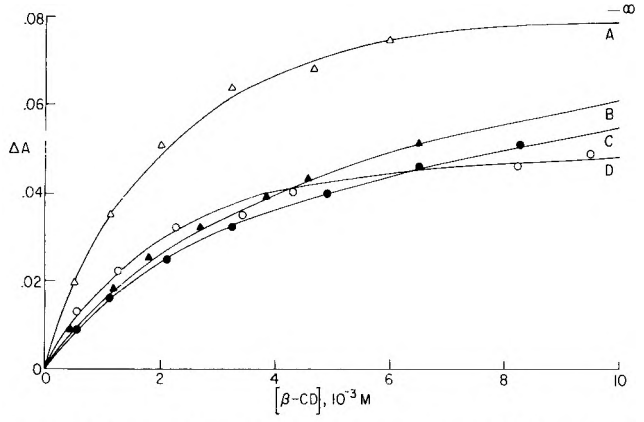


**Figure 1.** Change in absorbance, $\Delta A$, at a wavelength of 510 nm plotted vs. aqueous cycloheptaamylose concentration in pH 5.7, 25 °C solutions that are $2 \times 10^{-5}$ M in 4-nitrophenylazo-2′- hydroxy-6′-sulfonaphthalene and 0.1 M in sodium salts of $SO_4^{2-}$ (curve A), $I^-$ (B), $ClO_4^-$ (C), $SCN^-$ (D). The hash mark identified by an ∞ sign is the $\Delta A$ at infinite cycloheptaamylose concentration determined from the Hildebrand–Benesi relation.

equilibrium constant as well as the extinction coefficient of the fully complexed form of the dye were obtained. Using molar units of concentration, a value $K_D = 7.7 \times 10^2$ was found for the stability constant of the cycloheptaamylose–dye system.

In the spectral competitive inhibition technique[2] for determining the equilibrium constants for the various salt–cycloheptaamylose systems a high concentration of inorganic salt is added to various solutions of cycloheptaamylose and dye. Assuming the lack of occupancy of the cycloheptaamylose binding site by both dye and salt, the equilibrium constants for the various salt–cycloheptaamylose systems are calculated from mass balance relations. The combination of eq 1 with

$$CD + X^- \underset{k_r}{\overset{k_f}{\rightleftharpoons}} CD{\cdot}X^- \qquad (2)$$

describes the interactions. The equilibrium constants are

$$K_D = [CD{\cdot}In]/[CD][In] \qquad (3)$$

$$K_{X^-} = [CD{\cdot}X^-]/[CD][X^-] = k_f/k_r \qquad (4)$$

The total concentrations of cycloheptaamylose and salt are conserved according to the mass balance equations:

$$CD_t = [CD] + [CD{\cdot}In] + [CD{\cdot}X^-]$$

$$X_t^- = [X^-] + [CD{\cdot}X^-] \qquad (5)$$

The observed absorbance, $A$, is given by

$$A = \epsilon_{In}[In] + \epsilon_{CD\cdot In}[CD{\cdot}In] \qquad (6)$$

Since the initial concentrations of all reagents are known as well as $K_D$, $\epsilon_{In}$, and $\epsilon_{CD\cdot In}$ the equilibrium constant for the salt–cycloheptaamylose system, $K_{X^-}$, can be readily obtained.

Figure 1 shows the effect of 0.1 M $ClO_4^-$, $SCN^-$, and $I^-$ on the absorbance of the dye–cycloheptaamylose system. All the ions studied showed similar effects with the exception of $Na_2SO_4$. Perchlorate anion showed the largest effect. Cramer used this method to calculate a $K_{X^-}$ value for the $ClO_4^-$–cyclohexaamylose system.[2] The equilibrium constant calculated in this manner was in good agreement with that obtained by an independent conductometric technique.[4] Table I contains the cycloheptaamylose results along with earlier data[4] for the same ions with cyclohexaamylose.

TABLE I: Stability Constants for Anion–Cycloamylose Complexes

| Anion | Cycloheptaamylose $K_{X^-}$, $M^{-1}$ Obsd[a] | Cycloheptaamylose $K_{X^-}$, $M^{-1}$ Calcd[b] | Cyclohexaamylose $K_{X^-}$, $M^{-1}$ [c] |
|---|---|---|---|
| $ClO_4^-$ | 26.7 | 20.2 | 28.9 |
| $SCN^-$ | 9.9[c] | 13.1 | 18.7 |
| $I^-$ | 18.0 | 17.5 | 12.4 |
| $NO_3^-$ | 5.5 | 7.4 | 1.4 |
| $Br^-$ | 6.5 | 5.5 | 3.5 |
| $Cl^-$ | 2.56 | 2.3 | N.B. |

[a] Determined by spectrophotometric competitive inhibition study. [b] Calculated from the $B^-$ structure breaking parameter correlation. [c] Calculated from conductimetric data and originally reported in ref 4.

TABLE II: Relaxation Parameters from Computer Analysis for Aqueous Cyclohexaamylose at 25 °C[a]

| $[\alpha\text{-CD}]_0$, M | $f_R$, MHz | $10^{17}A$, Np $cm^{-1}$ $s^2$ | $10^{17}B$, Np $cm^{-1}$ $s^2$ | $10^{18}$-RMS[b] |
|---|---|---|---|---|
| 0.102 | 12.01 | 52.1 | 26.8 | 0.71 |
| 0.0714 | 12.32 | 39.5 | 24.8 | 0.50 |
| 0.0500 | 12.66 | 36.9 | 23.0 | 0.51 |

[a] All symbols as defined in the text. [b] Root mean square deviation.

The calculated $K_{X^-}$ values for all anions except $SCN^-$ are independent of the cycloheptaamylose concentration as an equilibrium constant should be. In the case of $SCN^-$, a concentration dependent $K_{X^-}$ was observed, and a value of $K_{X^-} = 10.0$ was obtained at an extrapolated zero concentration of cycloheptaamylose. This is consistent with a value of $K_{X^-} = 9.9$ calculated by a conductometric technique.[4] Figure 1 shows that the asymptotic $\Delta A$ value in the case of $SCN^-$ is significantly smaller than the asymptotic $\Delta A$ value measured for the dye–cycloheptaamylose system in the presence of other salts. Thiocyanate anion at 0.1 M showed no effect on the absorption spectrum of the pure dye.

The ultrasonic absorption data, expressed as $(\alpha/f^2)$ Np $s^2$ $cm^{-1}$, were analyzed in terms of a single relaxation using the following relation

$$(\alpha/f^2) = A[1 + (f/f_r)]^{-1} + B \qquad (7)$$

where $A$ denotes the relaxation amplitude of the process, $f$ is the experimental frequency, $f_r$ is the relaxational frequency, and $B$ is the solvent absorption. Table II shows the experimental ultrasonic absorption relaxation frequencies and the calculated parameters $A$ and $B$ that give the best fit to eq 7 for the pure aqueous cyclohexaamylose solutions at different concentrations. The raw ultrasonic absorption data are available as supplementary material. (See paragraph at end of text regarding supplementary material.) The observed relaxation frequency is independent of the concentration of cyclohexaamylose and occurs at 12.3 MHz with an experimental error of ±0.5 MHz. As would be expected from solutions of increasing viscosity, the background absorption, $B$, at high frequencies was above that of pure water alone varying from an increase of $5 \times 10^{-17}$ Np $s^2$ $cm^{-1}$ over water for the most concentrated solution, 0.102 M, to $1 \times 10^{-17}$ Np $s^2$ $cm^{-1}$ over water for the 0.05 M solution.

A concentration independent relaxation in pure aqueous cyclohexaamylose can be described by

$$CD \underset{k_{-1}}{\overset{k_1}{\rightleftharpoons}} CD' \qquad (8)$$

TABLE III: Relaxation Parameters from Computer Analysis for Aqueous Complexation by Cycloheptaamylose[a]

| $[\beta\text{-CD}]_0$,[b] M | $[\text{Anion}]_0$,[b] M | $f_R$, MHz | $10^{17}A$, Np cm$^{-1}$ s$^2$ | $10^{17}B$, Np cm$^{-1}$ s$^2$ | $10^{18}$RMS[c] |
|---|---|---|---|---|---|
| | | Perchlorate | | | |
| 0.010 | 0.0116 | 18.28 | 22.6 | 21.7 | 0.55 |
| 0.019 1 | 0.0120 | 19.70 | 27.2 | 21.7 | 0.73 |
| 0.025 2 | 0.0114 | 20.56 | 39.4 | 21.7 | 0.79 |
| 0.010 1 | 0.0509 | 26.01 | 20.5 | 21.7 | 0.63 |
| | | Iodide | | | |
| 0.019 7 | 0.297 | 3.46 | 334.1 | 22.4 | 1.0 |
| 0.009 72 | 1.09 | 11.39 | 46.1 | 19.8 | 0.55 |
| 0.010 8 | 1.48 | 16.61 | 35.5 | 19.5 | 1.0 |
| | | Thiocyanate | | | |
| 0.011 6 | 0.560 | 4.62 | 192. | 21.00 | 1.59 |
| 0.024 0 | 1.51 | 11.20 | 41.3 | 21.00 | 1.0 |
| 0.028 5 | 1.92 | 13.67 | 44.5 | 19.97 | 1.1 |
| | | Bromide | | | |
| 0.010 6 | 0.981 | 8.04 | 76.5 | 20.3 | 0.81 |
| 0.010 0 | 1.52 | 12.03 | 38.5 | 19.6 | 0.60 |
| 0.011 2 | 1.98 | 15.28 | 33.8 | 17.3 | 0.79 |
| | | Nitrate | | | |
| 0.010 2 | 1.02 | 8.25 | 84.8 | 20.4 | 0.76 |
| 0.009 92 | 1.5 | 12.15 | 44.8 | 21.0 | 0.63 |
| 0.010 3 | 2.02 | 16.43 | 29.0 | 21.8 | 0.63 |
| | | Chloride | | | |
| 0.009 71 | 1.0 | 11.94 | 42.0 | 20.0 | 0.54 |
| 0.009 17 | 1.49 | 16.24 | 22.3 | 19.6 | 0.52 |

[a] All symbols as defined in the text. [b] The subscript zero on concentration denotes total initial concentrations. [c] Root mean square deviation.

for which

$$\tau^{-1} = k_1 + k_{-1} \quad (9)$$

Since the reciprocal relaxation time equals the sum of two rate constants and is independent of concentration (eq 9), in the absence of relaxation amplitude data at several temperatures the values of $k_1$ and $k_{-1}$ can be known only as the sum. Such first-order processes as reaction 8 are generally the result of conformational changes that alter the solvation of the sound absorbing solute.

Aqueous cycloheptaamylose, at 0.016 M, showed no similar absorption over the accessible 15–205-MHz frequency range. In this case only the solvent absorption was observed. The fact that the cyclohexaamylose showed an absorption whereas the cycloheptaamylose did not may be attributable to the more limited solubility of cycloheptaamylose in water. Using the relaxation amplitude calculated for cyclohexaamylose, the absorption of cycloheptaamylose, if it were present, at 0.016 M would only be marginally above that of the solvent and would therefore be immeasurable.

Ultrasonic absorption relaxation frequencies for aqueous cycloheptaamylose complexing with $ClO_4^-$, $SCN^-$, $NO_3^-$, $Cl^-$, $Br^-$, and $I^-$ are presented in Table III. Raw ultrasonic absorption data appear in an appendix (supplementary material). In these cases only one relaxation was detected which was concentration dependent on both cycloheptaamylose and salt. All the data are consistent with the complexation reaction of eq 2. When high concentrations of salt were employed (up to 2 M) variable backgrounds were used to fit the ultrasonic absorption data. The $B$ values decreased below that of pure water as the concentration of salt increased, being as low as $17 \times 10^{-17}$ Np s$^2$ cm$^{-1}$ in the most concentrated solution of NaBr. This background absorption was consistent with the observed absorption of only the salt and water alone. This depression of the solvent ultrasonic absorption by simple electrolytes is attributable to several factors.[13]

TABLE IV: Complexation Rate Constants, $k_f$, and Dissociation Rate Constants, $k_r$, for Several Anions and Aqueous Cycloheptaamylose at 25 °C

| Anion | $k_f$, M$^{-1}$ s$^{-1}$ | $k_r$, s$^{-1}$ |
|---|---|---|
| $ClO_4^-$ | $(2.0 \pm 0.1) \times 10^9$ | $(7.4 \pm 2) \times 10^7$ |
| $I^-$ | $(6.5 \pm 0.3) \times 10^7$ | $(3.6 \pm 1) \times 10^6$ |
| $SCN^-$ | $(4.4 \pm 0.2) \times 10^7$ | $(4.4 \pm 1) \times 10^6$ |
| $Br^-$ | $(4.5 \pm 0.2) \times 10^7$ | $(6.9 \pm 1) \times 10^6$ |
| $NO_3^-$ | $(4.5 \pm 0.2) \times 10^7$ | $(8.2 \pm 2) \times 10^6$ |
| $Cl^-$ | $(5.4 \pm 0.3) \times 10^7$ | $(2.1 \pm 0.5) \times 10^7$ |

The individual rate constants for anionic complexation, $k_f$ and $k_r$, were calculated using the following equation:

$$\tau^{-1} = k_f([\text{CD}] + [\text{X}^-] + K_{\text{X}^-}^{-1}) \quad (10)$$

Table IV contains the rate constants calculated in this manner.

## Discussion

Anions bind to cycloheptaamylose as they do to cyclohexaamylose to varying degrees depending on the anion. It is evident from the new data that cycloheptaamylose binds anions roughly as well as does cyclohexaamylose and in the same general order of stability. Increasing the ring size by one glucose residue does not seem to affect the nature of anionic complexation although ring size does play a significant role in hydrophobic binding.[3,10] One would expect the relaxation of torsional angle strain to be greater in cyclohexaamylose than in cycloheptaamylose due to the smaller size and therefore more rigid structure of the former. Thus the equivalence of equilibrium constants for cyclohexa- and cycloheptaamylose introduces some doubt as to the importance of the conformational relaxation as the principal driving force for ionic guest–host complexation in the cycloamyloses.

A correlation exists between the order of stability of the complexes and "structure breaking" properties of the free anions as has been shown in previous work on salt–cyclohexaamylose complexes.[4] A parameter which correlates

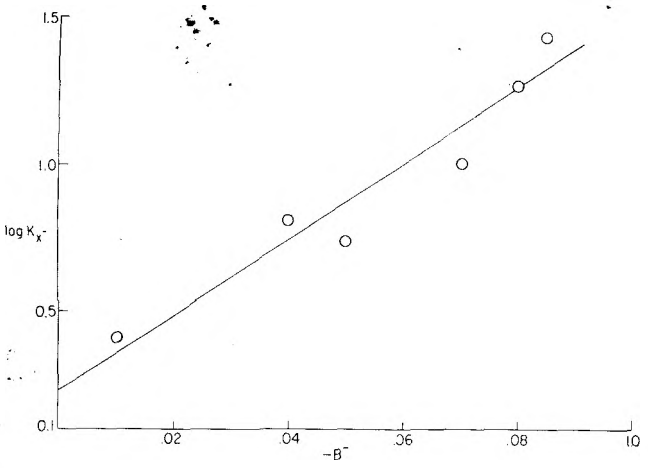


**Figure 2.** Logarithm of the stability constant $K_{X^-}$ for several aqueous cycloheptaamylose–salt solutions vs. values of the $B^-$ "structure breaking" parameter for the several anions. A least-squares straight line has been drawn with a correlation coefficient of 0.92. (The negative of $B^-$ values have been plotted for convenience.)

the "structure breaking" properties of the anions is the coefficient of the linear term of the concentration dependence of proton nuclear magnetic resonance relaxation rates in aqueous salt solutions, $B^-$.[14] If the logarithm of the equilibrium constant for the various salt–cycloheptaamylose systems is plotted against the $B^-$ value for each anion a good correlation is observed (Figure 2). The line $\log K_{X^-} = -12.5B^- + 0.242$ is the linear least-squares fit of the data with a correlation coefficient of 0.92. Table I contains the calculated equilibrium constants using the above relation. If one compares the similar correlation found[4] for cyclohexaamylose, $\log K_{X^-} = -26.5B^- - 0.75$, one finds that the magnitude of the slope term for cyclohexaamylose is significantly larger. This indicates that the salt–cycloamylose equilibrium constant for cyclohexaamylose is more sensitive to the $B^-$ values or "structure breaking" effects of the free anions.

The abnormal effect $SCN^-$ has on the spectral titration (see Figure 1) warrants some explanation. If the extinction coefficient varies continuously from $\epsilon_{In}$ characterizing free indicator to $\epsilon_{CD\text{-}In}$ of the complex depending upon the depth of penetration of dye into the cycloamylose cavity, the $SCN^-$ may be affecting this penetration depth. In other words, in the case of $SCN^-$ the assumption of no simultaneous complexation of dye and anion by cycloheptaamylose may be invalid. Results of x-ray studies[7] of crystalline complexes of cyclohexaamylose suggest the anion is probably located in the hydrophilic plane defined by the primary hydroxyl groups. Hydrophobic guests such as the dye are generally believed to be located within the hydrophobic cavity.[1] Since the cavity may have these two distinct regions, dual occupancy by different guests could conceivably occur in some cases. Binding sites for hydrophobic guests and ionic guests would each have their own unique driving force responsible for complexation.

The rate constants calculated for complexation, $k_f$ (see Table IV), are strikingly similar. All the anions with the exception of $ClO_4^-$ have roughly the same forward rate constant. The $ClO_4^-$ has a $k_f$ a factor of 30 larger than that measured for the rest of the anions and approaches the diffusion controlled limit. The decomplexation rate constant, $k_r$, for all the ions increases with decreasing equilibrium constant, again with the exception of $ClO_4^-$.

Since $ClO_4^-$ is anomalous with respect to $k_f$, the kinetics of complexation of $IO_4^-$ were also studied. Periodate ion reacts oxidatively with such sugars, hence the kinetics were measured immediately after preparation of the solutions. A slow degradation process was indeed observed. However, this reaction was slower than the time necessary to measure the kinetics of complexation. The amplitude of the ultrasonic absorption associated with this slow chemical process decreased in a few hours to a constant value identical with that observed in a pure aqueous periodate solution of the same concentration ($38.2 \times 10^{-17}$ Np cm$^{-1}$ s$^2$ for 0.05 M concentration). A 0.01 M cycloheptaamylose solution that was also 0.05 M in $IO_4^-$ gave rise to a $72.2 \times 10^{-17}$ Np cm$^{-1}$ s$^2$ ultrasonic absorption amplitude. Since the stability constant of eq 2 could not be measured, the correlation between log $K$ and $B^-$ (Figure 2) was used to calculate an equilibrium constant for the $IO_4^-$–cycloheptaamylose system, $K_{X^-}$(calcd) = 15.5. The kinetic data obtained demonstrated that $IO_4^-$ has a $k_f$ similar to that obtained for $ClO_4^-$.

Since all the $k_f$s for the anions, with the exception of $ClO_4^-$ and $IO_4^-$, are roughly equal and well below the diffusion controlled limit, some other process is rate limiting. When log $k_f$ is plotted vs. reciprocal anionic radius for all these anions no systematic trend is found suggesting that anion desolvation is not rate determining for $k_f$. It should be added parenthetically that a linear correlation of log $k_f$ with reciprocal ionic radius is well known for similarly charged cations, and the present range of anionic radii (3.19–1.81 Å) is quite comparable to that required in isovalent cations to convincingly demonstrate that cation desolvation is rate limiting in their complexation.

The conformational relaxation reported above for pure aqueous cyclohexaamylose could occur on the same time scale as a rate limiting conformational change in cycloheptaamylose in going from the uncomplexed to the complexed state[5-8] in all cases except $ClO_4^-$ and $IO_4^-$. The complexation mechanism could then be described as

$$CD + X^- \overset{K_0}{\rightleftharpoons} CD||X^- \overset{k_0}{\rightleftharpoons} CD\text{-}X^- \qquad (11)$$

where the first equilibrium is achieved very rapidly and may be described as the formation of a contact ion complex and the next step involves the slower rate-determining conformational change of the cycloamylose complex. To compare the measured first-order relaxation time of the conformational change of cyclohexaamylose to the overall second-order complexation rate constant $k_f$, it is necessary to calculate the equilibrium constant $K_0$ for contact ion formation since

$$k_f = K_0 k_0 \qquad (12)$$

Theoretical expressions exist[15] for $K_0$ from which a value $K_0 = 1.51 \pm 0.15$ is calculated. From this and measured values of $k_f$ it follows that $k_0 \simeq 3.4 \pm 0.7 \times 10^7$ s$^{-1}$ which is of the same order of magnitude as the $\tau^{-1} = k_1 + k_{-1} = 7.7 \times 10^7$ s$^{-1}$ measured for a conformational change in aqueous cyclohexaamylose. This similarity favors the speculation that a conformational change is rate determining in the anion complexation process.

The $ClO_4^-$ and $IO_4^-$ ions may not show this rate-limiting behavior because of their larger radii. They may be capable of forming a straddle type complex with either conformation of the cycloheptaamylose because these anions are too large to fit into the primary (smaller) side of the cycloheptaamylose. In such a case a cycloamylose conformational change would not be rate limiting for anion complexation.

*Acknowledgment.* This work was supported in part by an Office of Naval Research contract, by Grant AFOSR 73-2444C from the Directorate of Chemical Sciences of the Air Force Office of Scientific Research, and by a fellowship

to L.J.R. from the Commission for Cultural Exchange between the U.S. and Spain.

*Supplementary Material Available:* Appendices I and II contain respectively raw ultrasonic absorption data for aqueous cyclohexaamylose solutions and similar data for aqueous cycloheptaamylose solutions to which sodium salts have been added (8 pages). Ordering information is available on any current masthead page.

## References and Notes

(1) D. W. Griffiths and M. L. Bender, *Adv. Catal.*, **23**, 209 (1973).
(2) F. Cramer, W. Saenger, and H-CH. Spatz, *J. Am. Chem. Soc.*, **89**, 14 (1967).
(3) E. A. Lewis and L. D. Hansen, *J. Chem. Soc., Perkin Trans. 2*, 2081 (1973).
(4) J. F. Wojcik and R. P. Rohrbach, *J. Phys. Chem.*, **79**, 2251 (1975).
(5) W. Saenger, R. K. McMullan, J. Fayos, and D. Mootz, *Acta Crystallogr., Sect. B*, **30**, 2019 (1974).
(6) B. Hingerty and W. Saenger, *J. Am. Chem. Soc.*, **98**, 3357 (1976).
(7) A. Hybl, R. W. Rundle, and D. E. Williams, *J. Am. Chem. Soc.*, **87**, 2779 (1965).
(8) P. C. Manor and W. Saenger, *J. Am. Chem. Soc.*, **96**, 3630 (1974).
(9) D. French, M. L. Levine, J. H. Pazor, and E. Norbery, *J. Am. Chem. Soc.*, **71**, 353 (1949).
(10) R. P. Rohrbach, Ph.D. Thesis, Villanova University, Villanova, Pa., 1975.
(11) M. M. Farrow, S. L. Olsen, N. Purdie, and E. M. Eyring, *Rev. Sci. Instrum.*, **47**, 657 (1976).
(12) H. A. Benesi and J. H. Hildebrand, *J. Am. Chem. Soc.*, **71**, 2703 (1949).
(13) J. Stuehr and E. Yeager in "Physical Acoustics", Vol. II, Part A, W. P. Mason, Ed., Academic Press, New York, N.Y., 1965, Chapter 6.
(14) H. G. Hertz, *Water, Compr. Treat.*, **3**, 368 (1973).
(15) For references see P. Hemmes, *J. Am. Chem. Soc.*, **94**, 75 (1972).

# Calorimetric Studies of Complex Formation of Transition Metal Ions with 2,2′,2″-Terpyridine

**Kwang-Yil Kim**[†] **and George H. Nancollas***

*Chemistry Department, State University of New York at Buffalo, Buffalo, New York 14214* *(Received January 10, 1977)*

*Publication costs assisted by the State University of New York at Buffalo*

Calorimetric studies have been made at 25 °C of the formation of cobalt(II), nickel(II), and copper(II) complexes with 2,2′,2″-terpyridine at an ionic strength maintained constant at 0.1 M by the addition of potassium nitrate. The results have been combined with free energy data to provide $\Delta G$, $\Delta H$, and $\Delta S$ values for each of the equilibria. Values of the thermodynamic data strongly support the tridentate coordination of the ligand in these complexes. The temperature independent components of the enthalpy changes have been calculated and are compared with the values for other nitrogen coordinating ligands.

## Introduction

There has been considerable interest in the bidentate and tridentate analogues of the pyridine molecule as ligands for transition metal complex formation because of their similarity to the biologically important heterocyclic nitrogen ligands such as the porphyrins and purines. Although some thermodynamic studies have been made of transition metal complex formation with a number of bidentate nitrogen coordinating ligands including heterocyclic nitrogen compounds,[1-3] few tridentate ligands have been investigated. 2,2′,2″-Terpyridine is of particular interest because it forms very stable complexes with transition metal ions.[4-7] It is a weak base and values of the proton association constants have been reported by a number of workers.[6-9] In addition, equilibrium constants of complexation with some transition metals have been reported over a narrow temperature range from which approximate thermodynamic functions have been calculated.[4-6] The present study was undertaken in order to obtain more reliable thermodynamic data for the copper(II)-, cobalt(II)-, and nickel(II)-terpyridine systems using a direct calorimetric method.

## Experimental Section

2,2′,2″-Terpyridine, obtained from the J. T. Baker Chemical Co. and from G. Frederick Smith Chemical Co., was first recrystallized from petroleum ether, and again from aqueous methanol. The crystals were further purified by repeated vacuum sublimation at 90 °C. The pale yellow crystals had a mp of 89–91 °C (Frederick Smith Chemical Co., Columbus, Ohio; Manufacturer specification, 88–89 °C (before repurification); 86 °C, Holyer et al[4]). Reagent grade nitrates of copper(II), cobalt(II), and nickel(II) were employed, and their solution concentrations were determined both by EDTA titration and by passing through an ion-exchange column (Dowex 50W-X8) in the hydrogen form followed by titration of the eluted acid.

The electrode systems of the type

glass electrode | solution under study | satd KCl | $Hg_2Cl_2$ Hg

were standardized before and after each experiment with NBS standard buffer solutions as recommended by Bates.[10] In all experiments, potassium nitrate was added to the solutions so as to maintain an ionic strength within 5% of 0.10 M throughout the experiments. pH values were converted to hydrogen ion concentration by using a hydrogen ion activity coefficient 0.7816, calculated from the extended form of the Debye–Hückel equation proposed by Davies.[11] In order to obtain protonation data under conditions identical with those used in the calorimetric experiments, the proton association constants of terpyridine were determined by potentiometric titration of aqueous solutions of terpyridine with standard nitric acid at 25 °C. The calorimeter and its electrical calibration has been described previously.[12] Enthalpy changes for the formation of 1:1 metal complexes were determined by calorimetric titrations of approximately $3 \times 10^{-2}$ M metal ion solutions with 0.15 M terpyridine dihydronitrate solution. Terpyridine dihydronitrate solution was prepared

[†] Current address: Chemical Engineering Division, Argonne National Laboratory, Argonne, Ill. 60439

TABLE I: Thermodynamic Functions for the Protonation of Neutral Heterocyclic Nitrogen Ligands[a]

| | py | phen | bpy | | terpy | |
|---|---|---|---|---|---|---|
| $-\Delta G_1^p$, kJ mol$^{-1}$ | 29.5 | 27.6 | 25.1 | 26.3 | 26.6 | 26.5 ± 0.04 |
| $-\Delta G_2^p$, kJ mol$^{-1}$ | | | | | 18.7 | 19.5 ± 0.13 |
| $-\Delta H_1^p$, kJ mol$^{-1}$ | 20.6 | 16.5 | 15.3 | 16.8 | 2.9 | 17.2 ± 0.21 |
| $-\Delta H_2^p$, kJ mol$^{-1}$ | | | | | 28.5 | 24.8 ± 0.75 |
| $\Delta S_1^p$, J deg$^{-1}$ mol$^{-1}$ | 30.1 | 38.5 | 34.3 | (31.4) | 79.5 | 31.4 ± 0.8 |
| $\Delta S_1^p$, J deg$^{-1}$ mol$^{-1}$ | | | | | −33.5 | −18 ± 3 |
| Ref | 14 | 2 | 2 | 3 | 9 | This work |

[a] py, pyridine; phen, 1,10-phenanthroline; bpy, 2,2′-bipyridine; terpy, 2,2′,2″-terpyridine.

by dissolving purified terpyridine in a stoichiometric amount of a standardized nitric acid solution to provide a 1:2 molar ratio of terpyridine to nitric acid. The enthalpy changes for the formation of the 1:2 metal–terpyridine complexes were determined by titration of approximately $1.5 \times 10^{-2}$ M terpyridine dihydronitrate solution in the calorimeter with 0.15 M metal ion solutions.

## Results

*Protonation.* 2,2′,2″-Terpyridine, L, is protonated in two steps in the pH region of interest to form $HL^+$ and $H_2L^{2+}$ cations with corresponding proton association constants $K_1^p$ and $K_2^p$ at an ionic strength of 0.1 M given by,

$$K_1^p = [HL^+]/[L][H^+] \quad (1)$$

$$K_2^p = [H_2L^{2+}]/[HL^+][H^+] \quad (2)$$

where the square brackets refer to molarities.

Mass balance and electroneutrality require that

$$T_L = [H_2L^{2+}] + [HL^+] + [L] \quad (3)$$

and

$$2[H_2L^{2+}] + [HL^+] + [H^+] = [NO_3^-] + [OH^-] \quad (4)$$

It follows that if $\beta = [NO_3^-] + [OH^-] - [H^+]$, we may write

$$Y = K_1^p K_2^p X + K_1^p \quad (5)$$

in which

$$Y = \beta/[H^+](T_L - \beta)$$

and

$$X = [H^+](2T_L - \beta)/(T_L - \beta)$$

By a least-squares analysis of the linear plot of $X$ and $Y$, $K_1^p$ and $K_2^p$ values are obtained from the intercept and the slope, respectively. A typical such plot is shown in Figure 1 and calculated $\Delta G_1^p$ and $\Delta G_2^p$ values are given in Table I.

The heats of protonation of terpyridine, $\Delta H_1^p$ and $\Delta H_2^p$ for the equilibria represented by eq 1 and 2, respectively, were determined simultaneously in the pH region 3.5–6.7.

The ion species in solution were calculated using eq 1, 2, and

$$[L] = T_L/(1 + K_1^p[H^+] + K_1^p K_2^p[H^+]^2) \quad (6)$$

and the experimental heat is given by

$$Q_{expt} = Q_{HL} + Q_{H_2L} + Q_{H_2O} \quad (7)$$

where

$$Q_{HL} = \Delta H_1^p(\Delta n_{HL} + \Delta n_{H_2L}) \quad (8)$$

$$Q_{H_2L} = \Delta H_2^p(\Delta n_{H_2L}) \quad (9)$$

and

$$Q_{H_2O} = -\Delta H_w(\Delta n_{OH}) \quad (10)$$

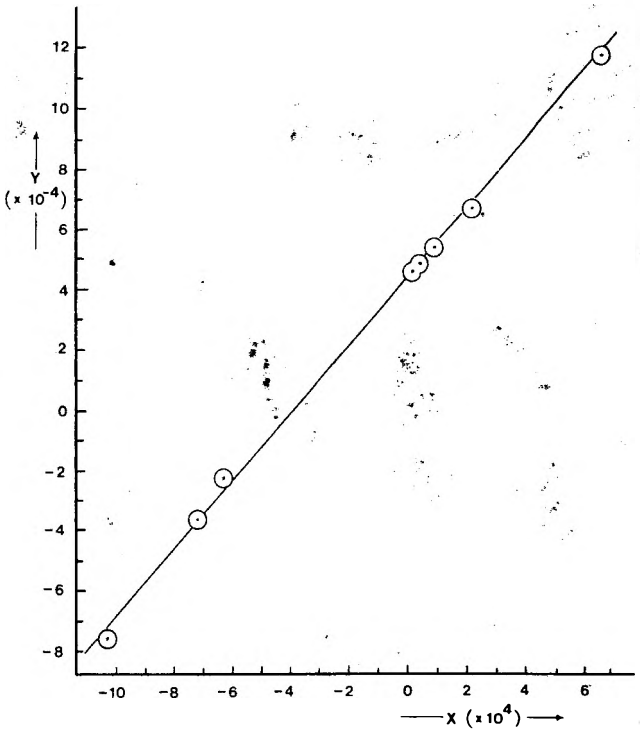


**Figure 1.** Plot of $X$ against $Y$ (eq 5) for the determination of protonation constants.

$\Delta H_w$ is the heat of water formation (−56.23 kJ mol$^{-1}$ at $I$ = 0.1 M). The $\Delta n$ values are the incremental changes in the number of moles of each constituent during the titration of L in the calorimeter with standard nitric acid. The equations can be rearranged to give

$$Y' = \Delta H_1^p X' + \Delta H_2^p \quad (11)$$

in which

$$Y' = (Q_{expt} - Q_{H_2O})/\Delta n_{H_2L}$$

and

$$X' = (\Delta n_{HL} + \Delta n_{H_2L})/\Delta n_{H_2L}$$

By a least-squares analysis of the plot of $Y'$ against $X'$, the heats of protonation, $\Delta H_1^p$ and $\Delta H_2^p$, were obtained from the slope and the intercept, respectively. A typical plot is shown in Figure 2 and the enthalpy values are given in Table I along with data for other heterocyclic nitrogen ligands for comparison.

*Metal Complex Formation.* Since the association constant, $K_1 = [ML^{2+}]/[M^{2+}][L]$, for the formation of the monocomplex with the metal ions is much larger than the corresponding protonation value, the heats of formation of the monocomplexes could be determined by direct titration of ligand, $H_2L^{2+}$, into metal(II) ion solutions. Terpyridine dihydronitrate was titrated into excess metal

TABLE II: Thermodynamic Functions for Metal Complex Formation with Nitrogen Ligands

| | den[a] | en[b] | phen | bpy | | terpy | |
|---|---|---|---|---|---|---|---|
| | | | Cobalt | | | | |
| $-\Delta G_1$, kJ mol$^{-1}$ | 45.6 | 33.9 | 40.6 | 33.9 | 48.1 | 54.2 | (54.2) |
| $-\Delta G_2$, kJ mol$^{-1}$ | 33.5 | 27.2 | 37.7 | 30.1 | 56.5 | 52.0 | (52.0) |
| $-\Delta G_3$, kJ mol$^{-1}$ | | 17.2 | 33.5 | 26.8 | | | |
| $-\Delta H_1$, kJ mol$^{-1}$ | 34.3 | 28.9 | 38.1 | 34.3 | 44.8 | 92.0 | 44.6 ± 0.1 |
| $-\Delta H_2$, kJ mol$^{-1}$ | 42.7 | 29.7 | 28.0 | 29.3 | | 51.0 | 49.0 ± 0.4 |
| $-\Delta H_3$, kJ mol$^{-1}$ | | 34.3 | 33.5 | 25.5 | | | |
| $\Delta S_1$, J deg$^{-1}$ mol$^{-1}$ | 37.7 | 16.7 | 8.8 | −1.5 | | −126 | 32 |
| $\Delta S_2$, J deg$^{-1}$ mol$^{-1}$ | −31.4 | −8.4 | 32.6 | 2.9 | | 0 | 10 |
| $\Delta S_3$, J deg$^{-1}$ mol$^{-1}$ | | −58.6 | 0.0 | 4.4 | | | |
| Ref | 23 | 24 | 2 | 2 | 4 | 5 | This work |
| | | | Nickel | | | | |
| $-\Delta G_1$, kJ mol$^{-1}$ | 60.5 | 43.9 | 49.4 | 40.2 | | 61.1 | (61.1) |
| $-\Delta G_2$, kJ mol$^{-1}$ | 45.6 | 36.4 | 46.4 | 38.5 | | 63.3 | (63.3) |
| $-\Delta G_3$, kJ mol$^{-1}$ | | 24.7 | 43.5 | 36.8 | | | |
| $-\Delta H_1$, kJ mol$^{-1}$ | 49.6 | 37.2 | 46.9 | 40.2 | | 39.7 | 54.1 ± 0.1 |
| $-\Delta H_2$, kJ mol$^{-1}$ | 56.3 | 39.1 | 38.9 | 39.3 | | | 59.8 ± 0.8 |
| $-\Delta H_3$, kJ mol$^{-1}$ | | 42.3 | 39.7 | 38.5 | | | |
| $\Delta S_1$, J deg$^{-1}$ mol$^{-1}$ | 35.6 | 23.0 | 8.8 | 0 | | | 23 |
| $\Delta S_2$, J deg$^{-1}$ mol$^{-1}$ | −35.6 | −10.5 | 25.5 | −2.9 | | | 12 |
| $\Delta S_3$, J deg$^{-1}$ mol$^{-1}$ | | −58.6 | 12.6 | −5.9 | | | |
| Ref | 23 | 24 | 2 | 2 | | 4 | This work |
| | | | Copper | | | | |
| $-\Delta G_1$, kJ mol$^{-1}$ | 90.4 | 61.1 | 51.9 | 44.8 | | ~74.1 | (74.1) |
| $-\Delta G_2$, kJ mol$^{-1}$ | 29.7 | 51.9 | 38.1 | 31.4 | | | |
| $-\Delta G_3$, kJ mol$^{-1}$ | | | 29.7 | 19.7 | | | |
| $-\Delta H_1$, kJ mol$^{-1}$ | 75.3 | 49.8 | 49.0 | 49.8 | | | 66.1 ± 0.4 |
| $-\Delta H_2$, kJ mol$^{-1}$ | 34.3 | 47.3 | 27.2 | 22.6 | | | |
| $-\Delta H_3$, kJ mol$^{-1}$ | | | 34.3 | 27.2 | | | |
| $\Delta S_1$, J deg$^{-1}$ mol$^{-1}$ | 50.2 | 37.7 | 10.0 | −17.2 | | | ~27 |
| $\Delta S_2$, J deg$^{-1}$ mol$^{-1}$ | −14.6 | 15.5 | 36.8 | 30.1 | | | |
| $\Delta S_3$, J deg$^{-1}$ mol$^{-1}$ | | | −15.5 | −25.9 | | | |
| Ref | 23 | 25 | 2 | 2 | | 6 | This work |

[a] den, diethylenetriamine. [b] en, ethylenediamine.

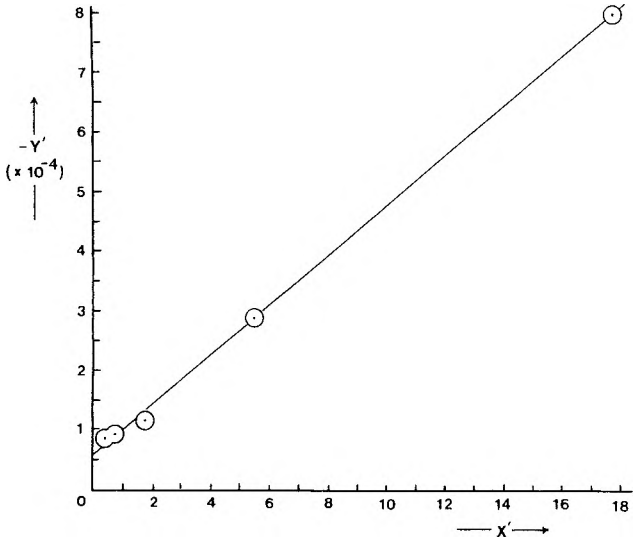


**Figure 2.** Plot of $X'$ against $Y'$ (eq 11) for the determination of the heats of protonation.

ion solution, and all added ligand was effectively deprotonated and complexed with the metal ion to form 1:1 species in the concentration ranges studied. The experimental heat, $Q_{expt}$, is given by

$$Q_{expt} = Q_{ML} + Q_{H_2L} + Q_{HL} + Q_{H_2O} \quad (12)$$

and $Q_{HL}$, $Q_{H_2L}$, and $Q_{H_2O}$ were calculated from eq 8–10. The concentration of species in the calorimeter was calculated from eq 1–3 and 6, together with the extended form of the Debye–Hückel activity coefficient expression proposed by Davies.[11] An iterative computational procedure was used in order to correct for the small deviations (<5%) of ionic strength from 0.10 M during the experiments. The molar heat of formation of the 1:1 complexes, $\Delta H_1 = Q_{ML}/\Delta n_{ML}$, is given in Table II along with other nitrogen ligand data for comparison. The heats of formation of the bis species, $ML_2^{2+}$, were determined by a direct titration of metal ion solutions into excess ligand solution. Owing to the much larger $\beta_2$ values for 1:2 complex formation[4,5] ($\beta_2 = [ML_2^{2+}]/[M^{2+}][L]^2$), as compared with those for protonation, effectively all the added metal ions were converted to the 1:2 species at metal to ligand molar ratios of 1:3 used in the experiments. The molar heats of bis-complex formation were calculated from the expression

$$\Delta H_{\beta_2} = Q_{ML_2}/\Delta n_{ML_2}$$

where $Q_{ML_2}$ represents the experimental heat of $ML_2$ formation given by

$$Q_{ML_2} = Q_{expt} - (Q_{HL} + Q_{H_2L} + Q_{H_2O})$$

The molar heat of formation of the bis from the monocomplex, i.e., $\Delta H_2$, for the reaction

$$ML^{2+} + L \rightleftarrows ML_2^{2+}$$

is given by $\Delta H_2 = \Delta H_{\beta_2} - \Delta H_1$ and the values are included in Table II along with other thermodynamic functions.

## Discussion

The proton association constants of 2,2′,2″-terpyridine in Table I are in good agreement with those reported by Offenhartz et al.[9] It can be assumed that terpyridine accepts two protons only when they are in nonadjacent positions and that the asymmetric doubly protonated form

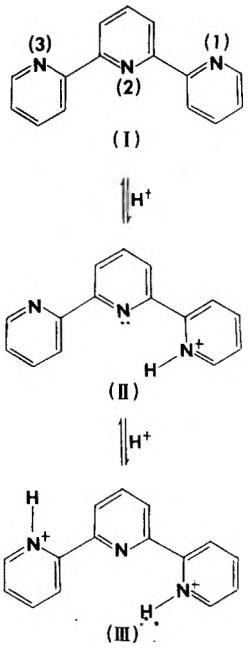


**Figure 3.** Possible protonation steps for terpyridine; I, neutral molecule; II, monoprotonated form; III, diprotonated form.

has no appreciable formation[9] in the pH region of interest since 2,2′-bipyridyl accepts only one proton down to pH 1.6.[13] Protonation of nitrogen (2) in Figure 3 is expected to be sterically restricted. The $\Delta G_1^{\mathrm{p}}$ values for the protonation of the first ring nitrogen in heterogeneous ligands vary little with changes in molecular structure. This observation has been made for the protonation of amines in general[14] and it can be seen (Table I) that the monoprotonation enthalpy of terpyridine obtained in this study is close to the corresponding values for other highly conjugated ligands. The widely different $\Delta H_1^{\mathrm{p}}$ value for terpyridine obtained by Offenhartz et al.[9] reflects the uncertainties in enthalpy values calculated from changes in the association constants over a limited range of temperature (13–36 °C).

The positive entropy change, $\Delta S_1^{\mathrm{p}}$, reflects the desolvation accompanying monoprotonation. Although the electron-withdrawing effect of a protonated pyridyl group of terpyridine, $N(1)H^+$ in Figure 3, is base weakening, the second protonation on N(3) should be almost independent of this effect because of the negligible inductive effect between $N(1)H^+$ and N(3). For the diprotonated form of terpyridine the charge to radius ratio is about double that of the monoprotonated species and a greater degree of solvation is to be expected. This is reflected by the more exothermic $\Delta H_2^{\mathrm{p}}$ as compared with $\Delta H_1^{\mathrm{p}}$ and by the negative entropy change, $\Delta S_2^{\mathrm{p}}$. Electrostatic and steric considerations also support these arguments. In the monoprotonated terpyridine, the protonated pyridyl group probably rotates about the C–C single bond to reach the more stable form II shown in Figure 3. For the second protonation, however, the pyridyl group carrying the $-N(3)H^+$ would retain structure III in Figure 3 and, with its less restricted surroundings as compared with $-N(1)H^+$, the $N(3)H^+$ would have more solvated water molecules associated with it.

Thermodynamic functions for formation of terpyridine complexes with Co(II), Ni(II), and Cu(II) are given in Table II along with data for other nitrogen coordinating ligands. The entropy changes are calculated by using $\Delta H$ values determined in this study ($I$ = 0.1 M) and reported $\Delta G$ values.[4-6] Although the latter were obtained at ionic strengths somewhat different from the 0.1 M of the present work [Co–terpy at $I$ = 0.24 M (NaCl);[5] Ni–terpy variable $I$ up to 0.1 M (NaCl);[4] and Cu–terpy at $I$ = 0.3 M ($K_2SO_4$)[6]] experimental data for other uncharged ligands, such as ethylenediamine, 1,10-phenanthroline, and 2,2′-bipyridine, indicate that, as expected, there is little variation in the association constant with change in ionic strength.[15]

In Table II are given values for the enthalpy changes calculated by previous workers from the temperature dependence of free energy and kinetic data. Although this method is subject to considerable errors, the $\Delta H_1$ value for Co(II) and Ni(II) are quite close to those obtained by Holyer et al.[4] from kinetic studies. The $\Delta H_2$ value for Co(II) complexation obtained by Prasad and Peterson[5] is also in quite good agreement but the large discrepancy in $\Delta H_1$ reflects the uncertainty involved in estimating the temperature coefficient of the first association constant. Comparison of $\Delta H$ values with those for the 2,2′-bipyridyl and 1,10-phenanthroline analogues in Table II suggests the coordination of all three terpyridines ring nitrogens with metal(II) ions. The same conclusion has been reached in x-ray diffraction studies in solids containing acetatoterpyridylcopper(II)[16] and solid dichloro-2,2′,2″-terpyridylcobalt(II)[17] in which all three nitrogens coordinate with metal ions with little strain. The same coordination has been observed in crystals of $\mu$-(2,2′;6,2″-terpyridylcadmium)-bis(pentacarbonylmanganese),[18] chloro(2,2′,-2″-terpyridine)palladium(II) chloride dihydrate,[19] dimethyldiisothiocyanato(terpyridyl)tin(IV),[20] and chloropentaaquoterpyridylpraseodymium(III) ion.[21]

In the case of metal ammines, the similarity of the heat changes for successive additions of ligand molecules is to be expected when the metal–nitrogen bond is uncomplicated by factors such as steric strain and changes of configuration.[22] For polyamine complex formation, however, there is a tendency for the successive enthalpy changes to become more exothermic[23] and it can be seen in Table II that similar trends are followed in this study. Values of $H_{\beta_2}$ (= $\Delta H_1 + \Delta H_2$) for Co (93.5 kJ mol$^{-1}$) and Ni (113.9 kJ mol$^{-1}$) terpyridine complexes (Table II) are quite close to the $\Delta H_{\beta_2}$ values for the reaction

$$M^{2+} + 3L \rightleftarrows ML_3^{2+}$$

89.1 for $Co(bpy)_3$,[2] 99.6 for $Co(phen)_3$,[2] 92.9 for $Co(en)_3$,[24] 118 for $Ni(bpy)_3$,[2] 125.5 for $Ni(phen)_3$,[2] and 118.6 kJ mol$^{-1}$ for $Ni(en)_3$.[24] This strongly suggests that terpyridine behaves as a terdentate ligand in both its cobalt and nickel complexes.

The separation of thermodynamic functions into temperature-dependent and temperature-independent components was first suggested by Gurney[26] for proton ionization reactions. The method was extended to metal complex formation by Nancollas,[27] and subsequently by Anderegg.[28] The temperature-independent part of the enthalpy,[29] $\Delta H_c$, is given by

$$\Delta H_c = \Delta H - (T - \nu)(\Delta S - \Delta n R \ln 55.5) \qquad (13)$$

where $\nu$ is a temperature characteristic of solvent (219 K for water). Some representative values of $-\Delta H_c/x$, where $x$ is the number of nitrogen atoms contained in the ligand molecule, are given in Table III. The similarity again points to the terdentate character of the terpyridine complexes for all three metal ions.

The formation of metal complexes with uncharged ligands is usually accompanied by smaller positive entropy changes than with charged ligands since the latter are more highly solvated. Nevertheless the positive $\Delta S_1$ and $\Delta S_2$ values in Table II indicate that changes in solvation are more important than librational changes of the terpyridine molecule when it complexes with the metal ions. In the

TABLE III: Values of $-\Delta H_c/x$ (kJ mol$^{-1}$)

| | den | en | phen | bpy | terpy |
|---|---|---|---|---|---|
| $Cu^{2+}$ | 27.2 | 27.6[a] | 25.9 | 25.5 | 23.8 |
| $Co^{2+}$ | 13.4 | 16.3 | 20.5 | 18.4 | 16.7 |
| $Ni^{2+}$ | 18.4 | 20.9 | 25.1 | 21.3 | 19.7 |
| Ref | 23 | 24 | 2 | 2 | This work |

[a] Data from ref 25.

monocomplex, coordination of all three nitrogen atoms with the metal ions and subsequent distribution of the charge over the aromatic rings would be expected to contribute to the overall positive entropy change. The data in Table II show that there is a striking increase in $\Delta S$ for the formation of the monoterpyridyl as compared with the monobipyridyl complexes.

## References and Notes


(1) S. Cabani, G. Moretti, and E. Scrocco, *J. Chem. Soc. (London)*, 88 (1962).
(2) G. Anderegg, *Helv. Chim. Acta*, **46**, 2813 (1963).
(3) R. L. Davies and K. W. Dunning, *J. Chem. Soc.*, 4168 (1965).
(4) R. Holyer, C. Hubbard, S. Kettle, and R. Willkins, *Inorg. Chem.*, **5**, 622 (1966).
(5) J. Prasad and N. C. Peterson, *Inorg. Chem.*, **8**, 1622 (1969).
(6) B. R. James and R. J. P. Williams, *J. Chem. Soc. (London)*, 2007 (1961).
(7) W. W. Brandt and J. P. Wright, *J. Am. Chem. Soc.*, **76**, 3082 (1954).
(8) R. B. Martin and J. A. Lissfelt, *J. Am. Chem. Soc.*, **78**, 938 (1956).
(9) P. O'D. Offenhartz, P. George, and G. P. Haight, Jr., *J. Phys. Chem.*, **67**, 116 (1963).
(10) R. Bates, "Determination of pH", Wiley, New York, N.Y., 1963.
(11) C. W. Davies, "Ion Association", Butterworths, London, 1962.
(12) A. P. Brunetti, M. C. Lim, and G. H. Nancollas, *J. Am. Chem. Soc.*, **90**, 5120 (1968).
(13) J. H. Baxendale and P. George, *Trans. Faraday Soc.*, **46**, 55 (1950).
(14) J. J. Christensen, R. M. Izatt, D. P. Wrathall, and L. D. Hansen, *J. Chem. Soc. A*, 1212 (1969).
(15) Stability Constants, *Chem. Soc., Spec. Publ.*, **No. 17** (1963); **No. 25** (1970).
(16) G. A. Zakrzewski, G. D. Andreetti, and E. C. Lingafelter, Paper 05, presented at the Meeting of the American Crystallographic Association, Ottawa, Ontario, Canada, Aug 16–22, 1970.
(17) E. Goldschmied and N. Stephenson, *Acta Crystallogr., Sect. B*, **26**, 1867 (1970).
(18) W. Clegg and P. J. Wheatley, *J. Chem. Soc., Dalton Trans.*, 90 (1973).
(19) G. M. Intille, C. E. Pfluger, and W. A. Baker, Jr., *J. Cryst. Mol. Struct.*, **3**, 47 (1973).
(20) D. V. Naik and W. R. Scheidt, *Inorg. Chem.*, **12**, 272 (1973).
(21) L. J. Radonovich and M. D. Glick, *Inorg. Chem.*, **10**, 1463 (1971).
(22) J. Bjerrum, "Metal Ammine Formation in Aqueous Solution", Haase & Son, Copenhagen, 1941.
(23) M. Ciampolini, P. Paoletti, and L. Sacconi, *J. Chem. Soc.*, 2994 (1961).
(24) M. Ciampolini, P. Paoletti, and L. Sacconi, *J. Chem. Soc.*, 4553 (1960).
(25) F. A. Cotton and F. E. Harris, *J. Phys. Chem.*, **59**, 1203 (1955).
(26) R. W. Gurney, "Ionic Processes in Solution", McGraw-Hill, New York, N.Y., 1953.
(27) G. H. Nancollas, *Q. Rev. Chem. Soc.*, **14**, 402 (1960).
(28) G. Anderegg, *Helv. Chim. Acta*, **51**, 1856 (1968).
(29) G. Degischer and G. H. Nancollas, *J. Chem. Soc. A*, 1125 (1970).


# Vibrational Spectra and Structure of 4-Chloro-1,2-butadiene


**W. C. Harris,* D. A. Coe, M. K. Parpart, and R. S. Pyron[†]**

*Department of Chemistry, Furman University, Greenville, South Carolina 29613*


*(Received November 30, 1976)*

*Publication costs assisted by the Petroleum Research Fund and the National Science Foundation*



Infrared and Raman spectra of gaseous, liquid (130–300 K), solid, and matrix isolated 4-chloro-1,2-butadiene have been recorded between 33 and 4000 cm$^{-1}$. The vibrational data are consistent with the predominance of a single skew conformation (i.e., Cl out of skeletal plane) at ambient temperature. These results are in sharp contrast to previous studies of structurally related molecules (i.e., 3-chloropropene and chloroacetaldehyde) for which two distinct conformers have been resolved. Conclusions from the vibrational data are based upon the measured depolarization ratios, the number of bands resolved (equal, approximately, to the 24 fundamentals expected for a single conformer), and the absence of significant band intensity variations with temperature. Spectral changes observed upon annealing the sample are attributed to the relaxation of an amorphous solid into an ordered polycrystalline form. The $-CH_2Cl$ torsional frequency is assigned to a weak infrared band centered at 102 cm$^{-1}$ for solid $CH_2{=}C{=}CHCH_2Cl$. By using a calculated $F$ value of 0.78 cm$^{-1}$, a barrier height ($V^*$) of 38 kcal/mol is determined from the assigned torsional frequency. The vibrational data measured for 4-chloro-1,2-butadiene are compared to a recent microwave study of the same system and a possible potential function for the molecule is developed.


## Introduction

In view of the careful experimental studies on molecules containing $C(sp^2)$–$C(sp^3)$ bonds during the past several years, conformational trends that accompany systematic functional group substitution have begun to emerge.[1,2] For instance, microwave experiments have shown that the cis form of $CH_2{=}CHCH_2F$ and $CH_2{=}CHCH_2CN$ is more stable than the skew conformer by 166 and 450 cal/mol, respectively.[3,4] The cis and skew conformations of $CH_2{=}CHCH_2Cl$ have also been assigned but the rotational study did not permit a quantitative determination of the more stable form; however, the spectral intensities suggested the cis form is probably less stable.[5] It should also be noted that Bothner-By and co-workers concluded from the analysis of NMR data that the 3-halopropenes exist in two rotameric forms and the population of the cis form decreases as one goes from the chlorine to iodine derivatives.[6] Similarly, the NMR studies suggested the amount of cis conformer decreased[7] as the substituent in 3-propene was varied from $CH_3$ to $i$-$C_3H_7$ to $t$-$C_4H_9$.

Given the observation that significant rotamer population changes can accompany simple functional group replacements for the propenes, a study of specific buta-

[†] Present address: Regional Director-Grants, Research Corporation, 6075 Roswell Road, N.E., Atlanta, Ga. 30328.

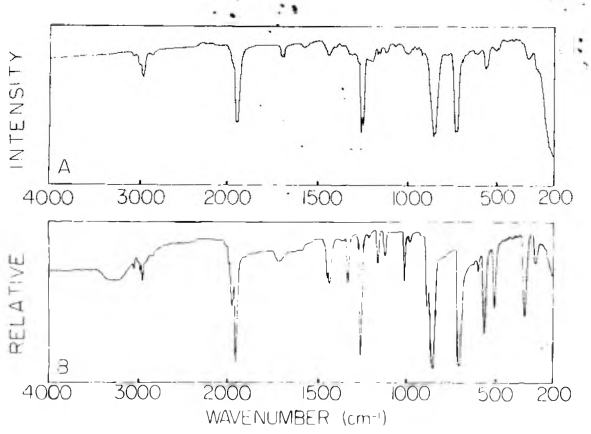


**Figure 1.** Infrared spectra of gaseous (top) and solid (bottom $CH_2{=}C{=}CHCH_2Cl$.

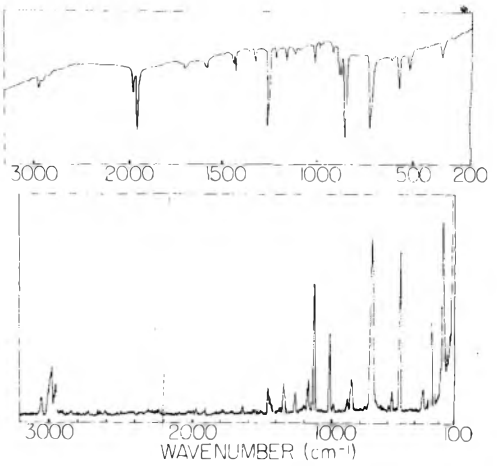


**Figure 2.** Infrared (top) and Raman (bottom) spectra of $CH_2{=}C{=}CHCH_2Cl$ isolated in an argon matrix.

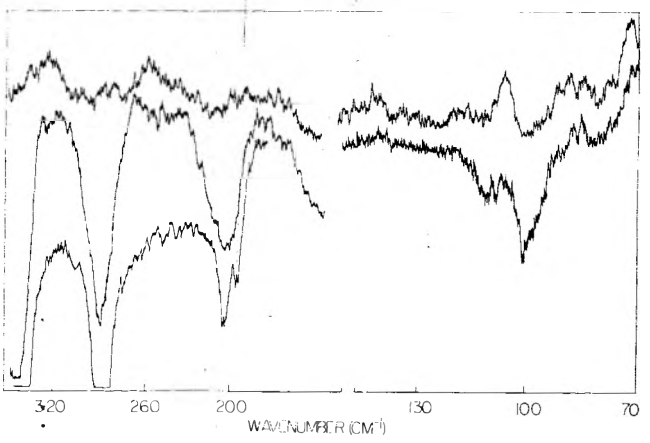


**Figure 3.** Far-infrared spectrum of solid $CH_2{=}C{=}CHCH_2Cl$.

diene systems which can also exhibit rotational isomerism about a $C(sp^2)$–$C(sp^3)$ single bond has been initiated. In the present report we consider the structure of 4-chloro-1,2-butadiene, $CH_2{=}C{=}CHCH_2Cl$, by examining the vibrational spectra as a function of temperature. Since there has not been a previous study of the infrared and laser-Raman data for $CH_2{=}CHCH_2Cl$, the vibrational spectra are investigated to provide information on the magnitude of the internal rotational barrier. During the course of the present study, Karlsson et al.[8] provided us with a summary of their recently completed microwave study of $CH_2{=}C{=}CHCH_2Cl$; thus, we shall compare the conclusions of the vibrational and rotational studies in a subsequent section of this paper when a proposed potential function for 4-chloro-1,2-butadiene will be discussed. Given the surprising conformational properties determined for 4-chloro-1,2-butadiene from the spectroscopic studies, the structure for $CH_2{=}C{=}CHCH_2Cl$ will be compared to structurally related molecules. Also included is a brief summary of the vibrational assignments for the 24 fundamentals of 4-chloro-1,2-butadiene.

## Experimental Section

The sample of 4-chloro-1,2-butadiene was synthesized by mixing 75 mL of concentrated HCl, 13 g of $CaCl_2{\cdot}2H_2O$, and 13 g of vinylacetylene (from 50% xylene solution) for 10 h at room temperature. The organic phase was separated and washed successively with 20 mL of aqueous $NaHCO_3$ and 20 mL of saturated brine. The product mixtures from three reactions were combined for distillation after drying. The 4-chloro-1,2-butadiene sample was obtained in 28% yield in a fraction boiling at 86.5–89.0 °C. Sample authenticity was established by comparison of its boiling point and refractive index (1.4775) with literature values. The NMR spectrum consisted of signals at $\delta$ 5.3 (m), 4.9 (m), and 4.0 (m) with relative areas of 1.0:1.9:2.0 (theoretical 1:2:2) and was in agreement with that reported by Ferguson.[9] The sample used for spectroscopic studies was prepared by careful fractionation on an annular teflon spinning band column. The fraction boiling at 87.0 °C was shown by GLPC to have a purity of greater than 99%.

Infrared spectra were obtained by using Perkin-Elmer Model 621 and Beckman Model IR-11 spectrophotometers (see Figures 1–3). A standard 10-cm gas cell equipped with CsI windows was used to obtain the mid-infrared spectrum of the gas phase. A Cryogenic Technology Incorporated Model Spectrim closed cycle refrigerator was utilized to record the spectra for crystalline and matrix isolated 4-chloro-1,2-butadiene between 200 and 4000 $cm^{-1}$. In order to record the far-infrared spectrum (down to 33 $cm^{-1}$) of solid 4-chloro-1,2-butadiene, a standard low temperature cell fitted with polyethylene windows and operating with liquid nitrogen as the cryogenic fluid was employed.

All Raman spectra were recorded on a modified Jarrell-Ash Model 500 spectrophotometer. The spectra were excited by the 488.0-nm line from a CRL-52B argon ion laser. Whereas Raman spectra for the liquid state were measured after sealing the sample in a standard capillary cell, spectra for the gaseous material were obtained by utilizing a multipass gas cell (see Figure 4). Raman spectra for solid and matrix isolated 4-chloro-1,2-butadiene were obtained by depositing the sample onto a copper wedge maintained at 15 K by the CTI cryostat described earlier (see Figures 4 and 5). Variable temperature Raman studies on the liquid state were conducted after a capillary tube had been affixed to the copper substrate with Dow-Corning high vacuum silicon grease. A thermocouple attached to the copper surface was used to measure temperatures between 130 and 300 K. The positions of the sharp Raman lines are expected to be accurate to ±2 $cm^{-1}$ (see Tables I and II).

## Results

Since studies of related molecules (see Tables III and IV) would suggest that a pair (i.e., cis and skew) of distinct conformers could be identified from the vibrational spectra of 4-chloro-1,2-butadiene, the infrared and Raman spectra of all three physical states were studied in detail. In principle, it should be possible to distinguish between a cis and skew conformer of 4-chloro-1,2-butadiene by comparing Raman depolarization ratios with group theoretical predications. Whereas a cis or trans structure has

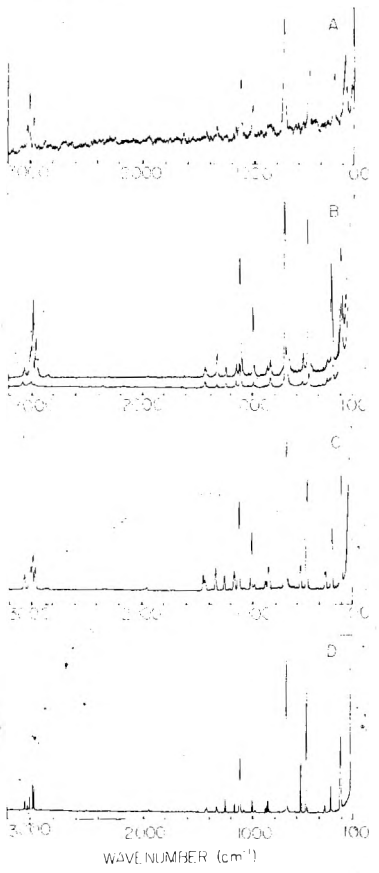


**Figure 4.** Raman spectra of (A) gaseous $CH_2$=C=$CHCH_2Cl$; (B) liquid $CH_2$=C=$CHCH_2Cl$ displaying depolarization traces; (C) unannealed solid $CH_2$=C=$CHCH_2Cl$; (D) annealed solid $CH_2$=C=$CHCH_2Cl$.

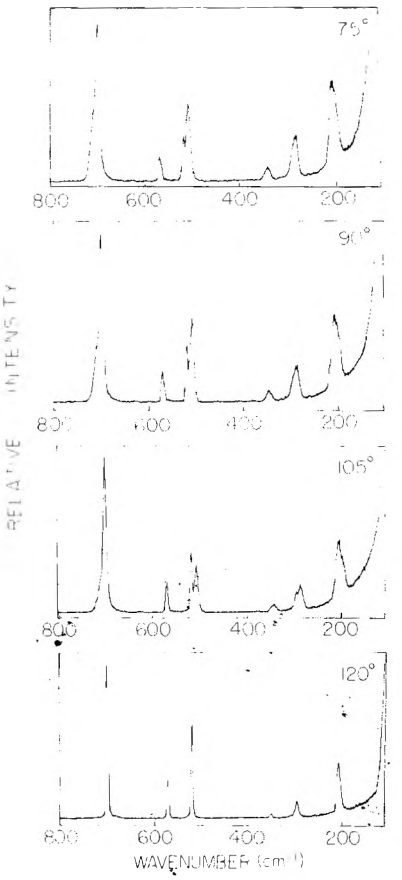


**Figure 5.** Raman spectra of solid $CH_2$=C=$CHCH_2Cl$ indicating the spectral changes that occur upon annealing.

$C_s$ symmetry and gives rise to 15 polarized (a′) and 9 depolarized (a″) bands, a skew form has $C_1$ symmetry and all 24 fundamentals are expected to be polarized. Inspection of Table I reveals that all but two of the measured Raman transitions have $\rho$ values less than 0.70. Since a polarized Raman line can have a depolarization ratio between 0 and 0.75, these two bands may also be considered polarized. In view of the depolarization ratios and the fact that none of the Raman fundamentals disappear when the spectrum of the crystal is recorded (see Figure 4), it is concluded that the vibrational data for 4-chloro-1,2-butadiene are most consistent with a single skew form.

The above structural conclusions are also supported by a recent rotational study by Karlsson et al.[8] which was interpreted for a single skew structure. It is important to note, however, that Karlsson et al. could not rule out the possible presence of up to 10% of a second conformer and suggested that the infrared spectrum should be studied "to prove the absence of other rotamers."[8] As noted above, the vibrational data appears to support the conclusion advanced from the microwave study that a single skew form of 4-chloro-1,2-butadiene is predominant at ambient temperature. If there is a second conformer, its vibrational frequencies are coincident[10] with the skew form.

## Vibrational Assignment and $-CH_2Cl$ Torsional Barrier

Since no previous infrared or Raman data have been reported for 4-chloro-1,2-butadiene, a tentative vibrational assignment is proposed for the 24 fundamentals expected for this system. In view of the lack of symmetry and isotopic data for $CH_2$=C=$CHCH_2Cl$, the assignment is based principally on assignments for similar systems: 3-chloropropene,[11,12] allene,[13] 3-methyl-1,2-butadiene,[14] 3-methylpropene,[15] chlorocyclobutane,[16] and chlorocyclopentane.[17] The assignment proposed for $CH_2$=C=$CHCH_2Cl$ is listed in Tables I and II. Since the assignment corresponds well with the earlier studies,[11-17] a detailed discussion is not considered appropriate.

It is of interest, however, to review the assignment of the low frequency fundamentals since such modes are typically important to conformational studies. In particular, Table III reveals that the skeletal atom stretches will often appear as discrete bands (doublets) if a pair of rotational conformers are present. In the assignment for 4-chloro-1,2-butadiene, however, there is no clear evidence for spectral transitions from a second conformer (see Figures 1–4). The C–C–C stretching fundamentals are centered at 1955 and 1126 $cm^{-1}$, respectively. In a previous study[11] of $H_2C$=$CHCH_2Cl$, however, it was reported that distinct bands could be assigned to the C=C stretching mode of each conformer (see Table IV). The C–C and C–Cl stretching motions are expected to give rise to intense Raman lines in the 500–800-$cm^{-1}$ region on the basis of related studies.[16,17] As such, the bands in this spectral region have been assigned to the C–C and C–Cl stretching modes of 4-chloro-1,2-butadiene and, again, there is no evidence for conformer doublets.

The fundamentals remaining to be assigned are the carbon-skeleton bending motions, the C–Cl bends and a $-CH_2Cl$ torsional mode. Since all of these fundamentals are expected below 600 $cm^{-1}$, they occur in a relatively uncomplicated region of the spectrum and have been assigned to the bands summarized in Table I. We might note that our assignment of the 102-$cm^{-1}$ band (see Figure 3) to the $-CH_2Cl$ torsion is supported[11] by comparable assignments for $C_3H_5Cl$ and $C_3H_5Br$. For each of the halogenated propenes, the $-CH_2X$ (X = Br, Cl) torsional

TABLE I: Infrared and Raman frequencies for 4-Chloro-1,2-butadiene[a] ($cm^{-1}$)

| Infrared | | Raman | | Infrared | | Raman | | Raman | | | |
|---|---|---|---|---|---|---|---|---|---|---|---|
| Gas | Rel int | Gas | Rel int | Matrix | Rel int | Matrix | Rel int | Liquid | Rel int | DP ratio | Approx description |
| 3080(br) | vw | | | | | 3071 | 11 | 3062 | 5 | 0.77 | =CH stretch |
| | | | | | | | | 3012 | 14 | | =CH stretch |
| | | 3030 | 22 | | | | | 3001 | 14 | 0.16 | =CH stretch |
| 3006(br) | w | 3012 | 49 | | | 3005 | 30 | 2990 | 48 | 0.12 | $-CH_2$ stretch |
| 2968 | m | 2971 | 29 | 2971 | mw | 2970 | 19 | 2962 | 25 | 0.06 | $-CH_2$ stretch |
| | | | | 2934 | w | | | | | | |
| 2874 | vw | | | 2867 | w | | | | | | |
| | | | | 1982 | m | | | | | | |
| 1955 | s | | | 1957 | s | | | | | | C=C=C asym stretch |
| 1716(R) | | | | | | | | | | | |
| 1711(ctr) | w | | | 1706 | w | | | | | | |
| 1706(P) | | | | | | | | | | | |
| | | 1635 | 8 | | | | | | | | |
| | | | | 1451(sh) | m | | | | | | |
| | | | | | | | | | | | $=CH_2$ deformation |
| | | | | 1445 | mw | 1441 | 14 | | | | |
| 1444 | mw | 1438 | 8 | 1434 | mw | 1431 | 9 | 1438 | 7 | 0.57 | $-CH_2$ deformation |
| | | | | 1363 | w | | | | | | |
| | | | | 1336(sh) | mw | | | | | | |
| 1331(br) | w | 1339 | 12 | 1327 | m | 1332 | 17 | 1331 | 14 | 0.20 | =CH bend |
| 1263(R) | s | | | | | | | | | | |
| 1258(Q) | s | 1254 | 4 | 1254 | s | 1254 | 14 | 1251 | 6 | 0.57 | $-CH_2$ bend |
| 1252(P) | s | | | | | | | | | | |
| 1218 | w | | | 1222 | m | | | | | | |
| 1172(R) | | | | | | | | | | | |
| 1166(ctr) | w | 1166 | 9 | 1164 | m | 1164 | 19 | 1161 | 9 | 0.59 | 2 x 851 = 1162 |
| 1161(P) | | | | | | | | | | | |
| 1128(R) | | | | | | | | | | | |
| 1124(ctr) | w | 1126 | 53 | 1122 | w | 1122 | 75 | 1120 | 69 | .23 | C=C=C sym stretch |
| 1121(P) | | | | | | | | | | | |
| 1012 | w | 1015 | 28 | 1014 | | 1012 | 45 | 1008 | 40 | .10 | $-CH_2$ bend |
| | | | | 990 | w | | | | | | |
| 976 | w | | | 975 | w | | | | | | |
| 924 | w | | | 919 | mw | | | | | | |
| | | | | 884 | m | 888 | 8 | 882 | 6 | .29 | $=CH_2$ bend |
| | | 871 | 8 | 876(sh) | m | | | 872 | 4 | | $=CH_2$ bend |
| 852 | s | 859 | 8 | 848 | s | 853 | 19 | 852 | 10 | .73 | $=CH_2$ bend |
| 736(R) | | | | | | | | | | | |
| 731(ctr) | s | 732 | 100 | 718 | s | 711 | 100 | 711 | 100 | .24 | C-C stretch |
| 726(P) | | | | | | | | | | | |
| 696 | w | | | | | | | | | | |
| | | | | 608 | w | | | | | | |
| 569(R) | | | | | | | | | | | |
| 565(ctr) | m | | | 567 | m | 568 | 12 | 581 | 14 | .49 | =CH bend |
| 561(P) | | | | | | | | | | | |
| 514(br) | w | 516 | 50 | 511 | m | 511 | 93 | 509 | 88 | .10 | C-Cl stretch |
| 342 | m | | | 339 | m | 342 | 13 | 340 | 7 | .57 | C-Cl bend |
| | | 287 | 43 | | | 288 | 51 | 289 | 58 | .18 | C-Cl bend |
| | | 187 | 59 | | | 204 | 98 | 200 | 55 | .65 | Skeletal bends |

[a] vw = very weak, w = weak, mw = medium weak, m = medium, s = strong, sh = shoulder, br = broad, ctr = center, DP = depolarization ratio.

fundamental has been assigned to bands between 50 and 94 $cm^{-1}$, respectively. It should be emphasized that our reported torsional frequency (102 $cm^{-1}$) for $CH_2$=C=C-$HCH_2Cl$ was measured for the solid state at reduced temperatures. An effort was made to detect the gas phase counterpart of this 102-$cm^{-1}$ torsional transition at path lengths up to 8.2 m, but the 1 ← 0 frequency was not resolved. Clearly, however, the torsional fundamental for gaseous $CH_2$=C=$CHCH_2Cl$ should be centered significantly below 100 $cm^{-1}$, which dictates several populated excited torsional states at ambient temperature. In fact, Karlsson et al.[8] suggest the torsional frequency for gaseous 4-chloro-1,2-butadiene is centered between 60 and 70 $cm^{-1}$ on the basis of microwave measurements in support of our assignment.

In the absence of torsional frequencies from each conformer or a manifold of transitions originating from the ground and excited torsional levels of skew $CH_2$=C=$CHCH_2Cl$, we can calculate only a total barrier height,[10] $V^*$ ($V^* = V_1 + 4V_2 + 9V_3$). The 1 ← 0 $-CH_2Cl$ torsional transition determines $V^*$ by the expression $V^* = \bar{\nu}^2/F$. In this definition $\bar{\nu}$ is the 1 ← 0 torsional frequency and $F$, a reduced moment of inertia constant, is calculated from assumed geometrical parameters. By using an $F$ value of 0.782 $cm^{-1}$, $V^*$ is calculated to be 38.0 kcal/mol.

## Discussion

The results of this work do not appear to be in accord with any previous study of molecules containing $C(sp^2)$–$C(sp^3)$ bonds since only transitions from a single conformation are resolved in the vibrational spectra. It is, of course, possible that the vibrational frequencies for a second conformer could be coincident with the frequencies for the skew form, but this is considered unlikely when the results of the complementary microwave study[8] are considered. Both the vibrational and rotational investi-

TABLE II: Vibrational Frequencies for Solid 4-Chloro-1,2-butadiene ($cm^{-1}$)

| Raman annealed solid | Rel int | Infrared unannealed solid | | Raman unannealed solid | Rel int | Approx description |
|---|---|---|---|---|---|---|
| 3051 | 8 | 3062 | vw | 3060 | 10 | =CH stretch |
| 3026 | 4 | | | | | =CH stretch |
| 3008 | 8 | | | 3001 | 14 | =CH stretch |
| 2978 | 16 | 2987 | w | 2983 | 23 | $-CH_2$ stretch |
| 2968 | 16 | 2960 | m | 2961 | 14 | $-CH_2$ stretch |
| 1976 | 1 | 1972 | m | 1979 | 1 | |
| | | 1953 | s | 1954 | 2 | C=C=C asym stretch |
| | | 1721 (br) | w | | | |
| 1438 | 2 | 1444 | m | 1442 | 12 | $=CH_2$ deformation |
| 1426 | 4 | 1430 | m | 1431 | 8 | $-CH_2$ deformation |
| | | 1362 | vw | | | |
| 1337 | 6 | 1330 | m | 1332 | 15 | =CH bend |
| 1327 | 5 | | | | | |
| 1253 | 8 | 1254 | s | 1252 | 10 | $-CH_2$ bend |
| | | 1215 | w | | | |
| 1170 | 6 | 1164 | m | 1163 | 13 | |
| 1118 | 32 | 1123 | m | 1122 | 60 | C=C=C sym stretch |
| 1083 | 3 | | | | | |
| 1008 | 7 | 1013 | m | 1011 | 37 | $-CH_2$ bend |
| 983 | 3 | 984 | w | 984 | 3 | |
| 884 | 3 | 886 | m | 887 | 5 | $=CH_2$ bend |
| 877 | 5 | | | | | $=CH_2$ bend |
| 867 | 8 | | | | | |
| 859 | 3 | 850 | s | 858 | 15 | $=CH_2$ bend |
| 702 | 100 | 704 | s | 702 | 100 | C-C stretch |
| | | 604 | w | | | |
| 571 | 29 | 569 | m | 569 | 15 | =CH bend |
| 521 | 70 | 512 | m | 511 | 79 | C-Cl stretch |
| 355 | | 344 | m | 345 | 12 | C-Cl bend |
| 301 | 17 | 285 | m | 289 | 40 | C-Cl bend |
| 215 | 41 | 208 | mw | 207 | 70 | skeletal bend |
| | | 198 (sh) | | | | skeletal bend |
| | | 102 | w | | | $-CH_2Cl$ torsion |

TABLE III: Typical Frequency Splittings for Conformer Vibrational Modes

| Molecule | Vibration | Conformer | Frequency, $cm^{-1}$ | Ref |
|---|---|---|---|---|
| $N_2F_4$ | N-N stretch | Trans | 600 | 24 |
| | | Cis | 588 | |
| $P_2(CH_3)_4$ | P-P stretch | Trans | 455 | 25 |
| | | Skew | 429 | |
| $CH_2=CHCH_2Cl$ | C=C stretch | Cis | 1647 | 11 |
| | | Skew | 1642 | |
| $CH_2=CHCH_2Br$ | C=C stretch | Cis | 1645 | 11 |
| | | Skew | 1637 | |

TABLE IV: Conformer Bands Identified[a] for the Cis and Skew Forms of $CH_2=CHCH_2Cl$ below 1700 $cm^{-1}$

| Vibrational mode | Cis, $cm^{-1}$ | Skew, $cm^{-1}$ |
|---|---|---|
| C=C stretch | 1647 | 1642 |
| $=CH_2$ bend | 1430 | 1412 |
| $CH_2$ bend | 1177 | 1100 |
| =CH bend | 1050 | 987 |
| C-C stretch | 923 | 938 |
| =CH bend | 550 | 590 |
| CCC bend | 513 | 409 |
| CCCl bend | 253 | 290 |

[a] Taken from ref 11.

gations suggest that a single, skew conformer is the predominant structure for 4-chloro-1,2-butadiene at room temperature. This result is even more interesting in view of the detailed microwave analysis published for the cis and trans forms of chloroacetaldehyde by Ford.[18] Although the trans form of chloroacetaldehyde is reported to be more stable than the cis form, the trans structure is slightly higher in energy than the skew forms. The proposed potential function for chloroacetaldehyde (see Figure 6) is analogous to that determined previously for small ring systems (i.e., methylene oxide[19] and cyclobutanone[20]) which have a small bump at the planar conformation.

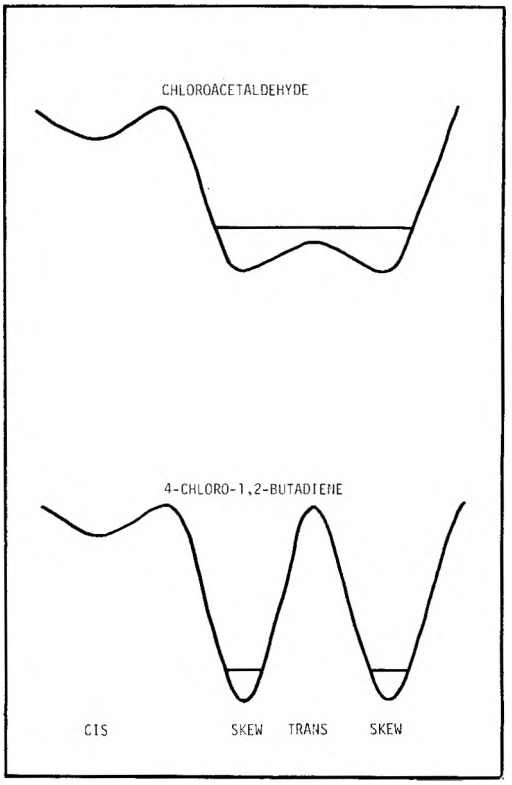


**Figure 6.** Schematic potential energy functions for chloroacetaldehyde (top) and 4-chloro-1,2-butadiene (bottom). The $V = 0$ level is believed to be slightly above the bump corresponding to the trans conformation of chloroacetaldehyde.

Since the vibrational and rotational studies provide no evidence for a second conformer of 4-chloro-1,2-butadiene, a potential function for $CH_2{=}C{=}CHCH_2Cl$ modeled after that suggested for chloroacetaldehyde is illustrated in Figure 6. If one assumes that the vibrational frequencies for a second conformer of 4-chloro-1,2-butadiene would not be degenerate with those measured for the skew, it is possible to estimate a minimum magnitude for $\Delta H$ based upon limitations imposed by signal detection. If it assumed, conservatively, that the vibrational experiment could not detect less than 5% of a second conformer (i.e., cis), the resultant $\Delta H$ would be on the order of 1.3 kcal/mol. This $\Delta H$ value is appreciably greater than the enthalpy differences determined for the chloropropene and chloroacetaldehyde, which underscores the delicate balance of forces that dictate conformational properties of structurally related molecules.

*Acknowledgment.* Acknowledgment is made to the donors of the Petroleum Research Fund, administered by the American Chemical Society, for support of this research and The Research Corporation for providing funds to obtain the Beckman IR-11 far-infrared spectrophotometer. A grant provided by the Southern Regional Education Board supported the computer calculations. It is a pleasure to acknowledge the generous support provided by a Camille and Henry Dreyfus Teacher-Scholar grant (W.C.H.) and the support provided M.K.P. by a NSF-URP grant. Finally, the generous support provided by the Research Corporation for the Postdoctoral fellowship (D.A.C.) is acknowledged. In addition, we wish to thank L. L. Tomsyck and R. G. Posey for synthetic assistance.

## References and Notes

(1) E. B. Wilson, *Chem. Soc. Rev.*, **1**, 293 (1972).
(2) G. J. Karabatsos and D. J. Fenoglio, "Rotational Isomerism about $sp^2$-$sp^3$ Carbon-Carbon Single Bonds", in "Topics in Stereochemistry", E. L. Eliel and N. L. Allinger, Ed., Wiley-Interscience, New York, N.Y., 1970.
(3) E. Hirota, *J. Chem. Phys.*, **42**, 2071 (1965).
(4) K. V. L. N. Sastry, V. M. Rao, and S. C. Dass, *Can. J. Phys.*, **46**, 959 (1968).
(5) E. Hirota, *J. Mol. Spectrosc.*, **35**, 9 (1970).
(6) A. A. Bothner-By and H. Gunther, *Discuss. Faraday Soc.*, **34**, 127 (1962).
(7) A. A. Bothner-By, C. Naar-Colin, and H. Gunther, *J. Am. Chem. Soc.*, **84**, 2748 (1962).
(8) F. Karlsson, M. Granberg, and R. Vestin, private communication.
(9) R. C. Ferguson, *J. Phys. Chem.*, **68**, 1594 (1964).
(10) G. L. Carlson, W. G. Fateley, and R. E. Witkowski, *J. Am. Chem. Soc.*, **89**, 6437 (1967).
(11) C. Sourisseau and B. Pasquier, *J. Mol. Struct.*, **12**, 1 (1972).
(12) K. Radcliffe and J. L. Wood, *Trans. Faraday Soc.*, **62**, 2038 (1966).
(13) R. C. Lord and P. Venkateswarlu, *J. Chem. Phys.*, **20**, 1237 (1972).
(14) W. C. Harris and C. T. Longshore, *J. Chem. Phys.*, **57**, 4661 (1972).
(15) C. M. Pathak and W. H. Fletcher, *J. Mol. Spectrosc.*, **31**, 32 (1969).
(16) J. R. Durig and A. C. Morrisey, *J. Chem. Phys.*, **46**, 4854 (1967).
(17) J. R. Durig, J. M. Karriker, and D. W. Wertz, *J. Mol. Spectrosc.*, **31**, 237 (1969).
(18) R. G. Ford, *J. Chem. Phys.*, **65**, 354 (1976), and a private communication that suggested the potential function represented in Figure 6.
(19) S. I. Chan, T. R. Borgers, J. W. Russell, H. L. Strauss, and W. D. Gwinn, *J. Chem. Phys.*, **44**, 1103 (1961).
(20) L. H. Scharpen and V. W. Laurie, *J. Chem. Phys.*, **49**, 221 (1968).
(21) J. R. Durig and J. W. Clark, *J. Chem. Phys.*, **48**, 3216 (1968).
(22) J. R. Durig and J. S. DiYorio, *Inorg. Chem.*, **8**, 2796 (1969).

# A Carbon-13 and Proton Nuclear Magnetic Resonance Study on the Structure and Mobility of Nonionic Alkyl Polyoxyethylene Ether Micelles

**Anthony A. Ribeiro and Edward A. Dennis***

*Department of Chemistry, University of California at San Diego, La Jolla, California 92093* *(Received February 7, 1977)*

*Publication costs assisted by the National Science Foundation*

$^{13}C$ (natural abundance) and $^1H$ nuclear magnetic resonance spectra of a homogeneous nonionic surfactant, *n*-dodecyl octaethylene glycol monoether, and $^{13}C$ spectra for the oligomeric series of di- to hexaethylene glycol are assigned. Measurements of the $^{13}C$ spin-lattice relaxation times ($T_1$) suggest that the surfactant exhibits segmental motions in both the hydrophobic alkyl and the polar polyoxyethylene chains. In organic solvents, the oxyethylene groups of the surfactant appear similar in mobility to those of the ethylene glycols. The surfactant forms micelles in aqueous media, and decreases in $T_1$ for all carbons are observed, consistent with restriction of the molecules from free tumbling upon micelle formation. In contrast, hexaethylene glycol exhibits no significant changes in $T_1$ between organic solvents and aqueous media. The structure of the nonionic micelle was investigated with paramagnetic $Mn^{2+}$ ions, and a detailed analysis of the relaxation data was attempted to obtain the rates of internal motions of the methylene groups and the terminal methyl group spinning. The results are consistent with a classical structure for the nonionic micelle, with the hydrophobic alkyl chains in an interior region and the polar oxyethylene chains forming an external palisade layer exposed to solvent molecules. The data also suggest that a restriction of internal motion occurs at the hydrophobic-hydrophilic interface, and that progressively increasing fluidity occurs away from the interface in both the nonpolar interior and polar exterior regions of the nonionic micelle.

Nonionic polyoxyethylene surfactants are currently used to solubilize membrane phospholipids,[1,2] and are the major means of purifying membrane-bound proteins and enzymes with retention of their biological activity.[3] These amphipathic surfactant molecules self-associate in aqueous and nonaqueous media to form micellar aggregates of differing sizes and shapes.[4-6] An understanding of the detailed arrangement, local configuration, relative mobility of various groups in the surfactant micelle, and the degree of water penetration is therefore of considerable interest.

We wish to present detailed $^{13}C$ and $^1H$ NMR studies on the solution structure of a homogeneous alkylpolyoxyethylene (APE) surfactant as well as $^{13}C$ NMR studies on a number of ethylene glycols which serve as excellent

analogues for the polar portion of the polyoxyethylene surfactants. Previous $^1H$ NMR studies of APE surfactants[7-9] have considered the mesomorphic and micellar states in aqueous media. From chemical shifts, Corkill et al.[7] suggested considerable interaction of water with the polyoxyethylene group and speculated that water might penetrate the micellar core to the alkyl $CH_2$ group closest to the polyoxyethylene head group. However, from average proton $T_1$ relaxation times, Clemett[8] concluded that there is no significant water penetration to the hydrophobic core of APE micelles.

These early studies were carried out at low field strengths where resolution of overlapping lines was difficult, and two of the above studies assumed that the polyoxyethylene protons of surfactant micelles can be treated as chemically equivalent.[8,9] More recently, $^1H$ NMR at high field strengths (220 MHz) and natural abundance $^{13}C$ NMR studies have resolved individual resonance lines in octylphenolpolyoxyethylene (OPE) surfactants,[1,10,11] and have suggested that the polyoxyethylene chain can exhibit chemically shifted resonances sensitive to the micellar structure. The present study proposes detailed $^{13}C$ and $^1H$ NMR spectral assignments for the primary APE surfactants and considers the localized structure and mobility of the hydrophobic alkyl and hydrophilic oxyethylene chains from chemical shifts, spin–lattice relaxation times ($T_1$), line widths, and the effects of shift reagents and paramagnetic ions on these parameters. Some preliminary $^{13}C$ NMR results for this system have been reported.[12]

## Experimental Section

*n*-Dodecyl octaethylene glycol monoether ($C_{12}EO_8$) was obtained from Nikko Chemicals Co., Ltd. Thin layer chromatography on silica gel G with ethyl acetate:acetic acid:water, 30:5:4 (v:v:v), gave a single spot. This solvent system will separate oligomeric molecules differing in only one oxyethylene unit (R. Robson, unpublished data). 2-Methoxyacetic acid, 2-methoxyethanol, diethylene ($EO_2$), triethylene ($EO_3$), and tetraethylene glycol ($EO_4$) were obtained from Aldrich; hexaethylene glycol ($EO_6$) and bis(2-chloroethyl) ether were obtained from Curtin Scientific Co. Deuterated solvents were obtained from Mallinckrodt. 2-Methoxyethanol deuterated in the 1 position was prepared by reduction of 2-methoxyacetic acid with $LiAlD_4$. The $^1H$ and $^{13}C$ NMR spectra were consistent with its structure based on comparison of the chemical shifts and splitting patterns observed for 2-methoxyethanol and 2-methoxyacetic acid.

Continuous wave $^1H$ NMR spectra were obtained at 220 MHz on a Varian HR-220 spectrometer previously described.[2] Proton decoupled $^{13}C$ NMR spectra were obtained at 25.03 MHz on a JEOL PFT-100/Nicolet 1085 Fourier transform system also previously described.[11] The 90° pulse was 14 μs. Probe temperature on both systems was 40 ± 1 °C except as noted.

$^{13}C$ NMR spin–lattice relaxation times ($T_1$) were measured according to Vold et al.[13] Peak heights ($I_\tau$) were hand-measured on expanded spectra of appropriate regions and the $T_1$ values were obtained from the slope of plots of log ($I_\infty - I_\tau$) vs $\tau$. Generally 8–14 useful $I_\tau$ values were obtained for each carbon atom. For routine work and $T_1$ runs, spectra were generally obtained over 5000 Hz using 4K channels. For line widths, spectra were obtained over a spectral window of 2500 Hz using 16K channels, so that the digital resolution was 0.31 Hz/channel.

$T_1$ measurements in organic solution were made in 10-mm custom-made thick-walled tubes with a capillary constriction to prevent vortexing upon spinning of samples.

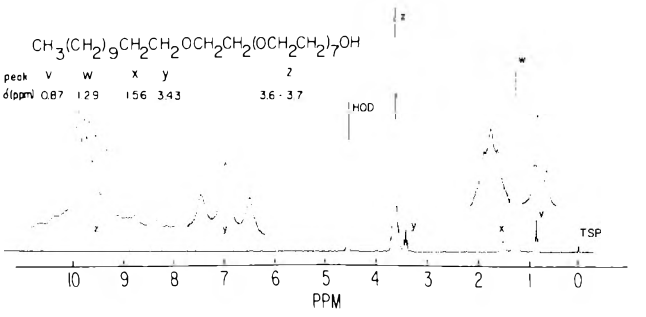


**Figure 1.** 220-MHz $^1H$ NMR spectrum of 0.1 M $C_{12}EO_8$ in $D_2O$ containing TSP. The full spectrum was recorded at 2500 Hz sweep width. The expanded spectrum of the alkyl peaks was recorded at 250 Hz sweep width and that of the oxyethylene region was recorded at 100 Hz sweep width. Spin decoupling experiments show that peak y collapses to a singlet upon irradiating peak x suggesting that these peaks comprise a first-order AX system ($J/\Delta\nu$ = 0.017 at 220 MHz).

These samples were thoroughly degassed by 5–6 freeze–pump–thaw cycles. $T_1$ measurements on samples in $D_2O$ were made in 10-mm NMR sample tubes (Wilmad) fitted with Teflon vortex plugs. For chemical shift determinations and titration experiments, these NMR sample tubes were fitted with a coaxial insert containing $CCl_4$.

## Results

A representative $^1H$ NMR spectrum of $C_{12}EO_8$ micelles in $D_2O$ is shown in Figure 1. At 220 MHz, three methylene triplets (peaks v, x, and y) and a methylene envelope are observed for the alkyl chain while the polyoxyethylene protons give several closely spaced, chemically shifted lines (peak z); these oxyethylene lines were not previously resolved at lower field strengths.[7-9] The triplets v, x, and y are assigned to the C-12 (terminal methyl), C-1, and C-2 methylene protons of the alkyl chain. The asymmetric oxyethylene band of chemically shifted lines is similar to that previously observed for OPE micelles in $D_2O$.[1,2,10] In contrast, the oxyethylene protons of the polyethylene glycols (up to the octamer) are known to be chemically equivalent.[14]

Because the common commercial nonionic OPE surfactants possess polydisperse oxyethylene moieties, it was possible that polydispersity could have contributed to the various oxyethylene lines observed for the OPE micelles. The present spectrum of the homogeneous surfactant suggests that the oxyethylene lines are indicative of subtle differences in the local, segmental environment of each polyoxyethylene proton in a micellar structure. Examination of the accumulated evidence using a combination of chemical shifts, proton $T_1$ values, and intensity changes as a function of oxyethylene chain length suggests that the protons on the low field side of the oxyethylene band arise from oxyethylene units at the end of the chain, while protons on the high field side correspond to interior oxyethylene units closer to the hydrophobic part of the molecule.[1,10,15] A more detailed assignment will require the synthesis of deuterated analogues.

$^{13}C$ NMR spectra of $C_{12}EO_8$ micelles in $D_2O$ and an ethylene glycol in $CDCl_3$ are shown in Figures 2 and 3, respectively. In contrast to the $^1H$ spectra, the $^{13}C$ spectra show well-resolved resonances in both the alkyl and oxyethylene regions. $^{13}C$ chemical shifts and proposed assignments for several linear alkyl glycol ether derivatives are listed in Table I. The assignment for the C-2 to C-12 carbons of the alkyl chain is based on previous assignments for aliphatic compounds[19-24] while the C-1 carbon is readily assigned from the data for the dialkyl ethers (Table I).

In micelles in $D_2O$, the oxyethylene carbons of the surfactant give rise to a major resonance (peak i, 69.8 ppm),

TABLE I: $^{13}C$ NMR Chemical Shifts ($\delta$) of Alkyl Polyoxyethylene Ethers, Ethylene Glycols, and Ether Derivatives[a]

$CH_3CH_2CH_2CH_2(CH_2)_6CH_2CH_2(OCH_2CH_2)_6OCH_2CH_2OCH_2CH_2OH(\text{-}OCH_3)$
a b f d e c j i h k g l

| Compound | Solvent | a | b | f | d | e | c | j | i | h | k | g | l |
|---|---|---|---|---|---|---|---|---|---|---|---|---|---|
| $CH_3(CH_2)_{11}(OCH_2CH_2)_8OH$ | $D_2O$ | 13.8 | 22.6 | 31.9 | 29.4 | 29.8 | 26.1 | 71.0 | 69.8 | 69.6 | 71.9 | 60.5 | |
| $CH_3(CH_2)_{11}(OCH_2CH_2)_8OH$ | $CDCl_3$ | 14.0 | 22.6 | 31.7 | 29.4 | 29.6 | 26.2 | 71.5 | 70.6 | 70.2 | 72.7 | 61.7 | |
| $CH_3(CH_2)_{11}(OCH_2CH_2)_8OH$ | $CD_3OD$ | 14.3 | 23.5 | 32.9 | 30.3 | 30.5 | 27.0 | 72.2 | 71.4 | 71.1 | 73.5 | 62.1 | |
| $CH_3OCH_2CH_2OH$[b] | $CDCl_3$ | | | | | | | | | | 73.7 | 61.5 | 58.8 |
| $CH_3CH_2OCH_2CH_2OH$[c] | $CDCl_3$ | 15.0 | | | | | | 66.5 | | | 72.0 | 61.5 | |
| $CH_3CH_2CH_2CH_2OCH_2CH_2OH$[c] | $CDCl_3$ | 13.9 | 19.3 | 31.8 | | | | 71.1 | | | 72.2 | 61.6 | |
| $CH_3OCH_2CH_2OCH_3$[c] | Dioxane | | | | | | | 72.3 | | | | | 58.6 |
| $CH_3OCH_2CH_2OCH_3$[d] | Dioxane | | | | | | | 72.2 | | | | | 58.3 |
| $CH_3CH_2CH_2CH_2OCH_3$[d] | Dioxane | 14.2 | 19.9 | 32.4 | | | | 72.8 | | | | | 58.3 |
| $(CH_3CH_2CH_2CH_2)_2O$[e] | | 14.6 | 20.3 | 33.1 | | | | 71.2 | | | | | |
| $H(OCH_2CH_2)_2OH$[b] | $CDCl_3$ | | | | | | | | | | 72.4 | 61.5 | |
| $H(OCH_2CH_2)_2OH$[b] | $CDCl_3$ | | | | | | | | | | 72.3 | 61.4 | |
| $H(OCH_2CH_2)_3OH$ | $CDCl_3$ | | | | | | | | | 70.3 | 72.7 | 61.4 | |
| $H(OCH_2CH_2)_3OH$ | $D_2O$ | | | | | | | | | 69.6 | 71.7 | 60.4 | |
| $H(OCH_2CH_2)_4OH$ | $CDCl_3$ | | | | | | | | 70.5[f] | 70.2 | 72.7 | 61.5 | |
| $H(OCH_2CH_2)_4OH$ | $D_2O$ | | | | | | | | 69.7[f] | 69.5 | 71.7 | 60.5 | |
| $H(OCH_2CH_2)_6OH$ | $CDCl_3$ | | | | | | | | 70.5 | 70.3 | 72.7 | 61.6 | |
| $(ClCH_2CH_2)_2O$[b] | $CDCl_3$ | | | | | | | | | | 71.3 | 42.7 ($CH_2Cl$) | |

[a] Except as noted, data are given for 0.4 M solutions at 40 °C. In $CDCl_3$ and $CD_3OD$, shifts are referenced to internal TMS. In $D_2O$, an external $CCl_4$ reference was used and shifts are converted to the TMS scale by $\delta^{TMS} = \delta^{CCl_4} + 96.05$ ppm. The conversion factor is that determined under our experimental conditions and is close to that previously reported.[16] [b] Data for 1.5 M $CH_3OCH_2CH_2OH$, 1.0 M $H(OCH_2CH_2)_2OH$, and 1.6 M $(ClCH_2CH_2)_2O$ obtained at 30 °C. [c] Data of Johnson and Jankowski,[17] spectra 92, 216, and 93. The assignments shown here for peaks g and k are the reverse of that given in ref 17. [d] Data of Dorman et al.[18] [e] Data of Lippmaa and Pehk as listed by Stothers[16] on p 144. [f] Peak i results from only the two most interior carbons.

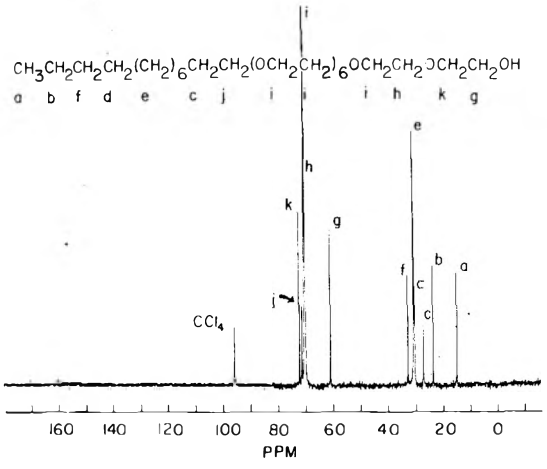


**Figure 2.** Natural abundance $^{13}C$ NMR spectrum of 0.4 M $C_{12}EO_8$ in $D_2O$ obtained with 800 scans, a pulse recycle time of 30 s, and 4K points over a 5000 Hz sweep width.

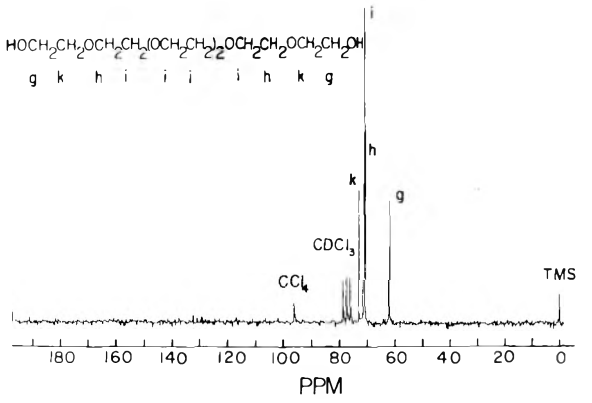


**Figure 3.** Natural abundance $^{13}C$ NMR spectrum of 0.4 M $EO_6$ in $CDCl_3$ obtained with 150 scans, a pulse recycle time of 20 s, and 4K points over a 5000 Hz sweep width.

a shoulder resonance line (peak h, 69.4 ppm) and two well-resolved peaks (peak g, 60.5 ppm; peak k, 71.9 ppm). Similar carbon resonances are observed for the homologous series of OPE surfactants[11] and for the glycol derivatives of Table I and indicate that peaks (h, i) arise from interior oxyethylene units while peaks (k, g) arise from the terminal oxyethylene group. Peak k is assigned to the first methylene group of the penultimate oxyethylene group from the spectrum of triethylene glycol. Peak i, however, presumably includes contributions from the other methylene group of the penultimate oxyethylene unit as well as all other interior oxyethylene units, as the intensity of this peak increases with increasing oxyethylene content.

Regarding the terminal oxyethylene unit, previous work has assigned peak g and peak k respectively to the penultimate and the terminal oxymethylene carbons.[17] However, although the terminal alcoholic carbon of primary alcohols generally appears at about 67 ppm,[16,19] there appears no a priori reason to expect that the terminal oxymethylene should be shifted up- or downfield from this position, and we have noted that the reverse assignment for peaks g and k might be possible.[11] Since the published $^{13}C$ NMR data on ethers was minimal,[16-18] we gathered additional evidence for an unequivocal assignment, as summarized in Tables I and II. Comparison of the $^{13}C$ NMR shifts for 2-methoxyethanol, diethylene glycol, and bis(2-chloroethyl) ether under the same experimental conditions suggests that peak g arises from the terminal oxymethylene and peak k from the penultimate oxymethylene carbons. Additional evidence (Table II) was obtained by titrating various glycol derivatives with the paramagnetic shift reagent $Yb(DPM)_3$, or $C_{12}EO_8$ micelles in $D_2O$ with the paramagnetic relaxation reagent $Mn^{2+}$. The experiments consistently show that peak g is somewhat more perturbed than peak k by the titrating agent. Furthermore, 1,1-dideuterio-2-methoxyethanol was synthesized and the $^{13}C$ NMR spectrum lacks peak g, showing that peak g results from the terminal oxymethylene line. Thus, we have reversed the assignments of ref 17.

As the solvent is changed from $D_2O$ to $CDCl_3$ to $CD_3OD$, the alkyl chain exhibits small but significant downfield shifts while the oxyethylene chain exhibits much larger

TABLE II: Observed Changes in $^{13}C$ NMR Parameters for Terminal Oxyethylene Unit of *n*-Dodecyl Octaethylene Glycol Monoether, Diethylene Glycol, and Methoxyethanol

| Compound | Solvent | Metal ion (8.4 mM) | Chemical shift, ppm | | Line width, Hz | |
|---|---|---|---|---|---|---|
| | | | Peak g | Peak k | Peak g | Peak k |
| 0.4 M $CH_3(CH_2)_{11}(OCH_2CH_2)_8OH$ | $D_2O$ | None | 60.5 | 71.9 | 2.0 | 1.7 |
| | | $Mn^{2+}$ | 60.5 | 71.9 | 49 | 8.7 |
| 0.4 M $CH_3(CH_2)_{11}(OCH_2CH_2)_8OH$ | $CDCl_3$ | None | 61.7 | 72.7 | | |
| | | $Yb^{3+}$ | 62.5 | 73.1 | | |
| 1.0 M $H(OCH_2CH_2)_2OH$ | $CDCl_3$ | None | 61.5 | 72.4 | | |
| | | $Yb^{3+}$ | 62.6 | 73.1 | | |
| 1.5 M $CH_3OCH_2CH_2OH$[a] | $CDCl_3$ | None | 61.5 | 74.0 | | |
| | | $Yb^{3+}$ | 61.9 | 74.2 | | |
| $CH_3OCH_2CD_2OH$[b] | $CDCl_3$ | None | | 73.6 | | |

[a] $Yb^{3+}$ shift reagents are known to coordinate to alcohol functional groups and to produce downfield shifts.[25,26] No shift changes are observed for the methoxy carbon (58.9 ppm) in the absence/presence of $Yb^{3+}$. [b] No resonance was detected in the 61 ppm region; the methoxy carbon signal was at 58.9 ppm.

TABLE III: $^{13}C$ NMR Spin-Lattice Relaxation Times ($T_1$) of *n*-Dodecyl Octaethylene Glycol Monoether and Various Ethylene Glycols

$CH_3CH_2CH_2CH_2(CH_2)_6CH_2CH_2(OCH_2CH_2)_6OCH_2CH_2OCH_2CH_2O$
a b f d e c j i h k g

| Compound | Solvent | Pulse recycle time, s | a | b | f | d | e | c | j | i | h | k | g |
|---|---|---|---|---|---|---|---|---|---|---|---|---|---|
| $CH_3(CH_2)_{11}(OCH_2CH_2)_8OH$ | $D_2O$ | 8.0 | 2.3 | 1.7 | 1.1 | 0.63 | 0.48 | 0.45 | 0.45 | 0.65 | 0.67 | 1.5 | 1.4 |
| $CH_3(CH_2)_{11}(OCH_2CH_2)_8OH$ | $CDCl_3$ | 17.5 | (7.4) | 5.1 | 3.4 | | 1.9 | 1.4 | 1.3 | 1.8 | 1.9 | 3.9 | 3.6 |
| $CH_3(CH_2)_{11}(OCH_2CH_2)_8OH$ | $CD_3OD$ | 15 | 5.6 | 5.1 | 3.6 | 2.1 | 1.9 | 1.4 | 1.7 | 2.3 | 2.2 | 3.5 | 3.6 |
| $H(OCH_2CH_2)_4OH$ | $CDCl_3$ | 20 | | | | | | | | 1.9 | 2.6 | 3.1 | 2.9 |
| $H(OCH_2CH_2)_6OH$ | $CDCl_3$ | 15 | | | | | | | | 1.9 | 2.2 | 2.7 | 2.8 |
| $H(OCH_2CH_2)_6OH$ | $D_2O$ | 15 | | | | | | | | 1.9 | 2.1 | 2.9 | 2.9 |

[a] $T_1$ values reported in seconds for 0.4 M samples. Ideal $T_1$ measurements require $5T_1$ recycling times. At $3T_1$ transient magnetizations equilibrate to about 95% of equilibrium value. Delay times below $3T_1$ are not sufficient for return to equilibrium magnetization, and apparent $T_1$ values obtained under these circumstances are lower limit values. Parentheses are placed around apparent $T_1$ values.

TABLE IV: Calculated Correlation Times ($\tau_{eff}$)[a] for *n*-Dodecyl Octaethylene Glycol Monoether and Various Ethylene Glycols

$CH_3CH_2CH_2CH_2(CH_2)_6CH_2CH_2(OCH_2CH_2)_6OCH_2CH_2OCH_2CH_2OH$
a b f d e c j i h k g

| Compound | Solvent | a | b | f | d | e | c | j | i | h | k | g |
|---|---|---|---|---|---|---|---|---|---|---|---|---|
| $CH_3(CH_2)_{11}(OCH_2CH_2)_8OH$ | $D_2O$ | 6.8 | 14 | 21 | 37 | 49 | 52 | 52 | 36 | 35 | 16 | 17 |
| $CH_3(CH_2)_{11}(OCH_2CH_2)_8OH$ | $CDCl_3$ | (2.1) | 4.6 | 6.9 | | 12 | 17 | 18 | 13 | 12 | 6.0 | 6.5 |
| $CH_3(CH_2)_{11}(OCH_2CH_2)_8OH$ | $CD_3OD$ | 2.8 | 4.6 | 6.5 | 11 | 12 | 17 | 14 | 10 | 11 | 6.9 | 6.5 |
| $H(OCH_2CH_2)_4OH$ | $CDCl_3$ | | | | | | | | 12 | 9.0 | 7.5 | 8.0 |
| $H(OCH_2CH_2)_6OH$ | $CDCl_3$ | | | | | | | | 12 | 11 | 8.6 | 8.3 |
| $H(OCH_2CH_2)_6OH$ | $D_2O$ | | | | | | | | 12 | 11 | 8.0 | 8.0 |

[a] In picoseconds. Calculated from $\tau_{eff} = r_{CH}^6/KT_1N_H$ where $r_{CH}$ is the internuclear distance (assumed 1.09 Å). $T_1$ is the spin-lattice relaxation time, $N_H$ is the number of attached protons, and $K$ is a constant. See ref 27 and 28.

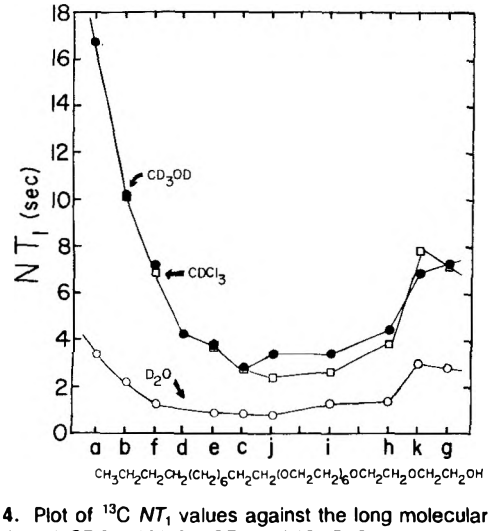


**Figure 4.** Plot of $^{13}C$ $NT_1$ values against the long molecular axis for $C_{12}EO_8$ in (□) $CDCl_3$, (●) $CD_3OD$, and (○) $D_2O$.

downfield shifts. Similar downfield shifts are observed for the ethylene glycols and the OPE surfactants.[11] Molecular motion in the ethylene glycols and $C_{12}EO_8$ in various solvents was monitored by determining $^{13}C$ $T_1$ relaxation times (Table III). Hexaethylene glycol shows similar $T_1$ relaxation times in $D_2O$ and $CDCl_3$, while $C_{12}EO_8$ shows decreased $T_1$ values in $D_2O$ compared to the values in $CD_3OD$ and $CDCl_3$ similar to observations for the OPE surfactants.[11] A plot of $^{13}C$ $NT_1$ values for $C_{12}EO_8$ is shown in Figure 4. In all solvents, the $NT_1$ appear shortest at the confluence of the alkyl and oxyethylene chains. The $NT_1$ values progress to higher values along both chains toward the chain terminal carbons.

Effective NMR correlation times, $\tau_{eff}$, calculated from the $T_1$ relaxation times appear in Table IV. The $\tau_{eff}$ values are calculated in the table by assuming relaxation due only to a heteronuclear dipolar interaction between a protonated carbon and its directly bonded protons.[27,28] Theories of dipolar relaxation, however, actually predict

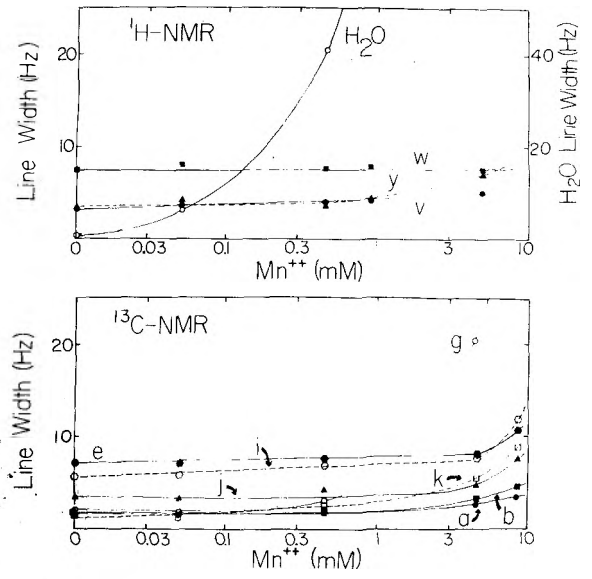


**Figure 5.** Observed $^1H$ NMR (top) and $^{13}C$ NMR (bottom) line widths for $C_{12}EO_8$ micelles in the presence of added paramagnetic $Mn^{2+}$ ions. Note that the points corresponding to zero added $Mn^{2+}$ have been plotted at the 0.01 position of the log scale.

that $T_1$ is double-valued with respect to motional correlation times. Fortunately, $T_2$, the spin–spin relaxation time is single-valued with respect to the correlation time. $T_2$* obtained from peak line widths is commonly used as a lower limit to $T_2$. The resolved single carbon resonances of $C_{12}EO_8$ in organic solution and in $D_2O$ all exhibit narrow line widths (1.5–3.6 Hz at a digital resolution of 0.31 Hz/channel) and suggest motions in the short correlation time regime. At 25 MHz, the motional narrowing region of the short correlation time side occurs when $T_1$ exceeds about 0.17 s; all of the experimentally determined $T_1$ values appear to satisfy this condition, allowing calculation of $\tau_{eff}$ as in Table IV.

The penetration of metal ions into micelles in $D_2O$ was investigated by observing NMR line width changes for the resolved lines of $C_{12}EO_8$ in $D_2O$ in the presence of paramagnetic $Mn^{2+}$ ions (Figure 5). Since it was not possible to identify the proton oxyethylene resonances, we used $^{13}C$ NMR results for these groups. With the addition of $Mn^{2+}$, the HOD resonance line representing bulk solvent immediately broadens while no changes are observed for other lines. Further addition of $Mn^{2+}$ broadens the peaks of the terminal oxyethylene (peak g) preferentially with smaller effects for other oxyethylene groups. Thus the data suggest an association between the end hydroxyl and $Mn^{2+}$ ions. Unfortunately, the end hydroxyl proton was not observed because it is exchangeable with solvent. Because paramagnetic effects decrease with the sixth power of distance, smaller effects are expected for other oxyethylene units. At higher concentrations, it is possible that some $Mn^{2+}$ may penetrate into the oxyethylene layer and even up to the C-1 methylene group as suggested by some degree of line broadening in both the $^1H$ and $^{13}C$ spectra. In contrast the terminal alkyl carbons and protons exhibit only a small amount of line broadening, suggesting these groups are well secreted from the paramagnetic ion.

## Discussion

*Aggregation State, Relaxation Times, and Mobility of $C_{12}EO_8$ in Solution.* The nonionic polyoxyethylene surfactants exhibit solvent dependent aggregation states.[5,6] Solvents with two or more potential hydrogen bonding centers enhance micelle formation similar to that in water.[29] Thus micelle formation has been reported in ethylene glycol[30] and formamide.[29,31,32] In contrast, in hydrocarbon solvents, such as decane or cyclohexane, inverted micelles may form.[6] Linear hydrogen bonding solvents with a single hydrogen bonding center, however, do not support micelle formation[29] and several reports clearly show the destruction of micelles by the lower alcohols ethanol and methanol.[33-37] Consequently, we made our $NT_1$ measurements for $C_{12}EO_8$ in the organic solvents methanol and chloroform for comparison with the results for aqueous micelles. Presumably in methanol, a relatively good hydrogen bonding solvent, $C_{12}EO_8$ behaves as a monomer while in chloroform, a weaker hydrogen bonding solvent, the exact aggregation state is not clear at this time.

The $^{13}C$ NMR spin–lattice relaxation of directly protonated carbon atoms can be effected by two kinds of molecular motion: (i) overall molecular tumbling with an average rate $(\tau_0)^{-1}$ which contributes equally to $1/NT_1$ at every carbon atom of a given spherical molecule, and (ii) internal rotations about single bonds which are independent of the motions about all other bonds with rate $(\tau_i)^{-1}$ between the $j$th and $j$th + 1 carbon. Consequently, in large molecules carbon atoms which do not partake in internal motion will have the same effective correlation times while carbon atoms which undergo internal rotations can have shorter correlation times (longer $T_1$ for short side of $T_1$ minimum). Thus, the protonated carbons of rigid rings often have identical $NT_1$ values while the $NT_1$ of long, flexible carbon chains can progressively increase along a chain from the rigid part of a molecule to the chain terminus, a process termed segmental motion.[28] The latter phenomenon in particular has been noted in the long alkyl chains of 1-decanol,[19] $C_{10}$–$C_{20}$ alkanes,[20] and ionic micelles.[21-24]

Recently we found that OPE surfactant molecules have identical $NT_1$ values in the rigid phenyl ring and in the hindered methyl and methylene carbons of the isooctyl group, suggesting that these carbons reflect only the molecular tumbling of the surfactant; also in the oxyethylene chain we found larger $NT_1$ values which progressively increase away from the phenyl ring and imply that segmental motions can occur in this chain in an analogous manner to that for the alkyl chain.[11] The present data for the APE molecule, which is completely flexible, show that segmental motions are exhibited in *both* the alkyl and the oxyethylene chains.

A more rigorous analysis of the calculated $\tau_{eff}$ for $C_{12}EO_8$ requires a detailed model of the chain motion. Recently, Levine and co-workers[38,39] have shown, for both isotropic and anisotropic tumbling, that for carbon atoms four bonds away from the tumbling center (usually the center of mass) the $^{13}C$ relaxation times are independent of the tumbling motion of the molecule. For these carbons, the effective rotational motions can be simply analyzed in terms of the overall rotation of the molecule (viewed rigid) with an average rate $(\tau_0)^{-1}$ and internal rotations about single bonds with rate $(\tau_i)^{-1}$. The difference in $(\tau_i)^{-1}$ for individual adjacent carbon atoms (denoted as $[\tau(j, j + 1)]^{-1}$) is then a measure of internal motions, as by definition $\tau_0$ is constant for the $C_{12}EO_8$ molecule.

For the alkyl chain, the calculated differences in correlation times $\tau(j, j + 1)$ suggest the least internal motion occurs about the bond between carbon atoms c and j as shown in Table V. The terminal methyl group, however, appears to undergo rapid internal rotation about the terminal bond. The rotational potential barrier about this terminal bond can be estimated from

$$\tau(\mathrm{a,b}) = A \exp(V_r/RT)$$

TABLE V: Correlation Times $\tau(j, j+1)$ Corresponding to Differences in Rates of Internal Motion[a] for *n*-Dodecyl Octaethylene Glycol Monoether and Various Ethylene Glycols

| Compound | Solvent | $\tau$(a,b) | $\tau$(b,f) | $\tau$(f,d) | $\tau$(c,j) | $\tau$(g,k) |
|---|---|---|---|---|---|---|
| $CH_3(CH_2)_{11}(OCH_2CH_2)_8OH$ | $D_2O$ | 13 | 39 | 50 | ∞ | 233 |
| $CH_3(CH_2)_{11}(OCH_2CH_2)_8OH$ | $CDCl_3$ | 3.9[b] | 14 | | 233 | 47 |
| $CH_3(CH_2)_{11}(OCH_2CH_2)_8OH$ | $CD_3OD$ | 7.1[b] | 16 | 16 | 78 | 233 |
| $H(OCH_2CH_2)_4OH$ | $CDCl_3$ | | | | | 117 |
| $H(OCH_2CH_2)_6OH$ | $CDCl_3$ | | | | | 231 |
| $H(OCH_2CH_2)_6OH$ | $D_2O$ | | | | | ∞ |

[a] In picoseconds. Calculated from $[\tau(j, j+1)]^{-1} = [\tau_{eff}(j)]^{-1} - [\tau_{eff}(j+1)]^{-1} = [\tau_i(j)]^{-1} - [\tau_i(j+1)]^{-1}$ assuming $\tau_{eff}^{-1} = \tau_0^{-1} + \tau_i^{-1}$, where $\tau_0$ is constant. Note that the values given for $\tau$(c,j) and $\tau$(g,k) are subject to large errors since the $\tau_{eff}$ values for each carbon pair are quite similar. Thus, the values of $\tau(j, j+1)$ for these carbon pairs are clearly large, but are not quantitatively significant. [b] Similar values of $\tau$(a,b) in the 4-8-ps range have been observed for the terminal $CH_3$ group of *n*-alkanes,[20] alkyl bromides,[38] alkyl amines,[23] alkyl ammonium salts,[23] and alkyl borides[39] in solutions of low viscosity typically about 1-2 cP.

where $A$ (the preexponential factor) is taken as the rate of methyl group rotation in the gas phase.[20,28] Values of 2.2 and 2.6 kcal/mol are obtained for $C_{12}EO_8$ in $CDCl_3$ and $CD_3OD$, respectively; similar values of 2.6 kcal/mol have been reported for methyl group rotation in an entire series of neat primary alkanes.[20]

For the oxyethylene chain, quantitative treatment with the model is possible only where data are available for two adjacent carbons. Treatment of the terminal unit of $C_{12}EO_8$ and the ethylene glycols gives relatively large values for $\tau(j, j+1)$, suggesting much less internal motion about the intervening C–C bond, when compared to the values for the carbon pairs at the alkyl chain terminus.

*Structure and Mobility of Nonionic Surfactant Micelles.* In water at 25 °C, the cmc of $C_{12}EO_8$ is about $7 \times 10^{-5}$ M.[40] Concentrations ca. 50 000 times that value are used in this work and thus our measurements in water refer to the surfactant in the micellar state, and any effects due to single molecules are presumed negligible. In micelles, the nonionic surfactant molecules presumably associate with their hydrophobic alkyl chains in an interior core, and their more polar polyoxyethylene chains forming an exterior palisade layer. Early work on polydisperse $C_{12}EO_8$[41] and on polydisperse[42] and homogeneous[43-45] samples of other $C_{12}EO_n$ ($n$ = 6–14) suggest a micelle molecular weight of 50 000–100 000 at 25 °C. Becher and Arai[41] suggested that the polydisperse $C_{12}EO_8$ surfactant forms micelles that are prolate ellipsoids. Tanford et al.[46] have now determined that homogeneous $C_{12}EO_8$ forms micelles of about 65 000 and have suggested from calculations with various models that $C_{12}EO_8$ micelles are oblate ellipsoids. We[47] have suggested from calculations that Triton X-100 micelles are either oblate ellipsoids or spherical (nonclassical) micelles and similar considerations should apply to $C_{12}EO_8$ micelles.

Presumably, the dominant contributions to relaxation phenomena in micelles are from the overall reorientation of surfactant molecules in micelles and the internal motions about single bonds. Experimentally, this appears plausible since the $NT_1$ parameters clearly suggest similar motional trends for $C_{12}EO_8$ in micelles and in the organic solvents. In micelles, however, the $NT_1$ values for both the alkyl and oxyethylene chains are clearly decreased. Furthermore, increases in the calculated $\tau(j, j+1)$ suggest decreases in internal motion about single bonds. Although bulk solvent viscosity differences might be suggested to account for the decrease in $NT_1$,[28] this possibility appears unlikely as the $NT_1$ values for the oxyethylene chain of hexaethylene glycol, determined under similar conditions as those for $C_{12}EO_8$, are similar in $CDCl_3$ and $D_2O$. The most plausible interpretation for the decrease in relaxation times for $C_{12}EO_8$ then is that upon micelle formation both a restriction of individual molecules from free tumbling and a restriction of internal motions about single bonds occurs.

The site of greatest immobilization for the surfactant molecules in micelles appears to be at the bond between carbon atoms c and j as these carbons show the smallest $NT_1$ values and their calculated $\tau(j, j+1)$ is very large. These are precisely the carbons that should constitute the hydrophobic/hydrophilic interface as the methylene group (corresponding to carbon atom j) is clearly in a rather polar environment, being shifted downfield of the other methylene groups in both the $^1H$ and $^{13}C$ NMR spectra (Figures 1 and 2).

The internal motions occur to a greater extent for the terminal methyl and penultimate groups than for other methylene groups. If one assumes that the former groups are located closer to the center of the hydrophobic core and the latter groups closer to the interface, increasing motions are suggested toward the inner core of the micelle from the interface. In this hydrophobic interior core, terminal methyl group rotation is calculated to face a barrier of 3.0 kcal/mol. Analogous calculations with $NT_1$ data at 34 °C[23] for ionic micelles yield a methyl group rotation barrier of 2.5 kcal/mol. Thus, although the data might indicate a slight immobilization of methyl group rotation for $C_{12}EO_8$ micelles as compared to organic solutions of $C_{12}EO_8$, neat alkanes, and ionic micelles, it appears that, to a first approximation, similar methyl group motions occur in all these systems.

For the polyoxyethylene chain in micelles, the $^{13}C$ relaxation data are consistent with increasing mobility from the interface toward the terminal unit, which is most likely at the periphery of the nonionic micelle; these phenomena have been previously noted in the OPE micelles.[11]

A major question involving the detailed structure of nonionic micelles concerns the extent and nature of their hydration by solvent molecules.[4,5] Some confusion exists in the literature on the role of water penetration into the hydrophobic core of these nonionic polyoxyethylene micelles.[48] $^{19}F$ NMR studies on partially fluorinated APE surfactants have suggested that water penetrates to the fluorocarbon group, and on the implicit assumption that the fluorocarbon group samples the hydrophobic core, imply that water does penetrate into the core.[49] The $^1H$ NMR chemical shift and $T_1$ relaxation time studies[1,8,10] on the OPE and APE systems, however, have suggested that water does not penetrate to the alkyl chain. Consistent with these studies, the $Mn^{2+}$ titration results (Figure 5) suggest that on the NMR time scale, the alkyl chain is never exposed to solvent but well-secreted in the hydrophobic core. The disparate $^{19}F$ evidence appears discountable by the suggestion that partially fluorinated moieties are actually phobic and not philic with hydrocarbon chains, and fluorinated surfactant micelles may not

be representative of "protonated" surfactant micelles.[50]

*Acknowledgment.* We thank Dr. John Wright and Mr. Rick Freisen for aid in the operation of the HR-220 and PFT-100 NMR systems and Mr. Robert Robson for help in the synthesis of 1,1-dideuterio-2-methoxyethanol. This work was supported by the National Science Foundation, Grant BMS 75-03560 and PCM 76-21552. The UCSD NMR/MS Research Resource Center was operated by the National Institutes of Health, Grant RR-00,708.

## References and Notes

(1) A. A. Ribeiro and E. A. Dennis, *Biochemistry*, **14**, 3746 (1975).
(2) A. A. Ribeiro and E. A. Dennis, *Biochim. Biophys. Acta*, **332**, 26 (1974).
(3) A. Helenius and K. Simons, *Biochim. Biophys. Acta*, **415**, 29 (1975).
(4) P. Becher in "Nonionic Surfactants, Surfactant Science Series", Vol. 1, M. J. Schick, Ed., Marcel Dekker, New York, N.Y., 1967, pp 478–515.
(5) G. C. Kresheck, *Water: Compr. Treat.*, **4**, 95–167 (1975).
(6) J. H. Fendler and E. J. Fendler, "Catalysis in Micellar and Macromolecular Systems", Academic Press, New York, N.Y., 1975.
(7) J. M. Corkill, J. F. Goodman, and J. Wyer, *Trans. Faraday Soc.*, **65**, 9 (1969).
(8) C. J. Clemett, *J. Chem. Soc., A*, 2251 (1970).
(9) F. Tokiwa and K. Tsuji, *J. Phys. Chem.*, **75**, 3560 (1971).
(10) F. Podo, A. Ray, and G. Némethy, *J. Am. Chem. Soc.*, **95**, 6164 (1973).
(11) A. A. Ribeiro and E. A. Dennis, *J. Phys. Chem.*, **80**, 1746 (1976).
(12) A. A. Ribeiro and E. A. Dennis in "Colloid and Interface Science", Vol. II, "Aerosols, Emulsions and Surfactants", Academic Press, New York, N.Y., 1976, pp 325–338.
(13) R. L. Vold, J. S. Waugh, M. P. Klein, and D. E. Pehlps, *J. Chem. Phys.*, **48**, 3831 (1968).
(14) K. J. Liu, *Macromolecules*, **1**, 213 (1968).
(15) A. A. Ribeiro, Ph.D. Thesis, University of California at San Diego, 1975, pp 96–101; *Diss. Abstr. B*, **36**, 5609 (1976).
(16) J. B. Stothers, "Carbon-13 NMR Spectroscopy", Academic Press, New York, N.Y., 1972.
(17) L. F. Johnson and W. C. Jankowski, "Carbon-13 NMR Spectra", Wiley-Interscience, New York, N.Y., 1972.
(18) D. E. Dorman, D. Bauer, and J. D. Roberts, *J. Org. Chem.*, **40**, 3729 (1975).
(19) D. Doddrell and A. Allerhand, *J. Am. Chem. Soc.*, **93**, 1558 (1971).
(20) J. R. Lyerla, Jr., H. M. McIntyre, and D. A. Torchia, *Macromolecules*, **7**, 11 (1974).
(21) E. Williams, B. Sears, A. Allerhand, and E. H. Cordes, *J. Am. Chem. Soc.*, **95**, 4871 (1973).
(22) R. T. Roberts and C. Chachaty, *Chem. Phys. Lett.*, **22**, 348 (1973).
(23) G. C. Levy, R. A. Komoroski, and J. A. Halstead, *J. Am. Chem. Soc.*, **96**, 5456 (1974).
(24) J. M. Brown and J. D. Schofield, *J. Chem. Soc., Chem. Commun.*, 434 (1975).
(25) W. De W. Horrocks, Jr., and J. P. Sipe, III, *J. Am. Chem. Soc.*, **93**, 6800 (1971).
(26) C. C. Hinckley, *J. Am. Chem. Soc.*, **91**, 5160 (1969).
(27) D. Doddrell, V. Glushko, and A. Allerhand, *J. Chem. Phys.*, **56**, 3683 (1972).
(28) J. R. Lyerla, Jr., and G. C. Levy, *Top. Carbon-13 NMR Spectrosc.*, **1**, 79–147 (1974).
(29) A. Ray, *Nature (London)*, **231**, 313 (1971).
(30) A. Ray and G. Némethy, *J. Phys. Chem.*, **75**, 809 (1971).
(31) C. McDonald, *J. Pharm. Pharmacol.*, **22**, 148 (1970).
(32) C. McDonald, *J. Pharm. Pharmacol.*, **22**, 774 (1970).
(33) M. J. Sasaki and N. Sata, *Kolloid. Z.*, **199**, 49 (1964).
(34) M. J. Schick and A. H. Gilbert, *J. Colloid. Sci.*, **20**, 464 (1965).
(35) P. Becher, *J. Colloid. Sci.*, **20**, 728 (1965).
(36) P. Becher and S. E. Trifiletti, *J. Colloid. Interface Sci.*, **43**, 485 (1973).
(37) K. Deguchi, T. Mizuno, and K. Meguro, *J. Colloid Interface Sci.*, **48**, 474 (1974).
(38) Y. K. Levine, N. J. M. Birdsall, A. G. Lee, J. C. Metcalfe, P. Partington, and G. C. K. Roberts, *J. Chem. Phys.*, **60**, 2890 (1974).
(39) Y. K. Levine, P. Partington, and G. C. K. Roberts, *Mol. Phys.*, **25**, 497 (1973).
(40) K. Deguchi and K. Meguro, *J. Colloid Interface Sci.*, **38**, 596 (1972).
(41) P. Becher and H. Arai, *J. Colloid Interface Sci.*, **27**, 634 (1968).
(42) M. J. Schick, S. M. Atlas, and F. R. Eirich, *J. Phys. Chem.*, **66**, 1326 (1962).
(43) J. M. Corkill, J. F. Goodman, and R. H. Ottewill, *Trans. Faraday Soc.*, **57**, 1627 (1961).
(44) R. R. Balmbra, J. S. Clunie, J. M. Corkill, and J. F. Goodman, *Trans. Faraday Soc.*, **58**, 1661 (1962).
(45) D. Attwood, P. H. Elworthy, and S. B. Kayne, *J. Phys. Chem.*, **74**, 3529 (1970).
(46) C. Tanford, Y. Nozaki, and M. F. Rohde, *J. Phys. Chem.*, to be submitted for publication (personal communication).
(47) R. J. Robson and E. A. Dennis, *J. Phys. Chem.*, in press.
(48) N. Nishikido, Y. Moroi, and R. Matuura, *Bull. Chem. Soc. Jpn.*, **48**, 1387 (1975).
(49) N. Muller and F. E. Platko, *J. Phys. Chem.*, **75**, 547 (1971).
(50) P. Mukerjee and K. J. Mysels, *ACS Symp. Ser.*, **No. 9**, 239–252 (1975).

# On the Correlation between Electron Spin–Lattice Relaxation Times and Hydrogen Atom Decay Kinetics in Sulfuric Acid Glasses X-Irradiated at 4 to 90 K

**Larry Kevan* and Andrzej Plonka†**

*Department of Chemistry, Wayne State University, Detroit, Michigan 48202* *(Received July 12, 1976; Revised Manuscript Received March 2, 1977)*

The electron spin–lattice relaxation time measured by progressive saturation methods at 77 K for trapped hydrogen atoms in sulfuric acid glasses is found to be sensitive to the x-irradiation temperature from 4 to 90 K. This effect of irradiation temperature qualitatively correlates with similar effects on the H atom decay kinetics at 77 K and suggests that the spin–lattice relaxation time may be diagnostic for differences in trap limited radical decay kinetics.

## Introduction

It is somewhat remarkable, but true, that an entity as reactive as a hydrogen atom can be trapped following $\gamma$ irradiation of various oxyacid ices at 77 K.[1] At 77 K the H atoms do decay slowly but only to the extent of about 5% in 50 h. Furthermore, the decay rate becomes slower with time. The H atom decay kinetics can be speeded up and more easily studied by increasing the temperature above 77 K or by adding reactive solutes such as alcohols. Recent kinetic studies by electron spin resonance at 77 K have suggested that the environment of the trapped H atom changes with time at a given temperature[2] and that it depends upon the irradiation temperature at which the H atoms are formed.[3] The environmental changes have been interpreted as due either to a dynamic, thermally

† On leave from the Institute of Applied Radiation Chemistry, Technical University of Lodz, Lodz, Poland.

activated redistribution of H atoms from shallower to energetically deeper preformed traps,[2] or to a thermally activated relaxation of the matrix around a trapped H atom in a given trap.[3]

The electron spin–lattice relaxation time measures the rate of magnetic energy transfer from a radical to its environment and is thus expected to be a sensitive probe of the interaction of a trapped H atom with its environment.[4] If the environmental interaction does control the H atom decay kinetics we expect that the spin–lattice relaxation time may correlate with decay rates and give molecular insights into how the decay process occurs. To assess this postulate we need first to explore whether the same factors that affect H atom decay rates give measurable differences between electron spin–lattice relaxation times.

In this work we investigate the effect of irradiation temperature at which H atoms are formed on the relative electron relaxation times measured by a progressive saturation technique. For irradiation temperatures between 4 and 90 K we find that the relaxation time for H atoms at 77 K are distinguishable.

## Experimental Section

The aqueous solutions 6 M in $H_2SO_4$ without and with 0.05 M $FeSO_4$ added were prepared from Baker Analyzed sulfuric acid and ACS certified ferrous sulfate (Fisher Scientific Co.).

To prepare the acid glass samples the above solutions were poured into cylindrical containers made from thin aluminum foil (diameter 2.5 mm, height 10 mm) immersed in liquid nitrogen. A small piece of copper wire introduced into the freezing solution enabled easy handling of the frozen samples. The aluminum foil was striped off under liquid nitrogen and the samples were x-irradiated at temperatures from 4 to 90 K. For irradiation at 4 and 77 K liquid helium or liquid nitrogen dewars were used. All other irradiations were performed with the use of a cold helium gas flow system. In each case the tail section of the dewar was in contact with the beryllium window of a Siemens x-ray tube (AGW 61) driven by a Kristalloflex-2 power supply. At 60 kV and 50 mA the dose rate was equal to about 8.8 Mrad/h, as estimated from a comparison of the amount of trapped hydrogen atoms produced by x-rays to the hydrogen atom yield from a Co-60 $\gamma$ source which had a calibrated dose rate of 0.16 Mrad/h.

The acid glass samples were typically x-irradiated for 15 min, transferred quickly into another dewar for measurement to avoid background signals, and electron spin resonance spectra were recorded at 6-kHz magnetic field modulation with a Varian V-4500 spectrometer. A balanced mixer type microwave bridge, built in this laboratory, was used in the place of the Varian bridge.

The microwave magnetic field $H_1$, in mG, was estimated from the relation[5] for a Varian $TE_{104}$ cavity with a quartz insert used in the present experiments:

$$H_1 = 2.22 \times 10^3 P^{1/2}$$

where the microwave power, $P$, is in watts. The microwave power was measured with a thermistor connected to a Hewlett-Packard power meter (HP 431 C).

## Results

The microwave power saturation behavior of the main transition and of one of the proton spin–flip satellites of the high field hydrogen line, measured at 90, 77, 55 and 4 K for 6 M $H_2SO_4$ glass x-irradiated at 90 K, is presented in Figure 1. It is evident that with temperature decrease the saturation of the main transition and of the satellite

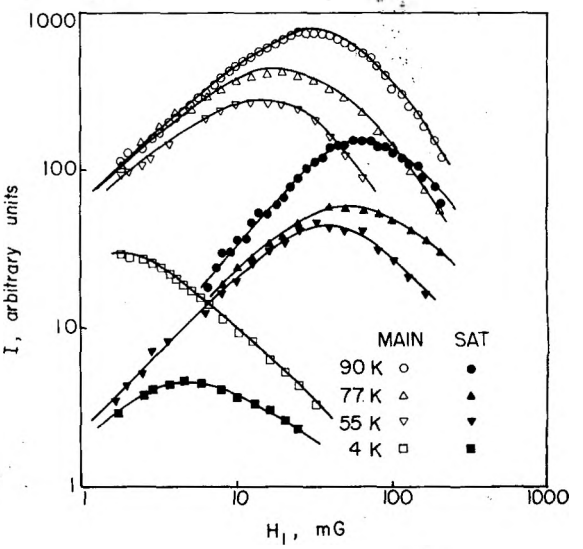


**Figure 1.** Microwave power saturation curves on a log–log scale for the main high field ESR line and for one of the single spin–flip satellite lines due to trapped H atoms in 6 M $H_2SO_4$ glass x-irradiated (2.2 Mrad) at 90 K and measured at 90, 77, 55, and 4 K.

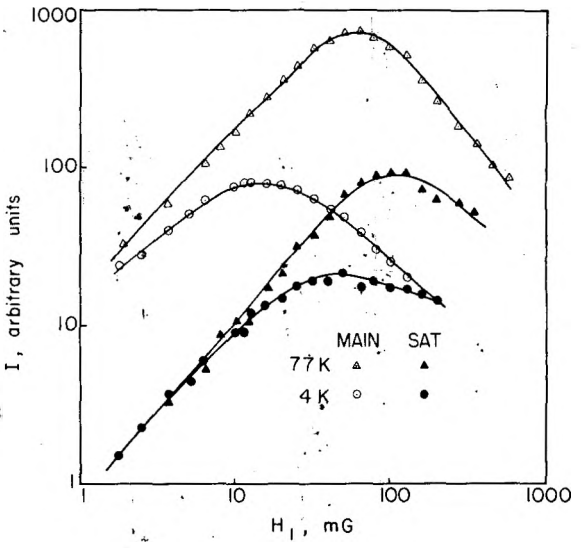


**Figure 2.** Microwave power saturation curves on a log–log scale for the main high field ESR line and for one of the single spin–flip satellite lines due to trapped H atoms in 6 M $H_2SO_4$ glass containing 0.05 M of $FeSO_4$ x-irradiated (2.2 Mrad) at 77 K and measured at 77 and 4 K.

occur at successively lower values of $H_1$. The vertical position of the curves was adjusted so that all satellite transition curves reach the same values at low microwave power below saturation. This also adjusts the scale of the main transition curves. This procedure is justified from the results for 6 M $H_2SO_4$ glass, containing 0.05 M of $FeSO_4$ (see Figure 2) in which the saturation occurs at higher values of $H_1$ due to cross relaxation of H with $Fe^{2+}$.[6] The occurrence of saturation at lower power as the measurement temperature decreases (Figure 1) is compatible with $T_1$ increasing at lower temperature.

For measurement at 77 K the saturation behavior of the glasses irradiated at 90, 77, and 4 K are all different and do not even show a monotonic trend with irradiation temperature; see Figure 3. The H atoms produced by irradiation at 77 K are more easily saturated than those produced by irradiation at either 90 or 4 K. Thus, the saturation behavior reflects the temperature of the matrix at which the H atoms were originally trapped as well as the temperature of measurement. All measurements were

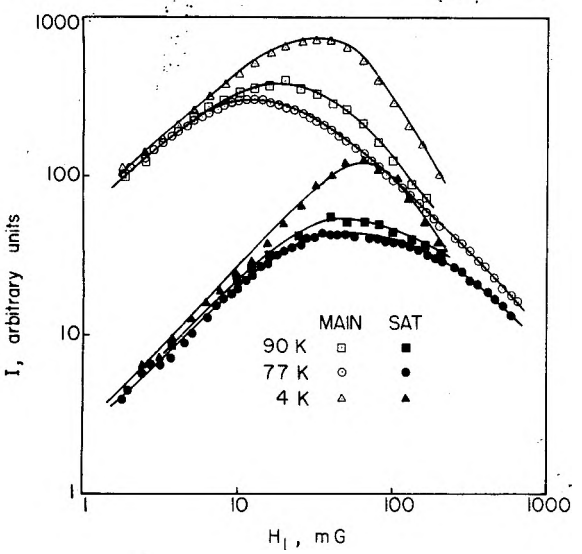


**Figure 3.** Microwave power saturation curves on a log–log scale for the main high field ESR line and for one of the single spin–flip satellite lines due to trapped H atoms in 6 M $H_2SO_4$ glass x-irradiated (2.2 Mrad) at 90, 77, and 4 K and measured at 77 K.

begun within 30 min after irradiation, so that the temporal history of each sample was similar.

## Discussion

Although the relaxation times obtained from saturation studies under fast passage conditions, as we have, have doubtful absolute validity, we may use them for valid comparisons within a given paramagnetic system.[4,5] The saturation parameter $Z$ for an inhomogeneously broadened line under fast passage conditions is given by

$$Z = [1 + (2\gamma H_1^2 T_1/\pi H_m)]^{-1} \quad (1)$$

The spin–lattice relaxation time $T_1$ may be calculated by finding the numerical value of $H_1$ for which the signal intensity is one-half of what it would be in the absence of saturation. Substituting $H_{1/2}$ for $H_1$ at $Z = 1/2$ the spin–lattice relaxation time is given by[4]

$$T_1 = \pi H_m/2\gamma H_{1/2}^2 \quad (2)$$

where $H_m$ denotes the modulation amplitude and $\gamma$ is the gyromagnetic ratio of the electron.

Making use of relation 2 we have estimated $T_1$ at 77 K for samples x-irradiated at 77 K to be equal to about 2.0 ms. This value has been confirmed by direct $T_1$ measurements by the saturation recovery method on a pulsed ESR spectrometer. For samples irradiated at 90 K the relaxation times measured at 90, 77, and 55 K are equal to 0.25, 0.84, and 1.4 ms, respectively. This trend for $T_1$ with temperature is typical and appears independent of matrix relaxation effects. No additional matrix relaxation is expected when cooling the matrix below its irradiation temperature.

The striking effect of irradiation temperature on $T_1$ (Figure 3) is shown by the following results which are coded by irradiation temperature/observation temperature: 77 K/77 K, 2.0 ms; 90 K/77 K, 0.84 ms; and 4 K/77 K, 0.27 ms. This effect of irradiation temperature on the spin–lattice relaxation time seems analogous to the effect of irradiation temperature on the H atom decay kinetics in sulfuric acid matrices containing 2-propanol.[3] Two types of relative kinetic behavior were found in those studies. The initial relative slopes of $d[H]/dt$ were respectively 0.08, 1.0, and 2.0 for 90 K/77 K, 77 K/77 K, and 63 K/77 K irradiation and observation temperatures; while the relative slopes after about 80 min of decay had changed to 0.32, 1.0, and 0.17 for 90 K/77 K, 77 K/77 K, and 63 K/77 K, respectively. For the decays at longer times the 77 K/77 K slope was larger than for higher or lower irradiation temperatures. We cannot make a quantitative comparison of the kinetic and relaxation time results because the experimental conditions are different, but the qualitative features do suggest that the spin–lattice relaxation time may be diagnostic for differences in trap limited radical decay kinetics.

Earlier work has shown that changes in the environment of a trapped H atom with time (100 h at 77 K) may be probed by measuring a change in the ratio of satellite to main line intensities.[2] Although the quantitative analysis of H atom to matrix proton distances was carried out incorrectly in that work,[7] the decrease in the ratio with time does indicate an increase in this distance. In our studies on a much shorter time scale no significant changes in the satellite to main line ratio were observed as a function of irradiation temperature. Thus $T_1$ measurements appear to be somewhat more sensitive than satellite intensity measurements to environmental changes that affect radical decay kinetics.

Since we have shown that electron spin–lattice relaxation times are distinguishable under conditions that lead to different radical decay kinetics, we are optimistic that $T_1$ data will be useful in unraveling the subtleties of the complex radical decay features typically observed in irradiated solids. It will be more incisive to make rapid and direct measurements of $T_1$ by pulsed electron spin resonance techniques which can be directly compared with instantaneous radical decay rates under the same experimental conditions. Such investigations are in progress.

*Acknowledgment.* This research was supported by the U.S. Energy Research and Development Administration under Contract No. E(11-1)-2086. We thank Dr. D. Becker for the direct measurement of $T_1$ by pulsed electron spin resonance.

## References and Notes

(1) R. Livingston, H. Zeldes, and E. H. Taylor, *Discuss. Faraday Soc.*, **19**, 166 (1955).
(2) E. D. Sprague and D. Schulte-Frohlinde, *J. Phys. Chem.*, **77**, 1222 (1973).
(3) J. Kroh and A. Plonka, *J. Phys. Chem.*, **79**, 2600 (1975).
(4) J. Zimbrick and L. Kevan, *J. Chem. Phys.*, **47**, 5000 (1967).
(5) B. L. Bales and L. Kevan, *J. Chem. Phys.*, **52**, 4644 (1970).
(6) S. K. Wong and J. K. S. Wan, *J. Chem. Phys.*, **55**, 4940 (1971).
(7) M. Bowman, L. Kevan, and R. N. Schwartz, *Chem. Phys. Lett.*, **30**, 208 (1975).

# Mechanism of Spin Diffusion in Electron Spin Resonance Spectra of Trapped Electrons in Aqueous Glasses. Electron–Electron Double Resonance Studies

**Ding-ping Lin[1] and Larry Kevan***

*Department of Chemistry, Wayne State University, Detroit, Michigan 48202* *(Received December 28, 1976)*

Electron–electron double resonance (ELDOR) has been used to test the validity of the noninteracting spin packet model for inhomogeneously broadened ESR lines. For trapped electrons in 10 M $NaOD/D_2O$ glassy ice the saturation of field-swept ELDOR spectra fits the above mentioned model in contrast to earlier work on trapped electrons in protiated matrices. In the protiated matrix spin diffusion produces significant interaction between the spin packets. The difference between the protiated and deuterated matrices suggests that nuclear relaxation is the mechanism for spin diffusion. The deuterated matrices show no structure in frequency-swept ELDOR spectra due to deuteron spin–flip transitions whereas structure due to proton spin–flips is seen in protiated matrices.

## Introduction

Electron spin resonance (ESR) spectra of trapped radicals in disordered solids are typically inhomogeneously broadened due to unresolved hyperfine interaction with matrix nuclei. Inhomogeneous broadening arises because the average static magnetic field varies for different spins and this variation can be associated with different nuclear configurations around the unpaired spins. To describe the microwave power saturation behavior of inhomogeneously broadened ESR lines Portis originally introduced a "noninteracting spin packet" model in which he assumed that each set of electron spins that interacted with the same nuclear configuration formed a homogeneously broadened spin packet.[2] The various spin packets superimpose to produce the observed inhomogeneously broadened line.

This noninteracting spin packet model has been widely used to interpret power saturation behavior of ESR lines in terms of radical spatial distributions and to deduce the magnetic relaxation parameters $T_1$, spin–lattice relaxation time, and $T_2$, spin–spin relaxation time.[3] Portis originally assumed that the spin packet width was much less than the observed inhomogeneous line width.[2] Castner[4] generalized the model so that this assumption was not necessary. Recently, Bowman et al.[5] have further extended the model to include ESR detection by magnetic field modulation which is the common experimental method now used. We now explore the interaction between spin packets.

Communication or interaction between spin packets can be described as spin diffusion within an ESR line. Portis[6] apparently first introduced the concept of spin diffusion and considered the specific mechanism of electron spin–electron spin dipolar interaction. In later treatments others[7-9] have considered a variety of mechanisms of spin diffusion, including electron spin–lattice relaxation, exchange interactions, nuclear relaxation, instantaneous diffusion by microwave pulses, and even macroscopic diffusion of individual radicals. Thus spin diffusion now broadly means transfer of saturation between spin packets without implying any specific mechanism.

Electron–electron double resonance (ELDOR)[10] has been used to incisively study the spin packet model for trapped electrons in KCl crystals (F centers)[11] and for trapped electrons in $\gamma$ irradiated 10 M NaOH aqueous glass.[12] In both cases the noninteracting spin packet model fails quantitatively, although not qualitatively, and indicates the existence of significant spin diffusion. ELDOR is ideal for such studies because two microwave frequencies are used which can be applied to different spin packets in a single ESR line. In the present work we investigate the mechanism of spin diffusion for trapped electrons in aqueous glasses by changing the magnetic matrix nuclei from protons to deuterons. The results indicate that nuclear relaxation is involved and, interestingly, that the noninteracting spin packet model is satisfactory for deuterated matrices.

## Experimental Section

Fresh solutions of 10 M $NaOD/D_2O$ were prepared from 40 wt % $NaOD/D_2O$ and $D_2O$ from Stohler Isotope Chemicals. Samples were sealed in 4-mm o.d. suprasil quartz tubes, frozen rapidly in liquid nitrogen to the glassy state, and irradiated with $^{60}Co$ $\gamma$ rays at 77 K at a dose rate of 0.21 Mrad $h^{-1}$. Trapped electrons ($e_t^-$) and $O^-$ are the paramagnetic species produced by irradiation, with $O^-$ downfield from $e_t^-$.

The ELDOR spectrometer and operating procedures have been described.[12] Magnetic field modulation at 100 kHz with a peak-to-peak amplitude of 0.6 G was used to record the spectra. The maximum pumping microwave magnetic field at 0 dB was $H_{1p}$ = 0.68 G. Field-swept ELDOR spectra are obtained with both pumping and detecting microwave frequencies held constant. Frequency-swept ELDOR spectra are obtained by sweeping the pumping microwave frequency $f_p$ while holding the detecting microwave frequency $f_d$ and the magnetic field constant; different frequency swept spectra may be obtained for different magnetic field positions. The detecting microwave power was kept below the saturation region, 2 $\mu$W, for the trapped electrons. Different sets of spectra at various temperatures were studied and analyzed to compare with the data on protiated systems[12] under similar conditions.

## Results

The field-swept ELDOR spectra for $e_t^-$ at $\Delta f = f_p - f_d$ = 6 MHz at various pump powers are shown in Figure 1. As the spectrum is swept from low to high field the pump frequency lags the detecting frequency when $\Delta f$ is positive as it is here. In Figure 1 at -39 dB with effectively no pump power applied, the usual ESR spectrum is seen. As the pump power increases, the spectra become asymmetric as the high field part of the derivative curve diminishes. The low field peak of the derivative curve slowly decreases. These results are similar to those previously observed for

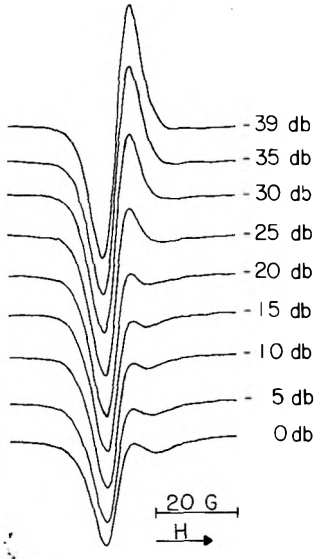


**Figure 1.** Field-swept ELDOR spectra of trapped electrons in 10 M $NaOD/D_2O$ glassy ice $\gamma$ irradiated to 2.3 Mrad at 77 K and measured at 40 K. The pumping frequency is higher than the detecting frequency by 6 MHz and the pumping microwave powers are shown in dB below the maximum; −39 dB corresponds to the ESR spectrum unperturbed by pumping power.

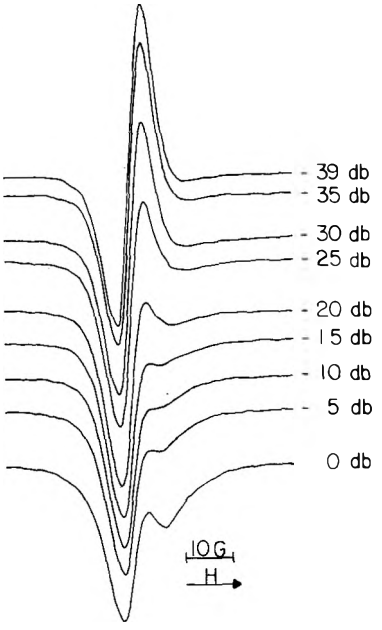


**Figure 2.** Field-swept ELDOR spectra of trapped electrons in 10 M $NaOD/D_2O$ glassy ice $\gamma$ irradiated to 5.3 Mrad and measured at 77 K. The pumping frequency is higher than the detecting frequency by 6 MHz and the pumping microwave powers are shown in dB below the maximum; −39 dB corresponds to the ESR spectrum unperturbed by pumping power.

$e_t^-$ in 10 M $NaOH/H_2O$ except that the high field peak of the derivative curve decreases more rapidly with pump power in the deuterated matrix. This will be seen to be consistent with less spin diffusion in the deuterated matrix.

Figure 2 shows the same type of ELDOR spectra as in Figure 1 at a higher dose of 5.3 Mrad. The same type of behavior is observed except that the ELDOR spectra appear to be more strongly saturated at high pump power.

Figure 3 shows field-swept ELDOR data for 0 dB pumping power for various $\Delta f$ from 50 to 6 MHz. At $\Delta f$ = 40–50 MHz no difference is observed between the spectra with and without pumping power. At $\Delta f$ = 30 MHz the ESR line shape is distorted constituting an ELDOR response. This frequency difference corresponds to about

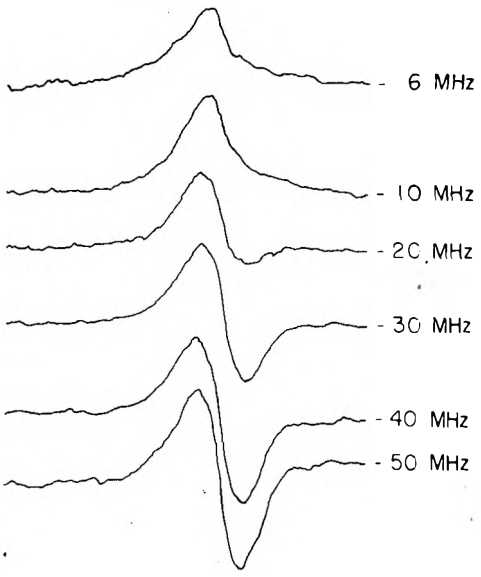


**Figure 3.** Field-swept ELDOR spectra of trapped electrons in 10 M $NaOD/D_2O$ glassy ice $\gamma$ irradiated to 2.3 Mrad and measured at 77 K. The pumping microwave frequency is higher than the detecting microwave frequency by the amounts indicated. The pump power is 0 dB.

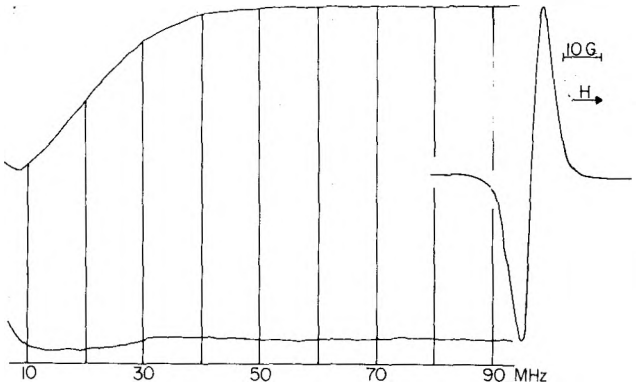


**Figure 4.** Frequency-swept ELDOR spectra of trapped electrons in 10 M $NaOD/D_2O$ glassy ice $\gamma$ irradiated to 2.3 Mrad and measured at 77 K with the pumping frequency higher than the detecting frequency. The frequency difference is given on the abcissa. The pump power is 0 dB. The trapped electron ESR spectrum is also shown on the right. The ELDOR spectra were obtained when sitting on the high field and low field derivative maxima of the ESR spectrum.

twice the ESR derivative line width $\Delta H_{ms}$ of 5.4 G = 15.1 MHz.

Frequency-swept ELDOR spectra are shown in Figure 4 for the magnetic field set on each derivative peak of the ESR line. There is no evidence of structure in these spectra as is observed in the spectra in the protiated matrix.[12]

## Spectral Analysis

The field-swept ELDOR spectra show the saturation of the ESR spectrum under ELDOR conditions. We analyze the spectra with the noninteracting spin packet model for ELDOR developed for $e_t^-$ in protiated matrices.[12] For detecting microwave power below the saturation region our signal is proportional to the imaginary part of the magnetic susceptibility at the detecting angular frequency given by

$$\chi''(\omega_d) = C\int_0^\infty [(a\{a^2 + [(\omega_d - \omega')/\Delta\omega_G]^2\}^{-1} \exp\{-[(\omega' - \omega_0)/\Delta\omega_G]^2\})/(1 + Sa^2\{a^2 + [(\omega_p - \omega')/\Delta\omega_G]^2\}^{-1})]\, d(\omega'/\Delta\omega) \quad (1)$$

where $C$ is a constant, $a = \Delta\omega_L/\Delta\omega_G$, $S = \gamma^2 H_{1p}{}^2 T_1 T_2$, $\gamma$

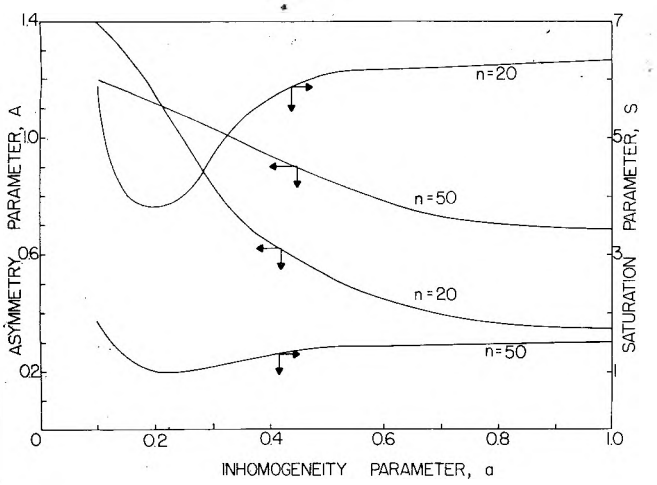


**Figure 5.** Theoretical analysis plot for pump saturation of field-swept ELDOR spectra with $\Delta f = 6$ MHz. The various parameters are defined in the text and $n$ varies with pump microwave power.

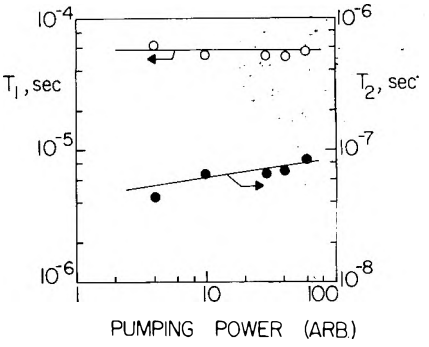


**Figure 6.** Dependence of $T_1$ and $T_2$ for trapped electrons in 10 M NaOD/$D_2O$ based on the ELDOR saturation measurements in Figure 2 and the noninteracting spin packet model vs. relative pumping microwave power.

$= 1.76 \times 10^7$ G$^{-1}$ s$^{-1}$, and $\omega_p = 2\pi f_p$. The spin packets are assumed to be Lorentzian with a half-width at half-height of $\Delta\omega_L = T_2^{-1}$, and the distribution of spin packets is taken as Gaussian, in agreement with the observed ESR line shape, with a half-width at half-height of $\Delta\omega_G = \gamma\Delta H_{ms}(\ln 2/2)^{1/2}$. The frequencies $\omega_0$ and $\omega'$ are the centers of the observed line and the spin packet, respectively. Equation 1 is integrated numerically. Our experiments at 100-kHz magnetic field modulation correspond to fast modulation conditions[12] so the theoretical field-swept ELDOR spectra are given by $d\chi''/d\omega_d$.

We will characterize the shape of simulated field-swept ELDOR spectra for $f_p > f_d$ in terms of an asymmetry parameter $A(n)$ dependent upon the pump power and use this to deduce values of $T_1$ and $T_2$.[12] The constancy of $T_1$ and $T_2$ vs. pumping power will serve as a criterion for the adequacy of the noninteracting spin packet model. $A(n)$ is defined as the value of the low field derivative peak height, measured from the baseline and normalized to 1.0 in the absence of pump power, when the high field derivative peak height has decreased to $n$% of its value in the absence of pump power. Thus $A(n)$ characterizes the ELDOR saturation. One should note that $A(n)$ can be greater than unity. The saturation of the ELDOR line shape in terms of $A(n)$ depends on the inhomogeneity parameter $a$ as shown in Figure 5 for $n = 50$ and 20. The dependence of the saturation parameter $S(n)$ for a given pump power corresponding to $n$ also depends on $a$ and $S$ for a given $n$ from theoretical curves such as those shown in Figure 5. $T_2$ is then determined from $a = 1.7/T_2\gamma\Delta H_{ms}$ and $T_1$ is determined from $S = \gamma^2 H_{1p}{}^2 T_1 T_2$. Figure 6 shows the $T_1$ and $T_2$ values calculated from the results shown in Figure 2. The values are obtained for $n = 90$ to 20 and correspond to a 15-fold range in pumping power.

## Discussion

The objective of the present experiment is to test the noninteracting spin packet model for inhomogeneously broadened ESR lines in deuterated disordered matrices. For ELDOR experiments this model is represented by eq 1. One test of the model is given by Figure 6. The model predicts that $T_1$ and $T_2$ should be constants independent of pumping microwave power. Figure 6 suggests that the model is satisfactory for trapped electrons in deuterated aqueous matrices. This implies that spin diffusion does not occur at a faster rate than spin–lattice relaxation.

In contrast to the deuterated matrix, similar experiments on $e_t^-$ in 10 M NaOH/$H_2O$ have shown that the noninteracting spin packet model is not satisfactory.[12] In the protiated matrix $T_1$ decidedly decreases with increasing pumping microwave power and implies that the spin packets do interact. This interaction occurs phenomenologically by spin diffusion characterized by a time $T_D$ such that $T_2' \leq T_D < T_1'$ where $T_1'$ and $T_2'$ are the relaxation times in the absence of spin diffusion. In both protiated and deuterated matrices $T_2$ increases slightly with increasing pump power; this small effect is not understood in detail.

The different relative importance of spin diffusion in the protiated and deuterated matrices suggests that the spin diffusion mechanism involves nuclear relaxation via an electron–nuclear dipolar (END) interaction. In this case the spin diffusion time is about $\gamma_H{}^2/\gamma_D{}^2 \sim 42$ times longer in the deuterated matrix compared to the protiated matrix and is consequently much less important in deuterated matrices. The nuclear gyromagnetic ratios have been used to make this estimate. The other mechanisms of spin diffusion mentioned in the Introduction[7-9] are not directly dependent on the gyromagnetic ratio of the matrix nuclei.

A related indication of the different importance of spin diffusion in protiated and deuterated matrices is given by the pumping power range over which the high field peak of the derivative ESR line decreases to the baseline; see spectra in Figures 1 and 2. In the deuterated matrices this range is about 20 dB in pump power. However in protiated matrices this range is about 30 dB.[12] When significant spin diffusion occurs, some effective desaturation occurs for the detected spin packet which causes saturation to occur more slowly with pumping power.

Finally we comment on the absence of structure in the frequency-swept ELDOR spectra in deuterated matrices (see Figure 4). This stands in contrast to the structure observed in protiated matrices.[12] The structure in protiated matrices was originally assigned to isotropic hyperfine structure, but subsequent analysis has shown that the isotropic hyperfine constant is much smaller[13,14] and that the structure in the ELDOR spectra is due to forbidden transitions involving simultaneous proton and electron spin-flips.[15] At our magnetic field deuteron spin-flip lines should occur with a spacing of about 2.2 MHz. However, the intensity of the deuteron spin-flip lines in ESR spectra will be reduced by about $\gamma_H{}^2/\gamma_D{}^2 \sim 42$ times relative to proton spin-flip lines. Although the spin-flip transition probabilities may be altered somewhat in ELDOR spectra they still appear too weak to be observed.

*Acknowledgment.* This research was supported by the U.S. Energy Research and Development Administration under Contract No. E(11-1)-2086. Larry Kevan thanks

Drs. T. Higashimura and H. Hase at the Research Reactor Institute of Kyoto University and the Japanese Society for the Promotion of Science for their cooperation and support while this work was completed.

## References and Notes

(1) Present address: Edward Waters College, Jacksonville, Fla.
(2) A. M. Portis, *Phys. Rev.*, **91**, 1071 (1953).
(3) See, for example, D. P. Lin and L. Kevan, *J. Chem. Phys.*, **55**, 2629 (1971).
(4) T. G. Castner, *Phys. Rev.*, **115**, 1506 (1959).
(5) M. K. Bowman, H. Hase, and L. Kevan, *J. Magn. Reson.*, **22**, 23 (1976).
(6) A. M. Portis, *Phys. Rev.*,**104**, 584 (1956).
(7) W. B. Mims, K. Nassau, and J. D. McGee, *Phys. Rev.*, **123**, 2059 (1961).
(8) J. R. Klauder and P. W. Anderson, *Phys. Rev.*, **125**, 912 (1962).
(9) E. L. Wolf, *Phys. Rev.*, **142**, 555 (1966).
(10) L. Kevan and L. D. Kispert, "Electron Spin Double Resonance Spectroscopy", Wiley-Interscience, New York, N.Y., 1976.
(11) P. R. Moran, *Phys. Rev.*, **135**, 247 (1964).
(12) H. Yoshida, D. F. Feng, and L. Kevan, *J. Chem. Phys.*, **58**, 3411 (1973).
(13) B. L. Bales, M. K. Bowman, L. Kevan, and R. N. Schwartz, *J. Chem. Phys.*, **63**, 3008 (1975).
(14) P. A. Narayana, M. K. Bowman, L. Kevan, V. F. Yudanov, and Yu. D. Tsvetkov, *J. Chem. Phys.*, **63**, 3365 (1975).
(15) D. F. Feng, F. Q. H. Ngo, and L. Kevan, unpublished work.

# Laser Photolysis Study of the Photoracemization of 1,1′-Binaphthyl

**Masahiro Irie,* Kikuo Yoshida, and Koichiro Hayashi**

*The Institute of Scientific and Industrial Research, Osaka University, Osaka, Suita, Japan* *(Received April 8, 1976; Revised Manuscript Received February 24, 1977)*

The photoracemization mechanism of 1,1′-binaphthyl has been studied from the effect of additives as well as by a laser photolysis method. The effect of additives revealed that photoracemization occurs in the triplet excited state. The rotation process along the intraannular C–C bond, which causes the racemization, was directly followed by measurement of time-resolved triplet–triplet (T–T) absorption spectra of 1,1′-binaphthyl at low temperature with the laser photolysis technique. The almost rectangular conformation changed to a less twisted coplanar conformation with a rate constant of $1.0 \times 10^4$ $s^{-1}$ at −150 °C. The potential energy surface along the photoracemization coordinate was also discussed.

## Introduction

Photoresolution of a racemic mixture by means of circularly polarized light was first observed for the oxalate complex of chromium(III) by Stevenson et al.[1] This is a unique example of photoresolution. They suggested that the illumination of circularly polarized light on a racemic mixture would induce optical activity, if the photochemical reaction undergone by an isomer is only in inversion to its enantiomer.

Although several works have dealt with the photoracemization of biphenyl derivatives and sulfoxides,[2,3] these works are limited to systems in which the racemization is accompanied by irreversible side reactions and has a low quantum yield. Up to the present moment, the mechanism of photoracemization has not yet been established.

The purpose of this study is to reveal fundamental processes involved in the photoracemization of 1,1′-binaphthyl and to apply the information to the study of photoresolution.[4] 1,1′-Binaphthyl is one of the simplest chiral hydrocarbons.[5,6] The racemization is expressed as follows:

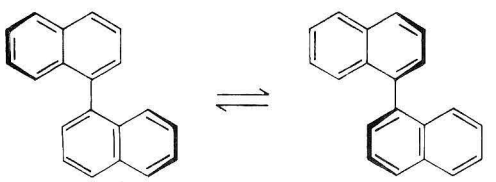

*R*(−)-1,1′-binaphthyl *S*(+)-1,1′-binaphthyl

Its dissymmetry is molecular in nature and enantiomer conversion is induced by rotation along the intraannular bond. Information about the fundamental processes of the racemization reaction is of importance not only for photoresolution study but also for study of the electronic structure of the excited state of nonplanar compounds.[7-9]

## Experimental Section

1,1′-Binaphthyl was resolved by the method of Pincock et al.[10] The optically active 1,1′-binaphthyl thus obtained had an $[\alpha]^{20}D$ of 156°. Tetrahydrofuran and 2-methyltetrahydrofuran were distilled twice over calcium hydride. Triplet quenchers or sensitizers, dibenzalacetone, fluorenone, piperylene, benzophenone, and acetophenone, were of analytical grade and used as received. All samples were degassed by the freeze–thaw cycle in vacuo.

Photoillumination was carried out with a super-high-pressure lamp (1 kW), the wavelength being selected by Toshiba glass filters. The reaction was followed by measuring $[\alpha]^{20}D$ with a Hitachi polarimeter (Type PO-B).

Triplet–triplet (T–T) absorption measurement was carried out with a ruby laser photolysis apparatus (JEOL, JLS-R9). The fundamental wavelength of 694 nm was doubled to 347 nm by use of a second harmonic generator of RDP. The second harmonic thus obtained has the pulse width of 20 ns and a photon number of $1 \times 10^{17}$ per pulse. The time constant of the monitoring system is less than 10 ns.

## Results

(i) *Photoracemization under Stationary Light.* Figure 1 shows the dependence of the rate of photoracemization of 1,1′-binaphthyl in tetrahydrofuran at 0 °C on the wavelength of illuminating light. Photoexcitation of the absorption band of 1,1′-binaphthyl (which has an absorption tail around 340 nm) results in racemization, while no racemization is observed by light passed through a UV-39 filter ($\lambda > 365$ nm) or in the dark at 0 °C. This

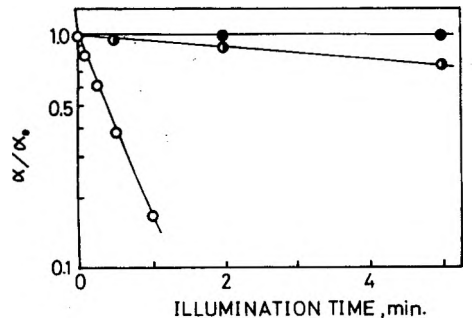


**Figure 1.** Photoracemization of 1,1′-binaphthyl ($2.0 \times 10^{-2}$ M) in tetrahydrofuran with light passed through (○) UV-31 (λ >270 nm), (◑) UV-35 (λ >330 nm), and (●) UV-39 (λ >365 nm) filters at 0 °C.

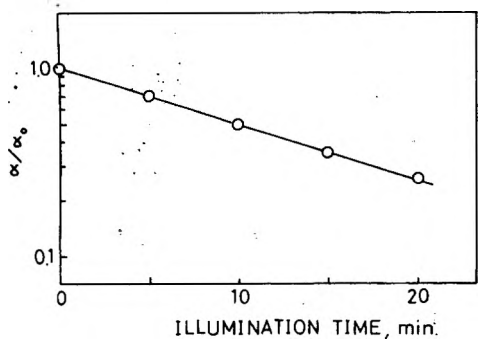


**Figure 2.** Photosensitized racemization of 1,1′-binaphthyl ($3.2 \times 10^{-2}$ M) in tetrahydrofuran at 0 °C in the presence of benzophenone ($1.2 \times 10^{-3}$ M) with a mercury line of 366 nm.

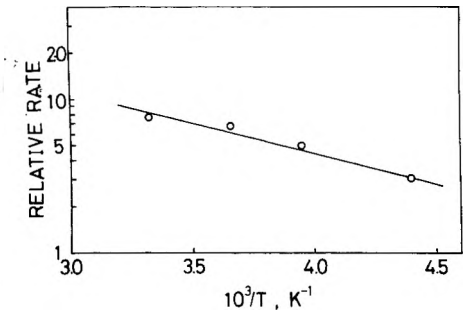


**Figure 3.** Temperature dependence of the rate of photoracemization of 1,1′-binaphthyl ($2.1 \times 10^{-2}$ M) in tetrahydrofuran.

result shows that 1,1′-binaphthyl inverts to its enantiomer in its photoexcited state. In the above experiments the concentration of 1,1′-binaphthyl measured by gas chromatography as well as by ultraviolet absorption remained constant even after almost complete racemization and no side product was detected by gas chromatography. This indicates that the only photochemical reaction undergone by the isomer is inversion to its enantiomer. The photoracemization proceeded similarly in other solvents, such as toluene and methylene chloride.

In the presence of air the rate of racemization is remarkably suppressed to a few percent of that of the degassed sample. This oxygen effect suggests that the inversion occurs in the triplet state. To substantiate this mechanism, effects of the addition of several triplet sensitizers or quenchers on the racemization rate were examined.[11] A sensitizing experiment with a mercury line of 366 nm revealed that photoexcitation of acetophenone or benzophenone, which has a triplet energy higher than 65 kcal/mol, causes appreciable racemization, as shown in Figure 2. The excitation of fluorenone or dibenzalacetone, however, does not result in racemization. Fluorenone and dibenzalacetone have a triplet energy less

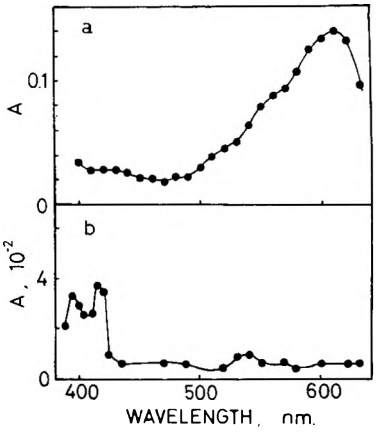


**Figure 4.** Triplet-triplet absorption spectrum of 1,1′-binaphthyl (a) at 25 °C taken at 2 μs after the pulse and (b) at −196 °C taken at 14 ms after the pulse in the laser photolysis of 2-methyltetrahydrofuran solution containing $3.9 \times 10^{-2}$ M 1,1′-binaphthyl and $2.2 \times 10^{-3}$ M benzophenone.

than 55 kcal/mol. This result indicates that the triplet excited state is responsible for the racemization reaction and the triplet energy is around 60 kcal/mol, which agrees with the reported value.[12]

The rate of photoracemization with light which passed through a UV-31 filter (λ >270 nm) was suppressed by the addition of piperylene, which is a triplet quencher with a triplet energy of 57 kcal/mol. The concentration dependence of the rate gave a quenching constant of $4.3 \times 10^3$ $M^{-1}$. This value suggests a lifetime for the intermediate longer than 0.4 μs, which is much longer than the fluorescence lifetime. The effects of these additives prove unambiguously that racemization occurs in the triplet state of 1,1′-binaphthyl.

The rate of photoracemization depended on the temperature. It decreased at a lower temperature. The temperature dependence of the rate in the range between −45 and 25 °C gave an activation energy of 1.9 kcal/mol in tetrahydrofuran as shown in Figure 3. This value is much smaller than that of thermal racemization, for which ~22 kcal/mol is reported.[13]

The quantum yield of racemization was also measured at 0 °C. The quantum yield was found to depend on the concentration of 1,1′-binaphthyl; it increased with an increase of the concentration of 1,1′-binaphthyl. Values of 1.0 and 1.4 were obtained at concentrations of $1.0 \times 10^{-2}$ and $2.0 \times 10^{-2}$ M, respectively. The high quantum yield means that the photoracemization of 1,1′-binaphthyl is a very efficient reaction.

(ii) *Primary Processes.* In order to clarify the primary processes involved in the racemization reaction, direct observation of the dynamic behavior of the triplet excited state is indispensable, since quenching and sensitizing experiments prove that the triplet excited state is responsible for the racemization reaction.

Figure 4a shows the transient T–T absorption spectrum of 1,1′-binaphthyl at 25 °C observed 2 μs after the pulse in 2-methyltetrahydrofuran solutions containing $3.9 \times 10^{-2}$ M 1,1′-binaphthyl and $2.2 \times 10^{-3}$ M benzophenone. The spectrum is the same as that observed by pulse radiolysis and ascribed to the T–T absorption of 1,1′-binaphthyl by Kira et al.[12] In our system benzophenone is added as an energy absorber, since 1,1′-binaphthyl has no absorption at the wavelength of a ruby laser pulse of 347 nm. The concentration of 1,1′-binaphthyl is so adjusted that the energy absorbed by benzophenone is effectively transfered to 1,1′-binaphthyl (at 2 μs after the pulse the T–T absorption of benzophenone was not detected).

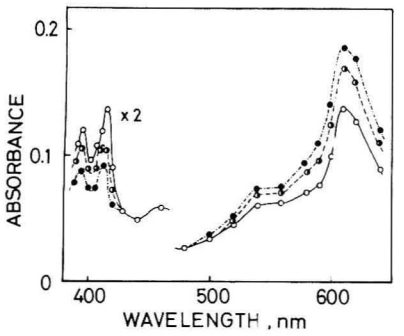


**Figure 5.** Triplet–triplet absorption spectrum of 1,1′-binaphthyl at −150 °C taken at (—) 10, (- - -) 30, and (- · -) 60 μs after the pulse in the laser photolysis of the 2-methyltetrahydrofuran solution containing 7.9 × $10^{-2}$ M 1,1′-binaphthyl and 1.9 × $10^{-3}$ M benzophenone.

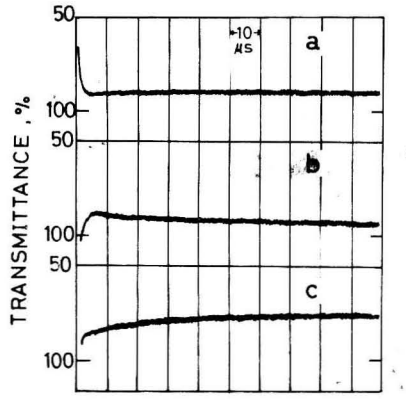


**Figure 6.** Oscillograms at (a) 530, (b) 417, and (c) 600 nm at −150 °C in the laser photolysis of 2-methyltetrahydrofuran solution containing 7.9 × $10^{-2}$ M 1,1′-binaphthyl and 1.9 × $10^{-3}$ M benzophenone.

The broad T–T absorption is completely different from the T–T absorption of naphthalene itself, which has an absorption around 420 nm. The large spectral difference indicates that two naphthalene rings of 1,1′-binaphthyl have considerable interaction in the triplet excited state. The appearance of the intramolecular interaction in the triplet state is explained by an increase of the overlap between the two aromatic planar ring systems. This is brought about as a result of the change of the interplanar angle to a more planar geometry. The rotation along the intraannular bond in the triplet state is considered to be the initial step of the racemization reaction.

The T–T absorption spectrum of 1,1′-binaphthyl 14 ms after the pulse at −196 °C in 2-methyltetrahydrofuran is shown in Figure 4b. A high concentration of 1,1′-binaphthyl is also adopted so that 1,1′-binaphthyl effectively accepts the triplet energy of excited benzophenone. The spectrum is similar to the T–T absorption of naphthalene. Rotation along the intraannular C–C bond is inhibited at −196 °C due to rigidity of the matrix and the conformation of the ground state is maintained also in the excited state. The similarity of the T–T absorption spectrum in the ground state conformation to the spectrum of naphthalene indicates that the two naphthalene rings are almost in a rectangular conformation to each other in the ground state and the electronic interaction between them is negligible.

Although the rigidity of the matrix prevents rotation of the naphthalene rings at −196 °C, intramolecular rotation becomes possible at higher temperatures due to the decrease of rigidity of the matrix. This is directly observable.

Figure 5 shows the time dependence of the T–T absorption spectrum of 1,1′-binaphthyl at −150 °C in the microsecond region. The absorption around 420 nm (which is attributable to the triplet state of 1,1′-binaphthyl in an almost rectangular conformation) decreases with time, while the absorption around 610 nm (which is attributable to a triplet state in a less twisted coplanar conformation) increases during the first 100 μs. The spectrum change shows clearly that the rectangular conformation changes to the coplanar one in the triplet excited state in the microsecond region at −150 °C.

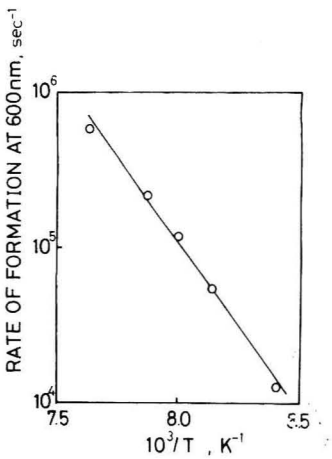


**Figure 7.** Dependence of the rate of formation of the absorption at 600 nm on temperature in the laser photolysis of 2-methyltetrahydrofuran solution containing 7.9 × $10^{-2}$ M 1,1′-binaphthyl and 1.9 × $10^{-3}$ M benzophenone.

In order to analyze the formation process of the coplanar conformation quantitatively, transient absorptions were followed at 530, 417, and 600 nm, as shown in Figure 6. The absorption at 530 nm is due to the T–T absorption of benzophenone, which is formed immediately after the pulse and decays in a few microseconds completely, giving its energy to 1,1′-binaphthyl. The absorption at 417 nm is formed concomitantly with a decrease of the absorption at 530 nm and decays slowly. This shows the formation of the rectangular conformation triplet state of 1,1′-binaphthyl as a result of the acceptance of triplet energy from excited benzophenone.

On the other hand, the absorption at 600 nm is formed slowly together with a decrease of the absorption at 417 nm. The decay at 417 nm follows first-order kinetics and the decay rate is 0.9 × $10^4$ $s^{-1}$. The rate of formation at 600 nm obtained was 1.0 × $10^4$ $s^{-1}$. The coincidence of the two rates clearly indicates that the coplanar conformation is formed from the rectangular conformation in the triplet excited state.

The temperature dependence of the rate of formation of the coplanar conformation was measured in 2-methyltetrahydrofuran in the temperature region between −154 and −142 °C, as shown in Figure 7. The slope gives an activation energy of 9.3 kcal/mol. The high value is considered to reflect a special temperature dependence of the local viscosity of the solvent surrounding excited 1,1′-binaphthyl in this temperature region. Below −160 °C the spectrum change due to rotation as well as racemization was not observed.

## Discussion

Two mechanisms, vibrational "hot" ground state and excited singlet state mechanisms, have been proposed for photoracemization of biphenyl derivatives by Mislow[2] and Zimmerman.[4] Mislow et al. interpreted the photoracemization of 1,11-dimethyldibenzo[*a*,*c*][1,3]cycloheptadiene as due to the vibrational "hot" ground state formed as a result of internal conversion of an electronically excited state. Zimmerman et al., on the other hand, preferred the explanation by the direct rotation in the

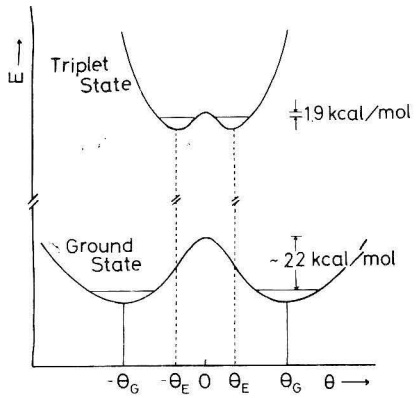


**Figure 8.** Schematic diagram of the ground and triplet states of 1,1′-binaphthyl.

singlet excited state for the racemization of 2,2′-dimethyl-6,6′-diethylbiphenyl. As a possible explanation of the reaction, Zimmerman et al. also proposed a mechanism involving reversible benzvalene formation.

None of these mechanisms is applicable to the racemization reaction of 1,1′-binaphthyl. The vibrational "hot" ground state cannot account for the high quantum yield, which results from a chain reaction via rather stable intermediates, because of its short lifetime. The quenching and sensitizing experiments remove the possibility of a singlet excited state being responsible for racemization. It is not necessary to consider the benzvalene-like mechanism for this compound, since no side reaction was detected with the experimental conditions used.

The quenching and sensitizing experiments prove clearly that racemization occurs in the triplet excited state of 1,1′-binaphthyl.

Post et al.[9] have proposed a coplanar conformation for the excited singlet state of 1,1′-binaphthyl. They regarded this as due to the large difference of $S_n \leftarrow S_1$ absorption spectrum, fluorescence spectrum, and the decay time in a fluid solution as compared to a rigid solution. Our result of racemization, however, indicates that the conformation in the excited state keeps the original chirality and inversion to the enantiomer does not occur in that state. The optical property of the singlet excited state observed in a fluid solution is presumably caused by a small conformational change in the interplanar angle around the rectangular conformation. Not only the change of the intramolecular angle but also the change in the electronic state due to an intramolecular charge transfer interaction in cooperation with the surrounding solvent should be taken into account for the remarkable spectral changes proposed for 9,9′-dianthryl.[8,14]

On the other hand, the spectrum change observed in the triplet state by laser photolysis is unambiguously ascribed to rotation along the intraannular C–C bond, since the spectrum does not depend on the polarity of the solvent and racemization is really observed in this state.

The rotation along the intraannular C–C bond in the triplet state is an exothermic reaction as shown schematically in Figure 8. In the excited state the bond order between the intraannular C–C bond is expected to increase. Therefore, the potential energy curve for the excited state is steeper than that of the ground state and the resulting greater resistance to twist leads to a smaller angle between the two naphthalene rings in the excited state. The stabilization energy gained by the decrease of the angle from the equilibrium angle $\theta_G$ of the ground state to the angle of $\theta_E$ of the triplet state is considered to cause rotation along the C–C bond, giving more planar conformation. The activation energy for the rotation obtained from the laser experiment is attributable to the difference between the activation energy of the replacement of the solvent molecules by the rotation and stabilization energy of the triplet excited state to the most stable conformation. The rather high value in comparison with photoracemization is presumably due to the fact that the temperature range used for a laser experiment is close to the glass transition temperature of the solvent.[15] The value is expected to become equal to or less than the value of racemization when it is measured in the same temperature region, though at this moment it is difficult because of the limitation of the time resolution of the laser pulse.

The spectrum change due to rotation along the C–C bond is the primary step of racemization and is a necessary step for racemization. The racemization was not observed below the temperature in which the spectrum change in the triplet state was not detected and rotation was suppressed.

For inversion to the enantiomer 1,1′-binaphthyl has to overcome the barrier at the angle of 0° due to steric hindrance of hydrogens at the 2 and 8 positions in the coplanar conformation. The barrier in the ground state is reported as ~22 kcal/mol.[13] The barrier in the triplet state measured from the temperature dependence of the rate of photoracemization is 1.9 kcal/mol. The value is considered to be the minimum estimation of the barrier, since some excess vibrational energy from the singlet excited state after intersystem crossing may contribute to the photoracemization rate. However, it is certain that the barrier in the triplet excited state is much smaller than the ground state. The smaller value is an unexpected result, since the higher bond order in the excited state causes a smaller bond distance and gives rise to large steric hindrance. The low barrier observed in the triplet state suggests that the electronic stabilization energy gained as a result of the interaction of the two naphthyl rings is superior to steric hindrance.

*Acknowledgment.* The authors express their thanks to Professor T. Fukui, Osaka University, for use of the Hitachi polarimeter for optical activity determinations.

## References and Notes

(1) K. L. Stevenson and J. F. Verdieck, *J. Am. Chem. Soc.*, **90**, 2974 (1968).
(2) (a) K. Mislow and A. J. Gordon, *J. Am. Chem. Soc.*, **85**, 3521 (1963); (b) K. Mislow, M. Axelrod, D. R. Rayner, H. Gotthardt, L. M. Coyne, and G. S. Hammond, *ibid.*, **87**, 4958 (1965).
(3) H. E. Zimmerman and D. S. Crumrine, *J. Am. Chem. Soc.*, **94**, 498 (1972).
(4) We found that the optical activity of 1,1′-binaphthyl is induced by the use of circular polarized light in tetrahydrofuran. The details will be published in our next paper.
(5) M. M. Harris and A. S. Meller, *Chem. Ind. (London)*, 1082 (1961).
(6) S. F. Mason and R. H. Seal, *Tetrahedron*, **30**, 1671 (1974).
(7) H. Suzuki, "Electronic Absorption Spectra and Geometry of Organic Molecules", Academic Press, New York, N.Y., 1967, p 261.
(8) F. Schneider and E. Lippert, *Ber. Bunsenges. Phys. Chem.*, **72**, 1155 (1968).
(9) M. F. M. Post, J. Langelaar, and J. D. W. Van Voorst, *Chem. Phys. Lett.*, **32**, 59 (1975).
(10) (a) R. E. Pincock and K. R. Wilson, *J. Am. Chem. Soc.*, **93**, 1291 (1971); (b) K. R. Wilson and R. E. Pincock, *ibid.*, **97**, 1474 (1975).
(11) S. L. Murov, "Handbook of Photochemistry", Marcel Dekker, New York, N.Y., 1973.
(12) A. Kira and J. K. Thomas, *J. Phys. Chem.*, **78**, 196 (1974).
(13) A. K. Colter and L. M. Clemens, *J. Phys. Chem.*, **68**, 651 (1964).
(14) N. Mataga, private communication.
(15) T. Furutsuka, T. Imura, T. Kojima, and K. Kawabe, *Tech. Rep. Osaka Univ.*, **24**, 367 (1974). The dielectric constant of 2-methyltetrahydrofuran is reported to deviate from normal temperature dependence below −133 °C and to decrease drastically below −156 °C.

# Radiation Induced Racemization of 1,1′-Binaphthyl in Tetrahydrofuran and Toluene

**Masahiro Irie,* Takehiko Yorozu, Kikuo Yoshida, and Koichiro Hayashi**

*The Institute of Scientific and Industrial Research, Osaka University, Suita, Osaka, Japan* *(Received April 8, 1976; Revised Manuscript Received February 24, 1977)*

Radiation induced racemization of 1,1′-binaphthyl has been studied in tetrahydrofuran and toluene. The effect of additives proved that the racemization reaction in tetrahydrofuran occurs mainly in a radical anion state of 1,1′-binaphthyl, while in toluene the reaction occurs mainly in the triplet excited state. The low activation energies of the reaction in both solvents, 1.1 kcal/mol in tetrahydrofuran and 1.9 kcal/mol in toluene, as compared to thermal racemization indicate that the introduction of an electron to the lowest vacant molecular orbital causes an electronic structure change favorable to rotation along the intraannular C–C bond. The conformational change in the radical anion state is directly followed by the measurement of the absorption spectrum change at a low temperature. The concentration dependence of the $G$ value of the racemization in both solvents clearly indicates a chain reaction with chain carriers of the radical anion state in tetrahydrofuran and the triplet excited state in toluene. The chain reaction via the triplet excited state in toluene gives a $G$ value as high as 30.

## Introduction

The study of the isomerization process induced by photoillumination[1] as well as radiation[2] has yielded ideas concerning the potential-energy surface along the isomerization coordinate. It has also provided invaluable information about the electronic structure of the intermediate state through which isomerization occurs.[1]

Cis–trans isomerization of diastereomers has been thoroughly studied from the kinetic view point and from the electronic structure of the intermediate state.[1] The isomerization, for example, cis–trans isomerization of stilbene, is now well known to be induced by photoillumination,[1] by radiation,[2] and also by alkali metal reduction of it to a radical anion.[3] The study of isomerization of enantiomers, however, is limited to a few cases, such as biphenyl derivatives[4,5] or sulfoxides,[6] presumably due to the difficulty of the resolution of the enantiomer. The isomerization study of biphenyl derivatives is expected to provide information about the conformational change induced by the rotation of the single bond between two aromatic rings in the intermediate state as well as its barrier.[7]

In a previous paper[8] we described the photoracemization process of 1,1′-binaphthyl. It was proved that racemization occurs in the triplet excited state and the barrier to rotation in the excited state is much less than in the ground state. The purpose of this paper is to extend the study to the reaction by radiation. The effect of radiation on solutions yields several kinds of reactive intermediates. The contribution of these intermediates to the racemization process of 1,1′-binaphthyl was examined in several solvents and the differences in the behavior of the conformational change between the intermediates were discussed.

## Experimental Section

1,1′-Binaphthyl was resolved by the same method as before.[8] The optical activity thus obtained gave an $[\alpha]^{20}D$ of 154°. Tetrahydrofuran, methylene chloride, and toluene were distilled twice over calcium hydride. Triplet quenchers of the same compounds were used as described in a previous paper.[8] Each sample was degassed by a freeze–thaw cycle in vacuo at less than $10^{-5}$ mmHg.

$\gamma$-Irradiation was carried out by $^{60}Co$ $\gamma$ rays with a dose rate of $9.2 \times 10^5$ rads/h. The reaction was followed by measuring $[\alpha]^{20}D$ with an Hitachi polarimeter (Type PO-B). The absorption spectra of the $\gamma$-irradiated samples were measured with a conventional recording spectrometer (Hitachi EPS-3T). The temperature of the samples was controlled by the use of appropriate cooling solvents and thermocouples.

The transient absorption spectra of the irradiated samples were measured by a pulse radiolysis apparatus as described previously.[9]

## Results and Discussion

(i) *Racemization in Solutions.* Figure 1 shows the dependence of the rate of racemization of 1,1′-binaphthyl induced by $\gamma$ irradiation of solvents at 0 °C. $\gamma$-Irradiation of solutions of 1,1′-binaphthyl in tetrahydrofuran and toluene causes racemization, though the reaction is scarcely observed in methylene chloride. The reaction follows first-order kinetics to a conversion of 80% of the initial optical activity. The decomposition product of 1,1′-binaphthyl was not detected either in tetrahydrofuran or in toluene by gas chromatography even after 80% conversion. The concentration of 1,1′-binaphthyl measured by gas chromatography as well as by absorption measurements remained constant. This means that the racemization reaction does not involve a bond-breaking process but proceeds merely by rotation along the intraannular C–C bond.

The dependence of the rate on solvents suggests that the reaction occurs either via the radical anion or triplet excited state of 1,1′-binaphthyl. The possibility of a radical cation state is removed, since it is generally held that radical anion, radical cation, and triplet excited states of added solutes are predominant transient intermediates generated in tetrahydrofuran, methylene chloride, and toluene solutions, respectively.[10] The absence of the racemization reaction in methylene chloride also indicates that the neutralization process of the radical cation of 1,1′-binaphthyl with negative entities, presumably $Cl^-$, does not lead to the formation of the triplet excited state of 1,1′-binaphthyl, since the formation of the triplet excited state was proved to result in the racemization reaction.[8]

In order to substantiate the above mechanisms (via radical anion state in tetrahydrofuran and via triplet excited state in toluene), the effects of additives (anion and triplet quenchers) were examined. The addition of methylene chloride suppressed the rate of racemization considerably in a tetrahydrofuran solution, though the rate was slightly affected in toluene as shown in Figure 2. Methylene chloride is well known to capture electrons by

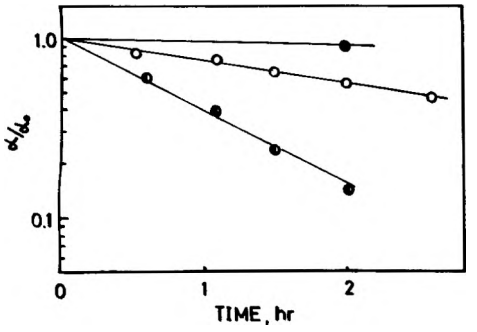


**Figure 1.** Radiation induced racemization of 1,1′-binaphthyl ($8.0 \times 10^{-3}$ M) in (◐) toluene, (O) tetrahydrofuran, and (●) methylene chloride at 0 °C. The dose rate was $9.2 \times 10^5$ rads/h.

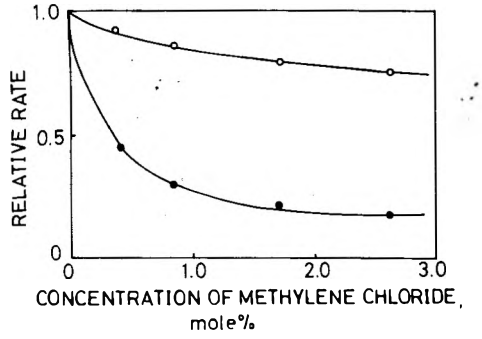


**Figure 2.** Effect of the addition of methylene chloride on the rate of racemization of 1,1′-binaphthyl ($8.0 \times 10^{-3}$ M) in (●) tetrahydrofuran and (O) toluene irradiated to a dose of $1.4 \times 10^6$ rads with a dose rate of $9.2 \times 10^5$ rads/h at 0 °C.

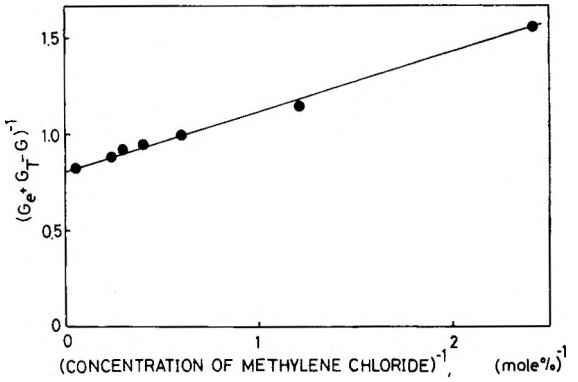


**Figure 3.** Dependence of $1/(G_e + G_T - G)$ on the concentration of added methylene chloride in tetrahydrofuran at 0 °C. $G$ and $(G_e + G_T)$ are $G$ values for racemization in the presence and absence of methylene chloride, respectively. $G_e$ and $G_T$ express the $G$ values attributable to the radical anion and to triplet mechanisms, respectively.

a dissociative electron capture reaction and to inhibit the formation of radical anions. The decrease of the rate by the addition of methylene chloride clearly proved that the racemization reaction in tetrahydrofuran proceeds through a radical anion state of 1,1′-binaphthyl.

The racemization, however, was not completely inhibited even when the concentration of methylene chloride was increased to 30 vol %, where almost all of the radical anion is considered to be quenched. This suggests the contribution of another intermediate in the racemization reaction, presumably the triplet excited state. To estimate the contribution quantitatively, the value of $1/(G_e + G_T - G)$ is plotted as a function of concentration of methylene chloride in Figure 3 following eq 2. $G$ expresses the G value of racemization in the presence of methylene chloride. $G_e$ and $G_T$ are $G$ values attributable to the radical anion mechanism and to the triplet excited state mechanism in the absence of methylene chloride, respectively.

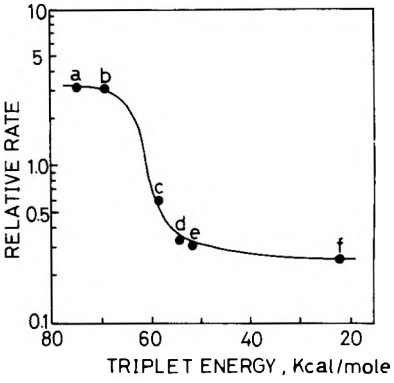


**Figure 4.** Effect of additives on the rate of radiation induced racemization of 1,1′-binaphthyl ($8.0 \times 10^{-3}$ M) in toluene at 0 °C. The additives were (a) acetophenone, (b) benzophenone, (c) piperylene, (d) fluorenone, (e) dibenzalacetone, and (f) oxygen. The concentration of the additives was $2 \times 10^{-3}$ M.

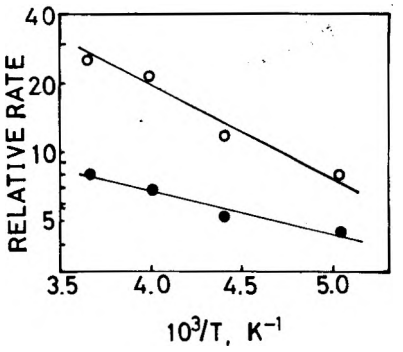


**Figure 5.** Temperature dependence of the rate of radiation induced racemization of 1,1′-binaphthyl ($8.0 \times 10^{-3}$ M) in (●) tetrahydrofuran and (O) toluene solutions.

$$G = G_e \frac{k_{eR}}{k_{eR} + k_q[CH_2Cl_2]} + G_T \quad (1)$$

$$\frac{G_e}{G_e + G_T - G} = 1 + \frac{k_{eR}}{k_q[CH_2Cl_2]} \quad (2)$$

$k_{eR}$ and $k_q$ are the rate of racemization in the radical anion state and the rate of quenching, respectively. In the above equation it is assumed that methylene chloride does not affect the formation of the triplet state. The intercept gives the value of $G_e$ of 1.2. $G_T$ value is obtained to be 0.15 by the subtraction of $G_e$ from the initial value $(G_e + G_T)$ in the absence of methylene chloride. These values show the large contribution of the radical anion state in comparison with the triplet excited state to the racemization reaction in tetrahydrofuran.

The ineffectiveness of the addition of methylene chloride coincides with the triplet mechanism in toluene solution. The effect of triplet quenchers in toluene solution is shown in Figure 4. In this experiment the quenchers were added in the same concentration. The quenchers, which have a triplet energy less than 55 kcal/mol, remarkably suppressed the reaction, while the addition of acetophenone and benzophenone with a triplet energy larger than 65 kcal/mol had no effect on the reaction. This effect of triplet quenchers proves unambiguously that the racemization reaction proceeds through a triplet excited state in toluene. The contribution of the radical anion state, however, is not removed completely, since the addition of methylene chloride decreased the reaction rate to some extent. Methylene chloride possibly quenches the ionic precursor of the triplet state in toluene.[11]

The temperature dependences of the reaction rates in tetrahydrofuran and toluene are shown in Figure 5. The

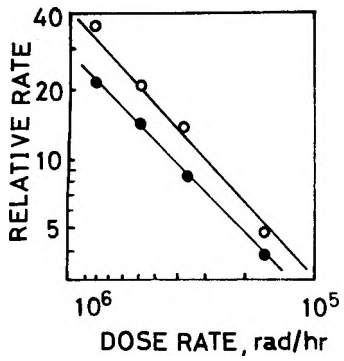


**Figure 6.** Dose rate dependence of the rate of radiation induced racemization of 1,1′-binaphthyl ($8.0 \times 10^{-3}$ M) in (●) tetrahydrofuran and (○) toluene solutions at 0 °C.

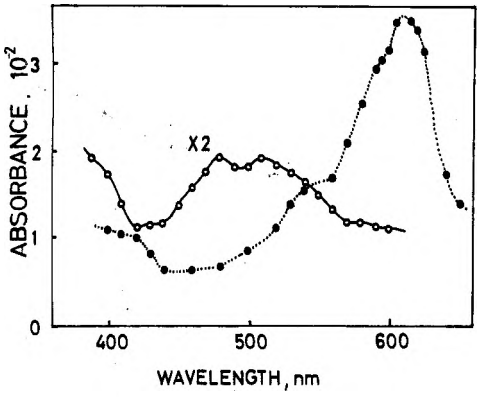


**Figure 7.** Transient absorption spectra of 1,1′-binaphthyl at room temperature taken at 2 μs after the pulse in the pulse radiolysis of (○) tetrahydrofuran and (●) toluene solutions containing $4 \times 10^{-3}$ M 1,1′-binaphthyl.

slopes give activation energies of 1.1 and 1.9 kcal/mol in tetrahydrofuran and in toluene, respectively. The value of 1.9 kcal/mol is the same as the value observed for photoracemization in toluene, in which the triplet excited state of 1,1′-binaphthyl is responsible for the racemization reaction.

The activation energy of 1.1 kcal/mol in tetrahydrofuran represents the barrier necessary for the naphthyl ring to rotate along the intraannular C–C bond in the radical anion state of 1,1′-binaphthyl. The contribution of the triplet state formed by the neutralization reaction is removed in tetrahydrofuran, since the activation energy is lower than the value necessary for the triplet state, 1.9 kcal/mol.

The low barrier in both cases (triplet excited state and radical anion state), in comparison with the barrier in the ground state, which is reported to be ~22 kcal/mol,[12] suggests a similarity of the electronic structure in the triplet excited state and the radical anion state. The electronic structure change induced by the introduction of an electron to the lowest vacant molecular orbital is considered to be responsible for the conformational change, which gives rise to the racemization reaction.

The dose rate dependences on the rate of the reaction in tetrahydrofuran and toluene are shown in Figure 6. In both cases first-order dependence is obtained, which means that the reaction is a one molecule reaction and does not need the help of more than two reactive species.

(ii) *Spectroscopic Study.* The formation of the radical anion of 1,1′-binaphthyl in tetrahydrofuran and the triplet excited state in toluene were further confirmed by the pulse radiolysis method. Figure 7 shows the absorption spectra obtained 2 μs after the pulse in tetrahydrofuran (solid line) and in toluene (dotted line). The spectrum in

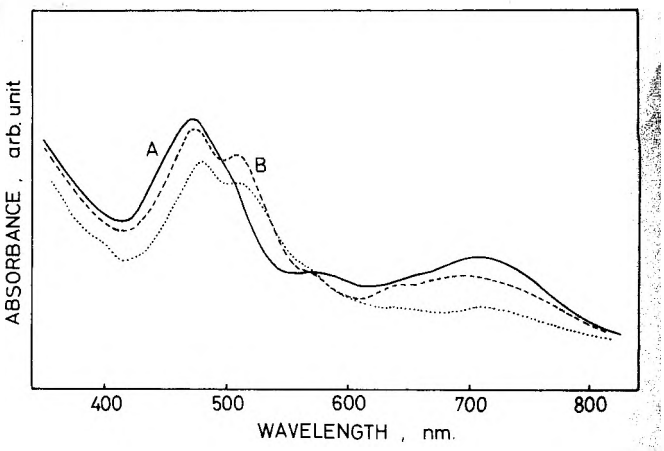


**Figure 8.** Absorption spectra of 2-methyltetrahydrofuran solution containing $5 \times 10^{-2}$ M 1,1′-binaphthyl at (A, ——) 77 and (B, - - -) 100 K irradiated to a dose of $1.9 \times 10^5$ rads at 77 K. The radical anion of 1,1′-binaphthyl obtained by sodium reduction (· · ·) is also shown.

tetrahydrofuran is similar to the spectrum of the radical anion formed by sodium reduction of 1,1′-binaphthyl and is certainly attributable to the radical anion of 1,1′-binaphthyl. It decayed following second-order decay kinetics. The existence of the triplet state in the spectrum is not discerned, which implies that the contribution of the triplet state is small.

The spectrum in toluene is similar to the spectrum obtained by laser photolysis in tetrahydrofuran and is safely attributable to the triplet–triplet absorption of 1,1′-binaphthyl. The presence of the radical anion is not discerned in the spectrum, which indicates that the triplet excited state is much more predominant in the intermediates rather than the radical anion in an irradiated toluene solution. The triplet state decayed according to first-order decay kinetics and the rate constant obtained was $7.1 \times 10^4$ $s^{-1}$.

In the above experiments the spectrum of the radical anion or triplet–triplet absorption indicates that the naphthyl ring of 1,1′-binaphthyl has already rotated into an almost coplanar conformation within 2 μs after the pulse. The rotation process in a solution at room temperature is considered to be too fast to be detected by a conventional microsecond pulse radiolysis method.

In order to follow the rotation process in a radical anion state directly, a spectroscopic study at a low temperature was carried out. Figure 8A shows the spectrum of 1,1′-binaphthyl irradiated in 2-methyltetrahydrofuran at 77 K. According to the criterion of Hamill,[13] the spectrum is attributable to the radical anion of 1,1′-binaphthyl. The conformation of the radical anion, however, is considered to be almost rectangular and to be different from the stable conformation of the radical anion state, since at 77 K rotation of the naphthyl ring is suppressed. On raising the temperature, the spectrum changed at 100 K to that in Figure 7B. The maximum at 710 nm observed at 77 K decreases and a new peak appears at 505 nm. Above 100 K the spectrum did not show any noticeable change in shape but decreased. It disappeared above 118 K.

The spectrum observed above 100 K is similar to the spectrum obtained by a pulse radiolysis method at room temperature as well as that of a radical anion formed by reduction with an alkali metal. This spectrum is attributable to the radical anion of 1,1′-binaphthyl in a less twisted coplanar conformation.

The spectrum change at 100 K corresponds to the conformational change from rectangular to coplanar. The change occurs at a lower temperature for the radical anion

state than for the triplet excited state in which the rotation occurs about 120 K.[8] This fact suggests that the most stable conformation of a radical anion state is more planar than that of a triplet state. The stabilization energy gained by rotation from the rectangular conformation to the most stable coplanar one is larger for the radical anion state in comparison with the triplet excited state. The lower activation energy of the racemization in the radical anion state coincides with the above argument.

Racemization at a lower temperature was also measured in order to correlate the spectrum change observed above with the racemization reaction itself. 2-Methyltetrahydrofuran solutions containing $8.0 \times 10^{-3}$ M of optically active 1,1′-binaphthyl were irradiated at 77 K to a dose of $1.5 \times 10^{6}$ rads. Then they were warmed quickly to a given temperature and kept for 1 h at that temperature. After that the optical activity of the sample was measured at room temperature.

Racemization to 32% conversion was observed at 100 ± 2 K, though no reaction was detected at 110 ± 2 K. The sample quickly warmed to room temperature did not show any racemization. These results indicate that rotation of the naphthyl ring along the C–C bond, which results in racemization, occurs below 100 K. Above 110 K the neutralization reaction between the radical anion of 1,1′-binaphthyl and positive charges becomes faster than the racemization reaction in this viscous matrix.

(iii) *Concentration Dependence of G Values.* Figures 9A and B show the dependence of the $G$ value of racemization on the concentration of 1,1′-binaphthyl in tetrahydrofuran and toluene, respectively. In both cases the $G$ value increases with an increase of concentration and shows a value as high as 30, which is much higher than the value of the yield of the primary radical anion or the triplet excited state ($G$ value of ~3). This fact suggests a chain reaction via the radical anion as well as the triplet excited state in the racemization reaction as follows:

$$S \rightsquigarrow S^{+}, e, S^{*} \quad (3)$$

$$R\text{-}BN + e \rightarrow R\text{-}BN^{-}\cdot \quad (4)$$

$$(S\text{-}BN + e \rightarrow S\text{-}BN^{-}\cdot)$$

$$R\text{-}BN^{-}\cdot \rightarrow S\text{-}BN^{-}\cdot \quad (5)$$

$$(S\text{-}BN^{-}\cdot \rightarrow R\text{-}BN^{-}\cdot)$$

$$S\text{-}BN^{-}\cdot + R\text{-}BN \rightarrow S\text{-}BN + R\text{-}BN^{-}\cdot \quad (6)$$

$$(R\text{-}BN^{-}\cdot + S\text{-}BN \rightarrow R\text{-}BN + S\text{-}BN^{-}\cdot)$$

$$R\text{-}BN^{-}\cdot + (+) \rightarrow R\text{-}BN \quad (7)$$

$$(S\text{-}BN^{-}\cdot + (+) \rightarrow S\text{-}BN)$$

$$R\text{-}BN + S^{*} \rightarrow {}^{3}R\text{-}BN^{*} \quad (8)$$

$$(S\text{-}BN + S^{*} \rightarrow {}^{3}S\text{-}BN^{*})$$

$${}^{3}R\text{-}BN^{*} \rightarrow {}^{3}S\text{-}BN^{*} \quad (9)$$

$$({}^{3}S\text{-}BN^{*} \rightarrow {}^{3}R\text{-}BN^{*})$$

$${}^{3}S\text{-}BN^{*} + R\text{-}BN \rightarrow S\text{-}BN + {}^{3}R\text{-}BN \quad (10)$$

$$({}^{3}R\text{-}BN^{*} + S\text{-}BN \rightarrow R\text{-}BN + {}^{3}S\text{-}BN^{*})$$

$${}^{3}R\text{-}BN^{*} \rightarrow R\text{-}BN \quad (11)$$

$$({}^{3}S\text{-}BN^{*} \rightarrow S\text{-}BN)$$

where S, e, and (+) are solvent, electron, and positive charge, respectively. R–BN and S–BN indicate the two enantiomers of 1,1′-binaphthyl. By repetition of processes 5 and 6 in the case of the radical anion, and reactions 9 and 10 in the case of the triplet excited state, the yield of racemization is considered to increase.

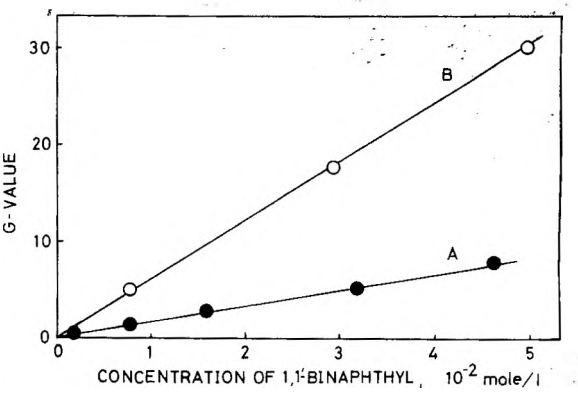


**Figure 9.** Dependence of $G$ value of the racemization of 1,1′-binaphthyl on the concentration of 1,1′-binaphthyl in (A, ●) tetrahydrofuran and (B, ○) toluene at 0 °C.

The chain reaction through radical anion state is reported for stilbene, in which a very high $G$ value of 210 is obtained.[14] For diastereomers, such as stilbene, the energies of triplet excited states or the radical anion states of two isomers are inherently different. The difference prevents the chain reaction of isomerization via the triplet state for stilbene, though the low energy difference of the two isomers in the radical anion state allows the chain reaction via the radical anion state.

On the other hand, enantiomers have the same energy in a triplet excited state as well as in a radical anion state and a chain reaction is expected to occur in both cases. The kinetic chain length depends on the lifetime of the intermediate states. The chain reaction via the triplet state observed for the racemization reaction of 1,1′-binaphthyl is, as far as the authors know, the first example of a chain reaction with a carrier of the triplet excited state.

*Acknowledgment.* The authors express their thanks to Dr. S. Taniguchi, Mr. S. Fujita, and Mrs. S. Irie, Radiation Center of Osaka Prefecture, Osaka, Japan, for their kind assistance in the pulse radiolysis experiment. They also express their thanks to Mr. P. Williams, University of Kent, England, for kindly reading the manuscript.

## References and Notes

(1) For example: (a) J. Saltiel, S. W. L. Chang, E. D. Megarity, A. D. Rousseau, P. T. Shannon, B. Thomas, and A. K. Uriarte, *Pure Appl. Chem.*, **41**, 559 (1975); (b) S. Yamauchi and T. Azumi, *J. Am. Chem. Soc.*, **95**, 2709 (1973); (c) S. Malkin and E. Fischer, *J. Phys. Chem.*, **68**, 1153 (1964); (d) R. H. Dyck and D. S. McClure, *J. Chem. Phys.*, **36**, 2326 (1962).
(2) (a) H. P. Lehmann, *J. Phys. Chem.*, **73**, 20 (1969); (b) R. R. Hentz, D. B. Peterson, S. B. Srirastava, H. F. Barzynski, and M. Burton, *Ibid.*, **70**, 2362 (1966); (c) R. A. Caldwell, D. G. Whitten, and G. S. Hammond, *J. Am. Chem. Soc.*, **88**, 2659 (1966).
(3) S. Sorensen, G. Levin, and M. Szwarc, *J. Am. Chem. Soc.*, **97**, 2341 (1975).
(4) K. Mislow and A. J. Gordon, *J. Am. Chem. Soc.*, **85**, 3521 (1963).
(5) H. E. Zimmerman and D. S. Crumrine, *J. Am. Chem. Soc.*, **94**, 498 (1972).
(6) K. Mislow, M. Axelrod, D. R. Rayner, H. Gotthardt, L. M. Coyne, and G. S. Hammond, *J. Am. Chem. Soc.*, **87**, 4958 (1965).
(7) H. Suzuki, "Electronic Absorption Spectra and Geometry of Organic Molecules", Academic Press, New York, N.Y., 1967, p 261.
(8) M. Irie, K. Yoshida, and K. Hayashi, *J. Phys. Chem.*, preceding paper in this issue.
(9) S. Fujita, H. Horii, and S. Taniguchi, *J. Phys. Chem.*, **77**, 2868 (1973).
(10) A. Henglein, W. Schnabel, and J. Wendenburg, "Einfuhrung in die Strahlenchemie", Verlag Chemie, GmbH-Weinhein/Bergstrasse, 1969, p 247.
(11) A. Singh, *Radiat. Res. Rev.*, **4**, 1 (1972).
(12) A. K. Colter and L. M. Clemens, *J. Phys. Chem.*, **68**, 651 (1964).
(13) W. H. Hamill, "Radical Ions", E. T. Kaiser and L. Kevan, Ed., Interscience, New York, N.Y., 1968, p 321.
(14) R. R. Hentz, K. Shima, and M. Burton, *J. Phys. Chem.*, **71**, 461 (1967).

# Mercury Photosensitized Production of Free Radicals in Organic Glasses. 2[1]

**Bruce J. Brown and John E. Willard***

*Department of Chemistry, University of Wisconsin, Madison, Wisconsin 53706* *(Received November 30, 1976)*

*Publication costs assisted by the United States Energy Research and Development Administration*

Knowledge of the mechanism of the Hg photosensitized production of trapped radicals in 3-methylpentane glass has been extended by investigation of the effects of light intensity (234 and 200–300 nm) and of temperature (5–77 K) on the rates of radical production. At 77 K the Hg is removed by 254-nm light with a quantum yield near unity, producing a nonparamagnetic Hg species. Continuing radical production occurs by photoactivated reaction of this species. Competing reactions involve one or more other intermediates, the relative roles of which are governed by the light intensity, wavelength, and temperature. Many of the radicals are produced in configurations such that their ESR sensitivity changes reversibly with temperature in the range between 5 and 45 K, the apparent radical concentration being several fold higher at the higher temperature.

## Introduction

Mercury photosensitized production of trapped radicals in 3-methylpentane (3MP) glass at 77 K by 254-nm light is accompanied by the production of one or more Hg-containing intermediates which can be photolytically decomposed by other wavelengths in the 200–300-nm range, regenerating Hg and making possible the production of several radicals per Hg atom.[2] The radicals must be present in the regions of the parent Hg atoms and their spacing and probability of reacting with each other and with Hg or an intermediate must depend on the extent of diffusion between successive photon absorptions. In the work of the present paper we have investigated the effects on the radical production rate of changing the interval between photon absorptions (by changing the incident light intensity) and of changing the rates of diffusion (by changing the temperature). We have extended information on the optical absorption spectra which grow in the 200–300-nm region as a result of the photosensitization process. New evidence on the rate of Hg removal by 254-nm light relative to the rate of radical growth indicates that radical formation occurs primarily by photoactivation of an intermediate rather than by the initial step of Hg activation. A unique temperature dependence of the apparent radical concentration measured by ESR has been observed.

## Experimental Section

*Sample Preparation.* Phillips Pure Grade 3MP was further purified, degassed, and sealed under vacuum in 2.5 × 2.5 cm quartz optical cells or 3-mm i.d. Suprasil ESR tubes, with a drop of Hg included. After standing overnight, and a period of vigorous shaking in a water bath at 55 °C, the samples were immersed in liquid nitrogen to form the glass. The spectra of liquid solutions of Hg in 3MP at six temperatures are shown in Figure 1, and the spectrum of one glassy solution at 77 K in Figure 2. Assuming the value of $7.35 \times 10^3$ $M^{-1}$ $cm^{-1}$ [3] for the extinction coefficient at $\lambda_{max}$, the data of Figure 1 indicate a concentration of $7 \times 10^{-6}$ M at 25 °C. Assuming the same extinction coefficient for $\lambda_{max}$ at 77 K, the Hg concentrations in the solutions obtained by quenching from 55 °C varied from $2.7 \times 10^{-6}$ to $26 \times 10^{-6}$ M with an average of $11.6 \times 10^{-6}$ M and an average deviation of $\pm 4.6 \times 10^{-6}$ M. The variation undoubtedly reflects variable loss of Hg from solution during the quenching process. It is probable that this loss was less, and more constant, for the samples prepared in 3-mm i.d. tubes for the ESR studies of intensity and temperature effects.

When glassy 3MP is cooled below ~65 K, it always cracks and if the cooling is done by sudden exposure to ≪60 K in a 3-mm i.d. fused silica ESR tube, the tube as well as the 3MP cracks. This can be avoided by allowing the cracking of the 3MP to occur at 60–65 K[4] while slowly introducing the sample into the cold He gas flow from the variable temperature device used. The cracking does not interfere with ESR measurements or, as far as we have observed, alter the properties of the matrix other than to hasten its approach to the annealed condition[5] and to reduce its light transmission. Spectrophotometric measurements are precluded at temperatures much less than 77 K by the excessive light scattering in cracked samples of the thickness required by the dilute Hg solutions.

*Spectrophotometric Measurements.* The spectra of the 3MP–Hg glasses at 77 K were measured with a Cary spectrophotometer, using two 2.5 cm × 2.5 cm fused silica sample cells in series to give a light path of 5 cm in the liquid nitrogen cryostat described earlier.[2] For photolysis, the cryostat was rotated 90° so that the entrance light pipe faced a hole in the side of the Cary sample compartment. This allowed illumination of the sample with the 254-nm radiation from a Vycor filtered Hanovia SC2537 end window low pressure Hg arc or the broad band focused beam from a quartz-jacketed AH4 medium pressure Hg lamp. Intensity measurements made with a Yellow Springs thermopile light meter indicated that the beam entering the cryostat box was diverging, giving an average intensity at the inner face of the exit light pipe about one-third that at the point of entrance to the box. Typical averages of the entrance and exit intensities were 0.36 mW $cm^{-2}$ for the Hanovia lamp and 35.5 mW $cm^{-2}$ for the AH4.

*ESR Measurements.* ESR measurements were made at 77 K with the sample under liquid $N_2$ in the finger of a Varian ESR dewar, or, at temperatures between 4 and 77 K, with the sample in a Heli-Tran (Air Products Co.) helium flow dewar. Varian 4501 and E-15 spectrometers were used, with 4531 type cavities, one of which has an open waveguide in the cavity wall and the other a slotted wall to admit photolyzing light. The spectra were taken in the X-band using 100-kHz modulation and microwave powers at which saturation was shown to be negligible over the temperature range of this work. The first derivative ESR spectra were fed to a Northern Scientific NS-570 signal averager-data processor, with NS-111 tape cassette accessory, for storage and double integration. The radical concentrations were estimated by comparison of the magnitude of the doubly integrated signal with that of a pitch sample with known spin concentration.

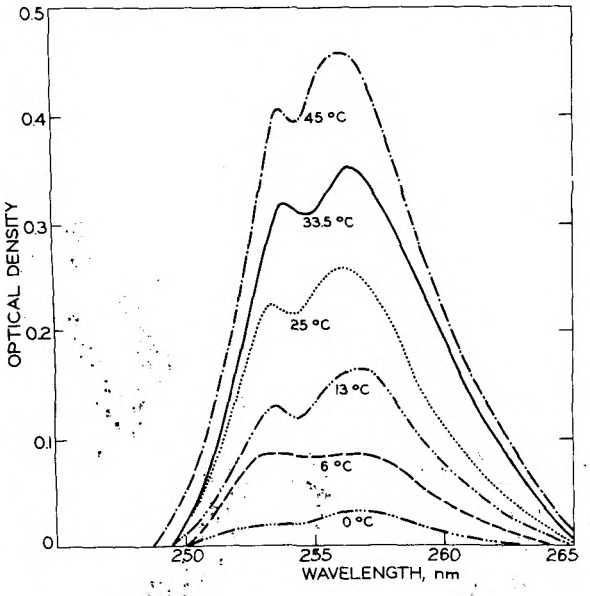


**Figure 1.** Absorption spectra of saturated solutions of Hg in 3MP at different temperatures using a 5-cm light path. The background due to absorption by the quartz cells has been subtracted.

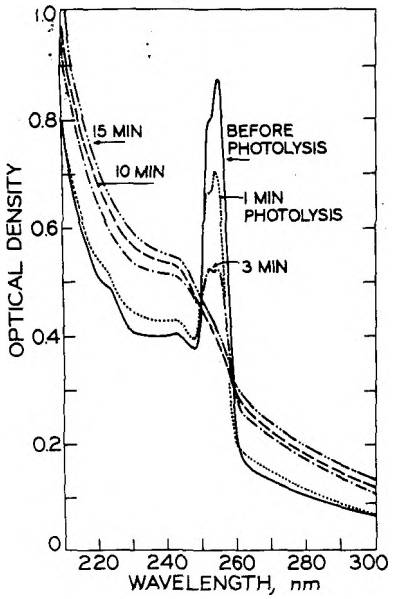


**Figure 2.** Effect of 254-nm photolysis with SC2537 lamp with Vycor filter on absorption spectra of 3MP–Hg solution at 77 K using a 5-cm light path. The background absorption from 300 to 210 nm is due to the quartz.

Photolysis of samples in the ESR cavities were made with the AH4 lamp at total intensities on the sample of ~20–100 mW $cm^{-2}$, dependent on which cavity was used. The intensity of the light in the 250–260-nm region of the AH4 spectrum (i.e., the region absorbed by Hg in 3MP glass) was estimated to be ~4% of the total intensity from a knowledge of the spectrum and selective filtering experiments. Photolyses of ESR samples with 254-nm light were done outside the ESR cavity with the finger of the ESR sample dewar in the center of a spiral Vycor low pressure Hg lamp, giving ~35 mW $cm^{-2}$ on the sample, and at 2.3 cm outside the lamp where the intensity was ~3.7 mW $cm^{-2}$.

## Results

*Spectral Changes During Photolysis.* When solutions of Hg in 3MP glass are exposed to 254-nm radiation, the absorption in the 250–265-nm region due to Hg drops,

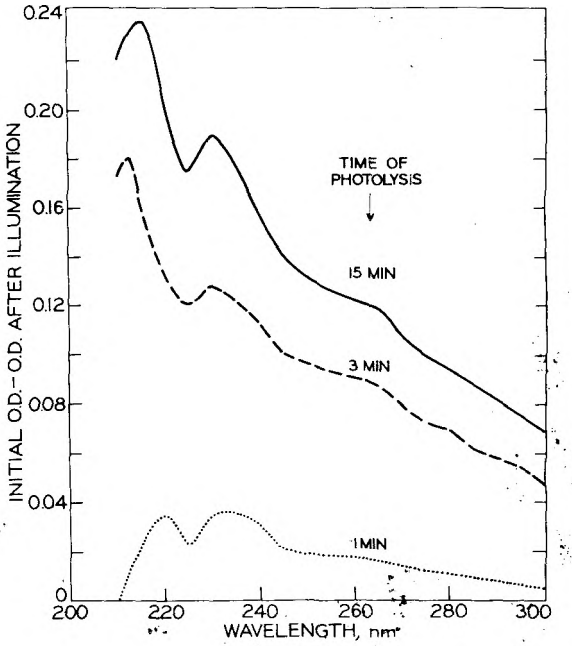


**Figure 3.** Absorption by products of 1-, 3-, and 15-min photolyses of Figure 2, obtained by subtracting the spectrum before photolysis from spectra after photolyses (omitting the 250–260-nm region of Hg absorption).

while that at both higher and lower wavelengths increases (Figure 2). Subtraction of the spectrum before illumination from that after has previously been found to yield a broad difference spectrum (Figure 3 of ref 2) with $\lambda_{max}$ at 238 ± 3 nm, attributable to 3-methylpentyl radicals. When such subtraction is done for the spectra for different times of irradiation of the sample of Figure 2, the difference spectra of Figure 3 are obtained. In addition to the peak in the region of 225–245 nm, these show a peak with $\lambda_{max}$ in the 215–220-nm region. The accuracy of the subtractions in this steeply rising region of the spectra is relatively poor but this peak appears to be real. The peak was found for each time of illumination used, both with the AH4 and SC2537 lamp.

Further evidence that species in addition to 3-methylpentyl radicals contribute to the absorption induced in the 200–300-nm region by photosensitization includes nonuniform spectral changes on standing in the dark and on prolonged illumination.

When an Hg–3MP sample from which the Hg had been bleached by 254-nm light was exposed to the AH4 lamp, filtered (25 mm of 0.17 g of KI/100 mL of $H_2O$) to remove >99% of the 254-nm radiation while passing wavelengths >260 nm, the Hg, measured by its absorption at 254 nm, was regenerated to a steady state value equal to 15% of its original concentration in a few minutes. This value did not change on continued illumination for 2 h, during which the filter solution was periodically renewed to avoid depletion.

*Effect of Light Intensity on Rate of Radical Production.* Figures 4 and 5 show the growth of radical concentration with time of photolysis of 3MP–Hg solutions at 77 K for two intensities of 254-nm monochromatic light from the Vycor spiral low pressure Hg lamp, and three intensities of broad band light from the AH4 medium pressure Hg lamp, respectively. Within the error of measuring the initial slopes, the initial rates of radical production are proportional to the first power of the incident light intensity for each lamp, but the rates are some sixfold lower for the monochromatic 254 nm from the low pressure lamp than for the same intensity from the 250–260-nm region

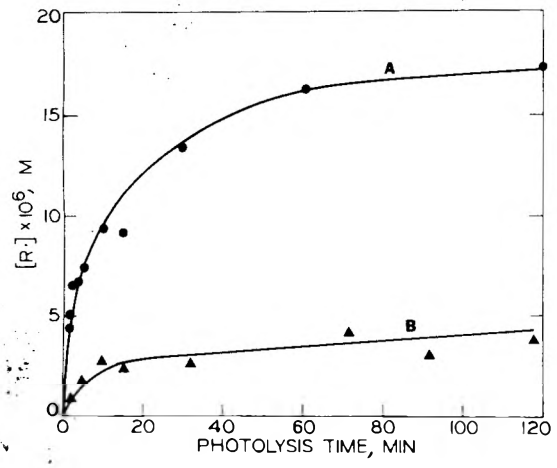


**Figure 4.** Growth of radical concentration in two samples of 3MP–Hg glass exposed to different light intensities from Vycor low pressure Hg lamp at 77 K: ●, sample in center of spiral, 35 mW $cm^{-2}$; ▲, sample at side of spiral, 3.7 mW $cm^{-2}$.

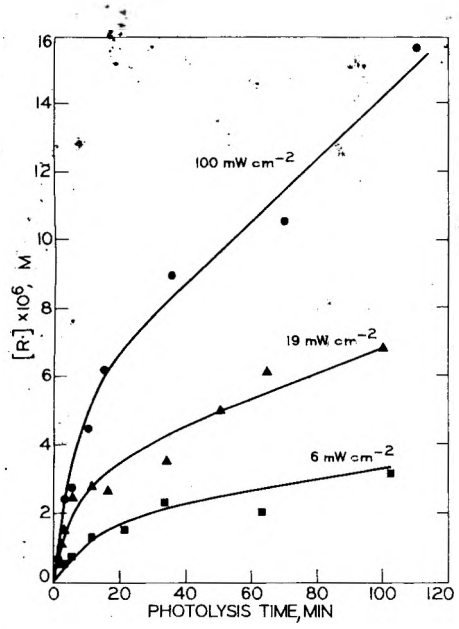


**Figure 5.** Growth of radical concentration in three samples of 3MP–Hg glass exposed to different light intensities from AH4 medium pressure Hg lamp at 77 K. The intensities in the 250–260-nm range absorbed by Hg are about 4% of the total intensities shown on the figure.

of the AH4 accompanied by the wavelengths from that lamp which are not absorbed by Hg. The ratio of the concentrations of the radicals at the plateaus of the curves for the 254-nm illuminations (Figure 4) is 3.9, much lower than the ratio of the light intensities, which is >9. To avoid the uncertainties in interpretation of such experiments imposed by the irreproducibility in the concentration of Hg in 3MP glass on successive refreezings of a sample (noted in the Experimental Section), we have done experiments with both the AH4 lamp and with monochromatic 254-nm radiation in which the light intensity was changed without melting the sample. Two tests with the monochromatic 254-nm light were made by first exposing a sample 2.3 cm from the external surface of the helical Vycor lamp (3.7 mW $cm^{-2}$) and then, after the radical concentration appeared to have reached its steady state plateau, to the full light in the center of the helix (35 mW $cm^{-2}$). Figure 6 shows that this ninefold increase in intensity on the sample increased the steady state radical concentration of the plateau by a factor of only ~1.1, although continuous illumination of two samples at the same two intensities (Figure 5) produced plateau concentrations which differed by a factor of ~4. With the AH4 lamp an increase in intensity to 100 mW after 100 min illumination at 20 mW (full spectrum of the lamp) increased the rate by a factor of 3, while in two other experiments on a somewhat different time scale the relative enhancement was considerably less.

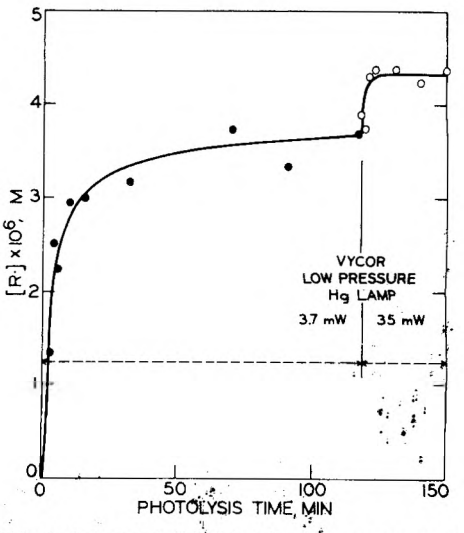


**Figure 6.** Effect of change in light intensity during exposure of a single sample on the growth of radical concentration, using Vycor low pressure Hg lamp: ●, 3.7 mW $cm^{-2}$; O, 35 mW $cm^{-2}$.

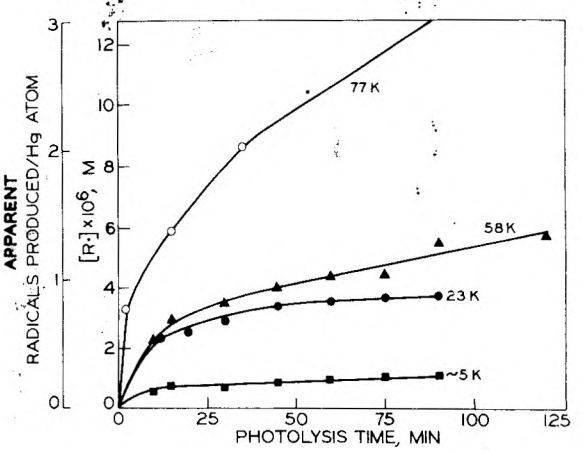


**Figure 7.** Apparent concentration of trapped radicals as a function of time of illumination of 3MP–Hg glass at 77, 58, 23, and 5 K with light from AH4 medium pressure Hg lamp. At 5 and 23 K the true radical concentrations are higher than indicated in the figure because the radicals are present in a configuration that is relatively insensitive to ESR detection (see text).

*Temperature Dependence of Radical Production and Detection.* Figure 7 shows that radical production occurs during exposure of 3MP–Hg samples to AH4 light at 58, 23, and 5 K as well as at 77 K. In this work it has unexpectedly been found that at temperatures less than ~50 K the apparent concentrations of the radicals deduced from the double integrals of the ESR spectra depend on the temperature of measurement (Figure 8). The data of Figure 8 have been normalized for the Boltzmann $1/T$ dependence of the ESR sensitivity and to the ratio of spins to area of the strong pitch reference. The shapes and line widths of the spectra do not change significantly with temperature. All measurements were made at a microwave power which was demonstrated for each temperature of Figure 8 to be below the onset of saturation effects. It appears that this unique temperature sensitivity of the ESR response to radical concentration must result from a pairing–unpairing equilibrium of closely associated radicals which is controlled by a temperature dependent

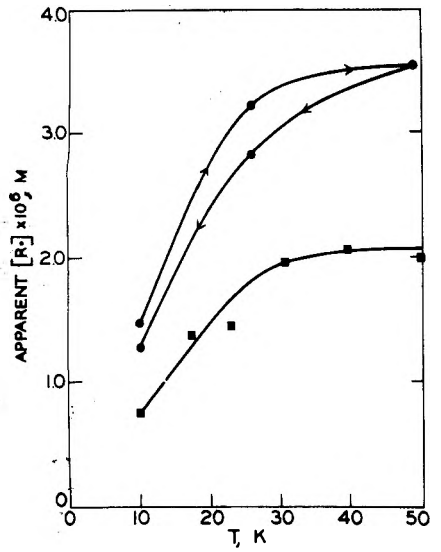


**Figure 8.** Variation in apparent radical concentration with temperature for radical populations produced at 10 K by AH4 illumination of Hg in 3MP glass. The data were taken at a power where the ESR signals are unsaturated and have been corrected for the Boltzmann $1/T$ intensity dependence. The arrows on the upper two curves indicate the sequence of successive measurements on the same sample.

matrix deformation or phonon flux. Continuing investigations of this phenomenon in the Hg system and other systems by D. D. Wilkey of our laboratory indicate that the true rate of radical growth from the Hg photosensitization at 5 K is equal to that at 23 K. When a sample photolyzed at 5 K is warmed to 23 K, the ESR signal increases to a value equal to that of an identical sample exposed throughout at 23 K. Radicals produced with greater interradical distances, by $\gamma$ irradiation of 3MP, do not show the unusual temperature dependence of the ESR signal intensity.

*Radical Decay Rates.* Periodic measurement over 1 h of the doubly integrated first derivative signals of radicals produced by 200–300-nm AH4 Hg photosensitization in 3MP at 5, 58, and 77 K and measured at these temperatures showed 0, 0, and 3% decay $h^{-1}$, respectively. The rate for radicals produced at 77 K by 254-nm SC2537 radiation appeared to be ~10% $h^{-1}$. The initial concentrations in the four determinations were $1.1 \times 10^{-6}$, $5.6 \times 10^{-6}$, $16 \times 10^{-6}$, and $4.3 \times 10^{-6}$ M, respectively.

## Discussion

*Spectrometric Evidence for Hg-Containing Reaction Intermediates.* The broad absorption from 210 to 300 nm which results from 254-nm illumination of 3MP-Hg glass (Figure 2) is in the region where radicals produced by radiolysis in the liquid,[6] gas,[7] and glass[8a] phases absorb. It must be the envelope of the absorption of the radicals which are seen by ESR plus any Hg-containing compounds formed which absorb in this region. The presence of such compounds is implied by the 215–220 nm peak and by the changes in spectral shape, noted in the Results section, but the spectra of the plausible products (HgH, $HgH_2$, $HgC_6H_{13}$, $Hg(C_6H_{13})_2$, $HHgC_6H_{13}$) are not well enough known to make the data useful in selecting which may be present.

In the present work which has included a search in the 3000–9000-G range where lines of mercury–alkyl radicals have been reported,[8b] we have found, as in the earlier work,[2] no ESR signal assignable to a paramagnetic Hg species (e.g., HgH or $HgC_6H_{13}$) produced in 3MP–Hg glass by 254-nm illumination. If such a species is formed, its ESR spectrum is obscured by the 3-methylpentyl radical spectrum or is too weak to be resolved.

*Rate of Hg Removal Relative to Radical Growth.* The estimated half-life for Hg disappearance in a sample of low optical density exposed to an intensity of ~0.36 mW $cm^{-2}$ at 254 nm is 50 s if the quantum yield is unity. The rate of removal of Hg in the experiment of Figure 2 is consistent with this estimate. At low optical densities, the half-life should be independent of the geometry of the sample and the concentration of Hg and inversely proportional to the light intensity. This being the case, the Hg in the ESR tubes exposed to 3.7 and 37 mW $cm^{-2}$ from the Vycor low pressure lamp (Figure 4) was removed with half-lives of ~6 and 0.6 s, respectively. For the AH4 illuminations of Figure 5, where ~4% of the indicated total intensity was in the 250–260-nm Hg absorption band, the estimated half-lives for the three experiments were ~6, 30, and 90 s. Thus, in the experiments of Figures 4 and 5, the Hg was nearly all removed before substantial radical growth occurred. Therefore, excited Hg atoms formed by absorption of a 254-nm photon must usually react with matrix molecules to form a Hg compound and no 3-methylpentyl radical. The only plausible Hg compounds seem to be $HgH_2$, formed by the reaction $Hg^* + C_6H_{14} \rightarrow HgH_2 + C_6H_{12}$, and HHgR formed in a concerted reaction, or by Hg abstraction to form HgH, followed by prompt combination with the geminate radical. To account for the subsequent growth of radicals (Figure 4), the compound must produce radicals on absorption of 254 nm, in a process for which the product of the extinction coefficient and the quantum yield ($\epsilon\phi$) is much lower than that for the initial removal of Hg.

*Implications of Shape of Radical Growth Curves and Intensity Effects.* Rationalization of the observed growth rate, intensity, and temperature effects requires processes which result in a gradually decreasing rate of radical production with time of illumination until a nearly flat plateau is reached with pure 254-nm light and a nearly constant continuing rate prevails with broad band AH4 light. At high intensities the available processes must favor formation of more than one radical per Hg atom in competition with a process which limits the formation to one or less at low intensities. In the absence of definitive evidence as to the species present, we shall use hypothetical intermediates as prototypes to discuss the characteristics that the correct intermediates must have. For this working model, we assume that HHgR formed in reaction 2 absorbs

$$Hg \xrightarrow[254\ nm]{h\nu} Hg^* \quad (1)$$

$$Hg^* + RH \rightarrow HHgR \quad (2)$$

$$HHgR \xrightarrow{h\nu} HgR + H^* \quad (3)$$

$$H^* + RH \rightarrow R + H_2 \quad (4)$$

254-nm light and produces hot H atoms (reaction 3), which form radicals by the hot abstraction process (reaction 4).[9] We further assume that HgR can absorb 254-nm photons to form HgR* (reaction 5), which abstracts H from RH or

$$HgR \xrightarrow{h\nu} HgR^* \quad (5)$$

decomposes to a radical and Hg (reaction 6), leaving HHgR

$$HgR^* \xrightarrow{+RH} HHgR + R\cdot \quad \text{or} \quad Hg + R\cdot \quad (6)$$

and/or Hg available for more radical production. To account for the effects of continuing illumination, intensity, and temperature on the growth rate, HgR must be re-

moved from further substantial participation in radical production by a reaction which competes with the (5)–(6) sequence, such as

$$HgR + R \rightarrow HgR_2 \quad (7)$$

the product of which has a negligible $\epsilon\phi$ value at 254 nm relative to the (1)–(4) and (5)–(6) sequences. At low light intensities the probability of photon absorption by HgR before occurrence of reaction 7 is low, resulting in a low R·/Hg ratio. With increasing light intensity the R·/Hg ratio goes up but at a rate that is less than proportional to the intensity because the lifetime of HgR relative to reaction 7 decreases with the increasing concentration of radicals in proximity to the HgR.

To account for the continued growth of radicals with 200–300-nm light in contrast to the steady state plateau with monochromatic 254-nm light, the species we have designated as $HgR_2$ must absorb and undergo photodecomposition (reaction 8) sufficiently at wavelengths within

$$HgR_2 \xrightarrow{h\nu} Hg + R_2 \text{ or } HgR + R \quad (8)$$

the broad band of exciting light to regenerate Hg or HgR which can then generate more radicals.

The properties ascribed above to HgR and $HgR_2$ are consistent with the observation (Figure 6) that a ninefold increase in 254-nm light intensity after the steady state plateau has been reached causes a very small change in the steady state radical concentration compared to the difference in the plateau concentrations for two separate samples illuminated throughout with the two different intensities (Figure 4). The smallness of the change is predictable if, as assumed, the plateau is reached when most of the Hg has been converted to $HgR_2$ and the latter does not absorb significantly at 254 nm. The data of Figure 5 showing relative rates of growth of radical concentration with different intensities of AH4 illumination can also be correlated with the postulated properties of the reaction intermediates.

*Temperature Effects.* As noted in the Results section, the rates of radical production at 5 and 23 K (and probably also 58 K) are indistinguishable after the measured apparent rates are adjusted for the unique temperature sensitivity of the ESR detection of radicals produced by the Hg photosensitization. The apparent large increase in rate of production from 58 to 77 K (Figure 7) cannot, however, be due to the type of temperature sensitivity illustrated in Figure 8, because this does not persist above ~50 K. The 58–77 K increase may result, in whole or in part, from a difference in the effective light intensity entering the sample at 77 K, where the 3MP glass is uncracked, as compared to lower temperatures where it is always cracked. It is plausible, however, that at least part of the effect may be the result of changes in the matrix properties. At temperatures below 77 K (which is approximately the glass transition temperature) the energy transfer characteristics of the matrix may be such that HHgR which has absorbed a photon is stabilized, rather than dissociating by reaction 3, or that the probability of HgR from reaction 3 combining promptly with the geminate R from reaction 4 is significant.

Another effect reducing the growth rate of radicals at temperatures below 77 K may be the increased probability of radical–radical reactions (reactions 9a and 9b) because

$$C_6H_{13} + C_6H_{13} \rightarrow C_{12}H_{26} \quad (9a)$$

$$\hookrightarrow C_6H_{12} + C_6H_{14} \quad (9b)$$

the radicals successively produced from a single Hg atom are in closer proximity as a result of slower diffusion of the Hg, HgH, and HHgR between successive photon absorptions.

*Other Considerations.* It has been estimated[2] that for 3MP–Hg samples saturated at 25 °C and quenched to 77 K, followed by irradiation in the center of the Vycor spiral, the ratio of trapped radicals at the plateau to Hg atoms initially present is 3, and that in similar samples with AH4 lamp illumination the ratio was still growing when 11 radicals had been produced per Hg atom. If these were produced from adjacent molecules by immobile Hg atoms, they would be rapidly removed by radical–radical combination. It may be estimated that an Hg atom in 3MP glass at 77 K undergoes an average diffusive displacement of ~0.07 Å $s^{-1}$, which is sufficient to provide several tens of angstroms separation between the sites of formation of radicals produced on the time scales of Figures 4–7.

The decay kinetics of 3-methylpentyl radicals produced by $\gamma$ irradiation of 3MP at 77 K have been reported earlier[10] and used to estimate the diffusion coefficients at 77 and 87 K. Photon absorption by radicals in $\gamma$-irradiated hydrocarbon glasses[11] has been shown to facilitate removal of part of the intraspur radical population.

HgH formed by reaction 10 has been observed as a

$$Hg^* + RH \rightarrow HgH + R \quad (10)$$

transitory intermediate in gas phase reactions of alkanes photosensitized by Hg.[12] However, the absence of significant growth in radical concentration in 3MP glass at 77 K during the short time required for the Hg to be removed rules out this reaction as an important contributor to the Hg-sensitized production of radicals. If it occurs, it must be followed promptly by combination of the HgH with the R to form HHgR.

*Acknowledgment.* We express our appreciation to Dr. D. D. Wilkey for experimental checks of some of the data, and to Dr. G. H. Morine for a helpful suggestion about interpretation of the results.

## References and Notes

(1) This work has been supported in part by the U.S. Energy Research and Development Administration under Contract No. AT(1101)-1715 and by the W. F. Vilas Trust of the University of Wisconsin.
(2) N. Bremer, B. J. Brown, G. H. Morine, and J. E. Willard, *J. Phys. Chem.*, **79**, 2187 (1975).
(3) (a) J. N. Spencer and A. F. Voigt, *J. Phys. Chem.*, **72**, 464 (1968); (b) R. R. Kuntz and G. J. Mains, *ibid.*, **68**, 408 (1964).
(4) M. A. Long and J. E. Willard, *J. Phys. Chem.*, **74**, 1207 (1970).
(5) (a) D. Shooter and J. E. Willard, *J. Phys. Chem.*, **76**, 3167 (1972); (b) M. A. Neiss and J. E. Willard, *ibid.*, **79**, 783 (1975).
(6) (a) L. W. Burggraf and R. F. Firestone, *J. Phys. Chem.*, **78**, 508 (1974); (b) R. H. Schuler and L. K. Patterson, *Chem. Phys. Lett.*, **27**, 369 (1974).
(7) H. Christensen, G. Nilsson, K. Thomas, and T. Reitberger, *Chem. Phys. Lett.*, **22**, 533 (1973).
(8) (a) G. H. Morine, Ph.D. Thesis, University of Wisconsin–Madison, 1975; (b) B. W. Fullam and M. C. R. Symons, *J. Chem. Soc., Dalton Trans.*, 1086 (1974).
(9) (a) L. Perkey and J. E. Willard, *J. Chem. Phys.*, **60**, 2832 (1974); (b) D. D. Wilkey and J. E. Willard, *ibid.*, in press.
(10) M. A. Neiss and J. E. Willard, *J. Phys. Chem.*, **79**, 783 (1975).
(11) E. D. Sprague and J. E. Willard, *J. Chem. Phys.*, **63**, 2603 (1975).
(12) (a) A. B. Callear and R. E. M. Hedges, *Trans. Faraday Soc.*, **66**, 615 (1970); (b) A. B. Callear and P. M. Wood, *J. Chem. Soc., Faraday Trans. 2*, **68**, 302 (1972); (c) A. C. Vikis and D. J. LeRoy, *Can. J. Chem.*, **50**, 595 (1972); **51**, 1207 (1973).

# Volume Changes in the Proton Ionization of Amines in Water. 1. Morpholines and Piperazines

**S. Cabani,* V. Mollica,**

*Istituto di Chimica Fisica, Università di Pisa, Via Risorgimento 35, 56100 Pisa, Italy*

**L. Lepori, and S. T. Lobo[1]**

*Laboratorio di Chimica Quantistica ed Energetica Molecolare del C.N.R., Via Risorgimento 35, 56100 Pisa, Italy* *(Received November 19, 1976)*

*Publication costs assisted by Consiglio Nazionale delle Ricerche, Rome*

Apparent molar volumes, $\Phi_v$, at various concentrations in water at 25 °C of some cyclic bifunctional amines [morpholine, 4-methylmorpholine, piperazine, 1-methylpiperazine, 1,4-dimethylpiperazine, 1,4-diazabicyclo-[2.2.2]octane (triethylenediamine)] and their mono- and dihydrochlorides have been determined. The volume changes $\Delta V_1°$ and $\Delta V_2°$, involved in the first and second proton ionizations from the protonated amines, have been calculated from the limiting partial molar volumes $\bar{V}_2°$. Furthermore, the volumes of ionization for the bifunctional cyclic amines have been compared with those for the monofunctional amines and the relationship between entropies and volumes of ionization has been examined.

## Introduction

Volume changes, $\Delta V°$, in the proton ionization process of amines in aqueous solution have become the subject of considerable attention because such data can provide information on solute–solvent interactions.[2-8] However, compared with enthalpies and entropies of ionization[9,10] much less is known about $\Delta V°$.

This led us to commence studies on the infuence of substituents on $\Delta V°$ of some polyfunctional organic compounds containing nitrogen, varying in the number and type of radicals attached to the nitrogen atom. In this work, we report data for certain secondary and tertiary bifunctional cyclic amines, for which we have already reported data for transfer properties from the gaseous state to dilute aqueous solution[11] and heat capacity changes for proton ionization.[12,13]

The volume changes, $\Delta V°$, for proton ionization have been calculated from the limiting partial molar volumes ($\bar{V}_2°$) of the species involved in the reaction. $\bar{V}_2°$ values have been obtained from density measurements of aqueous solutions of the amine, of the monohydrochloride, and of the dihydrochloride as a function of concentration.

## Experimental Section

*Materials.* The amines examined [morpholine, 4-methylmorpholine, piperazine, 1-methylpiperazine, 1,4-dimethylpiperazine, and 1,4-diazabicyclo[2.2.2]octane (triethylenediamine)] were available commercially. All liquids have been purified by fractional distillation at atmospheric pressure after prolonged refluxing on metallic sodium. Piperazine (mp 110 °C) was purified by zone melting; triethylenediamine was sublimed twice under vacuum. The purity of these compounds, as examined by GLC, was found to be ≥99.5%.

Stock solutions of the mono- and dihydrochlorides of the amines were prepared, immediately prior to measurements, by addition of a stoichiometric quantity of amine to a standardized HCl solution. In the case of piperazine dihydrochloride, a commercial sample was used also. It was purified by recrystallization from ethanol and water (mp 320 °C). No appreciable difference was observed between the results obtained from the commercial solid sample and the prepared stock salt solution. The water used in all the experiments was first deionized and then distilled from an alkaline $KMnO_4$ solution.

*Apparatus and Measurements.* A differential hydrostatic balance, capable of a precision of 1 ppm, was used for the density measurements. The details of the method have been described earlier.[14] The solutions to be studied were prepared by successive additions of a weighed quantity of amine (B), or of stock solution of monohydrochloride (B·HCl), or of dihydrochloride (B·2HCl) of the amine to a known quantity of water.

In each case, the observed apparent molar volume ($\Phi_v^{obsd}$) was calculated from

$$\Phi_v^{obsd} = \frac{M}{d^0} - \left(\frac{d}{d^0} - 1\right)\frac{1000}{c} \qquad (1)$$

where $M$ is the formula weight of the solute, $c$ its molar concentration, and $d^0$ and $d$ are the density of water and of solution, respectively.

## Treatment of Data

From the $\Phi_v^{obsd}$ values obtained by using eq 1, the apparent molar volume $\Phi_v(I)$ of the species I (I = B, B·HCl, B·2HCl) has been calculated by applying corrections for hydrolysis (a), for acidic dissociation (b and c), and for disproportionation (d).

$$B + H_2O \rightleftarrows BH^+ + OH^- \qquad (a)$$

$$BH^+ \rightleftarrows B + H^+ \qquad (b)$$

$$BH_2^{2+} \rightleftarrows BH^+ + H^+ \qquad (c)$$

$$BH^+ \rightleftarrows {}^1/_2B + {}^1/_2BH_2^{2+} \qquad (d)$$

The values of $\Phi_v(I)$ are related to $\Phi_v^{obsd}(I)$ by the following general equation:

$$\Phi_v(I) = \Phi_v^{obsd}(I) - \alpha\Delta V \qquad (2)$$

where $\alpha$ is the degree of dissociation of species I, which is involved in processes a, b, c, or d, and $\Delta V$ is the corresponding reaction volume.

In Figure 1 are reported $\alpha$ values[15a] for processes a, b, and c vs. p$K$ values for the corresponding processes at the initial concentration $c^0 = 0.01$ M. Examination of Figure 1 shows that for the hydrochlorides of the monoamines

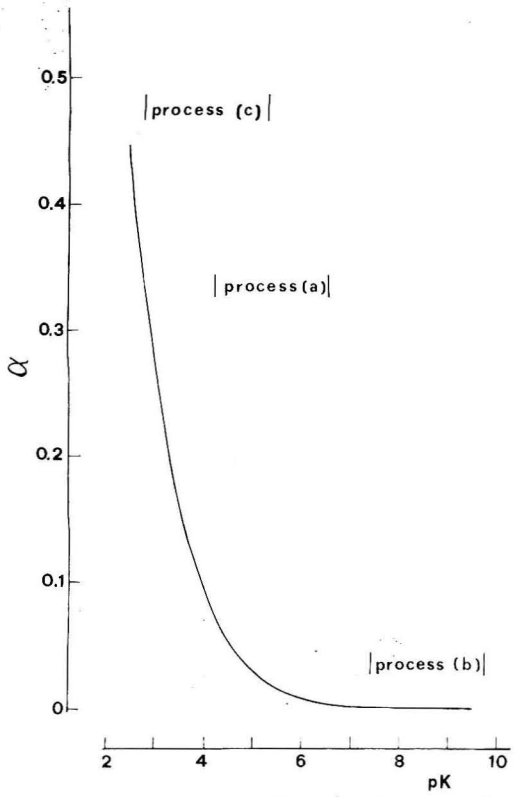


**Figure 1.** A correlation of $\alpha$ vs. p$K$ for $c_1^0 = 0.01$ mol L$^{-1}$. The p$K$ range for processes a, b, and c for the amines studied here is indicated.

studied, the degree of dissociation is always negligible ($\alpha < 0.002$). Consequently, $\Phi_v$(B·HCl) is practically equal to $\Phi_v^{obsd}$ and can be calculated directly from eq 1. For aqueous solutions of amines or diamine dihydrochlorides, however, $\alpha$ is nonnegligible and, hence, corrections must be applied to obtain $\Phi_v$ values for B and B·2HCl. A plot of $\alpha$[15b] vs. p$K$ for process d is shown in Figure 2. Although the degree of disproportionation is small ($\alpha < 0.02$) for the monohydrochlorides of the diamines examined here, a correction has been applied in all cases.

The procedure to be followed for hydrolysis, i.e., for process a, involving

$$\Phi_v(B) = \{\Phi_v^{obsd}(B) - \alpha[\Phi_v(BH^+OH^-) - V^\circ(H_2O)]\}/(1 - \alpha) \quad (3)$$

has already been described.[14] $V^\circ(H_2O)$ is the molar volume of liquid water.

For process c, which must be considered in the case of solutions containing the diamine and hydrochloric acid in the ratio 1:2, the corrected $\Phi_v$ values have been calculated by

$$\Phi_v(B{\cdot}2HCl) = \{\Phi_v^{obsd}(B{\cdot}2HCl) - \alpha[\Phi_v(B{\cdot}HCl) + \Phi_v(HCl)]\}/(1 - \alpha) \quad (4)$$

For process d, the corrected $\Phi_v$ values are given by

$$\Phi_v(B{\cdot}HCl) = \{\Phi_v^{obsd}(B{\cdot}HCl) - \alpha/2[\Phi_v(B) + \Phi_v(B{\cdot}2HCl)]\}/(1 - \alpha) \quad (5)$$

From eq 3–5, it is evident that the calculation of $\Phi_v$ of a diamine (B) or of its salts (B·HCl or B·2HCl) entails a knowledge of $\Phi_v$ of the other species present in solution. Experimental $\Phi_v^{obsd}$ values for B·HCl are used as initial values in an iterative procedure, which involves eq 3–5, successively. Three iterations were adequate to obtain convergent values of $\Phi_v$(I) (I = B, B·HCl, B·2HCl). The values of the equilibrium constants, needed for the calculation of $\alpha$, were obtained from the thermodynamic equilibrium constants reported in the literature and from the molal activity coefficients calculated from the Debye–Hückel limiting law.

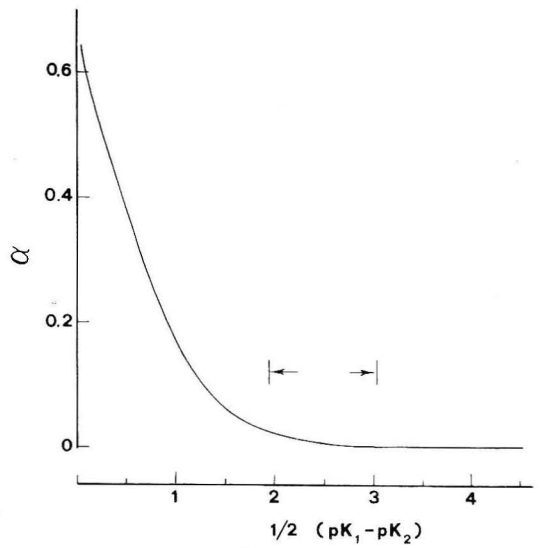


**Figure 2.** A correlation of $\alpha$ vs. $^1/_2(pK_1 - pK_2)$. The p$K$ range, covered by the amines examined, is indicated.

The accuracy of the above corrections depends on both the p$K$ uncertainty and the magnitude of the correction itself, the latter being a function of $\Delta V$ as well as of $\alpha$ (see eq 2), and consequently of concentration and p$K$ values. For the substances examined here, the magnitude of the corrections does not exceed 6 mL mol$^{-1}$ in any case, with an error which has been estimated to be always lower than 0.08 mL mol$^{-1}$.

The corrected $\Phi_v$ values, obtained via eq 3–5, were fitted to an equation of the type

$$\Phi_v = \bar{V}_2^\circ + S_v c^{1/2} + hc \quad (6)$$

which is the Redlich–Meyer equation for electrolytes,[16] where $S_v = 1.868$ and 9.706 mL L$^{1/2}$ mol$^{-3/2}$ for 1:1 and 1:2 electrolytes, respectively, at 25 °C. In the case of amines, $S_v = 0$. $\bar{V}_2^\circ$ is the partial molar volume at infinite dilution and $h$ is an empirical constant determined from experimental results. $c$ is the actual molar concentration of the solute related to the stoichiometric concentration $c^0$ by $c = (1 - \alpha)c^0$.

As an example, in Figure 3 are reported $\Phi_v$ values as a function of concentration for triethylenediamine for the free base, monohydrochloride, and dihydrochloride, with and without the corrections considered above.

## Results and Discussion

An alternative[5,17–19] to the hydrolysis correction applied above is to carry out density measurements of the amine in alkaline solutions, in order to suppress hydrolysis. The apparent molar volume of solute is then calculated directly from eq 1, where $d^0$ is the density of the alkaline solution;[5,17,18] a relationship based on Young's rule[19] has also been used. Both of these procedures, which are equivalent, do not take into account the terms arising from the deviation of the system from the above rule, i.e., terms that may not be negligible and that may not be predictable a priori. In Table I are compared $\bar{V}_2^\circ$ values of some nitrogen containing compounds in water and in aqueous alkaline solutions. That the $\bar{V}_2^\circ$ values in water are greater than those obtained from measurement in aqueous alkaline solutions is clearly evident. Sometimes the data of the same authors differ by as much as 0.8 mL mol$^{-1}$.

In the specific case of cyclic bifunctional amines, the difference between $\bar{V}_2^\circ$ obtained from measurement in water and in aqueous alkaline solutions appears to be

TABLE I: Comparison between the Values of $\bar{V}_2^\circ$ for Nitrogen Bases Obtained from Measurements in Water or in Aqueous Alkaline Solutions at 25 °C

| Substance | $\bar{V}_2^\circ$, mL mol$^{-1}$ | Medium | Ref |
|---|---|---|---|
| Piperidine | 92.13[a] | Water | 14 |
| | 91.97 | 0.1 N KOH | 14 |
| | 91.8 | Water | 18 |
| | 91.65 | 0.1 N NaOH | 18 |
| | 91.10 | 0.1 N KOH | 17 |
| 1-Methylpiperidine | 110.54 | Water | 14 |
| | 109.91 | 0.1 N KOH | 17 |
| Methylamine | 41.68 | Water | 20 |
| | 41.15 | 0.025 N KOH | 20 |
| | 40.0 | 0.025 N KOH | 5 |
| Dimethylamine | 59.80 | Water | 20 |
| | 59.0 | 0.025 N KOH | 20 |
| | 58.6 | 0.025 N KOH | 5 |
| Trimethylamine | 78.8 | Water | 20 |
| | 78.6 | 0.025 N KOH | 20 |
| | 77.9 | 0.025 N KOH | 5 |
| Triethylamine | 120.9 | Water | 20 |
| | 119.7 | 0.025 N KOH | 5 |

[a] The value of 92.53 mL mol$^{-1}$ reported earlier (ref 14) is incorrect due to a typographical error.

negligible, as is seen from the close agreement of our results with those of others (cf. Table II). By using the values of $\bar{V}_2^\circ$ reported in Tables II and III, and the value of $\bar{V}_2^\circ$(HCl) = 17.83 mL mol$^{-1}$ at 25 °C,[8] the volume changes in proton ionization have been calculated as follows:

$$\Delta V_1^\circ = \bar{V}_2^\circ(\mathrm{B}) + \bar{V}_2^\circ(\mathrm{HCl}) - \bar{V}_2^\circ(\mathrm{B{\cdot}HCl}) \quad (7)$$

$$\Delta V_2^\circ = \bar{V}_2^\circ(\mathrm{B{\cdot}HCl}) + \bar{V}_2^\circ(\mathrm{HCl}) - \bar{V}_2^\circ(\mathrm{B{\cdot}2HCl}) \quad (8)$$

The results are summarized in Table IV together with the values of the thermodynamic functions p$K$, $\Delta H^\circ$, and $\Delta S^\circ$ for proton ionization. To facilitate comparison, data for related compounds have been included in the table. The results are interpreted in terms of (1) introduction of a methyl group on the nitrogen atom of a cyclic amine and (2) introduction of a polar center in a cyclic monofunctional amine.

*Introduction of a Methyl Group on the Nitrogen Atom.* All secondary amines considered in Table IV have an almost constant value for $\Delta S_1^\circ = -8.5 \pm 1.5$ cal mol$^{-1}$ deg$^{-1}$, which is considerably less negative than that for the corresponding tertiary $N$-methylated amines ($\Delta S_1^\circ = -15.4 \pm 2$ cal mol$^{-1}$ deg$^{-1}$). This substantial difference in entropy on going from the secondary to the tertiary amine is accompanied by a decrease in basicity of the order of one p$K$ unit and a decrease in $\Delta H_1^\circ \simeq 3$ kcal mol$^{-1}$. $\Delta V_1^\circ$, however, remains practically unaffected on the introduction of a methyl group on the nitrogen atom of a cyclic secondary amine. This trend is similar to that shown by

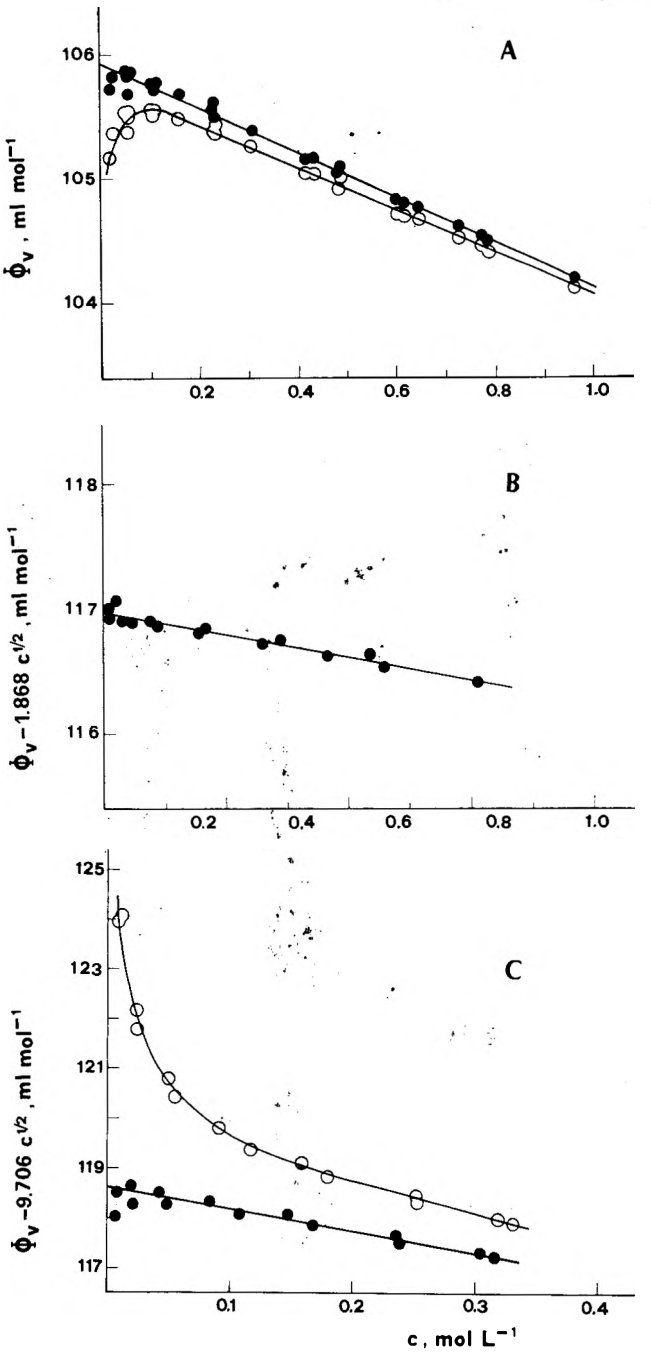


Figure 3. Apparent molar volumes of (A) triethylenediamine, (B) triethylenediamine monohydrochloride, (C) triethylenediamine dihydrochloride in aqueous solution at 25 °C, uncorrected (○) and corrected (●) for hydrolysis, disproportionation, and acidic dissociation, respectively. For the monohydrochloride, corrected and uncorrected data are practically identical.

TABLE II: Apparent Molar Volumes, $\Phi_V = \bar{V}_2^\circ + hc$, of Bifunctional Cyclic Amines in Water at 25 °C[a]

| Substance | No. of expt | Concn range, M | $\bar{V}_2^\circ$, mL mol$^{-1}$ | $h$, mL L mol$^{-2}$ | Ref |
|---|---|---|---|---|---|
| Morpholine | 23 | 0.03-1.03 | 82.56 ± 0.03 | −0.54 ± 0.05 | This work |
| | | | 82.54[b] | −0.478 | 18 |
| | | | 82.7 | | 21 |
| 4-Methylmorpholine | 12 | 0.02-1.08 | 101.28 ± 0.03 | −1.22 ± 0.06 | This work |
| Piperazine | 14 | 0.03-0.72 | 83.53 ± 0.03 | −0.93 ± 0.07 | This work |
| | | | 83.31[b] | −1.01 | 18 |
| 1-Methylpiperazine | 18 | 0.03-0.91 | 102.30 ± 0.03 | −1.95 ± 0.05 | This work |
| 1,4-Dimethylpiperazine | 21 | 0.03-0.84 | 121.00 ± 0.02 | −2.91 ± 0.05 | This work |
| Triethylenediamine | 25 | 0.02-0.95 | 105.93 ± 0.02 | −1.80 ± 0.05 | This work |
| | | 0.03-0.38 | 105.7 ± 0.1[c] | −1.5 | 19 |

[a] The reported uncertainties are standard deviations. [b] From measurements in 0.1 N NaOH solutions. [c] From measurements in 0.011 N NaOH solutions.

TABLE III: Apparent Molar Volumes, $\Phi_v = \bar{V}_2^\circ + S_v c^{1/2} + hc$, of Bifunctional Cyclic Amine Salts in Water at 25 °C[a]

| Substance | No. of expt | Concn range, M | $\bar{V}_2^\circ$, mL mol$^{-1}$ | $h$, mL L mol$^{-2}$ | Ref |
|---|---|---|---|---|---|
| Morpholine hydrochloride | 18 | 0.01–0.79 | 92.99 ± 0.04 | −0.17 ± 0.09 | This work |
| 4-Methylmorpholine hydrochloride | 17 | 0.01–0.67 | 111.71 ± 0.06 | −0.53 ± 0.19 | This work |
| Piperazine hydrochloride | 12 | 0.01–0.27 | 95.12 ± 0.06 | −0.30 ± 0.44 | This work |
| 1-Methylpiperazine hydrochloride | 10 | 0.02–0.51 | 113.97 ± 0.07 | −0.86 ± 0.25 | This work |
| 1,4-Dimethylpiperazine hydrochloride | 12 | 0.01–0.43 | 132.61 ± 0.05 | −1.15 ± 0.20 | This work |
| Triethylenediamine hydrochloride | 15 | 0.01–0.61 | 116.97 ± 0.06 | −0.90 ± 0.20 | This work |
| | | 0.03–0.29 | 117.03 ± 0.06 | −0.9 | 19 |
| Piperazine dihydrochloride | 15 | 0.02–0.22 | 99.26 ± 0.11 | −4.05 ± 0.96 | This work |
| 1-Methylpiperazine dihydrochloride | 12 | 0.01–0.41 | 117.48 ± 0.07 | −3.63 ± 0.40 | This work |
| 1,4-Dimethylpiperazine dihydrochloride | 13 | 0.01–0.40 | 135.76 ± 0.09 | −3.57 ± 0.45 | This work |
| Triethylenediamine dihydrochloride | 14 | 0.01–0.33 | 118.55 ± 0.14 | −4.01 ± 0.75 | This work |

[a] The $S_v$ values are 1.868 and 9.706 mL L$^{1/2}$ mol$^{-3/2}$ for mono- and dihydrochloride salts, respectively.[16] The reported uncertainties are standard deviations.

TABLE IV: Thermodynamic Parameters for Ionization of Selected Cyclic Amines in Water at 25 °C[a]

| | $BH^+ \rightarrow B + H^+$ | | | | $BH_2^{2+} \rightarrow BH^+ + H^+$ | | | |
|---|---|---|---|---|---|---|---|---|
| Substance | $pK_1$ | $\Delta H_1^\circ$, kcal mol$^{-1}$ | $\Delta S_1^\circ$, cal mol$^{-1}$ deg$^{-1}$ | $\Delta V_1^\circ$, mL mol$^{-1}$ | $pK_2$ | $\Delta H_2^\circ$, kcal mol$^{-1}$ | $\Delta S_2^\circ$, cal mol$^{-1}$ deg$^{-1}$ | $\Delta V_2^\circ$, mL mol$^{-1}$ |
| Morpholine | 8.49 | 9.33 | −7.6 | 7.4 | | | | |
| 4-Methylmorpholine | 7.73 | 6.56 | −13.6 | 7.4 | | | | |
| Piperazine | 9.73 | 10.25 | −10.1 | 6.2 | 5.33 | 7.43 | 0.5 | 13.7 |
| 1-Methylpiperazine | 9.10 | 8.40 | −13.5 | 6.2 | 4.94 | 4.00 | −9.2 | 14.3 |
| 1,4-Dimethylpiperazine | 8.23 | 6.66 | −15.4 | 6.2 | 4.18 | 3.96 | −5.8 | 14.7 |
| Triethylenediamine | 8.82 | 7.21 | −16.2 | 6.8 | 2.95 | 3.00 | −3.4 | 16.3 |
| Pyrrolidine | 11.31 | 13.03 | −8.0 | 3.9 | | | | |
| 1-Methylpyrrolidine | 10.46 | 9.05 | −17.5 | 4.5 | | | | |
| Piperidine | 11.12 | 12.76 | −8.1 | 3.2 | | | | |
| 1-Methylpiperidine | 10.08 | 9.44 | −14.4 | 2.9 | | | | |

[a] $pK$, $\Delta H^\circ$, and $\Delta S^\circ$ values were taken from ref 22 (morpholine, piperazine), ref 23 (4-methylmorpholine in 0.5 M $KNO_3$; a value of $pK_1 = 7.41$ at $\mu = 0$ was reported in ref 24), ref 25 (1-methylpiperazine, 1,4-dimethylpiperazine in 0.1 N $KNO_3$), ref 26 (pyrrolidine, piperidine, first ionization of triethylenediamine), ref 27 (second ionization of triethylenediamine at $\mu = 0.1$), ref 28 (1-methylpyrrolidine, 1-methylpiperidine). For pyrrolidine, 1-methylpyrrolidine, piperidine, 1-methylpiperidine the $\Delta V_1^\circ$ values were taken from ref 29.

the aliphatic methylamine series.[20]

The observed variation in $\Delta S_1^\circ$ on increasing the number of methyl groups on the nitrogen atom (primary → secondary → tertiary),[30] according to the model proposed by Trotman-Dickenson,[31] is due to the different number of molecules of hydration attached to the charged nitrogen center. Since water bound to a charged center has presumably a different volume than that of bulk water, a variation in $\Delta V_1^\circ$ would be expected on going from the secondary to the tertiary *N*-methylated amines. In order to rationalize the lack of variation in $\Delta V_1^\circ$, the following compensation phenomenon is proposed: the difference in the contribution to $\bar{V}_2^\circ$ of the methyl group in a neutral molecule and in the cation acid is equal to the difference in the contribution of a hydrogen atom attached to a neutral nitrogen atom and one bound to a charged nitrogen center.

An indirect confirmation of this hypothesis is furnished by the practically identical estimated values of the above differences. On the basis of intrinsic volumes reported by Edward,[32] the difference in volume of a hydrogen atom on N and $N^+$ centers, $\bar{V}_2^\circ(H_N) - \bar{V}_2^\circ(H_{N^+}) = 4.4$ mL mol$^{-1}$,[33] is predominantly attributed to the fact that the volume of the bulk water is larger than the volume of the water attached to a charged nitrogen center. On the contrary, the volume difference of a methyl group on N and $N^+$ centers, $\bar{V}_2^\circ(Me_N) - \bar{V}_2^\circ(Me_{N^+}) = 4.5$ mL mol$^{-1}$,[34] is due mainly to intrinsic effects, although effects associated with changes in the arrangement of water molecules around the methyl group might also be taken into consideration.[35,37-39] Unfortunately, the lack of data on the intrinsic volume of a methyl group bound to a charged nitrogen atom does not enable us to estimate the difference in volume of water molecules in the neighborhood of a methyl group, according to whether the nitrogen is charged or not.

*Comparison between Cyclic Monofunctional and Cyclic Bifunctional Amines.* The data in Table IV show that the introduction of a second polar group in a cyclic amine causes an increase in $\Delta V_1^\circ$. The greater the decrease in basicity caused by the presence of the hydrophilic group, the larger the increase in $\Delta V_1^\circ$ (cf. $pK_1$ and $\Delta V_1^\circ$, in the series piperidine → piperazine → morpholine and 1-methylpiperidine → 1-methylpiperazine → 4-methylmorpholine). $\Delta H_1^\circ$ shows a regular decrease which parallels the increase in $\Delta V_1^\circ$. However, $\Delta S_1^\circ$ is almost independent of the nature of the second group introduced.

Some indirect evidence for the larger value of $\Delta V_1^\circ$ in bifunctional amines, when compared with monofunctional

TABLE V: Differences, $\delta \bar{V}_2°$, of Limiting Partial Molar Volumes for Pairs of Molecules Differing in One Heteroatom[a]

| Process | X | $\delta \bar{V}_2°$, mL mol$^{-1}$ |
|---|---|---|
|  | $CH_2$ | 0.4 |
| | O | 1.6 |
| | NH | 1.0 |
| | $NCH_3$ | 1.0 |
| | $NH_2^+$ | 2.1 |
|  | $CH_2$ | 18.8 |
| | O | 20.3 |
| | NH | 19.7 |
| | $NCH_3$ | 19.7 |
| | $NHCH_3^+$ | 20.9 |
|  | $CH_2$ | 18.4 |
| | O | 18.7 |
| | NH | 18.8 |
| | $NCH_3$ | 18.7 |

[a] $\bar{V}_2°$ values for tetrahydropyran, piperidine, 1-methylpiperidine, and 1,4-dioxane have been taken from ref 14.

amines, can be obtained by considering the volume change, $\delta \bar{V}_2°$, for the hypothetical process of the type:

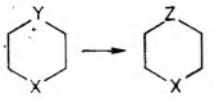 (9)

in which the Y group, e.g., ethereal O, is substituted by a Z group, e.g., NH; the X group in position 4 being $CH_2$, O, NH, $NCH_3$, $NH_2^+$, or $NHCH_3^+$. $\delta \bar{V}_2°$ is the formal difference of the contributions of Z and Y to $\bar{V}_2°$, and the changes in $\delta \bar{V}_2°$ on varying group X may be attributed to the different interactions between the groups in positions 1 and 4.

In Table V are reported values of $\delta \bar{V}_2°$ for process 9 cited above. The substitution of an ethereal oxygen by a nitrogen center causes a greater change in $\delta \bar{V}_2°$ in bifunctional compounds than in monofunctional compounds (X = $CH_2$). This confirms earlier observations, based on other thermodynamic properties[11,13] of neutral and charged species, that there are interactions between the polar centers in positions 1 and 4. These interactions produce a smaller effect on volumetric changes in the neutral molecule than in the charged species.

In order to confirm that the 1,4 interaction is responsible for the volume change, a comparison can be made between the experimental partial molar volume, $\bar{V}_2°$, for the cyclic bifunctional amine with the values, $\bar{V}_2*$, calculated from the following equation:

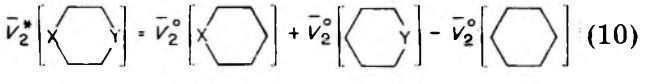 (10)

for which it is necessary to have a value for $\bar{V}_2°$ of cyclohexane and for the cyclic hexatomic monofunctional molecules. The values for $\bar{V}_2*$ obtained from eq 10 are partial molar volumes of bifunctional molecules, in which it is hypothesized that there are no interactions between polar groups X and Y.

From the data in Table VI, it is obvious that the experimental partial molar volumes differ, in all cases, from the partial molar volumes calculated using the hypothesis based on group additivity (eq 10). The experimental $\bar{V}_2°$ values for the neutral molecules is larger than the calculated $\bar{V}_2^*$ values, whereas the contrary holds true for the cation acids. This implies that the increase in $\Delta V_1°$ for proton ionization in bifunctional molecules, with respect

TABLE VI: Comparison between $\bar{V}_2°$ and $\bar{V}_2*$ Values of Bifunctional Cyclic Amines and Their Mono- and Dihydrochlorides in Water at 25 °C

| Substance | $\bar{V}_2°$, mL mol$^{-1}$ | $\bar{V}_2*$[a], mL mol$^{-1}$ | $\bar{V}_2° - \bar{V}_2*$, mL mol$^{-1}$ |
|---|---|---|---|
| 1,4-Dioxane | 80.96 | 81.0 | 0.0 |
| Morpholine | 82.56 | 81.4 | 1.2 |
| Morpholine·HCl | 92.99 | 96.0 | −3.0 |
| 4-Methylmorpholine | 101.28 | 99.8 | 1.5 |
| 4-Methylmorpholine·HCl | 111.71 | 114.7 | −3.0 |
| Piperazine | 83.53 | 81.8 | 1.8 |
| Piperazine·HCl | 95.12 | 96.4 | −1.3 |
| Piperazine·2HCl | 99.26 | 111.1 | −11.8 |
| 1-Methylpiperazine | 102.30 | 100.2 | 2.1 |
| 1-Methylpiperazine·HCl | 113.97 | 114.8 | −0.9 |
| 1-Methylpiperazine·2HCl | 117.48 | 129.8 | −12.3 |
| 1,4-Dimethylpiperazine | 121.00 | 118.6 | 2.4 |
| 1,4-Dimethylpiperazine·HCl | 132.61 | 133.5 | −0.9 |
| 1,4-Dimethylpiperazine·2HCl | 135.76 | 148.5 | −12.7 |

[a] Values obtained using eq 10. Cyclohexane has been assigned a $\bar{V}_2°$ value of 102.5 mL mol$^{-1}$ obtained as an average of (a) 103.1 mL mol$^{-1}$, estimated from group contributions reported by Høiland (ref 40) and from $\bar{V}_2°$ (cyclohexanol) = 103.54 mL mol$^{-1}$ (ref 20), and (b) a value of 101.8 mL mol$^{-1}$, estimated from $\bar{V}_2°$ (1,4-cyclohexanediol) = 105.3 mL mol$^{-1}$ (ref 41) and $\bar{V}_2°$ (cyclohexanol). The $\bar{V}_2°$ values for tetrahydropyran, 1,4-dioxane, piperidine, and 1-methylpiperidine have been taken from ref 14 and those of piperidine·HCl and 1-methylpiperidine·HCl from ref 29.

to monofunctional molecules, is due to the interaction between the centers in 1,4 positions, in both the neutral molecule and the cation acid. It is not possible, however, to establish without a doubt if the deviations from the additivity rule, caused by the interaction between the polar centers, is greater in the neutral molecule or the cation acid. For example, $\bar{V}_2° - \bar{V}_2*$ for morpholine is less than that for its corresponding hydrochloride, whereas for 1,4-dimethylpiperazine and its monohydrochloride the opposite is true. This uncertainty may be attributed to the ambiguity in the estimated value of $\bar{V}_2°$ for cyclohexane.

Notwithstanding this uncertainty, the large deviations from the additivity rule for the dications ($\bar{V}_2° - \bar{V}_2* \simeq -12$ mL mol$^{-1}$) indicate that it is the strong interactions between the positively charged nitrogen centers which lead to the unusually high $\Delta V_2°$ values for the proton ionization process represented by eq 8. The values of $\Delta V_2°$ will be discussed in greater detail in the following article.

*Acknowledgment.* This work has been supported through financial assistance from the Consiglio Nazionale delle Ricerche (C.N.R.).

## References and Notes

(1) Present address: Department of Chemistry, University of Calgary, Calgary, Alberta, Canada.
(2) W. Kauzmann, A. Bodanszky, and J. Rasper, *J. Am. Chem. Soc.*, **84**, 1777 (1962).
(3) L. G. Hepler, *J. Phys. Chem.*, **69**, 965 (1965).
(4) B. E. Conway, R. E. Verrall, and J. E. Desnoyers, *Z. Phys. Chem.*, **230**, 157 (1965).
(5) R. E. Verrall and B. E. Conway, *J. Phys. Chem.*, **70**, 3961 (1966).
(6) B. E. Conway and L. H. Laliberté, "Hydrogen Bonded Solvent Systems", A. K. Covington and P. Jones, Ed., Taylor and Francis, London, 1968, p 139.
(7) E. J. King, *J. Phys. Chem.*, **73**, 1220 (1969).
(8) F. J. Millero, *Chem. Rev.*, **71**, 147 (1971).
(9) J. W. Larson and L. G. Hepler, "Solute-Solvent Interactions", J. P. Coetzee and C. D. Ritchie, Ed., Marcel-Dekker, New York, N.Y., 1969.
(10) L. G. Hepler and E. M. Wooley, "Water: A Comprehensive Treatise", Vol. III, F. Franks, Ed., Plenum Press, New York, N.Y., 1973.
(11) S. Cabani, G. Conti, D. Giannessi, and L. Lepori, *J. Chem. Soc.*,

*Faraday Trans. 1*, **71**, 1154 (1975).
(12) S. Cabani, G. Conti, P. Gianni, and E. Matteoli, *Gazzetta*, **106**, 541 (1976).
(13) S. Cabani, G. Conti, and E. Matteoli, *J. Solution Chem.*, **5**, 125 (1976).
(14) S. Cabani, G. Conti, and L. Lepori, *J. Phys. Chem.*, **76**, 1338 (1972).
(15) (a) $\alpha$'s for processes a, b, and c are defined by the following relation: $\alpha = [-K + (K + 4Kc^0)^{1/2}]/2c^0$, where $K$ and $c^0$ are the dissociation constant and the initial concentration of B, $BH^+$, or $BH_2^{2+}$, respectively, in processes a, b, or c. (b) The value of $\alpha$ for process d is calculated from: $\alpha = 2(K_1/K_2)^{1/2}/[1 + 2(K_1/K_2)^{1/2}]$, where $K_1$ and $K_2$ are the dissociation constants for proton ionization processes b and c. In deriving $\alpha$, processes b and c for the products of disproportionation have been assumed to be negligible. This is a valid assumption for the solutions of the monohydrochlorides of the diamines here examined, because the difference between $c_B$ and $c_{BH_2^{2+}}$ does not exceed 1 ppm. The p$K$ for process d is related to p$K_1$ and p$K_2$ by p$K$ = $^1/_2$(p$K_1$ − p$K_2$).
(16) O. Redlich and D. M. Meyer, *Chem. Rev.*, **64**, 221 (1964).
(17) L. H. Laliberté and B. E. Conway, *J. Phys. Chem.*, **74**, 4116 (1970).
(18) O. Kiyohara, G. Perron, and J. E. Desnoyers, *Can. J. Chem.*, **53**, 2591 (1975).
(19) W. Y. Wen, N. Takeguchi, and D. P. Wilson, *J. Solution Chem.*, **3**, 103 (1974).
(20) S. Cabani, G. Conti, and L. Lepori, *J. Phys. Chem.*, **78**, 1030 (1974).
(21) M. V. Kaulgud and R. J. Patil, *J. Phys. Chem.*, **80**, 138 (1976).
(22) H. B. Hetzer, R. A. Robinson, and R. G. Bates, *J. Phys. Chem.*, **72**, 2081 (1968).
(23) M. J. Blais, O. Enea, and G. Berthon, *Thermochim. Acta*, **12**, 25 (1975).
(24) H. K. Hall, *J. Am. Chem. Soc.*, **80**, 63 (1958).
(25) G. Berthon, O. Enea, and K. Houngbossa, *Thermochim. Acta*, **9**, 379 (1974).
(26) F. M. Jones and E. M. Arnett, "Progress in Physical Organic Chemistry", Vol. II, A. Streitwieser and R. W. Taft, Ed., Wiley, New York, N.Y., 1974.
(27) J. W. Larson, G. L. Bertrand, and L. G. Hepler, *J. Chem. Eng. Data*, **11**, 595 (1966).
(28) S. Cabani, G. Conti, and L. Lepori, *Trans. Faraday Soc.*, **67**, 1933 (1971).
(29) S. Cabani, G. Conti, L. Lepori, and G. Leva, *J. Phys. Chem.*, **76**, 1343 (1972).
(30) D. H. Everett and W. F. K. Wynne-Jones, *Proc. R. Soc. London, Ser. A*, **177**, 499 (1940).
(31) A. F. Trotman-Dickenson, *J. Chem. Soc.*, 1293 (1949).
(32) J. T. Edward, *J. Chem. Educ.*, **47**, 261 (1970).
(33) The volume difference, 4.4 mL mol$^{-1}$, between a hydrogen atom bound to a neutral nitrogen atom, $\bar{V}_2°(H_N)$, and one bound to a charged nitrogen center, $\bar{V}_2°(H_N^+)$, has been evaluated by: $\bar{V}_2°(H_N) - \bar{V}_2°(H_N^+) = {}^1/_3[\bar{V}_2°(NH_3) - V(N)] - {}^1/_4[\bar{V}_2°(NH_4^+) - V(N^+)]$, where $\bar{V}_2°(NH_3)$ = 24.85 mL mol$^{-1}$ (ref 20) and $\bar{V}_2°(NH_4^+)$ = 12.46 mL mol$^{-1}$. The partial molar volume of the ammonium ion was obtained by adding the conventional partial molar volume of the $NH_4^+$ ion reported by Millero[8] and the value of $\bar{V}_2°(H^+)$ = −5.4 mL mol$^{-1}$ reported by R. Zana and E. Yeager (*J. Phys. Chem.*, **71**, 521 (1967)). The intrinsic volumes of a neutral nitrogen atom, $V(N)$ = 4.3 mL mol$^{-1}$, and a charged nitrogen center, $V(N^+)$ = 2.8 mL mol$^{-1}$, were taken from Edward.[32] If the above volume difference, 4.4 mL mol$^{-1}$, which includes intrinsic and solvent contributions, is combined with the intrinsic volumes of a hydrogen atom on N, $V(H_N)$ = 3.1 mL mol$^{-1}$, and on $N^+$, $V(H_N^+)$ = 1.4 mL mol$^{-1}$, a volume decrease of 2.7 mL mol$^{-1}$ is evaluated for the change bulk water → water bound to a >$NH^+$ group.
(34) The value of 4.5 mL mol$^{-1}$ for the volume difference of a methyl group bound to a neutral nitrogen atom, $\bar{V}_2°(Me_N)$, and one bound to a charged nitrogen center, $\bar{V}_2°(Me_N^+)$, has been calculated by: $\bar{V}_2°(Me_N) - \bar{V}_2°(Me_N^+) = {}^1/_3[\bar{V}_2°(NMe_3) - V(N)] - {}^1/_4[\bar{V}_2°(NMe_4^+) - V(N^+)]$, where $\bar{V}_2°(NMe_3)$ = 78.8 mL mol$^{-1}$ (ref 20) and $\bar{V}_2°(NMe_4^+)$ = 84.3 mL mol$^{-1}$ (ref 35). The $V(N)$ and $V(N^+)$ values are reported in ref 33. The value of the difference $\bar{V}_2°(Me_N) - \bar{V}_2°(Me_N^+)$ is practically identical with the value of 4.3 mL mol$^{-1}$ for the difference $\bar{V}_2°(Me_C) - \bar{V}_2°(Me_N^+)$, calculated from the limiting partial molar volumes of neopentane, $\bar{V}_2°(CMe_4)$ = 102 mL mol$^{-1}$ (ref 36), and of the $NMe_4^+$ ion, as well as from the intrinsic volumes of a carbon atom, $V(C)$ = 3.4 mL mol$^{-1}$, and of a charged nitrogen center:[32] $\bar{V}_2°(Me_C) - \bar{V}_2°(Me_N^+) = {}^1/_4[\bar{V}°(CMe_4) - V(C)] - {}^1/_4[\bar{V}_2°(NMe_4^+) - V(N^+)]$.
(35) R. Zana and E. Yeager, *J. Phys. Chem.*, **71**, 4241 (1967).
(36) Value estimated on the basis of $\bar{V}_2°$ determined by C. Jolicoeur and G. Lacroix (*Can. J. Chem.*, **54**, 624, (1976)) for pentaerythritol (101.81 mL mol$^{-1}$), 1,1,1-trihydroxymethylethane (102.3 mL mol$^{-1}$), 2,2-dimethyl-1,3-propanediol (102.34 mL mol$^{-1}$), and neopentanol (101.87 mL mol$^{-1}$).
(37) W. Y. Wen and S. Saito, *J. Phys. Chem.*, **68**, 2639 (1964).
(38) F. J. Millero and W. Drost-Hansen, *J. Phys. Chem.*, **72**, 1758 (1968).
(39) B. E. Conway, R. E. Verrall, and J. E. Desnoyers, *Trans. Faraday Soc.*, **62**, 2738 (1966).
(40) H. Høiland and E. Vikingstad, *Acta Chem. Scand., Ser. A*, **30**, 182 (1976).
(41) S. Cabani, L. Lepori, and E. Matteoli, *Chim. Ind. (Milano)*, **58**, 221 (1976).

# Volume Changes in the Proton Ionization of Amines in Water. 2. Amino Alcohols, Amino Ethers, and Diamines

**S. Cabani,* V. Mollica,**

*Istituto di Chimica Fisica, Università di Pisa, Via Risorgimento 35, 56100 Pisa, Italy*

**L. Lepori, and S. T. Lobo[1]**

*Laboratorio di Chimica Quantistica ed Energetica Molecolare del C.N.R., Via Risorgimento 35, 56100 Pisa, Italy* *(Received November 19, 1976)*

*Publication costs assisted by Consiglio Nazionale delle Ricerche, Rome*

From density measurements (25 °C) of aqueous solutions at various concentrations of solute, apparent molar volumes of some open-chain bifunctional amines, with the amine group being primary, secondary, and tertiary, have been determined. The compounds studied were 2-aminoethanol, 3-amino-1-propanol, 2-methoxyethylamine, 3-methoxy-1-propylamine, ethylenediamine, 1,3-diaminopropane, 2-(methylamino)ethanol, 2-(ethylamino)ethanol, 2-(dimethylamino)ethanol, 2-(diethylamino)ethanol, and their mono- and dihydrochlorides. $\Delta V_1°$ and $\Delta V_2°$ for the first and second steps of proton ionization have been calculated from the limiting partial molar volumes. $\Delta V_1°$ values of the above bifunctional amines are compared with the corresponding values for monofunctional amines. The difference in $\Delta V_1°$ caused by the introduction of the second hydrophilic center is discussed. The volumes and entropies of ionization of the amines and carboxylic acids are compared and the deviations of these functions from predictions based on simple electrostatic theories are considered.

## Introduction

The earlier work[2] on the volumes of ionization of cyclic bifunctional amines is here extended to some selected open-chain bifunctional amines. The compounds (2-aminoethanol, 3-amino-1-propanol, 2-methoxyethylamine, 3-methoxy-1-propylamine, ethylenediamine, 1,3-diaminopropane, 2-(methylamino)ethanol, 2-(ethylamino)ethanol, 2-(dimethylamino)ethanol, 2-(diethylamino)ethanol) have been chosen with a view to varying the amine from primary to secondary to tertiary, and to

specifically examine the influence of an oxygen ether, alcohol, and amine function on the volumetric properties of amines and their corresponding hydrochlorides.

While values for thermodynamic parameters of ionization, $\Delta G°$, $\Delta H°$, and $\Delta S°$, have been reported[3] for the above compounds, there are no corresponding $\Delta V°$ data, except for ethylenediamine.[4,5] In effect, $\Delta V°$ values are available only for ammonia,[6-8] open-chain aliphatic amines,[4-9] and alicyclic amines.[6,10] This enables the examination of $\Delta V°$ as a function of the number of hydrogen atoms attached to the nitrogen atom in monofunctional amines. The bifunctional compounds studied here now provide a more general picture of the ionization process. In addition, the volumetric behavior of the diamines, compared with that of the dicarboxylic acids, studied recently by Høiland,[11] enables us to examine the effect of the nature of the charged center and the separation of two charged centers on the volume of ionization.

## Experimental Section

*Materials.* 2-Aminoethanol, 3-amino-1-propanol, 2-methoxyethylamine, 3-methoxy-1-propylamine, ethylenediamine, 1,3-diaminopropane, 2-(methylamino)ethanol, 2-(ethylamino)ethanol, 2-(dimethylamino)ethanol, and 2-(diethylamino)ethanol were all of the purest grade (>99% purity) available commercially. The amino alcohols were distilled from calcium hydride and the amino ethers from metallic sodium, after refluxing for 48 h. Ethylenediamine was refluxed over potassium hydroxide pellets and the middle fraction obtained was redistilled. In all cases, the middle fraction was retained after checking the purity of the compounds, by GLC, to be better than 99.5%. 1,3-Diaminopropane was used without further purification. Stock solutions of the mono- and dihydrochlorides of the purified amines were prepared by the addition of the amine to a standard HCl solution. Deionized water was used in all experiments.

*Apparatus and Measurements.* Densities of the aqueous solutions of the amines and their salts were measured by a hydrostatic differential balance, which has been described earlier.[12] The observed apparent molar volume, $\Phi_v^{obsd}$, was calculated by

$$\Phi_v^{obsd} = \frac{M}{d^0} - \left(\frac{d}{d^0} - 1\right)\frac{1000}{c} \quad (1)$$

where $M$ is the formula weight of the solute and $d$ and $d^0$ are the densities of solution and water, respectively. The $\Phi_v^{obsd}$ values of the amines were corrected for hydrolysis, those of the dihydrochlorides for ionization, and those of the diamine monohydrochlorides for disproportionation following the procedure described earlier.[2] No correction was found necessary for the hydrochloride of monoamines studied here.

## Results

Table I shows the limiting partial molar volumes, $\bar{V}_2°$, and the slope, $h$, of the straight line that represents the concentration dependence of $\Phi_v$, which according to Redlich and Meyer[13] is

$$\Phi_v - S_v c^{1/2} = \bar{V}_2° + hc \quad (2)$$

$S_v$ is the theoretical limiting slope and is 0 for amines, 1.868 mL $L^{1/2}$ $mol^{-3/2}$ for monohydrochlorides, and 9.706 mL $L^{1/2}$ $mol^{-3/2}$ for dihydrochlorides at 25 °C. The values of $\Phi_v$, at concentrations $c$ of solute, have been obtained from $\Phi_v^{obsd}$ (eq 1) after the correction procedure described earlier[2] has been applied.

Of the substances examined here, $\bar{V}_2°$ values have been reported only for 2-aminoethanol,[14] ethylenediamine,[5,15] and for ethylenediamine and 1,3-diaminopropane dihydrochlorides.[16] These values are in good agreement with values determined by us.

From $\bar{V}_2°$ values reported in Table I, volume changes $\Delta V_1° = \bar{V}_2°(B) + \bar{V}_2°(HCl) - \bar{V}_2°(B·HCl)$ and $\Delta V_2° = \bar{V}_2°(B·HCl) + \bar{V}_2°(HCl) - \bar{V}_2°(B·2HCl)$ have been calculated for the following processes:

$$BH^+ \rightleftarrows B + H^+ \quad (3)$$

$$BH_2^{2+} \rightleftarrows BH^+ + H^+ \quad (4)$$

The value of $\bar{V}_2°$ assumed for HCl is 17.83 mL $mol^{-1}$.[17] The results obtained are reported in Tables II and III, in which are also reported data for some other amines[2,4-10,23] and the results of Høiland on monocarboxylic[18] and dicarboxylic acids.[11] $\Delta V_1°$, in the case of carboxylic acids, represents the volume change in the proton ionization for monocarboxylic acids:

$$AH \rightleftarrows A^- + H^+ \quad (5)$$

or in the first step of proton ionization for dicarboxylic acids:

$$AH_2 \rightleftarrows AH^- + H^+ \quad (6)$$

and $\Delta V_2°$ is the volume change for the second proton ionization of dicarboxylic acids:

$$AH^- \rightleftarrows A^{2-} + H^+ \quad (7)$$

Tables II and III also report values for p$K$, $\Delta H°$, and $\Delta S°$ for the above-mentioned processes (eq 3-7).

With the exception of $\Delta V_1°$ and $\Delta V_2°$ for ethylenediamine by Lawrence and Conway[5] and Kauzmann et al.,[4] there are no other data available for comparison with the compounds studied by us. The agreement of our data with the results of Lawrence and Conway is good, but the values differ considerably from those of Kauzmann et al., who used a dilatometric method.

## Discussion

It is apparent from the results reported in Tables II and III that $\Delta V_1°$ and $\Delta V_2°$ for amines vary systematically with the number and nature of the groups attached to the nitrogen atom, thus enabling a correlation of structure with volume of ionization. In particular, regular trends are observed in proton ionization volumes, either when the hydrocarbon chains are lengthened or when further hydrophilic centers are introduced in monofunctional compounds. These salient features will be examined in detail by considering carboxylic acids in conjunction with amines. In this context, the difference in sign for $\Delta V_1°$ and $\Delta V_2°$ of amines and carboxylic acids calls for a comment. Processes 3 and 4, which represent the ionization of amines, involve no change in the number of ions, whereas in processes 5, 6, and 7, corresponding to the ionization of carboxylic acids, there is an increase in the number of charged species, which produces an electrostrictive contraction in volume. However, the major point of interest is neither the sign nor the magnitude of $\Delta V°$, but the manner in which a change in structure, such as chain lengthening or substituent effects, influences $\Delta V°$ of amines and carboxylic acids.

When reporting $\Delta V°$ values for amines many authors[4,6,8,26,27] prefer to consider $\Delta V°$ for the process

$$B + H_2O \rightleftarrows BH^+ + OH^- \quad (8)$$

instead of process 3. However, in order to conform with the usual reporting of thermodynamic functions $\Delta G°$, $\Delta H°$, $\Delta S°$, and $\Delta C_p°$ for amine ionization in the literature,[3] it is more appropriate to report $\Delta V°$ values for processes 3 and 4.

TABLE I: Apparent Molar Volumes, $\Phi_v = \bar{V}_2^\circ + S_v c^{1/2} + hc$, of Bifunctional Aliphatic Amines and Their Hydrochlorides Salts in Water at 25 °C[a]

| Substance | No. of expt | Concn range, M | $\bar{V}_2^\circ$, mL mol$^{-1}$ | $h$, mL L mol$^{-2}$ |
|---|---|---|---|---|
| 2-Aminoethanol | 17 | 0.03–0.69 | 59.25 ± 0.02 | −0.03 ± 0.06 |
| | | | 58.8[b] | |
| 3-Amino-1-propanol | 12 | 0.03–0.47 | 75.21 ± 0.04 | −0.16 ± 0.11 |
| 2-Methoxyethylamine | 9 | 0.04–0.48 | 79.59 ± 0.03 | −0.23 ± 0.10 |
| 3-Methoxy-1-propylamine | 19 | 0.02–0.51 | 95.55 ± 0.04 | −0.59 ± 0.15 |
| Ethylenediamine | 22 | 0.02–0.61 | 62.88 ± 0.03 | −0.13 ± 0.07 |
| | | | 63.1 ± 0.4[c] | |
| | | | 62.1[d] | |
| 1,3-Diaminopropane | 18 | 0.03–0.55 | 78.83 ± 0.03 | −0.49 ± 0.12 |
| 2-(Methylamino)ethanol | 12 | 0.04–0.56 | 77.07 ± 0.02 | −0.59 ± 0.05 |
| 2-(Ethylamino)ethanol | 11 | 0.04–0.52 | 92.91 ± 0.02 | −1.08 ± 0.07 |
| 2-(Dimethylamino)ethanol | 14 | 0.03–0.52 | 94.17 ± 0.03 | −1.10 ± 0.08 |
| 2-(Diethylamino)ethanol | 16 | 0.03–0.55 | 123.04 ± 0.03 | −1.88 ± 0.08 |
| 2-Aminoethanol hydrochloride | 18 | 0.01–0.54 | 70.90 ± 0.05 | −0.32 ± 0.16 |
| 3-Amino-1-propanol hydrochloride | 14 | 0.01–0.41 | 87.40 ± 0.05 | −0.38 ± 0.22 |
| 2-Methoxyethylamine hydrochloride | 13 | 0.02–0.47 | 91.50 ± 0.04 | −0.69 ± 0.16 |
| 3-Methoxy-1-propylamine hydrochloride | 15 | 0.02–0.50 | 107.89 ± 0.03 | −1.07 ± 0.12 |
| Ethylenediamine hydrochloride | 13 | 0.02–0.55 | 74.05 ± 0.05 | +0.30 ± 0.17 |
| 1,3-Diaminopropane hydrochloride | 12 | 0.02–0.54 | 91.09 ± 0.07 | +0.16 ± 0.28 |
| 2-(Methylamino)ethanol hydrochloride | 14 | 0.02–0.43 | 89.49 ± 0.05 | −0.38 ± 0.17 |
| 2-(Ethylamino)ethanol hydrochloride | 13 | 0.02–0.49 | 106.03 ± 0.04 | −1.05 ± 0.16 |
| 2-(Dimethylamino)ethanol hydrochloride | 18 | 0.02–0.46 | 106.97 ± 0.04 | −0.86 ± 0.15 |
| 2-(Diethylamino)ethanol hydrochloride | 12 | 0.02–0.40 | 137.96 ± 0.04 | −2.12 ± 0.17 |
| Ethylenediamine dihydrochloride | 18 | 0.01–0.43[e] | 79.77 ± 0.08 | −5.02 ± 0.62 |
| | | | 80.10[f] | −5.5 |
| | | | 81.04[g] | |
| 1,3-Diaminopropane dihydrochloride | 15 | 0.02–0.41[h] | 98.88 ± 0.09 | −5.70 ± 1.00 |
| | | | 99.58[f] | −5.1 |

[a] $S_v$ is the theoretical limiting slope taken from Redlich and Meyer (ref 13); $S_v = 0$ for amines, 1.868 for monohydrochlorides, and 9.706 mL L$^{1/2}$ mol$^{-3/2}$ for dihydrochlorides. The reported uncertainties are standard deviations. [b] At 20 °C, ref 14. [c] Reference 5. [d] Reference 15. [e] The plot of $(\Phi_v - 9.706c^{1/2})$ vs. $c$ has been found a straight line up to $c$ = 0.25 M. [f] Reference 16. [g] Calculated using the value of 94.8 mL L$^{-1}$ for $\bar{V}_2^\circ$ of ethylenediamine·2HBr (ref 5) and $\bar{V}_2^\circ(Br^-) - \bar{V}_2^\circ(Cl^-) = 6.88$ (ref 17). [h] The plot of $(\Phi_v - 9.706c^{1/2})$ vs. $c$ has been found a straight line up to $c$ = 0.15 M.

*$\Delta V_1^\circ$ for Amines and Carboxylic Acids.* Table II shows that the $\Delta V_1^\circ$ values for compounds with a low number of carbon atoms always decrease as the hydrocarbon chain is lengthened. Moreover, the $\Delta V_1^\circ$ values of polyfunctional compounds are always larger than those for the monofunctional compounds, the latter corresponding to bifunctional compounds in which the hydrophilic center is replaced by hydrogen atoms.

In order to give an interpretation of these features, we have adopted the following criteria: (a) for an understanding of $\Delta V_1^\circ$ changes with chain lengthening, the methylene contribution to the limiting partial molar volume, $\bar{V}_2^\circ(CH_2)$, in a homologous series of neutral or charged compounds has been taken into account; (b) for an explanation of the effects of the introduction of a second hydrophilic group, we have considered the differences between the experimental, $\bar{V}_2^\circ$, and calculated, $\bar{V}_2^*$, limiting partial molar volumes of compounds of the type X-$(CH_2)_n$-Y. The $\bar{V}_2^*$ values have been calculated from

$$\bar{V}_2^*[X\text{-}(CH_2)_n\text{-}Y] = \bar{V}_2^\circ[X\text{-}(CH_2)_n\text{-}H] + \bar{V}_2^\circ[H\text{-}(CH_2)_n\text{-}Y] - \bar{V}_2^\circ[H\text{-}(CH_2)_n\text{-}H] \quad (9)$$

These quantities are the limiting partial molar volumes of hypothetical bifunctional molecules, which are free of interactions between the hydrophilic centers X and Y.

In Table IV are reported the values of the methylene contribution, $\bar{V}_2^\circ(CH_2)$, for some species of the type X-$(CH_2)_n$-Y, where X, Y = H, COOH, $COO^-$, $NH_2$, $NH_3^+$, etc., and $n$ is the number of methylene groups. Some interesting facts emerge from these results. In neutral compounds (e.g., $n$-alkylamines and carboxylic acids), $\bar{V}_2^\circ(CH_2)$, after an initial decrease, attains a constant value ($\simeq$16 mL mol$^{-1}$) for $n = 2$, which indicates that the influence of the hydrophilic center (X) on the hydration sphere of the hydrocarbon chain is felt up to the carbon atom in the $\beta$ position with respect to X. Also, in accordance with Sakurai et al.,[16] when the group X is $NH_3^+$, $\bar{V}_2^\circ(CH_2)$ diminishes with an increase in $n$; when, however, X is $COO^-$, $\bar{V}_2^\circ(CH_2)$ increases with increasing $n$. In both cases, constant values of $\bar{V}_2^\circ(CH_2)$ are reached for $n > 3$. Thus, irrespective of the type of group, the effect of the charged group is propagated up to the $\gamma$ carbon atom.

The $\Delta V_1^\circ$ trends in homologous series of amines and carboxylic acids can thus be attributed to effects, different both in magnitude and direction, that either neutral or charged centers exert on the hydration sphere of the hydrocarbon chain near them. For instance, the large decrease of $\Delta V_1^\circ$ in the series formic acid → acetic acid → propionic acid (see Table II) can be accounted for by the opposite trend that $\bar{V}_2^\circ(CH_2)$ contributions of the neutral and anionic forms, respectively, show in going from $n = 1$ to $n = 3$. On the contrary, in the case of primary monoamines the limiting value $\bar{V}_2^\circ(CH_2) = 16$ mL mol$^{-1}$ is reached for both the neutral and acid species with the same trend. As a consequence, the differences between $\Delta V_1^\circ$ of ammonia and primary amines with a large number of carbon atoms are much less than the differences found between the $\Delta V_1^\circ$ values of formic acid and carboxylic acids with a large number of carbon atoms.

The mechanism for the opposed change in volume around the hydrocarbon moiety adjacent to the charged

TABLE II: Thermodynamic Parameters for Ionization of Selected Amines and Carboxylic Acids in Water at 25 °C[a]

| Substance | $\Delta V_1°$, mL mol$^{-1}$ | p$K_1$ | $\Delta H_1°$, kcal mol$^{-1}$ | $\Delta S_1°$, cal mol$^{-1}$ deg$^{-1}$ |
|---|---|---|---|---|
| **Primary Amines** | | | | |
| Ammonia | 6.4[b] | 9.24 | 12.48 | −0.4 |
| Methylamine | 5.6[c] | 10.65 | 13.18 | −4.5 |
| Ethylamine | 5.4[d] | 10.68 | 13.71 | −2.9 |
| *n*-Propylamine | 4.7[e] | 10.57 | 13.84 | −1.9 |
| *n*-Butylamine | 4.3 | 10.64 | 13.98 | −1.8 |
| *n*-Pentylamine | 4.3 | 10.63 | 13.98 | −1.8 |
| *n*-Hexylamine | 4.3 | 10.64 | | |
| *n*-Heptylamine | 4.4 | 10.66 | | |
| 2-Aminoethanol | 6.2 | 9.49 | 12.08 | −2.9 |
| 3-Amino-1-propanol | 5.6 | 9.96 | 12.70 | −3.0 |
| 2-Methoxyethylamine | 5.9 | 9.39 | 12.08 | −2.5 |
| 3-Methoxy-1-propylamine | 5.5 | 10.01 | 12.84 | −2.7 |
| Ethylenediamine | 6.7[f] | 9.93 | 11.94 | −5.4 |
| 1,3-Diaminopropane | 5.6 | 10.47 | 13.19 | −3.7 |
| **Secondary Amines** | | | | |
| Dimethylamine | 5.1[g] | 10.78 | 12.04 | −8.9 |
| Diethylamine | 2.8[h] | 11.02 | 12.73 | −7.7 |
| Di-*n*-propylamine | 2.2 | 11.00 | 13.17 | −6.2 |
| Di-*n*-butylamine | 2.5 | 11.25 | 13.66 | −5.7 |
| 2-(Methylamino)ethanol | 5.4 | 9.88 | 11.06 | −8.1 |
| 2-(Ethylamino)ethanol | 4.7 | 9.96 | 11.40 | −7.4 |
| Piperidine | 3.2 | 11.12 | 12.76 | −8.1 |
| Morpholine | 7.4 | 8.49 | 9.33 | −7.6 |
| Piperazine | 6.2 | 9.73 | 10.25 | −10.1 |
| **Tertiary Amines** | | | | |
| Trimethylamine | 6.0[i] | 9.80 | 8.82 | −15.3 |
| Diethylmethylamine | 1.8 | | | |
| Triethylamine | 0.1[j] | 10.72 | 10.32 | −14.4 |
| 2-(Dimethylamino)ethanol | 5.0 | 9.26 | 8.74 | −13.1 |
| 2-(Diethylamino)ethanol | 2.9 | 9.81 | 9.66 | −12.5 |
| Triethanolamine | 4.0[k] | 7.76 | 8.16 | −8.2 |
| *N,N,N',N'*-Tetraethanol ethylenediamine | −0.2[l] | | | |
| 1-Methylpiperidine | 2.9 | 10.08 | 9.44 | −14.4 |
| 4-Methylmorpholine | 7.4 | 7.73 | 6.56 | −13.6 |
| 1,4-Dimethylpiperazine | 6.2 | 8.23 | 6.66 | −15.4 |
| Triethylenediamine | 6.8[m] | 8.82 | 7.21 | −16.2 |
| **Monocarboxylic Acids** | | | | |
| Formic acid | −8.4 | 3.75 | −0.08 | −17.4 |
| Acetic acid | −11.3 | 4.76 | −0.02 | −21.9 |
| Propionic acid | −13.3 | 4.88 | −0.14 | −22.8 |
| *n*-Butanoic acid | −13.9 | 4.82 | −0.64 | −24.2 |
| *n*-Pentanoic acid | −14.2 | | | |
| *n*-Hexanoic acid | −14.2 | | | |
| **Dicarboxylic Acids** | | | | |
| Oxalic acid | −6.7 | 1.27 | −1.02 | −9.2 |
| Malonic acid | −10.1 | 2.85 | 0.02 | −13.0 |
| Succinic acid | −12.9 | 4.21 | 0.76 | −16.7 |
| Glutaric acid | −13.2 | 4.34 | −0.12 | −20.3 |
| Adipic acid | −13.5 | 4.41 | −0.30 | −21.5 |
| Pimelic acid | −14.1 | 4.49 | −0.30 | −21.6 |

[a] The reported quantities refer to the following processes of protonic ionization: $BH^+ \rightleftarrows B + H^+$ (amines), $AH \rightleftarrows A^- + H^+$ (monocarboxylic acids), $AH_2 \rightleftarrows AH^- + H^+$ (dicarboxylic acids). The $\Delta V_1°$ values for amines are our data (this work and refs 2, 7, 10); the values for monocarboxylic acids were taken from ref 18, for dicarboxylic acids from ref 11. The p$K_1$, $\Delta H_1°$, and $\Delta S_1°$ values were taken: for amines from ref 3c, except for 2-methoxyethylamine and 3-methoxy-1-propylamine (ref 19), 4-methylmorpholine (ref 20), 1,4-dimethylpiperazine (ref 21); for monocarboxylic acids from ref 22; for dicarboxylic acids from ref 3a. [b] Other datum reported: 7.0 mL mol$^{-1}$ (ref 8). [c] Other data reported: 3.9 mL mol$^{-1}$ (ref 6), 3.4 mL mol$^{-1}$ (ref 4), 4.1 mL mol$^{-1}$ (ref 9). [d] Other datum reported: 3.1 mL mol$^{-1}$ (ref 4). [e] Other datum reported: 3.6 mL mol$^{-1}$ (ref 4). [f] Other data reported: 4.5 mL mol$^{-1}$ (ref 4), 5.5 mL mol$^{-1}$ (ref 5). [g] Other data reported: 3.8 mL mol$^{-1}$ (ref 6), 3.4 mL mol$^{-1}$ (ref 4), 3.9 mL mol$^{-1}$ (ref 9). [h] Other datum reported: 2.9 mL mol$^{-1}$ (ref 4). [i] Other data reported: 4.5 mL mol$^{-1}$ (ref 6), 4.5 mL mol$^{-1}$ (ref 4), 5.0 mL mol$^{-1}$ (ref 9). [j] Other datum reported: −1.0 mL mol$^{-1}$ (ref 9). [k] Reference 4. [l] Reference 4. [m] Other datum reported: 6.5 mL mol$^{-1}$ (ref 23).

nitrogen center and charged carboxylate group is not clear. Most likely these effects may be related to the different orientation of water molecules around these centers. The opposed behavior of expansivity and viscosity of solutions of salts of $RNH_3^+$ and $RCOO^-$[30] would seem to confirm this view. The different orientation of water molecules around the $COO^-$ and $NH_3^+$ centers is probably responsible also for the observed $\Delta S°$ trends in the series of *n*-alkylamines and carboxylic acids.

As far as the comparison polyfunctional–monofunctional compounds is concerned, Table V reports the experimental $\bar{V}_2°$ values of bifunctional compounds with the corresponding $\bar{V}_2^*$ values calculated from eq 9. A glance at this table indicates that $\bar{V}_2^*$ is always larger than $\bar{V}_2°$ and the

TABLE III: Thermodynamic Parameters for Ionization Process of Selected Diamines and Dicarboxylic Acids in Water at 25 °C[a]

| Substance | $\Delta V_2°$, mL mol$^{-1}$ | p$K_2$ | $\Delta H_2°$, kcal mol$^{-1}$ | $\Delta S_2°$, cal mol$^{-1}$ deg$^{-1}$ |
|---|---|---|---|---|
| Ethylenediamine | 12.1[b] | 6.85 | 11.00 | 5.6 |
| 1,3-Diaminopropane | 10.0 | 8.88 | 12.78 | 2.2 |
| Piperazine | 13.7 | 5.33 | 7.43 | 0.5 |
| 1-Methylpiperazine | 14.3 | 4.94 | 4.00 | −9.2 |
| 1,4-Dimethylpiperazine | 14.7 | 4.18 | 3.96 | −5.8 |
| Triethylenediamine | 16.3 | 2.95 | 3.00 | −3.4 |
| *N,N,N',N'*-Tetraethanol ethylenediamine | 14.1[c] | | | |
| Oxalic acid | −11.9 | 4.27 | −1.57 | −24.8 |
| Malonic acid | −18.6 | 5.70 | −1.15 | −29.9 |
| Succinic acid | −13.6 | 5.64 | 0.04 | −25.7 |
| Glutaric acid | −13.6 | 5.42 | −0.58 | −26.7 |
| Adipic acid | −13.5 | 5.41 | −0.64 | −26.9 |
| Pimelic acid | −13.6 | 5.42 | −0.90 | −27.9 |

[a] The reported quantities refer to the following processes of protonic ionization: $BH_2^{2+} \rightleftarrows BH^+ + H^+$ (diprotonated diamines), $AH^- \rightleftarrows A^{2-} + H^+$ (dicarboxylic acid monoanions). For amines the $\Delta V_2°$ values are our data (this work and ref 2); for dicarboxylic acids data were taken from ref 11. The p$K_2$, $\Delta H_2°$, and $\Delta S_2°$ values were taken from ref 3a (ethylenediamine, triethylenediamine at $\mu$ = 0.1, dicarboxylic acids), ref 24 (1,3-diaminopropane in $KNO_3$ 0.5 M), ref 25 (piperazine), ref 21 (1-methylpiperazine, 1,4-dimethylpiperazine in $KNO_3$ 0.1 M). [b] Other data reported: 10.0 mL mol$^{-1}$ (ref 4), 11.5 mL mol$^{-1}$ (ref 5). [c] Reference 4.

difference $\bar{V}_2° - \bar{V}_2*$ is strongly negative for the dications and less so for the monocations and neutral bases. This suggests that in neutral bifunctional amines and in their corresponding acid cations, the interaction between the two hydrophilic centers causes a contraction in the partial molar volume with respect to $\bar{V}_2*$ calculated on the basis of the group additivity rule, which assumes that the two centers behave independently of each other. The contraction in volume due to the interaction between two neutral centers is smaller than that between a neutral polar group and a charged nitrogen center. This would account for the larger volume of ionization, $\Delta V_1°$, of the bifunctional amine than the corresponding monofunctional amine. The same explanation has been proposed[2] to rationalize the larger $\Delta V_1°$ values for cyclic bifunctional amines compared to monofunctional amines.

As for the amines, the difference $\bar{V}_2° - \bar{V}_2*$ for dicarboxylic acids indicates the presence of interactions between hydrophilic centers, neutral or charged. In this case, however, such interactions do not always produce a contraction in volume, but can also cause a volume increase, as in the case of malonic acid.

*$\Delta V_2°$ for Diamines and Dicarboxylic Acids.* $\Delta V_2°$ for diprotonated diamines is positive and larger than $\Delta V_1°$ for monoprotonated amines (cf. Tables II and III). This has no parallel in the ionization of dicarboxylic acids, for which, with the exception of oxalic and malonic acids, the differences between $\Delta V_1°$ and $\Delta V_2°$ are very small.

The entropies, $\Delta S_2°$, corresponding to the second proton ionization of acids $AH^-$, have the same sign as $\Delta V_2°$. For the first three members, $\Delta V_2°$ increases in a similar manner to $\Delta S_2°$, but for homologues larger than succinic acid, $\Delta V_2°$ values are almost constant whereas the magnitude of $\Delta S_2°$ increases. For the dications of amines $BH_2^+$, in some instances $\Delta V_2°$ and $\Delta S_2°$ have the same sign, but in other cases they are opposed. Moreover, for an increase in $\Delta V_2°$, there is a decrease in $\Delta S_2°$ (cf. Figure 1).

These facts indicate that electrostatic interactions between charged centers are not predominant in determining the variation in $\Delta V_2°$ and $\Delta S_2°$ as the distance between the charges is increased. An evaluation of the importance of electrostatic terms in proton exchange involving diamines and dicarboxylic acids may be obtained

TABLE IV: Contributions of Methylene Group, $\bar{V}_2°(CH_2)$, to the Limiting Partial Molar Volume in a Homologous Series of Compounds of the type Y-$(CH_2)_n$-X[a]

| Y = X = | H COOH | H $COO^-$ | H $NH_2$ | H $NH_3^+$ | H $HSO_3^-$ | COOH COOH | COOH $COO^-$ | $COO^-$ $COO^-$ |
|---|---|---|---|---|---|---|---|---|
| *n* | | | | | | | | |
| 0 → 1 | 17.3 | 14.2 | 16.9 | 18.3 | | 18.1 | 14.8 | 8.1 |
| 1 → 2 | 15.9 | 14.4 | 16.7 | 16.8 | 17.7 | 15.7 | 12.9 | 17.9 |
| 2 → 3 | 16.6 | 15.6 | 15.7 | 16.5 | | 16.2 | 15.9 | 15.9 |
| 3 → 4 | 15.9 | 16.4 | 15.9 | 16.0 | | 16.5 | 16.2 | 16.2 |
| 4 → 5 | 15.5 | 15.7 | 15.9 | 16.0 | | 16.3 | 15.6 | 15.6 |
| 5 → 6 | | 15.7 | 16.0 | 15.9 | | | | |
| 6 → 7 | | 16.0 | 16.0 | 15.8 | | | | |
| 7 → 8 | | 15.7 | | 16.0 | | | | |
| Y = X = | OH $NH_2$ | OH $NH_3^+$ | $OCH_3$ $NH_2$ | $OCH_3$ $NH_3^+$ | $NH_2$ $NH_2$ | $NH_2$ $NH_3^+$ | $NH_3^+$ $NH_3^+$ | $NEt_3^+$ $NEt_3^+$ |
| *n* | | | | | | | | |
| 2 → 3 | 16.0 | 16.5 | 16.0 | 16.4 | 16.0 | 17.0 | 19.1 | |
| 3 → 4 | | | | | | | | 19.2 |
| 3 → 6 | | | | | | | 17.5 | |
| 4 → 6 | | | | | | | | 17.1 |
| 6 → 8 | | | | | | | | 16.1 |
| 8 → 10 | | | | | | | | 15.8 |

[a] The reported data (mL mol$^{-1}$) have been calculated by $\bar{V}_2°(CH_2) = \bar{V}_2°[Y\text{-}(CH_2)_{n+1}\text{-}X] - \bar{V}_2°[Y\text{-}(CH_2)_n\text{-}X]$, using the $\bar{V}_2°$ values taken from ref 28 and 29 (monocarboxylic acids); ref 30 (sodium *n*-alkanecarboxylates); ref 7 (*n*-alkylamines); ref 31 (*n*-alkylamine hydrobromides); ref 32 (bolaform electrolytes of the type $(CH_2)_n(Et_3NBr)_2$, with $n$ = 3, 4, 6, 8, 10); ref 16 (sodium salts of *n*-alkylsulfonic acids and $\alpha,\omega$-diamine dihydrobromides $(CH_2)_n(NH_3Br)_2$, with $n$ = 3, 6); ref 11 (dicarboxylic acids and their mono- and disodium salts); this investigation (all the other compounds).

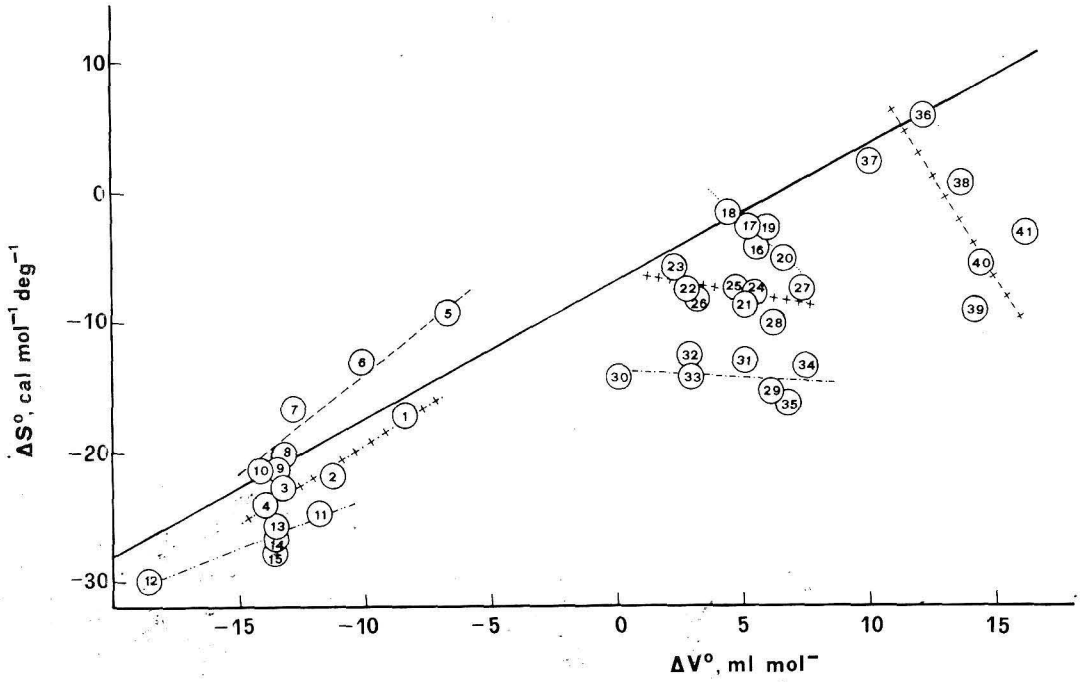


**Figure 1.** Ionization entropy changes $\Delta S^\circ$ plotted against ionization volume changes $\Delta V^\circ$ for organic solutes in aqueous solution at 25 °C. The solid line represent the Hepler curve (ref 35), the nonsolid lines, which fit homologous compounds, have been drawn only for an easier understanding of the figure. Monocarboxylic acids (·+·+·): 1, formic acid; 2, acetic acid; 3, propionic acid; 4, *n*-butanoic acid. Dicarboxylic acids, first ionization (– – –): 5, oxalic acid; 6, malonic acid; 7, succinic acid; 8, glutaric acid; 9, adipic acid; 10, pimelic acid. Dicarboxylic acids, second ionization (–·–·–): 11, oxalic acid; 12, malonic acid; 13, succinic acid; 14, glutaric and adipic acid; 15, pimelic acid. Primary amines (····): 16, methylamine; 17, ethylamine; 18, *n*-propylamine, *n*-butylamine, *n*-pentylamine; 19, 1,3-diaminopropane (first ionization), 2-aminoethanol, 3-amino-1-propanol, 2-methoxyethylamine, 3-methoxy-1-propylamine; 20, ethylenediamine (first ionization). Secondary amines (+++++): 21, dimethylamine; 22, diethylamine; 23, di-*n*-propylamine, di-*n*-butylamine; 24, 2-(methylamino)ethanol; 25, 2-(ethylamino)ethanol; 26, piperidine; 27, morpholine; 28, piperazine (first ionization). Tertiary amines (–·–·–): 29, trimethylamine, 1,4-dimethylpiperazine (first ionization); 30, triethylamine; 31, 2-(dimethylamino)ethanol; 32, 2-(diethylamino)ethanol; 33, 1-methylpiperidine; 34, 4-methylmorpholine; 35, triethylenediamine (first ionization). Diamines, second ionization (+–+–): 36, ethylenediamine; 37, 1,3-diaminopropane; 38, piperazine; 39, 1-methylpiperazine; 40, 1,4-dimethylpiperazine; 41, triethylenediamine. The $\Delta V^\circ$ and $\Delta S^\circ$ are reported in Tables II and III with the relative references.

by considering the process of disproportionation represented by eq 10 and 11, instead of examining eq 3 and 4 or 6 and 7:

$$2BH^+ \rightleftarrows BH_2^{2+} + B \quad (10)$$

$$2AH^- \rightleftarrows A^{2-} + AH_2 \quad (11)$$

For these processes, the change in volume or entropy is given by $\Delta X_d^\circ = j(\Delta X_1^\circ - \Delta X_2^\circ)$, where $X = V,S$ and $j = 1$ for diamines and $-1$ for dicarboxylic acids. Processes 10 and 11 are comparable because the number of charged species and protons involved are the same. Also, for the type of bonds being broken and formed, it is reasonable to assume that electrostatic factors are dominant. On the basis of Bjerrum's electrostatic model, $\Delta V_d^\circ$ and $\Delta S_d^\circ$ are predicted to be negative and to tend to zero when the distance between the two functional groups becomes increasingly large. The experimental results in Table VI confirm these predictions. However, for the dicarboxylic acids, succinic acid, and its higher homologues show no change in $\Delta V_d^\circ$, as if the two $COO^-$ groups in $A^{2-}$ are equivalent to two negative ions bearing a unit charge. This picture in reality, besides being unacceptable physically, is contrary to the trend shown by other thermodynamic properties, particularly $\Delta S_d^\circ$, which is nonnegligible and continually varies even for homologues larger than succinic acid.

Contrary to the case of the dicarboxylic acids, the formation of $BH_2^{2+}$ from $BH^+$ by disproportionation is accompanied by a remarkable volume decrease, even when the two centers of positive charge in the dication of 1,3-diaminopropane are separated by a distance approximately equal to the charge separation distance in the succinate anion. The volume contraction caused by the interaction between the two positively charged nitrogen centers is confirmed directly from the results in Table V and indirectly from the large values of $\bar{V}_2^\circ(CH_2)$ found for bolaform electrolytes, with the nitrogen atoms well separated (cf. Table IV). From the process of disproportionation examined above, the negative signs for $\Delta V_d^\circ$ and $\Delta S_d^\circ$ indicate that the electrostatic theory can qualitatively account for the behavior of the diamines and dicarboxylic acids in solution. However, the trends shown by $\Delta V_d^\circ$ and $\Delta S_d^\circ$ are not consistent with predictions based on the same theory. This inadequacy of the simple electrostatic theory is not surprising because of the complexities involved in aqueous solutions.

## Conclusions

The following conclusions may be drawn:

(a) $\bar{V}_2^\circ(CH_2)$ values in the homologous series of amines and carboxylic acids indicate that the polar centers $NH_2$ and COOH influence the hydration sphere associate with the hydrocarbon chain up to the $\beta$ carbon atom. In the case of the $NH_3^+$ and $COO^-$ groups the effect of the charged centers extends up to the $\gamma$ carbon atom; the positively charged nitrogen center causes a reduction in the volume of the hydrocarbon hydration sphere, whereas the opposite is true for the carboxylate group.

(b) The $\bar{V}_2^\circ$ values of bifunctional amines are always smaller than the $\bar{V}_2^*$ values calculated assuming no interaction between functional groups. The interaction between two neutral polar groups is smaller than that between a polar group and a charged center.

(c) In molecules containing two charged centers, the interaction between the charged centers results in a contraction in $\bar{V}_2^\circ$ compared with values calculated from

TABLE V: Comparison between the Experimental $\bar{V}_2^\circ$ and Calculated $\bar{V}_2^*$ Values of Aliphatic Bifunctional Compounds in Water at 25 °C

| Compound | $\bar{V}_2^\circ$, mL mol$^{-1}$ | $\bar{V}_2^{*a}$, mL mol$^{-1}$ | $\bar{V}_2^\circ - \bar{V}_2^*$, mL mol$^{-1}$ |
|---|---|---|---|
| 2-Aminoethanol | 59.25 | 62.4 | −3.2 |
| 2-Aminoethanol·HCl | 70.90 | 74.8 | −3.9 |
| 3-Amino-1-propanol | 75.21 | 77.9 | −2.7 |
| 3-Amino-1-propanol·HCl | 87.40 | 90.9 | −3.5 |
| Ethylenediamine | 62.88 | 65.6 | −2.7 |
| Ethylenediamine·HCl | 74.05 | 78.1 | −4.1 |
| Ethylenediamine·2HCl | 79.77 | 90.5 | −10.7 |
| 1,3-Diaminopropane | 78.83 | 81.3 | −2.5 |
| 1,3-Diaminopropane·HCl | 91.09 | 94.4 | −3.3 |
| 1,3-Diaminopropane·2HCl | 98.88 | 107.5 | −8.6 |
| 2-(Ethylamino)ethanol | 92.91 | 95.7 | −2.8 |
| 2-(Ethylamino)ethanol·HCl | 106.03 | 110.7 | −4.7 |
| 2-(Diethylamino)ethanol | 123.04 | 124.9 | −1.9 |
| 2-(Diethylamino)ethanol·HCl | 137.96 | 142.6 | −4.6 |
| Malonic acid | 67.22 | 66.5 | +0.7 |
| Malonic acid·Na salt | 55.96 | 53.9 | +2.0 |
| Malonic acid·2Na salt | 36.21 | 41.3 | −5.1 |
| Succinic acid | 82.94 | 84.7 | −1.8 |
| Succinic acid·Na salt | 68.88 | 70.5 | −1.6 |
| Succinic acid·2Na salt | 54.10 | 56.3 | −2.2 |
| Glutaric acid | 99.14 | 102.3 | −3.2 |
| Glutaric acid·Na salt | 84.77 | 87.0 | −2.3 |
| Glutaric acid·2Na salt | 69.98 | 71.6 | −1.8 |

[a] Values obtained using eq 9. The $\bar{V}_2^\circ$ values of hydrocarbons methane, ethane, propane were taken from Masterton (ref 33). The $\bar{V}_2^\circ$ values of the monofunctional molecules were taken from ref 34 (ethanol, 1-propanol); ref 7 (ethylamine, *n*-propylamine, diethylamine, triethylamine, and their hydrochlorides); ref 29 (monocarboxylic acids); ref 30 (sodium *n*-alkanecarboxylates). The experimental $\bar{V}_2^\circ$ values for dicarboxylic acids and their sodium salts were taken from ref 11.

TABLE VI: Volume and Entropy Changes in the Disproportionation Processes of Diamine Monocations and Dicarboxylic Acid Monoanions[a]

| Substance | $\Delta V_d^\circ$, mL mol$^{-1}$ | $\Delta S_d^\circ + R \ln 4$,[b] cal mol$^{-1}$ deg$^{-1}$ |
|---|---|---|
| Ethylenediamine | −5.4 | −8.3 |
| 1,3-Diaminopropane | −4.4 | −3.2 |
| Piperazine | −7.5 | −5.6 |
| 1,4-Dimethylpiperazine | −8.5 | −6.9 |
| Triethylenediamine | −9.5 | −9.9 |
| Oxalic acid | −5.2 | −12.9 |
| Malonic acid | −8.5 | −14.2 |
| Succinic acid | −0.7 | −6.3 |
| Glutaric acid | −0.4 | −3.7 |
| Adipic acid | −0.1 | −2.7 |
| Pimelic acid | +0.6 | −3.6 |

[a] $\Delta X_d^\circ = j(\Delta X_1^\circ - \Delta X_2^\circ)$, with $X = V, S$, and $j = 1$ for diamines, and $j = -1$ for dicarboxylic acids. The $\Delta X_1^\circ$ and $\Delta X_2^\circ$ values are reported in Tables II and III. [b] The $R \ln 4$ term is the correction for the statistical term of the reaction.

principle of group additivity. This contraction is very large for the diprotonated amines, but small for the dianions of carboxylic acids.

(d) For amines, the regular changes in $\Delta V_1^\circ$ and $\Delta V_2^\circ$, associated with chain lengthening or with the introduction of a second hydrophilic center, are determined by analogous regular changes of $\bar{V}_2^\circ$ of both neutral and charged species involved in the ionization process (see points a, b, c).

From the available volumes of ionization, there is no doubt that there is a correlation between $\Delta V^\circ$ and molecular structure of the species involved in the ionization process. However, there is no simple interrelation between $\Delta V^\circ$ and other thermodynamic parameters of ionization. Thus there are exceptions to the general tendency of $\Delta V^\circ$ to increase with increasing $\Delta S^\circ$,[35] e.g., amines (cf. Figure 1).

That thermodynamic functions, such as volumes and entropies of reaction in aqueous solution respond to the changes in molecular structure in a different manner, is not surprising. Even though the different behavior of these functions does not lend itself to an unequivocal interpretation, it can help in formulating a model for water structure around different types of ionic solutes and molecules.

*Acknowledgment.* This work has been supported through financial assistance from the Consiglio Nazionale delle Ricerche (C.N.R.).

## References and Notes


(1) Present address: Department of Chemistry, University of Calgary, Calgary, Alberta, Canada.
(2) S. Cabani, V. Mollica, L. Lepori, and S. T. Lobo, *J. Phys. Chem.*, preceding paper in this issue.
(3) For reviews see, for example, (a) J. W. Larson and L. G. Hepler, "Solute-Solvent Interactions", J. F. Coetze and C. D. Ritchie, Ed., Marcel Dekker, New York, N.Y., 1969; (b) L. G. Hepler and E. M. Woolley, "Water; A Comprehensive Treatise", Vol. III, F. Franks, Ed., Plenum Press, New York, N.Y., 1973; (c) F. M. Jones and E. M. Arnett, "Progress in Physical Organic Chemistry", Vol. II, A. Streitwieser and R. S. Taft, Ed., Wiley, New York, N.Y., 1974.
(4) W. Kauzmann, A. Bodanszky, and J. Rasper, *J. Am. Chem. Soc.*, **84**, 1777 (1962).
(5) J. Lawrence and B. E. Conway, *J. Phys. Chem.*, **75**, 2353 (1971).
(6) S. D. Hamann and S. C. Lim, *Aust. J. Chem.*, **7**, 329 (1954).
(7) S. Cabani, G. Conti, and L. Lepori, *J. Phys. Chem.*, **78**, 1030 (1974).
(8) R. H. Stokes, *Aust. J. Chem.*, **28**, 2109 (1975).
(9) R. E. Verrall and B. E. Conway, *J. Phys. Chem.*, **70**, 3691 (1966).
(10) S. Cabani, G. Conti, L. Lepori, and G. Leva, *J. Phys. Chem.*, **76**, 1343 (1972).
(11) H. Høiland, *J. Chem. Soc., Faraday Trans. 1*, **71**, 797 (1975).
(12) S. Cabani, G. Conti, and L. Lepori, *J. Phys. Chem.*, **76**, 1338 (1972).
(13) O. Redlich and D. M. Meyer, *Chem. Rev.*, **64**, 221 (1964).
(14) M. V. Kaulgud and K. J. Patil, *J. Phys. Chem.*, **80**, 138 (1976).
(15) M. V. Kaulgud and K. J. Patil, *J. Phys. Chem.*, **78**, 714 (1974).
(16) M. Sakurai, *Bull. Chem. Soc. Jpn.*, **46**, 1596 (1973).
(17) F. J. Millero, *Chem. Rev.*, **71**, 147 (1971).
(18) H. Høiland, *J. Chem. Soc., Faraday Trans. 1*, **70**, 1180 (1974).
(19) S. T. Lobo, Ph.D. Thesis, University of Calgary, Alberta, Canada, 1975.
(20) M. J. Blais, O. Enea, and G. Berthon, *Thermochim. Acta*, **9**, 379 (1975).
(21) G. Berthon, O. Enea, and K. Houngbossa, *Thermochim. Acta*, **12**, 25 (1975).
(22) J. J. Christensen, M. D. Slade, R. M. Izatt, and J. Tsang, *J. Am. Chem. Soc.*, **92**, 4164 (1970).
(23) W. Y. Wen, N. Takeguchi, and D. P. Wilson, *J. Solution Chem.*, **3**, 103 (1974).
(24) A. Vacca and D. Arenare, *J. Phys. Chem.*, **71**, 1495 (1967).
(25) H. B. Hetzer, R. A. Robinson, and R. G. Bates, *J. Phys. Chem.*, **72**, 2081 (1968).
(26) E. J. King, "Acid-Base Equilibria", Pergamon Press, Oxford, 1965.
(27) S. D. Hamann, "Modern Aspects of Electrochemistry", Vol. IX, B. E. Conway and J. O'M. Bockris, Ed., Plenum Press, New York, N.Y., 1976.
(28) E. J. King, *J. Phys. Chem.*, **73**, 1220 (1969).
(29) H. Høiland, *Acta Chem. Scand., Ser. A*, **28**, 699 (1974).
(30) M. Sakurai, T. Komatsu, and T. Nakagawa, *Bull. Chem. Soc. Jpn.*, **48**, 3491 (1975).
(31) P. A. Leduc, J. L. Fortier, and J. E. Desnoyers, *J. Phys. Chem.*, **78**, 1217 (1974).
(32) J. A. Burns and R. E. Verrall, *J. Solution Chem.*, **3**, 289 (1974).
(33) W. L. Masterton, *J. Chem. Phys.*, **22**, 1830 (1954).
(34) C. Jolicoeur and G. Lacroix, *Can. J. Chem.*, **54**, 624 (1976).
(35) L. G. Hepler, *J. Phys. Chem.*, **69**, 965 (1965).

# Homogeneous Nucleation in Metal Vapors. 2. Dependence of the Heat of Condensation on Cluster Size

**H. J. Freund and S. H. Bauer***

*Department of Chemistry, Cornell University, Ithaca, New York 14853* *(Received July 19, 1976; Revised Manuscript Received March 7, 1977)*

By shock heating moderately volatile metal bearing compounds [for example, $Fe(CO)_5$] highly diluted in argon, supersaturated metal vapors, $S = 50$–$3000$, at controlled densities and temperatures can be generated. The subsequent homogeneous condensation was followed by recording the turbidity of the gas as a function of distance behind the shock front. Determination of density gradients behind the shock front, using the laser-schlieren technique, provided measures of the rates and enthalpies of the exothermic reactions which occurred; in this case, the condensation of metal droplets. A model was developed which accounted for the observed density gradient profiles, and led to parameters which specify the particle size distribution as a function of time, and the average size (40–2000 atoms) to which the particles grow for any set of experimental conditions. These experiments also provide an estimate for the "binding energy" for the reaction $n\text{Fe} \rightarrow \text{Fe}_n$, $\Delta E_n/n = \Delta E_\infty(1 - n^{-0.25})$, where $\Delta E_\infty$ is the bulk energy of sublimation. This empirical representation is surprisingly well fitted by several theoretical calculations of binding energies of small clusters ($2 \leq n \leq 2000$).

## Introduction

In the first paper of this series[1] we described a shock-tube technique for preparing controlled levels of supersaturated iron vapor, and procedures for determining the dependence of the critical supersaturation on the temperature. The catastrophic onset of condensation was ascertained by recording either a rapid rise in the turbidity, or the appearance of black body emission from the glowing clusters. These investigations have now been extended, and more refined diagnostics were developed. The starting point of the present report was the observation by Kung and Bauer[1] that the nascent clusters had a black body temperature which was always higher than that of the carrier gas (50–150 K); clearly there was a lag in the transfer of the heat of condensation to the ambient medium. The goal of our current study is the development of sufficient statistical-thermodynamic data so that a purely kinetic molecular model could be developed without recourse to bulk-type properties; for example, we consider it unacceptable to discuss the free-energy increment for cluster formation in terms of a surface free energy for very small aggregates (range $5 \lesssim n \lesssim 50$), whereby one eventually substitutes bulk liquid magnitudes for the parameters of state. Here we take the first step, measurement of the enthalpy contribution to the free energy of cluster formation; in paper 5 we present estimates of the entropy term, and introduce a consistent kinetic model.

During the first decade of this century J. J. Thomson discussed the condensation from a supersaturated vapor in terms of a metastable equilibrium between two phases. The nascent clusters were treated as tiny drops of liquid, to which the Kelvin equation was applied. The meta-equilibrium vapor pressure ($p_n$) for a uniform assembly of such droplets (radius $r_n$), relative to that of the bulk liquid ($p_\infty$) is [2]

$$\ln (p_n/p_\infty) = \frac{2\sigma_n}{r_n \rho_n} \frac{1}{kT} \tag{1}$$

$\sigma_n$ and $\rho_n$ are the surface free energy and the monomer density, respectively, in a cluster size $n$. After six decades of evolution of theories for homogeneous condensation[3] this aspect of the model has not been fully relinquished, in spite of the fact that relation 1 connects obviously nonmeasurable quantities. One has but to inspect the interesting density profiles of relatively large clusters derived by Lee et al.[4] who performed a Monte-Carlo energy minimization calculation. Inspection of their Figure 9 (radial density curves for 13, 43, and 87 atom clusters) shows that there is no definable "surface" layer, nor can $\rho_n$ be defined, since $\rho(r)$ decreases gradually to zero, at a radius determined by an arbitrarily specified confining volume.

The obvious alternative to the application of bulk liquid concepts to clusters in the range $5 \lesssim n \lesssim 50$ is to treat them as large molecules. We undertook to measure their heats of condensation from monomers. To our knowledge this is the first such reported measurement, and while at this stage our data are crude, they are of sufficient accuracy to affirm several novel conclusions. Indirect estimates have been made on the basis of mass spectrometric analyses of clusters from effusion cells or from divergent nozzle flows, but values for $n > 10$ are not generally available. Gingerich and co-workers reported extensively on mass spectrometric measurements of metallic clusters which effuse from Knudsen cells.[5] They measured[6] relative populations of tin clusters ($1 < n < 8$) over the temperature range 1379–1651 K, but to deduce $\Delta H^\circ_n$ it was necessary to introduce third law estimates for the entropies ($\Delta S^\circ_n$). Configurational contributions were neglected. For lead ($1 < n < 5$) both second and third law values were obtained.[7] However, the accuracy of data on the relative concentrations of clusters from freely expanding jets, based on mass spectrometric detection, has been seriously questioned.[8]

There have been many theoretical studies of the dependence of energy content on cluster size. Among the recent reports, Anderson[9] using a low spin MO approximation estimated the binding energies for $2 \rightarrow 13$ atom clusters of Ti, Cr, Fe, and Ni. Baetzold[10] undertook extended Hückel and CNDO MO calculations; he obtained cluster binding energies for Ag and Ni. He considered the effect of dimensionality on the binding energy, and found that for small numbers of metals atoms, a linear configuration is more stable than a three-dimensional structure. Fripiat et al.[11] computed binding energies in Li crystals (at a fixed geometry) using the SCF $X\alpha$ scattered wave method. Another technique was introduced by Gelb et al.[12] (the diatomics-in-molecule approach) in their study of small clusters of Na atoms; Dykstra and Schaefer[13] applied the theory of self-consistent electron pairs to $Be_4$. Burton[14]

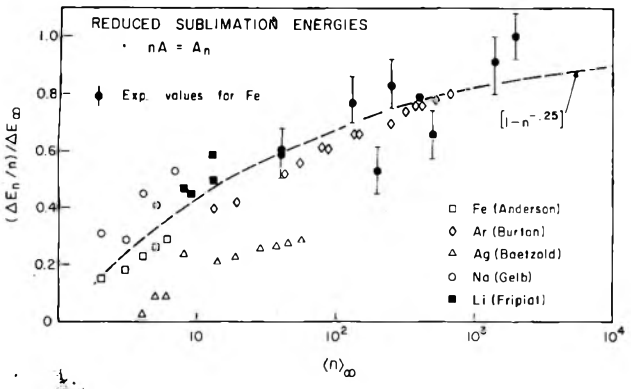


**Figure 1.** Theoretical (5 sets) and experimental values (1 set) for the reduced energy of condensation (per atom), as a function of cluster size. In the least-squares fitting of the points to a function of the form $\Delta E_n/n \equiv \Delta E_\infty(1 - an^{-b})$. Baetzold's values for Ag (three-dimensional calculations) were not included, but all other points were given equal weight. A correlation coefficient of 0.91 was obtained for best fit: $a = 0.96$ and $b = 0.235$. When $b \equiv 0.250$, the correlation coefficient declined inappreciably (to 0.90), for $a = 1.01_5$. Other computed points (including water) fall within a band of width ±0.1 about the empirical curve; for example, J. C. Owicki, et al., *J. Phys. Chem.*, **79**, 1794 (1975).

determined the binding energies for small spherical clusters of argon using a normal mode analysis with energy minimization, based on a Lennard-Jones pair potential. These theoretical data are plotted on a reduced scale in Figure 1. $[\Delta E_n/n]$ is the condensation energy per atom; $\Delta E_\infty$ is the corresponding energy released upon condensation to a macroscopic cluster. In view of the density profiles within small clusters[4] it is not surprising that the binding energy per atom for small $n$ is considerably less than that for the bulk.[15] The question to be answered is the general shape of the function which ties the $n = 2$ to the $n = 10^4$ points.

## Experimental Section

We have demonstrated[1] that there was a measurable time lag for transfer of the heat of condensation from the nascent clusters to the carrier gas. It follows that the heating rate is determined by the following: (i) the $n$mer growth rate, averaged over the instantaneous size distribution; (ii) the differential heat of condensation for monomer addition; and (iii) the heat transfer coefficient from the nascent clusters to the ambient argon. The thermal balance downstream from a shock front can be measured by the very sensitive "laser-schlieren" technique developed by Kiefer and Lutz[16] for their study of the vibrational relaxation time of $H_2$ and $D_2$. Since the shock heated gas remains essentially at constant pressure, it follows that

$$\frac{1}{\rho}\frac{d\rho}{dx} \propto -\frac{1}{T}\frac{dT}{dx}$$

Now, the index of refraction ($m$) is a linear function of the mass density ($\rho$): $m \equiv 1 + r(\rho/\rho_0)$, where $r$ is the Dale–Gladstone constant, which is additive for a mixture of gases: $r = \sum_i \xi_i r_i$; $\xi_i$ is the mole fraction, and $\rho_0$ is the reference density. Furthermore, the *gradient* in the index of refraction can be sensitively measured by the deflection of a narrow laser beam, using a long lever arm. Hence, the laser beam deflection is directly related to the *rate* of heat injection or removal from the carrier gas. The light is bent into the region of higher density. The density gradient is given in terms of the beam displacement $\delta$ (see Figure 2):

$$\partial\rho/\partial x = \delta/wrL \qquad (2)$$

For these experiments shock conditions were chosen so that the $Fe(CO)_5$ decomposed essentially within the shock

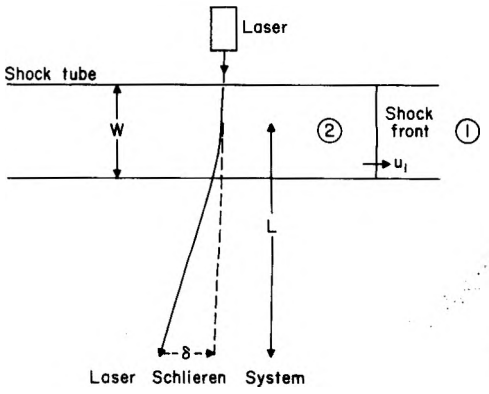


**Figure 2.** Schematic for the laser-schlieren system.

front. The estimated lifetime of the carbonyl at 1600 K is less than $10^{-10}$ s; its initial concentration was 0.5–1.2% of the argon. Hence the average molecular weight of the test gas changed inappreciably upon dissociation of the $Fe(CO)_5$ or condensation of the Fe. Upon differentiation of the (ideal) equation of state, subject to the shock conservation equations, one can derive ($\tilde{R}$ is the gas constant per unit mass):

$$\frac{\partial T_2}{\partial t} = \frac{\rho_1 u_1}{\rho_2{}^2 \tilde{R}}\left[\frac{\rho_1{}^2 u_1{}^2}{\rho_2{}^2} - \tilde{R}T_2\right]\frac{\partial \rho_2}{\partial x} \qquad (3)$$

The subscripts 1 and 2 refer to the unshocked and shocked conditions, respectively. The magnitude of $\tilde{R}$ is unchanged since the increment in molecular weight is small; $u_1$ is the shock speed. The local density behind the shock front is related to the corresponding temperature, and the initial conditions:

$$\rho_2 = \frac{1}{2}\left\{\frac{P_1 + \rho_1 u_1{}^2}{\tilde{R}T_2} + \left[\left(\frac{P_1 + \rho_1 u_1{}^2}{\tilde{R}T_2}\right)^2 - \frac{4\rho_1{}^2 u_1{}^2}{\tilde{R}T_2}\right]^{1/2}\right\} \qquad (4)$$

At any $t$ after shock arrival, $\partial\rho/\partial x$ is known; then following an interative procedure one can derive corresponding values for $\partial T/\partial x$. In turn, the temperature gradient is determined by the change in the specific enthalpy of the gas

$$\frac{\partial T_2}{\partial x} = \frac{1}{u_2}\frac{\partial T_2}{\partial t} = \frac{1}{c_p}\frac{\partial h_2}{\partial t}\frac{1}{u_2} \qquad (5)$$

where $c_p$ is the heat capacity of the gas (here also we neglected the small effect of the Fe), and $u_2$ is the shocked gas velocity. Integration with respect to time allows one to estimate the *total* change in the enthalpy (or temperature) due to condensation of the Fe atoms. An estimate of the sensitivity of our laser-schlieren system, expressed in terms of a general mechanism wherein several reactions occur concurrently,[17] is

$$(\partial\rho/\partial x) \propto \sum_j [\mathcal{R}_j^{(f)} - \mathcal{R}_j^{(r)}]\Delta H_j^\circ$$
$$\gtrsim 0.02 \text{ kcal cm}^{-3} \text{ s}^{-1} \qquad (6)$$

where $\mathcal{R}_j^{(f)}$ and $\mathcal{R}_j^{(r)}$ are the forward and reverse rates for the $j$th reaction, in mol cm$^{-3}$ s$^{-1}$, and $\Delta H_j^\circ$ is the corresponding net enthalpy change per mole.

## Experimental Details and Data

Figure 3 is a schematic of the overall experimental arrangement. Photomultiplier 2 records the schlieren

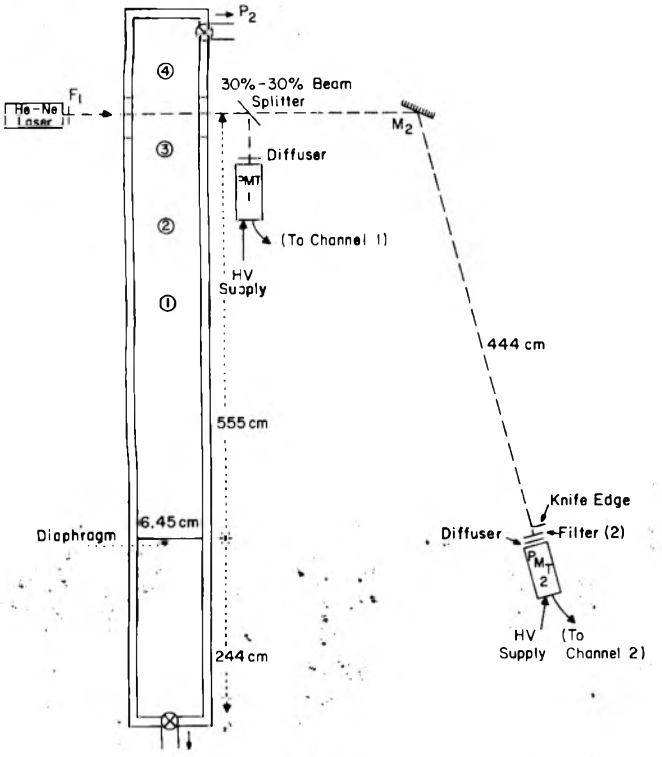


**Figure 3.** Schematic of overall experimental arrangement: $F_1$ and $F_2$ are a neutral density filter and narrow band filter, respectively; $P_2$ to pumps, sample reservoir, and pressure gauges; $M_2$ is mounted on a rotatable shaft for intensity level calibration. The distance from the center of the shock tube to the rotating mirror is 555 cm.

signal while photomultiplier 1 measures the attenuation of the beam by the turbidity of the shocked sample due to absorption and scattering by the growing clusters. This channel provides the necessary correction ratio for the schlieren signal, and a measure of the amount of material which had condensed at any time.

The shock tube is of stainless steel, of rectangular cross section, 6.35 cm by 4.45 cm. Shock waves were initiated by pressure bursting prescribed 16-mil aluminum diaphragms; the driver gas was He or $He/N_2$ mixtures. Before each run, the driven section was pumped to below $10^{-4}$ Torr. The combined leak-outgassing rate was $5 \times 10^{-3}$ Torr/min. Approximately 1 min was taken to fill the tube with the sample and to burst the diaphragm. Sample loading pressures ranged between 10 and 20 Torr. The $Fe(CO)_5$ was double distilled, and each time we retained only the middle fraction; ultra high purity argon was used as the diluent. The experiments were made with 0.5 or 1.22 mol % of the carbonyl.

Shock speeds were measured using two platinum film heat transfer gauges (no. 3 and 4 in Figure 3). Shock attenuation was found to be about 1%/m, but ideal shock equations were used to calculate the temperature. The light source was a Spectra-Physics Model 123 He–Ne laser, equipped with a model 235A exciter; its output power was specified at 7 mW. The beam width at the center of the shock tube was 0.9 mm at the $e^{-2}$ points. An EMI 9558 phototube was used in channel 1 and EMI 9658 in channel 2. Both phototubes have a $1/e$ response time of less than 200 ns. The calibration procedure via the rotating mirror has been described in a previous publication.[18] Initial and typical shock heated conditions are listed in Table I.

Figure 4 shows an oscilloscope record; (a) measures the density gradient which must be corrected for the beam attenuation using the lower trace (b). The latter is a measure of the change with time of the fraction of material condensed. Reduced graphs are illustrated in Figure 5 for

TABLE I: Typical Experimental Parameters

| | |
|---|---|
| $T_1 = 298$ K | $T_2 = 1600$–$1800$ K |
| $\rho_1 = (2.3\text{–}4.6) \times 10^{-5}$ g cm$^{-3}$ | $\rho_2 = (1\text{–}2) \times 10^{-4}$ g cm$^{-3}$ |
| $P_1 = (10\text{–}20)$ Torr | $P_2 = (0.3\text{–}0.7)$ atm |
| $\langle M \rangle = 39.7$ g mol$^{-1}$ | $u_1 = (1.37\text{–}1.46)$ mm $\mu$s$^{-1}$ |
| Post dissociation of $Fe(CO)_5$: mol % Fe = 1.15 | |
| $\partial\rho/\partial x = (10^{-7}\text{–}10^{-5})$ g cm$^{-4}$ | $dT_g/dt = (0.1\text{–}10)$ K $\mu$s$^{-1}$ |
| $dh_g/dt = (1\text{–}8) \times 10^3$ erg cm$^{-3}$ $\mu$s$^{-1}$ | |

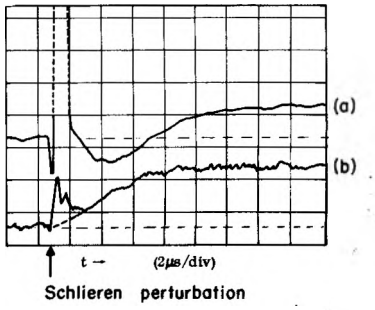


**Figure 4.** Dual beam scope traces: (a) schlieren signal, 0.05 V/division; (b) turbidity; 0.02 V/division. The zero level for this beam was displaced above the screen to permit recording of the small intensity loss. For this run, $T_2 = 1648$ K; $\rho_2 = 1.81 \times 10^{16}$ monomers cm$^{-3}$.

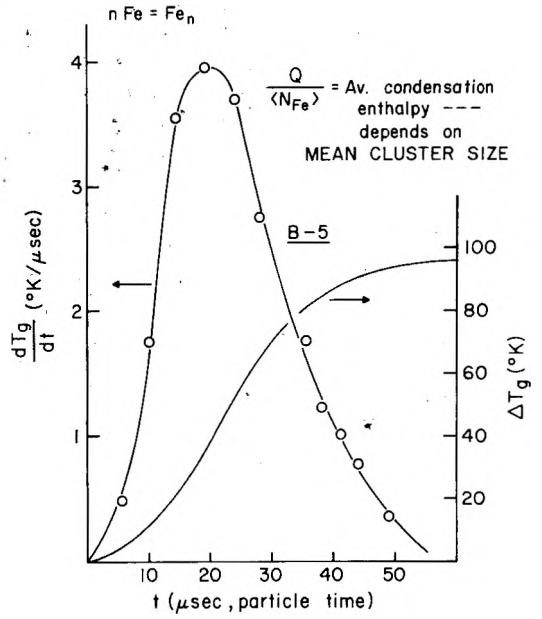


**Figure 5.** Reduced curves for the rate of temperature rise and the integrated increment in the temperature of the carrier gas.

run B-5. Via iterative calculations with eq 3–5, the total heat injected into the Ar per unit volume, $Q$, can be determined from the corrected density gradient trace. This quantity divided by the initial number density of iron atoms gives the heat released per Fe atom ($q$) due to the exothermic condensation step. These results are summarized in Table II.

Our initial assumption was that a narrow distribution of clusters, average size $\langle n \rangle$, is present during condensation. The reaction

$$\langle n \rangle Fe_g \rightarrow Fe_{\langle n \rangle} \qquad (7)$$

expresses the "phase" transformation which occurs. The mean enthalpy increment, per atom, for this reaction (or, the mean atomization energy per atom) may be identified with the experimentally determined quantity, $q$. The obvious check is satisfactory; the $q$ values are in the range $(4\text{–}6) \times 10^{-12}$ erg/atom, somewhat less than but close to the heat of condensation (per atom) to the bulk phase. For a distribution of finite width we must estimate an average

TABLE II: Experimental Parameters and Deduced Magnitudes of Heat Release

| Run no. | $P_1$(total), Torr | $u_1$[a] | $T_2$ ($t$ = 0), K | $N_{Fe}$ ($t$ = 0), cm$^{-3}$ | $S$[b] | $\Delta T$, K | $Q$, erg cm$^{-3}$ | $q$, erg atom$^{-1}$ |
|---|---|---|---|---|---|---|---|---|
| B-8 | 10.4 | 1.377 | 1617 | $1.80 \times 10^{16}$ | 2250 | 130 | $7.11 \times 10^4$ | $3.95 \times 10^{-12}$ |
| B-33 | 10.3 | 1.431 | 1747 | $1.82 \times 10^{16}$ | 310 | 143 | $7.95 \times 10^4$ | $4.36 \times 10^{-12}$ |
| B-5 | 10.2 | 1.405 | 1684 | $1.81 \times 10^{16}$ | 773 | 190 | $9.88 \times 10^4$ | $5.46 \times 10^{-12}$ |
| B-11 | 10.7 | 1.374 | 1609 | $1.89 \times 10^{16}$ | 2640 | 135 | $7.64 \times 10^4$ | $4.04 \times 10^{-12}$ |
| B-24 | 10.3 | 1.416 | 1710 | $1.82 \times 10^{16}$ | 536 | 181 | $9.44 \times 10^4$ | $5.2 \times 10^{-12}$ |
| A-24 | 20.4 | 1.449 | 1791 | $3.62 \times 10^{16}$ | 344 | 216 | $2.22 \times 10^5$ | $6.1 \times 10^{-12}$ |
| A-27 | 20.4 | 1.458 | 1814 | $3.60 \times 10^{16}$ | 307 | 238 | $2.38 \times 10^5$ | $6.6 \times 10^{-12}$ |
| A-21 | 20.8 | 1.425 | 1732 | $3.70 \times 10^{16}$ | 796 | 115 | $1.29 \times 10^5$ | $3.47 \times 10^{-12}$ |
| A-18 | 20.2 | 1.416 | 1710 | $3.59 \times 10^{16}$ | 1050 | 184 | $2.01 \times 10^5$ | $5.60 \times 10^{-12}$ |

[a] Shock speed, in mm $\mu$s$^{-1}$. $T_1$ = 298 K, $C_p$ = 0.131 cal$^{-1}$ g K$^{-1}$. [b] $S$ is the supersaturation ratio at $t$ = 0. $S = P_{Fe}/P_{Fe}^{eq}$.

size $\langle n \rangle_\infty$ for the different supersaturation ratios. Then we could determine the effect of cluster size on the enthalpy of the condensation reaction. To obtain $\langle n \rangle_\infty$ a specific model has to be inserted.

## Energy Transfer Model

The recorded beam deflection measures the rate of change of the enthalpy content of the gas sample probed by the beam; i.e., the rate of injection of energy into the carrier gas behind the incident shock wave, $dh_g/dt$. We sought the *simplest* model which reproduces the shape of these ($dh_g/dt$) traces. We shall point to the approximations which were made in the model and hope either to remove them or to justify them in depth at the next stage of its evolution. In the present form, four parameters were introduced which, upon evaluation to optimize the fit, relate the binding energy of small clusters to their size, and specify the change of the distribution function of sizes with time.

The rate of change of the energy content of the clusters, as they grow and concurrently cool, is the sum of two principal terms. The first is the rate of increase of its energy content due to monomer addition, and the second term is the loss of energy due to collisions with the cooler ambient gas. We neglected loss of energy due to radiation. The following definitions were used:

| | |
|---|---|
| $n$ | number of atoms per cluster; $n$ will be treated as a continuous variable |
| $E_p(n,t)$ | mean energy content at time $t$ of an $n$mer |
| $N_1(t)$ | monomer density at time $t$ |
| $N_g$ | carrier gas density |
| $\bar{c}_g$ | average speed of carrier gas molecules, averaged over the temperature range for the run |
| $\bar{c}_1$ | average speed of the monomer |
| $A(n)$ | surface area of $n$mer (assumed spherical) |
| $\alpha(n)$ | *net* sticking coefficient |
| $\Gamma(n)$ | energy increment for the addition of a monomer: $Fe_{n-1} + Fe \rightarrow Fe_n$ |
| $T_g$ | ambient gas temperature |
| $\theta(n)$ | fraction of excess energy transferred from *nmer* to the carrier gas, per collision with a gas molecule |

Then the rate of change of energy content of the clusters is given by

$$dE_p/dt = {}^1/_4 \{N_1(t)\bar{c}_1 A(n)\alpha(n)[{}^3/_2 kT_g + \Gamma(n)] - N_g\bar{c}_g A(n)\theta(n)[E_p(n,t) - E_p(n,t_\infty)]\} \quad (8)$$

We did not include a term for cooling due to evaporation; i.e., the loss of a monomer either spontaneously or induced by a sufficiently energetic collision with an Ar atom. The latter process is of low probability, but the former may be significant. To take this into consideration requires a considerably more complex model than is used in the present analysis.[19] However, in the accompanying paper (part 5) we demonstrated that during cluster growth for Fe evaporation is negligible for $n \gtrsim 15$. In addition, we assumed: (i) the second term of the right member of (8) is the *net* heat transfer due to collisions between clusters and the ambient gas; (ii) the gas temperature, $T_g$, and the number density, $N_g$, are constant with time. Although the temperature and the density obviously do change due to condensation, the fractional change in this dilute system is small; thus in (8), average values of the temperature and density are implied; (iii) in the following analysis we neglect (with justification) the translational energy, $(3/2)kT_g$, compared to $\Gamma(n)$; finally (iv) in formulating the cooling term, we assumed that all clusters of size $n$ (at any instant) have the same (mean) energy content $E_p(n,t)$. The introduction of another parameterized distribution function at this stage would hopelessly complicate the analysis. Tests of a hybrid model in which we introduced a transition layer between the hot cluster and the ambient gas showed that, to a very good approximation, the gas temperature in this layer was equal to the temperature of the surroundings.

Equation 8 can be simplified by writing (for $t > 0$):

$$Y(n,t) \equiv E_p(n,t) - E_p(n,t_\infty)$$

$$\Phi \equiv \frac{\pi N_g \bar{c}_g}{4}[3v_c/(4\pi)]^{2/3} \quad (9)$$

$$\varphi(t) \equiv \frac{\pi N_1(t)\bar{c}_1}{4}[3v_c/(4\pi)]^{2/3}$$

where $v_c$ is the volume per atom in the condensed phase, at the average temperature. Thus

$$dY(n,t)/dt = \varphi(t)n^{2/3}\Gamma(n)\alpha(n) - \Phi n^{2/3}\theta(n)Y(n,t) \quad (10)$$

This equation has an analytic solution if $\varphi(t)$ is specified. We may deduce $\varphi(t)$ from $N_1(t)$ by empirically fitting the observed turbidity curve to a polynomial of the form ($A + Bt + Ct^2 + Dt^3$), between $t$ = 0 and the time at which the trace levels off (end of condensation). Since the attenuation [$(I_1^0 - I_1) \propto \chi(t)$] measures the cluster density,[20] one may thus estimate the concentration of the remaining monomer.[21] The constant of integration for (10) is evaluated by setting $Y(n, 0) = 0$, since at $t$ = 0 no $n$mer had been generated.

The rate of energy transfer to the ambient gas is the product of the second term in eq 8 and the cluster distribution function, integrated over $n$:

$$\left(\frac{dh_g}{dt}\right) = \Phi \int_2^\infty dn\, N(n,t)n^{2/3}\theta(n)Y(n,t) \quad (11)$$

where we have identified the specific enthalpy with the energy transferred. $N(n, t)$ is defined as the number density of $n$mers, and we have assumed it has the general form[22]

$$N(n,t) = fn\exp(-gn^2) \quad (12)$$

The conservation condition requires

$$\int_2^\infty N(n, t)n\,dn = N(1, 0)\chi(t) \quad (13)$$

where $\chi(t)$ is the fraction of starting material which entered the condensed phase. The choice of this functional form is not overly restrictive in so far as these experiments are concerned. Indeed, a delta function was also tested, and while the overall fit for the experimental runs was not quite as good as with (12) it did indicate that the model is not particularly sensitive to the precise form of the distribution function. The normalization condition leads to $f = (4/\pi^{1/2})g^{3/2}N(1, 0)\chi(t)$, when the lower limit is set at zero (approximately). The median size $\langle n \rangle$ can be determined graphically from

$$\int_0^{\langle n \rangle} nN(n, t)\,dn = \int_{\langle n \rangle}^\infty nN(n, t)\,dn \quad (14)$$

The maximum of $[nN(n, t)]$ is at $g^{1/2}$. To a very good approximation $n$ at $N_{max}$ is equal to the median size. Since $g$ is a function of time, the average size is then specified by $\langle n(t) \rangle = [g(t)]^{-1/2}$; thus, $g(t)$ characterizes the time dependence of the condensation process. For this function we assumed a simple form

$$g(t) = [1 + \chi^\beta(t)\langle n \rangle_\infty^2]^{-1} \quad (15)$$

where $\beta$ and $\langle n \rangle_\infty$ are two parameters of the model. This is equivalent for large $n$ to

$$\langle n(t) \rangle \approx \chi^{\beta/2}(t)\langle n \rangle_\infty \quad (16)$$

The limiting median size ($t \rightarrow \infty$) is $\langle n \rangle_\infty$ when $\chi = 1$. The parameter $\beta$ determines how fast the clusters grow, i.e., when their growth rate becomes very steep. If $\beta$ is assigned too small a value, then from eq 16, the median size of the clusters in the early stages of condensation becomes much larger than that allowed by kinetic collision numbers. An optimum value is 2.5.

Consider next the heat transfer parameter, $\theta$. It is plausible to expect that it is a function of $n$. As the clusters grow, their vibrational distribution spreads out in frequency so that single collisions become less effective in abstracting energy from the conglomerate. We assumed

$$\theta = h/(n + 1) \quad (17)$$

where $h$ is a parameter independent of $n$. By optimizing the functional fit of the density gradients, we find $h = 0.024$. For very small clusters, $\theta$ is of the order of 1%. For a cluster with 50–200 kcal/mol of vibrational energy (accumulated heat of condensation), the energy transferred per collision is therefore several kilocalories; this is consistent with $\langle \Delta E \rangle$ magnitudes derived for the deexcitation of highly energized molecules undergoing unimolecular reactions.[23]

The sticking coefficient $\alpha$ is also a function of $n$. Some atoms will not stick simply because of their trajectories, e.g., glancing collisions. When some monomers strike a cluster, the latent heat may not get delocalized rapidly enough, and the incoming atom essentially reevaporates. Unfortunately, the variation of $\alpha$ with $n$ is not known; it appears to be between 0.1 and 1.0.[24] We assumed $\alpha$ was independent of $n$, and set it equal to unity. If its value is independent of $n$ but less than one, only the rate of energy transfer is affected by the corresponding multiplicative factor; the *shape* of the $dh_g/dt$ curve is not changed [$\alpha$ factors in the solution for $Y(n, t)$].

The energy deposited upon addition of one monomer to a cluster size $(n - 1)$ is given by

$$\Gamma(n) = |\Delta E^\circ_n - \Delta E^\circ_{n-1} - \Delta E^\circ_1| \quad (18)$$

TABLE III: Values of $\langle n \rangle_\infty$ Estimated by Fitting the Model to Density Gradients

| Run no. | Scale factor | $\langle n \rangle_\infty$ | $(\Delta H^\circ_n/\langle n \rangle)/\Delta H^\circ_\infty$ [a] |
|---|---|---|---|
| A-21 | 1.73 | 200 | 0.53 |
| A-18 | 2.23 | 130 | 0.85 |
| B-24 | 3.80 | 400 | 0.79 |
| B-8 | 2.27 | 40 | 0.60 |
| A-27 | 2.18 | 2000 | 1.00 |
| B-5 | 3.04 | 250 | 0.83 |
| A-24 | 1.83 | 1400 | 0.92 |
| B-33 | 1.53 | 500 | 0.66 |
| B-11 | 2.38 | 40 | 0.61 |

[a] $\Delta H^\circ_\infty = 6.6 \times 10^{-12}$ erg.

where $\Delta E^\circ_n$ is the energy of formation of an $n$mer from monomers. We assumed $\Delta E^\circ \approx \Delta H^\circ$ [at the temperatures of interest this introduces an error of 10–20%, depending on $n$]. Then the difference equation may be rewritten as

$$\Gamma(n) = d|\Delta H^\circ_n|/dn \quad (19)$$

where $|\Delta H^\circ_n|$ is the enthalpy for the reaction, $Fe_n \rightarrow n$Fe. To integrate eq 11, a functional form for $\Gamma(n)$ must be inserted. Recalling our objective, to evaluate $\langle n \rangle_\infty$ for plotting vs. $q$ (Table I), tests with several expressions showed that the results were not sensitive to the assumed form. Since these preliminary tests all gave values close to those plotted in Figure 1, we introduced at this point the empirical expression which well represents the reduced theoretical calculations:

$$\Delta H^\circ_n/n = \Delta H^\circ_\infty(1 - n^{-0.25}) \quad (20)$$

This leads to

$$\Gamma(n) = |\Delta H^\circ_\infty|(1 - 0.75n^{-0.25}) \quad (21)$$

Equation 11 was then integrated numerically and $dh_g/dt$ determined at various times. The theoretical curves were fitted to the experimental histograms in the following way: $\beta$ was held constant, $\langle n \rangle_\infty$ was first set at a value (from kinetic theory) at which condensation occurred very rapidly; $h$ was then adjusted until the best visual fit was obtained. For the remaining runs, $\langle n \rangle_\infty$ was used as an adjustable parameter. Representative graphs of the agreement attained between the calculated and experimental points are shown in Figure 6a–c. The theoretical values had to be multiplied by a constant scale factor, approximately 2.5, to normalize the values at the peaks.[25] The results are summarized in Table III. Fluctuations in the scale factor from run to run are attributable to our experimental error, and possibly inconsistent procedures in data reduction.

The curves in Figure 6a–c indicate that generally, during the early stages of condensation, the model predicts too fast a rate of energy input onto the carrier gas. This is due to the sensitivity of the model to the heat transfer parameter, $\theta(n)$. For small $n$, $\theta$ is large and energy transfer is efficient. It should be pointed out that experimentally, and in the computer model, the early stages of condensation incorporate the largest errors.

The model is relatively insensitive to changes in $\langle n \rangle_\infty$. Changes in $\beta$ affect the early stages of the energy transfer process when the clusters are quite small. While changes in either $\beta$ or $\langle n \rangle_\infty$ by 30% affect the fit only slightly, a change of 30% in the heat transfer parameter, $h$, is sufficient to spoil the fit. Figure 7a,b illustrate the magnitudes of these departures from optimum fit.

Using the values of $\langle n \rangle_\infty$ estimated from the model for each run, the experimental values of $\Delta H^\circ_n/\langle n \rangle$ were

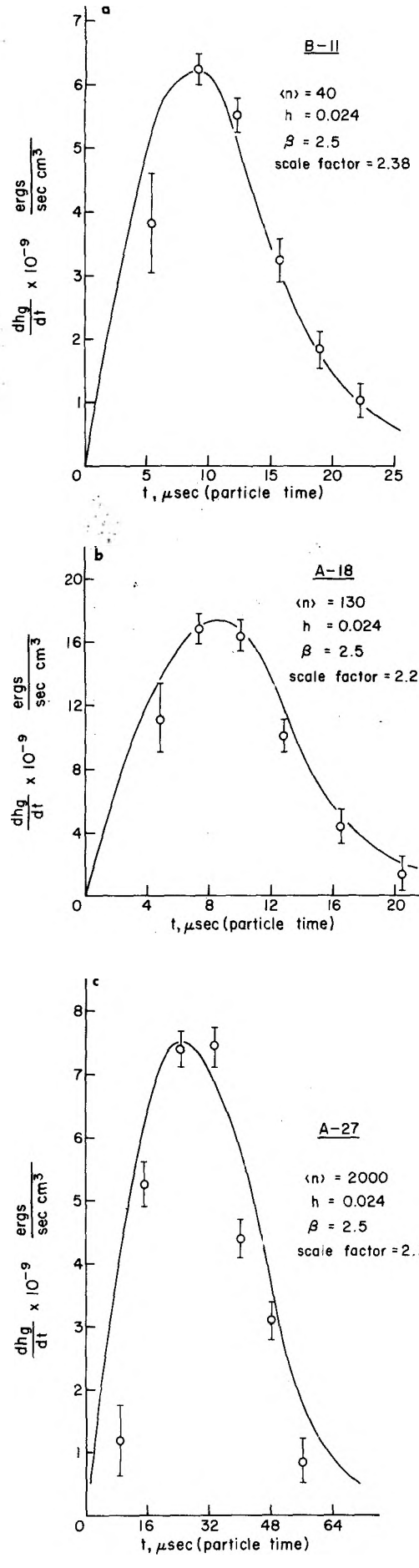


**Figure 6.** (a–c) Comparisons of computed $dh_g/dt$ curves with experimental points derived from density gradient traces, such as illustrated in Figure 5.

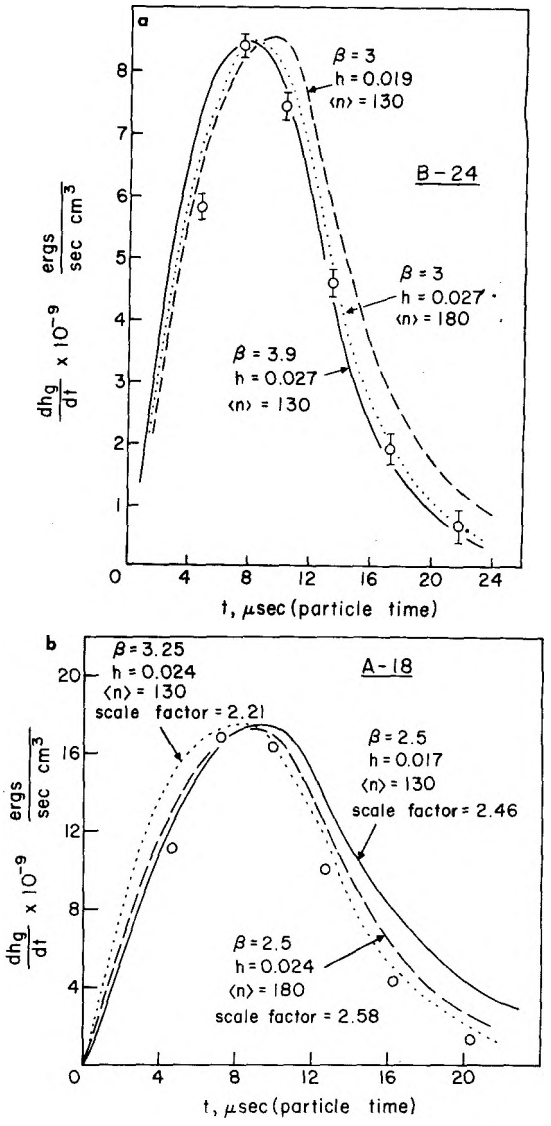


**Figure 7.** (a,b) Typical sensitivity tests for model parameters.

plotted vs. the average size. These were included in Figure 1, and they do cluster about the curve for

$$\Delta H^\circ_n/\langle n\rangle = \Delta H^\circ_\infty[1 - \langle n\rangle_\infty^{-0.25}]$$

quite well, providing a self-consistency check on the function used in developing the model. Furthermore, with the determined parameters, the time dependence of the distribution function may be plotted. Figure 8 shows $N(n, t)$ at a sequence of times during condensation for run A-18. The spreading out with time is due to the random growth process.

## Critique of Model

Considering the simplicity of the energy transfer model, it is remarkable that good agreement was obtained between the calculated and observed $(dh_g/dt)$ vs. $t$ curves. By using the hard-sphere kinetic theory for collision numbers we neglected long-range attractive forces when a monomer encounters a Fe cluster. Coagulation was neglected, but on our time scale it is an insignificant factor; the proper time dependence was obtained. The other obvious assumptions, such as spherical droplets and use of bulk density (to determine surface area from the numbers of atoms (per cluster), are very difficult to avoid.

Perhaps the most remarkable conclusion developed in this study is the empirical scaling law for $\Delta H^\circ_n$. Within $\pm 0.1|\Delta H^\circ_\infty|$, the large variety of theoretical calculations and

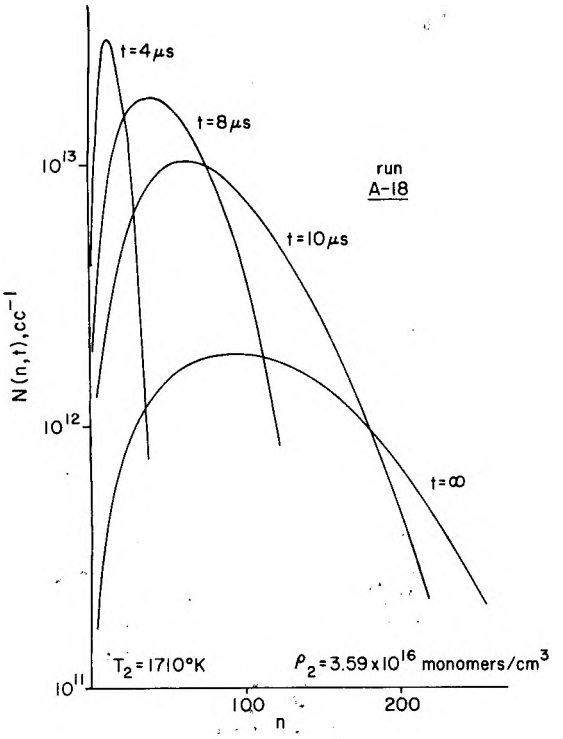


**Figure 8.** Evolution of the derived distribution function.

materials (for $n \lesssim 10^2$), and our experimental values for Fe vapor ($n \lesssim 2 \times 10^3$), all fit the $(1 - n^{-0.25})$ factor. It is plausible to postulate that for much larger $n$ this will drift over to $(1 - n^{-0.33})$, as is required for a model in which the total energy of a droplet is partitioned between the internal volume and a surface layer (ref 3b, p 4). However, it is for values of $n < 10^2$ that the empirical function is crucial for estimating magnitudes of $\Delta G°_n$; this is discussed in the accompanying manuscript.

*Acknowledgment.* This investigation was supported by the National Science Foundation through the Material Science Center of Cornell University. We are indebted to Professor Michael E. Fisher for many helpful discussions.

## References and Notes

(1) R. T. V. Kung and S. H. Bauer, "Shock Tube Research", 8th International Symposium, Chapman and Hall, London, 1971, paper No. 61.
(2) J. Frenkel, "Kinetic Theory of Liquids," Oxford University Press, London, 1946, Chapter VII.
(3) (a) W. J. Dunning, "Nucleation", A. C. Zettlemoyer, Ed., Marcel Dekker, New York, N.Y., 1969, Chapter I. (b) F. F. Abraham, "Homogeneous Nucleation Theory", Academic Press, New York, N.Y., 1974.
(4) J. K. Lee, J. A. Barker, and F. F. Abraham, *J. Chem. Phys.*, **58**, 3166 (1973).
(5) (a) K. A. Gingerich, *J. Crystal Growth*, **9**, 31 (1971); (b) *J. Chem. Phys.*, **66**, 483 (1977).
(6) K. A. Gingerich, A. Desideri, and D. L. Cocke, *J. Chem. Phys.*, **62**, 731 (1975).
(7) K. A. Gingerich, D. L. Cocke, and F. Miller, *J. Chem. Phys.*, **64**, 4027 (1976).
(8) J. B. Fenn, M. Sinka, and N. Lee, Report to Project SQUID, April, 1976, Yale University.
(9) A. B. Anderson, *J. Chem. Phys.*, **64**, 4046 (1976).
(10) R. C. Baetzold and R. E. Mack, *J. Chem. Phys.*, **62**, 1514 (1975).
(11) J. G. Fripiat, et al., *J. Mol. Catal.*, **1**, 59 (1976); R. P. Messmer, et al., *Phys. Rev. B*, **13**, 1396 (1976).
(12) A. Gelb, K. D. Jordan, and R. Silbey, *Chem. Phys.*, 9, 175 (1975).
(13) C. E. Dykstra and H. F. Schaefer, III, *J. Chem. Phys.*, **65**, 5141 (1976).
(14) J. J. Burton and C. L. Briant, *J. Chem. Soc., Faraday Trans. 2*, **69**, 540 (1973); *Acta Metall.*, **21**, 1225 (1973).
(15) W. D. Kristensen, E. J. Jensen, and R. M. J. Cotterill, *J. Chem. Phys.*, **60**, 4161 (1974).
(16) J. Kiefer and R. Lutz, *J. Chem. Phys.*, **44**, 648 (1966).
(17) J. A. Miller, Ph.D. Dissertation, Cornell University, January, 1974.
(18) P. M. Walsh and S. H. Bauer, *J. Phys. Chem.*, **77**, 1078 (1973).
(19) For example, see E. E. Salpeter, *J. Chem. Phys.*, **58**, 4331 (1973).
(20) For spherical absorbing scatterers, of dimensions much less than the wavelength of light, Mie theory gives for the ratio of transmitted to incident intensities

$$I/I_0 = \exp(-N_n l C_{ext})$$

$$C_{ext} = -(6\pi/\lambda) I_m[(m^2 - 1)/(m^2 + 2)]\langle v_n \rangle$$

where $l$ is the path length, $I_m$ [...] is the imaginary part of the complex index of refraction ratio, and $\langle v_n \rangle$ is the mean volume per unit $n$mer $= nv_c$.
(21) S. C. Graham and J. B. Homer, *Faraday Symp., Chem. Soc.*, **No. 7**. 85 (1973).
(22) C. G. Granqvist and R. A. Buhrman [*J. Appl. Phys.*, **47**, 2200 (1976)] found that for the finely dispersed metal powders they produced by evaporation under an inert gas atmosphere, the *logarithm* of the *particle diameter* had a Gaussian distribution.
(23) P. J. Robinson and K. A. Holbrook, "Unimolecular Reactions", Wiley-Interscience, London, 1972, Section 10-2.
(24) A sticking coefficient, $\alpha \approx 1/3$ was derived for lead clusters at relatively low supersaturations (30–1000) from growth rates based on light scattering data [paper 4 in this sequence]. This applies to clusters in the range of $10^3 < n < 10^6$, at temperatures 800–1100 K.
(25) That a scale factor other than unity had to be introduced for matching peak heights demonstrates that within the sensitivity of these experiments the hard sphere collision number, with $\alpha = 1$, *underestimates* the effective accretion number by ≈2.5. A refined treatment of accretion rates based on a realistic interaction potential for termolecular collisions is given in the accompanying manuscript.

# Homogeneous Nucleation in Metal Vapors. 3. Temperature Dependence of the Critical Supersaturation Ratio for Iron, Lead, and Bismuth

**D. J. Frurip and S. H. Bauer***

*Department of Chemistry Cornell University, Ithaca, New York 14853* *(Received July 19, 1976; Revised Manuscript Received March 7, 1977)*

The temperature dependence of the critical supersaturation ratio was measured for the onset of very rapid condensation from the vapors to "liquid" clusters for iron, lead, and bismuth. Controlled supersaturation levels were generated by shock heating corresponding organometallics, highly diluted in argon. Both incident and reflected shock regimes were used. While the conditions for attaining criticality differed markedly for the two modes of operation, the two sets of data check quite well. We demonstrated that even though the experiments are inherently subject to substantial random errors, none of the current theories for homogeneous nucleation satisfactorily predict, to within generously allocated error limits, the observed $S_c(T)$. Empirically the data are best represented by functions of the form $S_c(T) = 10^2 a \exp(-10^{-3} bT, \mathrm{K})$ with $0.7 \leq a \leq 2$ and $1.5 \leq b \leq 3.5$. We conclude that in view of the concurrent ambiguities in the magnitudes of the *assumed* flux currents and the dependence of the surface tension on temperature, one may question whether determination of $S_c(T)$ can provide a meaningful test for the classical theories of condensation.

## Introduction

This is a brief report on the determination of critical supersaturation ratios for avalanche condensation from the vapors of iron, lead, and bismuth, and of their dependence on the temperature. Our experimental approach [developed by Kung and Bauer,[1] and Homer and Prothero[2]] consisted of shock heating gaseous organometallics [$Fe(CO)_5$, $Pb(CH_3)_4$, and $Bi(CH_3)_3$] to temperatures such that all the ligands were stripped from the central metal atom within a few microseconds after passage of the shock front. Specified supersaturation levels with respect to the metal atoms were thus produced. The onset of condensation under essentially isothermal conditions was monitored by measuring the attenuation of an unpolarized He–Ne laser beam, as a function of time. A listing of the requisite turbidity equations is given below.

In a system which is sufficiently dilute, so that multiple scattering can be neglected, and the scattering–absorbing particles are randomly positioned, the transmitted intensity of monochromatic radiation is $I = I_0 \exp(-\tau l)$, where $\tau$ is the "turbidity", expressed in terms of $\tau = NC_{ext}$; $N$ is the number density of particles, and $C_{ext}$ is an extinction cross section. From Mie's full solution for small absorbing spheres[3] [$\lambda >>$ mean diameter], for unpolarized incident radiation

$$C_{ext} = -\frac{6\pi\langle v\rangle}{\lambda} I_m\left[\frac{m^2-1}{m^2+2}\right] \qquad (1)$$

where $\langle v\rangle$ is the mean particle volume, $\langle v\rangle = \int vP(v)\,dv$; $P(v)$ is the normalized distribution function, and $m$ is the complex index of refraction [$m \equiv n' - iq$]. Hence, for a condensing system, where the density of particles is changing and unknown, turbidity measurements alone are insufficient to determine particle sizes. However, it has been shown[4] that the recorded turbidity signal, $(I_0 - I)$, is directly proportional to the mass fraction of the metal condensed. Since the nucleation rate is extremely sensitive to the supersaturation ratio, $S$, it is expected and experimentally confirmed that $(I_0 - I)$ shows a very fast rise for high $S$, once condensation starts. As the supersaturation ratio is reduced, the nucleation rate decreases rapidly and approaches zero at the critical $S_c$. Then the transmitted signal shows little deviation from the initial light level.

TABLE I: Equilibrated Species Considered in NASA Program

| Precursor | Equilibrated species (gaseous) |
|---|---|
| $Fe(CO)_5$ | $Fe(CO)_5$, Fe, CO, Ar |
| $Pb(CH_3)_4$ | $Pb(CH_3)_4$, Pb, $CH_3$, $CH_2$, CH, $H_2$, $C_2H_6$, $C_2H_4$, $CH_4$, Ar |
| $Bi(CH_3)_3$ | $Bi(CH_3)_3$, Bi, $CH_3$, $CH_2$, CH, $H_2$, $C_2H_6$, $C_2H_4$, $CH_4$, Ar |

Detailed descriptions of the operation of shock tubes and the appropriate gas dynamic relations are given in standard texts.[5] To compute the temperature of the shock heated gas from the measured shock velocity, one must specify the thermodynamic state of the gas sample immediately after passage through the "shock front". In these studies one must adjust conditions so that dissociation of the metal bearing compound occurs very quickly compared to the subsequent condensation kinetics. To select appropriate shock parameters, we used the NASA "equilibrium shock" program.[6] Standard enthalpies of formation, standard entropies, the initial concentration of the parent compound, and appropriate heat capacity data must be inserted as parameters to perform the calculations. The temperature dependent free energy functions for all the product species must also be included. The species which we assumed to have attained equilibrium are listed in Table I.

No rate data are available for the unimolecular decomposition of $Fe(CO)_5$. By analogy with similar compounds, such as $Ni(CO)_4$, the rate is presume to be very fast at shock temperatures, 1500–2500 K.[1,7] We estimate that at 1500 K the half-life for the complete stripping of the CO groups is less than 1 ns. Vapor pressure data[8] for Fe and $Fe(CO)_5$ indicate that a sample of $Fe(CO)_5$ can be prepared at room temperature such that under typical incident shock conditions the concentration of Fe atoms is sufficiently supersaturated to condense. Experiments showed that at moderate supersaturation, the time for complete condensation of the Fe vapor was of the order of 50 $\mu$s. The experimental requirements are therefore met for $Fe(CO)_5$ at temperatures greater than 1500 K.



The Journal of Physical Chemistry, Vol. 81, No. 10, 1977

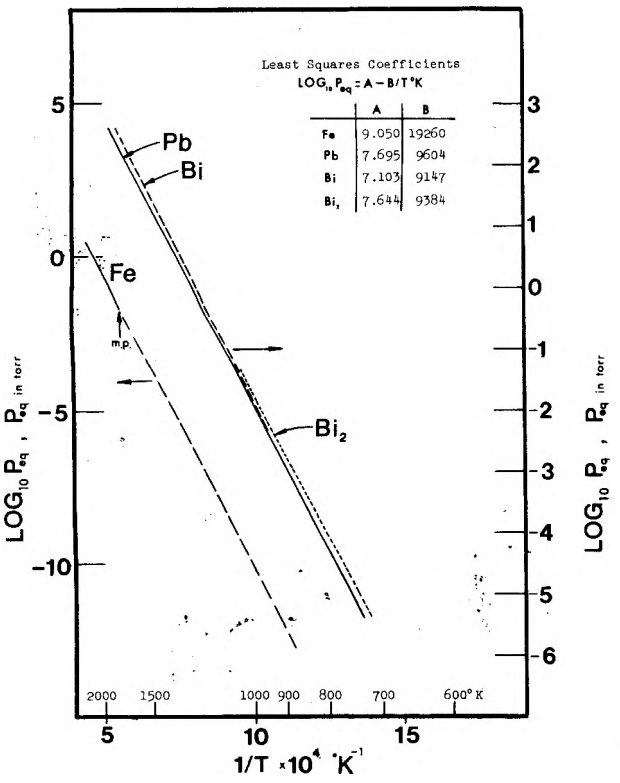


**Figure 1.** Vapor pressure data.

Homer and Hurle[9] measured the rate of decomposition of $Pb(CH_3)_4$ over the temperature range 890–1060 K, and found for the unimolecular rate constant

$$\log k_{TML} = (13.25 \pm 0.4) - (9.0 \pm 0.4) \times 10^3/T \text{ K} \quad (2)$$

As in the case of $Fe(CO)_5$, the removal of the first $CH_3$ group was assumed to be rate limiting and that the subsequent stripping of the remaining methyl groups occurs much faster. They noted that there were no reports of stable intermediate lead–methyl radicals. As will be described below, the time for complete condensation of lead at supersaturations near critical was experimentally determined to be of the order of 300 μs. Hence at least 90% of the TML should be decomposed within about one third of that time after passage of the shock front. By setting $t_{90\%} = \ln(10)/k_{TML} = 100$ μs we find that this condition is met for temperatures above 980 K. Vapor pressure data for Pb (Figure 1) show that large supersaturation ratios can easily be obtained at these temperatures for a dilute mixture (≈1%) of the TML in Ar. Thus, the experimental requirements are also met for TML, as long as the shocked gas temperature is above 980 K. The methyl radicals recombine rapidly to produce $C_2H_6(g)$, $C_2H_4(g) + H_2(g)$, and $CH_4(g) + CH_2(g)$, etc. These species, along with TML(g), $CH_3(g)$, Pb(g), and Ar(g), were considered to be in thermal equilibrium for calculating the shocked gas temperature (Table I).

Price et al.[10] determined the rate of decomposition of trimethylbismuth (TMB) over the temperature range 600–900 K, by measuring yields of $CH_4(g)$ and $C_2H_6(g)$ [$H_2$ and $C_2H_4$ were also observed but in minute amounts]. They observed that total decomposition to the free metal and methyl groups was fast relative to the initial bond rupture, and report for the unimolecular rate constant

$$\log k_{TMB} = 14.0 - 9.61 \times 10^3/T \text{ K} \quad (3)$$

As does TML, within 150 μs, 90% of TMB is decomposed at a temperature of 980 K. However, we decided to use an alternate technique for bismuth, as outlined below.

Experiments with reflected shocks, the technique developed by Kung and Bauer,[4] have two advantages: (1) the temperature range can be extended to lower values, and (2) the efficiency of data collection is considerably increased since a determination of $S_c(T)$ is obtained per successful run. The shock tube was *tuned* so that the reflected shock, head of the expansion fan, and contact surface met at approximately the same position in the shock tube. The net result is an exponential decay of temperature and pressure after a specified dwell time. The elevated temperature and relatively long residence time in the reflected shock regime results in rapid and complete decomposition of the TMB to generate an *undersaturated* vapor. However, after the expansion wave cools the shock heated gas the level of supersaturation rises, and eventually the Bi vapor becomes critically supersaturated and condensation sets in. With the NASA program one may calculate conditions in the expansion wave at the critical *take-off point*, using the instantaneous pressure, as measured by the piezoelectric sensor. The corresponding temperature in the expansion wave is given by the adiabatic relation

$$T_5/T_{5e} = (P_5/P_{5e})^{\gamma_5^{-1}/\gamma_5} \quad (4)$$

where the subscripts 5 and 5e refer to the reflected shock and expansion waves, respectively. For dilute samples, the heat capacity ratio, $\gamma_5$, is that of the inert gas diluent. Since the critical supersaturation condition is attained in every run, one $S_c(T)$ point is observed in every experiment. To obtain data over a wider range of temperatures, one need only vary the initial pressure of the test gas or change the sample composition.

## Experimental Section

*Sample Preparation.* Samples of the metalloorganics $Fe(CO)_5$, $Pb(CH_3)_4$, and $Bi(CH_3)_3$ were purified and diluted in argon, to concentrations 0.1–2.0 mol %; ultra-high-purity argon (99.999%) was used as a diluent. The mixtures were allowed to stand for a minimum of 24 h before use. The metal bearing compounds, all liquids with appreciable vapor pressures at room temperature, were obtained from Alfa Inorganics Co. The $Fe(CO)_5$ was doubly distilled and only the middle fraction was used in preparing the sample. The suppliers indicated that the $Bi(CH_3)$ was pure; it was used without further purification except for repeated freezing and outgassing. The $Pb(CH_3)_4$ was obtained as an 80% solution in toluene. This was purified to 99.5 ± 0.2% on a Hewlett Packard Model 700 gas chromatograph, using a 6-ft 10% Carbowax 20M prep-column. Adequate resolution of the toluene and TML peaks was available at a column temperature of 150 °C. During the latter stages of the experiments we obtained pure TML from the ROC-RIC Co. The experimental results remained unchanged.

*The Shock Tube.* A detailed description of the 1.5-in. brass shock tube used in this experiment has been published.[11] The length of the driver section was 4 ft; the test section was 13 ft long for the incident shock experiments, but was shortened to 10.5 ft for the reflected shock experiments. Lucite windows (1 in.) were mounted flush with the inside walls 10 ft 4 in. downstream from the diaphragm. The shock tube was operated in the single pulse mode using a $3.28 \times 10^4$ cm$^3$ dump tank. The diaphragms were mylar and ranged in thickness from 0.5 to 5 mil. Pure He or mixtures of He and $N_2$ were used as driver gases. A barium titanate pressure transducer upstream from the window actuated the electronics. Four platinum film gauges were used for measuring shock speeds. The output

from the gauges was amplified and fed into a Tektronix Model 535 oscilloscope, modified to provide 10 μs time marks to the raster display. Pressure history was monitored with a Kistler No. 610 quartz pressure transducer located immediately above the observation windows. The tube leak-outgassing rate was 0.5 mTorr/min.

*Optical Arrangement.* An unpolarized 1.5-mW Edmund Scientific He–Ne laser (6328 Å) was directed through the center of the shock tube windows. Care was taken to direct the incident and transmitted beams normal to the windows; this ensured that the beam was also perpendicular to the flow. At a distance of about 2.5 cm from the exit window, the beam passed through an adjustable iris which was set to be slightly larger than the beam diameter at that point (2 mm). An EMI-9634 phototube was located 1 m from the exit window; it had a $(1/e)$ rise time of 3.0 μs. The entrance to the phototube was masked with a 6328 ± 2 Å interference filter, and a ground glass diffuser. There are no Ar, Bi, Pb, Fe, Hg, or Na emission lines in the range 6328 ± 2 Å. The combination of the iris plus the relatively large distance between the phototube and the shock tube ensured that a negligible amount of black-body radiation from the condensing particles reached the detector. The phototube output (with the laser off), for every metal studied, showed no significant intensity from thermal emission. The output from the phototube was monitored simultaneously with the output from the pressure transducer on a Tektronix Model 502 dual beam oscilloscope. This allowed us to determine the exact shock arrival time in the incident shock experiments. In studies with reflected shocks this recorded the pressure history throughout the entire experiment and the essential data for calculating the temperature of the gas at the turbidity take-off point.

The powder that settled inside the tube was analyzed via powder x-ray diffraction. The results confirmed the presence of crystallites of the several metals. In addition, an analysis of the diffraction line widths gave crystallite sizes which agreed with an electron microscopic examination of particle sizes. To prevent any heterogeneous nucleation on the metal particles attached to the walls, the tube was thoroughly cleaned after each run with a cheesecloth swab moistened with ethanol.

## Data Reduction

*Incident Shock Experiments with Fe and Pb.* Figure 2 shows a typical set of turbidity traces for a single concentration of $Fe(CO)_5$, 0.74% in Ar. The four records are for the same initial sample pressure but for differing shock strengths. Shock arrival is indicated by the step function in the pressure recorded by the gauge in the plane of the observation window center. At low temperatures (high supersaturations), $(I_0 - I)$ shows a very rapid increase due to attenuation by the condensate, then a flat plateau. Freund[4] and Homer[9] demonstrated that "plateauing" occurs when all the monomer had entered the condensed phase. As the shock temperature was increased, the level of supersaturation decreased, and the rate of condensation slowed, indicated by the longer time for the $(I_0 - I)$ trace to attain the plateau. Eventually a temperature and a supersaturation level was reached where no condensation appeared within 500 μs past shock arrival. This condition is identified as the critical supersaturation ratio, $S_c$, at the temperature $T$. Its magnitude is given by the ratio of the calculated pressure of metal vapor behind the incident shock to the equilibrium vapor pressure at that shock temperature. The approach to $S_c$ was repeated several times, starting either with a new initial total pressure of the same mixture or at the same initial pressure but with new concentrations. Thus, we were able to collect critical supersaturation data over a extended range of temperatures.

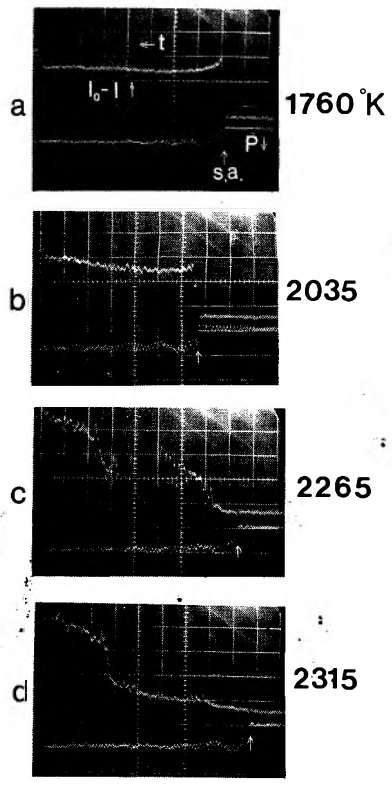


**Figure 2.** A typical set of traces for the incident shock experiments, showing pressure and transmitted intensity. For this sequence, 0.74% $Fe(CO)_5$ in Ar was subjected to increasing shock Mach numbers by increasing the diaphragm thickness, and thus the driver pressure. Shock arrival is indicated by the arrow (↑); lab time scale is 100 μs/division. Light extinction shows a rapid rise to a plateau, at the lower temperatures, due to very rapid condensation. As the supersaturation ratio is decreased the rise to the plateau becomes gradual. The critical condition was interpolated as being midway between 2265 and 2315 K. The fluctuating turbidity during later times in these two traces is probably due to diffusion of large particles into the narrow laser beam.

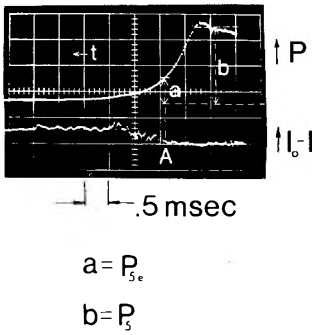


**Figure 3.** A typical oscilloscope record for a reflected shock experiment. Lab time scale = 0.5 ms/division.

*Reflected Shock Experiments with Bi.* A typical pressure–intensity record for a reflected shock in Bi vapor (diluted in Ar) is shown in Figure 3. The turbidity trace shows no evidence of condensation in the incident and reflected shock regimes, as expected, since the incident shock temperature is too low for rapid TMB decomposition while the reflected shock temperature is high enough to generate an undersaturated state. The decay of the pressure trace indicates the arrival of the expansion wave which cools the gas via an adiabatic expansion. Thus a temperature is reached such that the Bi vapor attains critical supersaturation, and begins to condense. That point appears in the turbidity trace where the laser beam

TABLE II: Physical Data for Fe, Bi, and Pb

| | Fe | Bi | Pb |
|---|---|---|---|
| Surface tension $\sigma(T)$, erg cm$^{-2}$ | 2187-0.22$T$ K | 418-0.07$T$ K | 514-0.09$T$ K |
| Liquid density $\rho(T)$, g cm$^{-3}$ | 8.5-8.5 × 10$^{-4}T$ K | 10.7-1.2 × 10$^{-3}T$ K | 10.7-1.3 × 10$^{-3}T$ K |
| Melting point-boiling point, K | 1808-3273 | 544-1723 | 600-1893 |
| $\Delta H_{vap}$, kcal/mol | 84.6 | 42.6 | 42.0 |
| Crystal structure | bccub | $O_h$ | fccub |

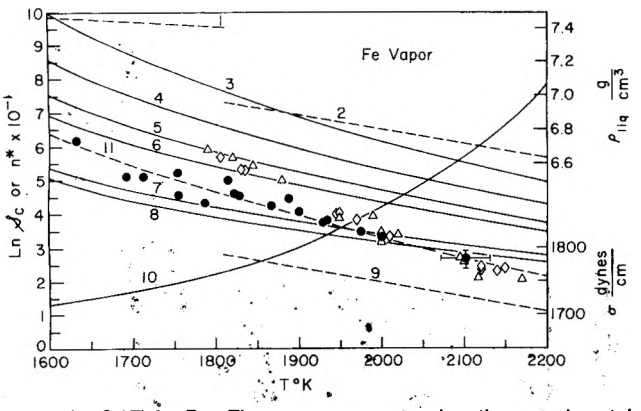


**Figure 4.** $S_c(T)$ for Fe. The curves superposed on the experimental points show theoretical values, according to the following key: (1) metal solid density (measured); (2) metal liquid density (measured); (3) classical theory with $J = 10^{16}$ cm$^{-3}$ s$^{-1}$; (4) classical theory with $J = 10^{12}$; (5) classical theory with $J = 10^{8}$; (6) classical theory with $J = 10^{5}$; (7) Lothe-Pound theory with $J = 10^{16}$; (8) Lothe-Pound theory with $J = 10^{12}$; (9) metal liquid (bulk) surface tension (measured); (10) critical size cluster; (11) best fit exponential to data points of this work (●). (◊) Kung's results from turbidity data in the expansion wave; (△) Kung's results from black-body emission data.

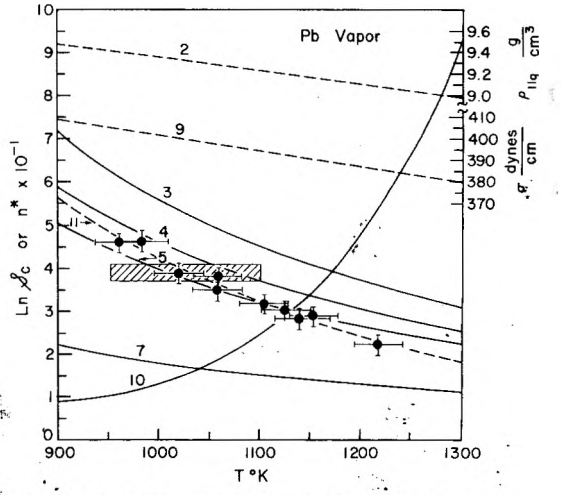


**Figure 5.** $S_c(T)$ for Pb. The key is the same as Figure 4.

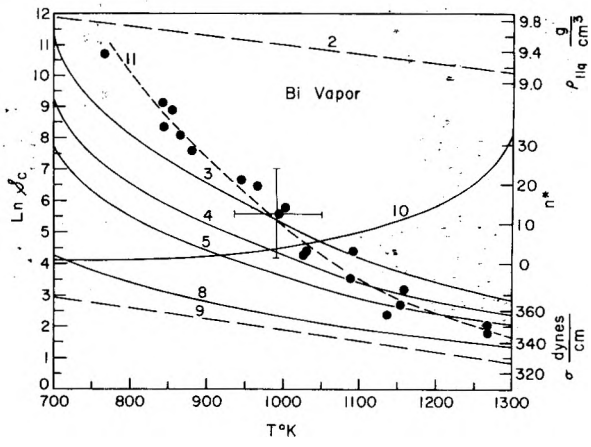


**Figure 6.** $S_c(T)$ for Bi. The key is the same as for Figure 4.

is first attenuated (point A in Figure 3); it is identified as the critical supersaturation ratio at the temperature $T_{5e}$, calculated from eq 4. The ratio $P_5/P_{5e}$ was measured directly from the recorded output of the transducer. To obtain data over a wide range of temperatures we had only to vary (judiciously) the following: diaphragm thickness, initial test section pressure, sample concentration, and molecular weight of the driver gas. The shock tube became "detuned" (i.e., the pressure history in the reflected and expansion waves showed some unwanted structure) when the above parameters were changed too drastically. The tube was then retuned by adjusting the length of the driver section for each temperature range.

We investigated the possibility of applying these techniques to the study of condensing silicon, using the precursors $Si(CH_3)_4$ and $SiH_4$. At incident shock temperatures (1000–1500 K), a 1% sample of TMS did not decompose fast enough to produce a critically saturated metal vapor. However, the absorption signal at 6328 Å showed an initial rise and return to zero (within 50 μs) which we attributed to a short lived absorbing intermediate in the decomposition process. A 1% sample of silane did show evidence of decomposition under these conditions, to form a critically supersaturated vapor. The attenuation signal showed a rise and plateau, characteristic of condensation. We conclude that silane is a good candidate for a source of silicon atoms.

## Comparison of the Experimental Results with Theory

The "classical" and Lothe-Pound (LP) predictions of $S_c(T)$ for Fe, Pb, and Bi are compared with our experimental points in Figures 4–6. A summary of the values for the bulk surface tension, $\sigma$, and the bulk (liquid) density, $\rho$, used in these calculations is given in Table II. Since no data are available for the temperature dependence of the surface tension of Fe(l), Kung and Bauer[1] estimated $\sigma(T)$ from surface entropy values; the same functional dependence was assumed here. In the case of iron, the experimental data spanned the bulk melting point. We extrapolated the values of $\sigma(T)$ and $\rho(T)$ from the liquid region into the solid region. In our search for the "best fit", the calculations were repeated for various values of the condensation current, $J$ (number of nuclei generated per second per centimeter$^3$). For the LP case, the value of the "replacement factor", $q_{rep}$, was set equal to unity. The moment of inertia of an $n$mer, $I_n$, inserted in the rotational partition function was assumed to be that for a sphere of uniform density

$$I_n = \frac{2}{5}nmr^2 = \frac{2}{5}nm\left(\frac{3n}{4\pi\rho_n}\right)^{2/3} \quad (5)$$

where $m$ is atomic mass and $\rho_n$ is the number of atoms per unit volume. In the classical BD theory $S_c(T)$ and $J$ are related via a cubic equation

$$\alpha(T)\ln^3 S - \ln J \cdot \ln^2 S - \beta(T) = 0 \quad (6)$$

where $\alpha(T)$ and $\beta(T)$ are collections of temperature dependent parameters. In the LP formulation an iterative process must be used to complete the calculation.

*Iron Vapor.* Inspection of Figure 4 shows that for reasonable values of the condensation current ($10^5 \leq J \leq 10^{16}$ s$^{-1}$ cm$^{-3}$), the experimental points exhibit a temperature dependence which is steeper than predicted by either theory, although they are closer to the LP envelope of curves than to the BD curves. Empirically, they are well expressed by

$$\ln S_c = 77.88 \exp[-1.57 \times 10^{-3} T \text{ K}] \quad (7)$$

with a correlation coefficient of 0.95. The results of Kung and Bauer were also included in Figure 4. Their values show a somewhat steeper temperature dependence, since their points superpose the present set for $T > 1900$ K but rise above them for lower temperatures. Note that they used the onset of black body radiation, rather than turbidity to ascertain the start of avalanche condensation, and operated with reflected shocks rather than incident shocks. On the whole, the agreement is very good. The deviation at lower temperatures may be due to the relatively large uncertainty in estimating the temperatures in the expansion wave.

We estimated the length of the error bars for the present data by noting that the largest single source of error in the turbidity experiments is the shock temperature. The maximum uncertainty in measuring the shock speed is ±0.02 mm $\mu$s$^{-1}$. To minimize the error in reading the finite width of the raster pulse measurements were made from peak to peak. This gave us a random error of about ±30 K in the calculated equilibrium temperatures. Because of the exponential temperature dependence of the equilibrium vapor pressure, the uncertainty in shock temperature results in maximum uncertainty in ln $S_c$ of ±0.25. The experimental uncertainty is therefore insufficient to bring our data down to the theoretical predictions.

It is interesting to note that Kung and Bauer estimated cluster temperatures to be 50–150 K higher than the ambient gas temperature due to the heat of condensation. The abscissa scale in Figures 4–6 should be $T_{\text{cluster}}$ since this determines the evaporation rate. For all the metals studied, the disparity between experiment and theory would be enhanced.

The condensation current, $J$, is an unmeasurable quantity in this experiment. One may inquire whether it is possible to fit the theoretical curves to the experimental points by using $J$ as an adjustable parameter. It is evident that the theoretical calculations are insensitive to value of $J$; for example, we must set $J \gtrsim 10^{24}$ s$^{-1}$ cm$^{-3}$ in order that the LP theory fit the lower temperature data. This is larger than any conceivable nucleation rate under the present conditions. At the other end, to fit the high temperature range requires $J \lesssim 1$ s$^{-1}$ cm$^{-3}$. This is obviously too slow, since we observed complete condensation of all the Fe monomer within 200 $\mu$s.

Since the theoretical curves are sensitive to the assumed value of the surface tension one can force fit the LP curves to the experimental points by selecting a temperature dependent surface tension. Curve 11 in Figure 4 shows the fit obtained by assuming the function

$$\sigma(T) = 4059 - 1.16T \text{ K, erg cm}^{-2} \quad (8)$$

The published surface tension values for Fe(l) at 1825 K[12,13] range from 1788 to 1865 erg cm$^{-2}$; eq 8 gives $\sigma = 1942$ erg cm$^{-2}$, which is only 0.4% above the largest experimental value. However, the temperature coefficient of 1.16 is much too large; similar factors for Bi and Pb were experimentally determined as 0.07 and 0.09, respectively. Also, since $\sigma \to 0$ as the temperature $T \to T_c$, one is led by eq 8 to a critical temperature for Fe of 3500 K, only 1700 K above its melting point, obviously much too low.

Note also that there is no break in the experimental data at the bulk melting point (1808 K). The clusters are generated with short-range order, as supercooled liquids, well above the nucleation temperature for transition to the solid phase.

*Pb Vapor.* Figure 5 shows the experimental points and the corresponding theoretical calculations for lead. Due to kinetic constraints on the rate of TML decomposition all the runs were made at temperatures greater than 980 K. As in the case of Fe vapor, the experimental points exhibit a temperature dependence which is too steep. The data were empirically fitted to an exponential function (curve 11)

$$\ln S_c = 69.4 \exp(-2.79 \times 10^{-3} T \text{ K}) \quad (9)$$

In contrast to the Fe data, the experimental values for Pb are close to the prediction of the classical BD theory with $J = 10^8$ s$^{-1}$ cm$^{-3}$. The uncertainty in the shock temperature leads to error bars about equal to those for Fe vapor, but they were insufficient to explain the observed deviations from theory. In this case, force fitting the experimental data to the BD curve, using $J$ as a parameter, leaves it within reasonable bounds.

The results of Homer and Hurle[9] are shown in Figure 5 as the shaded area. They did not find a temperature dependence for the critical supersaturation ratio over the range 950–1100 K. The center of the shaded envelope straddles our curve. One possible explanation for their temperature independence is that they calculated the shock temperature inserting the thermodynamic functions solely for the inert gas diluent. There is a substantial difference (≈100 K) between the calculated frozen and equilibrium temperatures. Due to the exponential temperature dependence of the equilibrium vapor pressure, Homer's calculated critical supersaturation ratios could be sufficiently changed to show the expected temperature effect.

*Bi Vapor.* Bismuth vapor has a unique feature in that the gas in equilibrium with the liquid contains a substantial concentration of dimers (Figure 1). Katz et al.[14] state that the corresponding definition of supersaturation ratio for a monomer–dimer equilibrium is

$$2\text{Bi(g)} \rightleftarrows \text{Bi}_2\text{(g)} \qquad K \equiv P_{\text{Bi}_2}/P_{\text{Bi}}^2 \quad (10)$$

$$S = (P_1 + P_2)/(P_{1\text{eq}} + P_{2\text{eq}}) = (P_1 + P_1^2 K)/(P_{1\text{e}} + P_{1\text{e}}^2 K) \quad (11)$$

This assumes that the distribution of dimers in the metastable regime is governed by the same equilibrium constant as for the undersaturated gas.

The results for Bi are shown in Figure 6. These data, which show the largest deviation from the theoretical predictions, are well represented by the exponential function

$$\ln S_c = 148 \exp[-3.39 \times 10^{-3} T \text{ K}] \quad (12)$$

with a correlation coefficient $r = 0.98$. For reflected, as well as for incident shock experiments, the largest uncertainty is due to the estimation of the temperature. We measured the incident shock speed and used only the initial pressure and the concentration of the sample as input to the NASA program. Since the reflected shock wave passes through the incident shock heated gas, conditions in the reflected shock are determined by the state of the previously shocked gas. Unfortunately, the NASA program was formulated for calculating reflected shock conditions for the extremes, either complete thermal

equilibrium or "frozen chemistry" in the incident shock. The reflected shock temperature, therefore, depends on whether the incident shock heated gas was thermally equilibrated. This, in turn, depends on the residence time in the incident shock. In typical runs the incident shock residence time was not long enough for complete thermal equilibrium yet not short enough to justify the assumption of "frozen" conditions. This resulted in a larger uncertainty in the *absolute* reflected shock temperature, ±60 K. We could not alleviate this problem simply by increasing the window to endplate distance, and thus increase the incident shock residence times. In order to obtain the correct conditions in the reflected shock and subsequent expansion wave, the incident shock temperature had to be in a range such that appreciable condensation will occur. Since we wanted to minimize condensation in the incident shock regime, we kept the incident shock residence times short by keeping the window to endplate distance small.

The uncertainty in the temperature results in an *absolute* uncertainty in ln $S$ of ±1.5 for the entire experimental temperature range. Nevertheless the uncertainty is insufficient to account for the steepness of the $T$ dependence, or remove the deviation between the low temperature experimental data and closest theoretical curve (BD, $J = 10^{16}$ s$^{-1}$ cm$^{-3}$). A force fit, using $J$ as a parameter, results in an unreasonably large estimate for $J$ ($\gtrsim 10^{21}$ s$^{-1}$ cm$^{-3}$) in the low temperature regime.

Furthermore, although the absolute error in the temperature is relatively large, the relative temperatures are properly related. For this reason, we believe that the observed temperature dependence is reliable.

## Conclusions and Comments

We investigated the possibility that contaminants affected the nucleation process. Since the nucleation rate is a strong function of the surface tension, the presence of oxygen at sufficient levels could lower the surface tension of the molten metals and thereby increase the nucleation rate. A mass spectrum was taken of the experimental mixtures of Ar + $Fe(CO)_5$; no $O_2$ was introduced during sample preparation, and the level of oxygen was *less than* 1% of the $Fe(CO)_5$ concentration. The measured outgassing-leak rate of the shock tube was less than 0.5 mTorr/min. A maximum of 2 min elapsed between the time the sample was introduced to the shock tube and diaphragm rupture. Thus, approximately 0.2 mTorr of $O_2$ could have been introduced. Since the sample typically contained 250 mTorr of the metal carrier the maximum *relative* oxygen concentration was 0.1%. To prove that this level of contamination had no effect on these experiments, a mixture of 0.5% $Fe(CO)_5$ and 0.005% $O_2$ was prepared (10 times the maximum $O_2$ contamination expected). Turbidity data from this sample were indistinguishable from our previous results. The presence of dust in the shock tube might also affect the nucleation rate. A series of turbidity runs were made on a 0.5% sample of $Fe(CO)_5$ that had passed through a 250-Å pore size Millipore filter prior to injection into the clean shock tube. Again, no differences were discernable. An additional argument against spurious dust affecting our $S_c$ values is the overall consistency of our data. The runs were made in a random sequence with respect to shock temperatures, yet they fall on a smooth curve. Contaminations by either ions or dust would have resulted in considerable scatter.

To demonstrate that the incident and reflected shock experiments gave the same results, we ran several reflected shocks for Pb and for Fe. The critical supersaturations determined by this method agreed within 10% with the incident shock results.

We conclude the following for iron: (1) The experimental data do not fit either the LP or BD prescriptions, but they lie closer to the LP curves. (2) The uncertainty inherent in our data and its analysis is insufficient to account for these deviations. (3) A force fit of the LP theory to the experimental points is possible using a modified surface tension function. However, the deduced function has an unreasonable temperature dependence. The classical BD theory does account for our data on Pb condensation, provided one uses a temperature dependent critical nucleation rate. Finally for Bi, our data lie closer to the classical theory prediction than to the LP, but no satisfactory fit to the data is possible. In view of the concurrent ambiguities in $J_{\text{critical}}$ and $\sigma(T)$, one may question whether the determination of $S_c(T)$ can provide a meaningful test of the classical theories of condensation.

## References and Notes

(1) R. T. V. Kung and S. H. Bauer, "Eighth International Shock Tube Symposium–Proceedings", Chapman and Hall, London, 1971.
(2) J. B. Homer, "Eighth International Shock Tube Symposium–Proceedings", Chapman and Hall, London, 1971.
(3) H. C. van de Hulst, "Light Scattering by Small Particles", Wiley, London, 1957.
(4) H. Freund, Ph.D. Thesis, Cornell University, August, 1975.
(5) E. F. Greene and J. P. Toennies, "Chemical Reactions in Shock Waves", Academic Press, New York, N.Y., 1964.
(6) S. Gordon and B. McBride, *NASA Spec. Publ.*, **No. 273** (1971).
(7) S. Matsuda, *J. Chem. Phys.*, **57**, 807 (1972).
(8) R. Hultgren, R. L. Orr, P. D. Anderson, and K. K. Kelley, "Selected Values of Thermodynamic Properties of Metals and Alloys", Wiley, New York, N.Y., 1963.
(9) J. B. Homer and I. R. Hurle, *Proc. R. Soc. London*, **61**, 327 (1972).
(10) S. J. Price and A. F. Trotman-Dickenson, *Trans. Faraday Soc.*, **54**, 1630 (1958).
(11) P. M. Jeffers, *J. Phys. Chem.*, **76**, 2829 (1972).
(12) T. J. Hugel, Ed., "Liquids: Structures, Properties, Solid Interactions", Elsevier, New York, N.Y., 1965.
(13) C. A. Hampel, Ed., "Encyclopedia of the Chemical Elements", Reinhold, New York, N.Y., 1968.
(14) J. L. Katz, H. Saltsburg, and H. Reiss, *J. Colloid Interface Sci.*, **21**, 560 (1966).

# Homogeneous Nucleation in Metal Vapors. 4. Cluster Growth Rates from Light Scattering

**D. J. Frurip and S. H. Bauer***

*Department of Chemistry, Cornell University, Ithaca, New York 14853* *(Received July 19, 1976; Revised Manuscript Received March 7, 1977)*

We describe an experimental arrangement for recording the turbidity developed in a metal vapor while it is undergoing homogeneous nucleation and condensation, and concurrently recording the intensity of light scattered at 90° by the growing clusters. The supersaturated vapors were generated by shock heating metalloorganics from which the attached groups ($CH_3$; CO) were stripped within the first few microseconds after passage through a shock front. The turbidity and scattered intensity data were collected with a time resolution of approximately 2 μs. Absolute time dependent scattering cross sections were evaluated for lead (vapor ⇄ clusters). The experimental configuration was calibrated with gases for which the scattering cross section are available (Ar and $CHF_2Cl$). From the ratio of $[I_{sca}/\ln(I_0/I)]$ we deduced separately the mean radii as a function of time, and the corresponding cluster densities. Our results are well accounted for by a simple kinetic theory model. As a consequence, we have an indirect procedure for estimating the condensation flux (nuclei generated $sec^{-1}$ $cm^{-3}$) at critical supersaturation and the time-dependent parameters for the cluster size distribution function.

## Introduction

Among the various diagnostics we tested for observing nucleation–condensation processes in metal vapors, we found four which proved generally applicable. The onset of avalanche condensation can be established by recording a sudden rise either in the black-body radiation emitted from the tiny particles or in the turbidity of the sample. Thus we determined the variation of the critical supersaturation ratio with temperature for iron,[1] lead, and bismuth.[2] The dependence of the heat of condensation on cluster size for iron was estimated from measurements of post-shock density gradients[3] [applied to clusters: $40 < n < 2000$]. In this report we demonstrate the use of light scattering to follow growth rates of clusters of lead [applied to $10^4 < n < 2 \times 10^6$]. As a consequence we obtained approximate net condensation fluxes and cluster size distributions. The latter were verified by electron microscopic examination of the final metallic powders.

Turbidity data provide values for the product of the number density, $N = \sum N_n$, and the average volume, $\langle v \rangle$. To uncouple the two magnitudes one must either estimate the density directly or introduce an assumption. In a procedure described by Kerker,[4] generally used for static systems, one assumes that the total mass of material is in the condensed phase; then, knowledge of the initial concentration is sufficient to uncouple $N$ from $\langle v \rangle$. In the present experiments, since we do not have a priori knowledge of $N(t)$, we measured simultaneously the turbidity and the intensity of light scattered from the growing clusters. For absorbing spheres, the latter is proportional to the product $N\langle v^2 \rangle$, thereby providing the means for estimating $N(t)$ and $\langle v \rangle$ separately.

Although light scattering measurements have been applied extensively to a variety of systems few studies were made of homogeneous nucleation from the gas phase. Vietti and Schuster[5] determined the growth rates of large ($\sim 10^4$ Å) water droplets in air by detection of oscillations in the intensity of scattered light from a He–Ne source. Stein[6] investigated the angular and wavelength dependence of scattered light from a cloud of ice particles formed by homogeneous nucleation in nozzle expansion, and determined the average particle size and the density as a function of the supersaturation ratio. Ethyl alcohol droplets were similarly studied by Clumpner.[7] He measured the angular dependence of Rayleigh scattering. Graham and Homer[8] investigated Rayleigh scattering from lead particles generated by shock pyrolysis of $Pb(CH_3)_4$. They were primarily interested in the coagulation process, after all the monomer had entered the condensed phase and did not investigate the early growth regime.

## Scattering-Turbidity Theory (A Brief Summary)

The ratio of transmitted to incident light intensity is

$$I/I_0 = \exp[-NlC_{ext}] \tag{1}$$

where the extinction coefficient is given by Mie theory,[9] for small absorbing spheres.

$$C_{ext} = \frac{-6\pi}{\lambda}\langle v \rangle I_m\left[\frac{m^2 - 1}{m^2 + 2}\right] \tag{2}$$

$$\ln (I/I_0) = \frac{6\pi}{\lambda}Nl\langle v \rangle I_m\left[\frac{m^2 - 1}{m^2 + 2}\right] \tag{3}$$

For Rayleigh scattering from spherical particles (size $<<$ λ), where the input beam is vertically polarized with respect to the scattering plane (Figure 1), the intensity of the scattered radiation at 90° is

$$I_{scat} = I_0 \frac{hw}{\bar{R}^2}C_{sca}N \tag{4}$$

where $h$ and $w$ are the dimensions of the viewing window at a distance $\bar{R}$ from the scattering sample; $C_{sca}$ is the corresponding cross section:

$$C_{sca} = \frac{9\pi^2}{\lambda^2}\langle v^2 \rangle\left|\frac{m^2 - 1}{m^2 + 2}\right|^2 \tag{5}$$

On dividing (4) by (3)

$$I_{scat}/\ln (I/I_0) = CG\frac{\langle v^2 \rangle}{\langle v \rangle} \tag{6}$$

with

$$C \equiv \frac{3\pi}{2\lambda^3 l}\left|\frac{m^2 - 1}{m^2 + 2}\right|^2 \Big/ I_m\left[\frac{m^2 - 1}{m^2 + 2}\right]$$

$$G \equiv hwI_0/\bar{R}^2$$

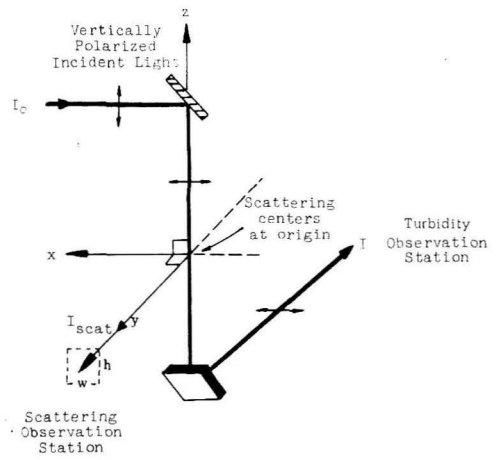


**Figure 1.** Relative orientations of incident, scattered, and transmitted rays.

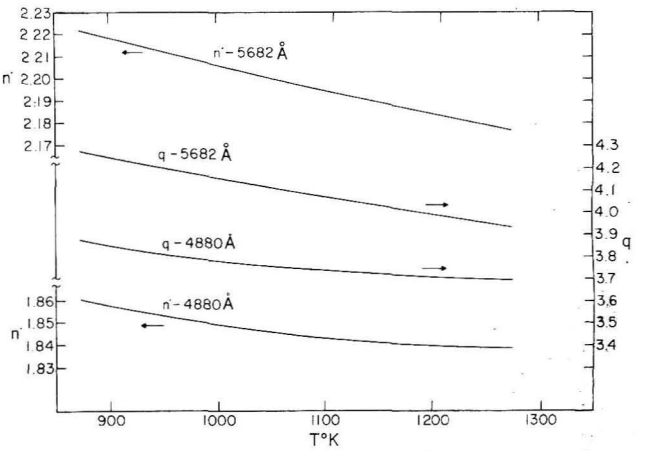


**Figure 2.** The real and imaginary components of the refractive index for liquid lead as a function of temperature.

If one assumes $\langle v^2 \rangle \approx \langle v \rangle^2$ (discussed below), the ratio of $I_{scat}$ to ln $(I/I_0)$ is directly proportional to the average particle volume. The constant $G$ is difficult to measure directly, since it depends critically on the experimental configuration. Hence, $G$ is determined by measuring the light scattered by a substance of known cross section. In this investigation we filled the shock tube to 1 atm with a gas of relatively large $C_{sca}$ [Ar; $CHF_2Cl$] and measured the scattered signal under exactly the same conditions as were used in the condensation experiment. The cross section for a gas with polarizability, $\alpha_p$, is

$$C_{sca} = \frac{(2\pi)^4}{\lambda^4}\alpha_p^2 \tag{7}$$

and the corresponding

$$G = \frac{I_c}{N'\alpha_p^2}\frac{\lambda^4}{(2\pi)^4}$$

where $I_c$ is the scattered light intensity from the calibrating gas and $N'$ is the density of the calibrating molecules. To facilitate data reduction, the above equations were combined:

$$\ln\left(\frac{C_{sca}}{C_{ext}}\right) = \ln\left[\frac{-I_{scat}}{(I_c)\ln(I/I_0)}\, l\frac{(2\pi)^4}{\lambda^4}N'\alpha_p^2\right] \tag{8}$$

For each pair of measurements, the right member of eq 8 was evaluated, and from a "master plot" of ln $(C_{sca}/C_{ext})$ vs. the mean radius, we read $\langle r \rangle$, defined by

$$\langle r \rangle \equiv [3\langle v \rangle/4\pi]^{1/3} \tag{9}$$

We confirmed that the growing droplets were indeed spherical. A polarizer was placed between the shock tube window and the collecting optics. When its axis was normal to the plane of polarization of the incident beam no signal above the noise limit was recorded from the illuminated sample region throughout the entire growth process. This is required by Rayleigh theory for spheres. Furthermore, electron microphotographs of the powder scraped from the shock tube walls showed that the final shapes of the particles were spherical.

The above scattering-turbidity analysis is valid only for single scattering conditions, satisfied when ln $(I/I_0) < 0.1$.[9] It is asserted that, for values of ln $(I_0/I)$ between 0.1 and 0.3, correction for multiple scattering may be necessary. In our experiments ln $(I_0/I)$ values were generally less than 0.3 for most of the observation time. Were multiple scattering significant we would have detected some depolarization of the scattered light. Since this was not the case, we concluded that multiple scattering introduced no appreciable errors in any of our measurements.

To deduce an average particle size from eq 8 one must insert values for the complex refractive index for the liquid at the wavelength of the scattered radiation, at the experimental temperature. The Drude free electron theory[10] provides the basic equations for macroscopic metals, in terms of the dc electrical conductivity, $\sigma_0$, the density of conduction electrons $N_e$, the electron relaxation time $\tau_e$, and the electron charge, $e$. The ac conductivity is

$$\sigma = {}^1/_4\sigma_0(\pi c\lambda)^{-2}\left[\frac{1}{k^2 + (1/2\pi c\tau_e)^2}\right] \quad k = 2\pi/\lambda \tag{10}$$

and the dielectric constant, $\epsilon$, is

$$\epsilon = 1 - \frac{\sigma_0}{c}\frac{1}{\pi\tau_e c}\left[\frac{1}{k^2 + (1/2\pi c\tau_e)^2}\right] \tag{11}$$

The complex refractive index, expressed in terms of $\epsilon$ and $\sigma$, is

$$m = n' - iq = \left[\epsilon(k) - \frac{2i\sigma(k)}{ck}\right]^{1/2} \tag{12}$$

On separating $m$ into its real and imaginary parts we have

$$n'^2 - q^2 = \epsilon(k) \text{ and } n'q = \sigma(k)/ck \tag{13}$$

Hodgson[11] measured $n'$ and $q$ for Pb(l) over the wavelength range 400–2500 nm and at two temperatures, 840 and 1059 K. He then evaluated $\epsilon(k)$ and $\sigma(k)$ from eq 13 and determined the best fit of values for $\tau_e$ and $\sigma_0$ from eq 10 and 11. The wavelength dependence was well reproduced, confirming that Drude theory adequately describes the optical properties of Pb(l). We extrapolated his data to higher temperatures by assuming that the free electron parameters $\tau_e$ and $\sigma_0/c$ were linear over the temperature range of interest (873–1273 K), and calculated $n'$ and $q$ for the wavelengths used in our experiments. The variation of $n'$ and $q$ with temperature is shown in Figure 2 for $\lambda$ 4880 and 5682 Å. With these values of $n'$ and $q$ in eq 2 and 5 we calculated the dependence of the scattering and extinction cross sections on particle radius, and plotted ln $(C_{sca}/C_{ext})$ vs. $\langle r \rangle$ in Figure 3. The variation of ln $(C_{sca}/C_{ext})$ with temperature for a given $\langle r \rangle$ is negligible.

One may properly question whether bulk values of $n'$ and $q$ are applicable to the tiny clusters generated in this experiment. Doremus[12] found significant deviations between the optical properties of small gold particles and bulk gold. He suggested that when the mean free path of

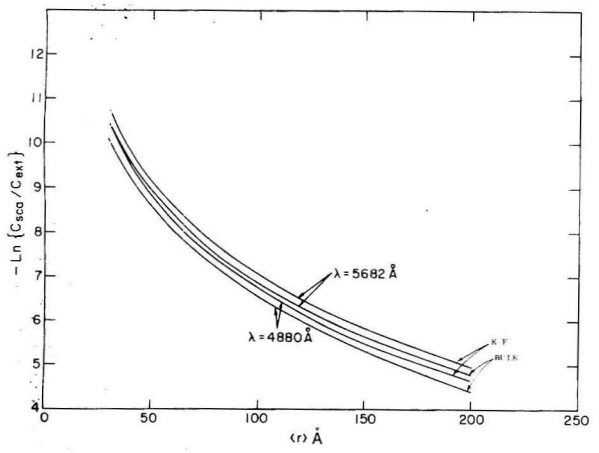


**Figure 3.** Size dependence of the ratio ($C_{sca}/C_{ext}$) at two wavelengths. In each case the upper curve is the KF theory for 1273 K, and the lower curve is the bulk value at 873 K. All other points for both the KF and Drude theories fall within the envelope.

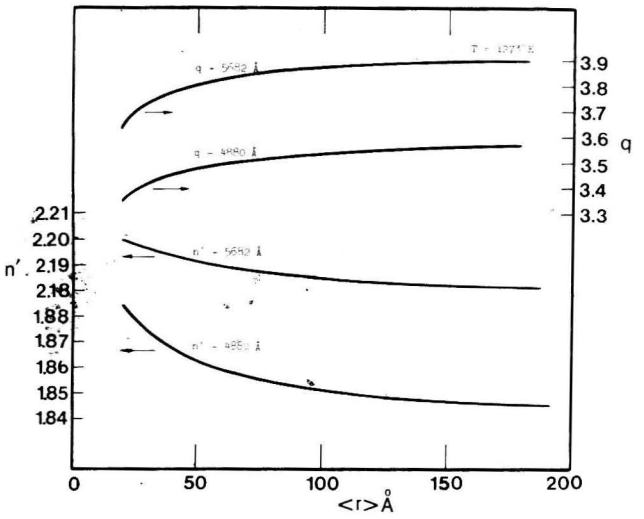


**Figure 4.** Dependence of the complex refractive indices on particle radius according to KF theory.

the electrons becomes equal to or less than the particle diameter, the Drude free electron theory breaks down. Kreibig and Fragstein[13] developed an extended free electron model which takes this effect into account. They introduce a size dependent free path

$$\frac{1}{l(r)} = \frac{1}{l_0} + \frac{1}{r} \tag{14}$$

where $l_0$ is the bulk mean free path. For Pb(l), $l_0$ can be derived from $\tau_e{}^0 v_F = l_0$, where $v_F$ is the Fermi velocity,[10] given by $v_F \simeq 1.16[3\pi^2 N_e]^{1/3}$. The magnitude of $N_e$ was determined by Hogdson.[11] Both the dc and ac conductivities depend on $\tau_e(l) = l(r)/v_F$, and therefore on the particle radius. With the Drude eq 10–13 [$\sigma_0(r) = N_e e^2 \tau_e(l)/m^*$], one may deduce the size dependence of $n'$ and $q$. Figure 4 shows graphs for Pb(l) at $T$ = 1273 K and λ 5682, 4880 Å. Similar curves were obtained for $T$ = 873 K. These $n'(r)$ and $q(r)$ values permit the recomputation of ln ($C_{sca}/C_{ext}$) vs. ⟨$r$⟩, also plotted in Figure 3. The temperature and size dependence of ln ($C_{sca}/C_{ext}$) is small, and all the values fall within a relatively narrow strip bordered on top by the KF theory curve for $T$ = 1273 K, and on the bottom by the bulk curve for $T$ = 873 K.

## Experimental Section

*The Shock Tube and Optical Systems.* The 2-in. i.d. shock tube used for this series of experiments has been

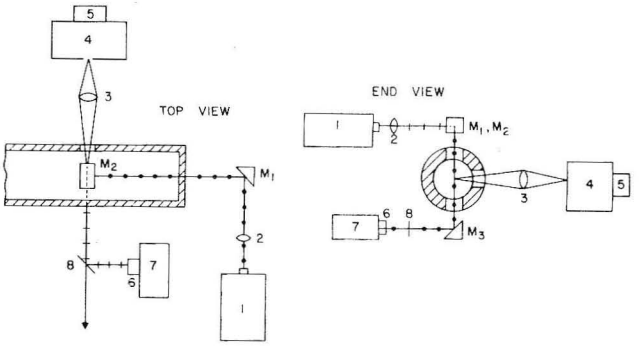


**Figure 5.** Schematic of the disposition of laser, mirrors and detectors around the shock tube: (1) $Ar^+$ or $Kr^+$ laser; (2) long focal length lens; (3) scattered light collection lens; (4) Spex monochrometer; (5) EMI-9558-B phototube; (6) neutral density filter stack; (7) EMI 9634 phototube (to measure turbidity); (8) thin glass plate. The response times for the phototubes was ≈2 μs.

described.[14] The following modifications were made. The driven section was lengthened to 13 ft 8 in.; two lucite windows were added at the observation station. Mylar diaphragms were used singly or in various combinations. The driver gas was either helium or hydrogen. The shock tube was operated in the single pulse mode; its leak rate (out-gassing) was ≈0.5 mTorr/min.

The optical arrangement is shown schematically in Figure 5. The light source was a Coherent Radiation Model 52-G argon ion or krypton ion laser. The argon laser was operated at 4880 Å with a power of ≈350 mW, while the krypton laser was operated at 5682 Å at a power of ≈80 mW. A 50-cm focal length lens focused the beam at the center of the shock tube. The beam diameter at the focus was ≈0.5 mm. The lens was mounted kinematically; two micrometer screws permitted fine adjustment of the beam position. The emitted laser radiation was vertically polarized; the reflections converted the beam to horizontal polarization, i.e., axial with the tube, to provide the maximum of scattered intensity.

The most difficult problem encountered was elimination of the stray light due to reflections and scattering by the front and back surfaces of the input and exit windows. Although the scattered intensity from the growing particles was much greater than the stray intensity, the calibration signal from the Ar or freon was of the same order of magnitude as the stray light. To minimize these extraneous signals the windows were arranged as shown in Figure 6. The entrance and exit windows were recessed behind aluminum spacers which fitted flush with the inside of the tube. A small hole, 0.040 in. diameter, was drilled in the center of each spacer and threaded to minimize internal reflections of the main beam and to trap any stray, off-axis radiation. Every part of the window cavity was blackened with Aqua-Dag. The exit window was similarly mounted, except that the front and back surfaces were set 30° to the laser beam to prevent reflections from the front surface of the exit window from returning into the shock tube. The inside of the shock tube near the windows was also blackened with Aqua-Dag.

To monitor the scattered light, a 1.75 in. diameter, 3.375 in. focal length collecting lens was placed next to the side window, 5.5 in. from the tube center. The collecting lens focused an image of the scattering volume onto the front slit of a Spex Minimate Model 1670 grating monochromator. A band width at half-height of 10 Å was obtained with 0.5-mm slits. There are no Pb, Ar, or Hg lines in the intervals 4880 ± 10 or 5682 ± 10 Å. In test runs, when we looked only at emission from the shock tube, no signal above the background was observed, demonstrating the

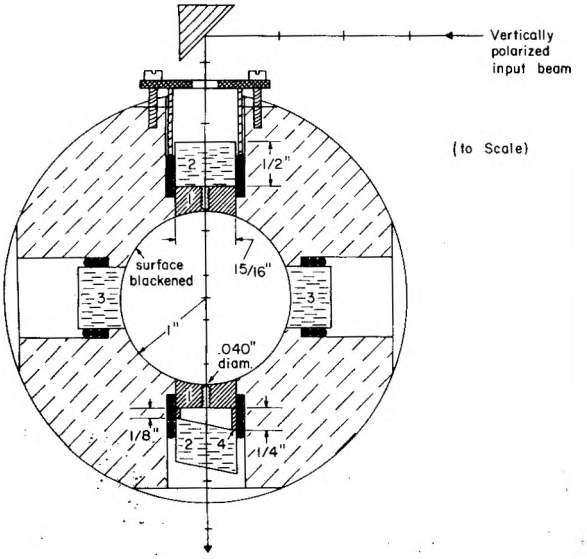


**Figure 6.** Detail of the window assembly: (1) aluminum spacers; (2) lucite windows; (3) 0.5-in. quartz windows; (4) truncated aluminum cylindrical spacer.

absence interference at the recording sensitivities used in these experiments. The output of both the turbidity and scattering phototubes was monitored on a Tektronix Model 502 dual beam oscilloscope. Amplified signals from the two pressure transducers, located near the observation station and used to measure the shock speed, were monitored on a Tektronix Model 535 oscilloscope.

In making the optical alignment we utilized the rapid photodecomposition of $Fe(CO)_5$ by green light. When a 20–60 Torr sample of ca. 1% $Fe(CO)_5$ was illuminated (in the shock tube) with any of the more powerful $Ar^+$ laser lines, or with the 5682-Å line of the $Kr^+$ laser, the carbonyl decomposed in the beam, and (presumably) iron particles condensed. The path of the beam through the sample was thus made strikingly visible, and the relatively large amount of scattered light was suitable for alignment of the optics. The laser beam was chopped mechanically at ~200 Hz, so that the location and wavelength setting of the monochromator (with attached phototube) was readily adjusted to obtain the maximum signal. The shock tube was then pumped to below $10^{-3}$ Torr for at least 5 min and filled to 800 Torr with either Ar or $CHF_2Cl$ (Freon-22). The scattered light intensity from the gas was then recorded. After recording the square wave signal due to the calibrating gas ($I_{gas + background}$), the tube was pumped to $<10^{-3}$ Torr and the background (stray light) square wave signal ($I_{background}$) was recorded. The difference between these two measurements is the intensity due to the gas scattering, defined as $I_c$. Signal to background ratios were typically 1.5–4. The system was realigned if this ratio was less than 1.5. With the tube evacuated, we also measured the square wave signal at the turbidity phototube, defined as $I_0$. In preparation for the shock, the chopper was removed and the laser beam was blocked with a mechanical shutter. None of the optics was disturbed after the calibration. The tube was pumped below $3 \times 10^{-4}$ Torr with a diffusion pump; the driven and driver sections were then filled to the desired pressures. Immediately prior to shock initiation, the mechanical shutter blocking the laser beam was opened.

The entire driven section, including the window assembly, was thoroughly cleaned after each experiment with a cheesecloth swab, moistened with ethanol. Conditions were varied by changing the test sample pressure or the sample concentration. The measured shock speed, initial

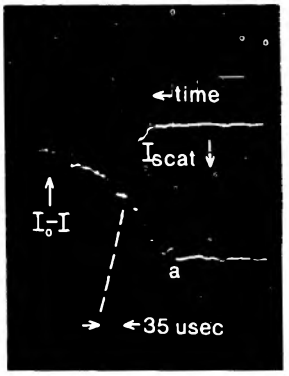


**Figure 7.** An "early time" scattering-turbidity trace. The shock arrives at time (a). The scope is set at 20 mV/division for $I_{scat}$ and 5 mV/division for ($I_0 - I$). The indicated time interval applies to the particles: $S$ = 65; $T$ = 1143 K.

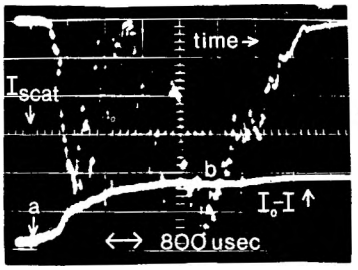


**Figure 8.** Typical scattering-turbidity trace recorded for "long times" showing large scattering spikes. Incident shock arrives at (a); the reflected shock arrives at (b). The turbidity ($I_0 - I$) remains essentially flat after point (b) due to particulate deposition on the windows. The indicated time is particle time. Scope settings: $I_{scat}$ at 1 V/division; ($I_0 - I$) 50 mV/division.

$Pb(CH_3)_4$ concentration, and the initial total pressure were used to calculate the shocked gas equilibrium conditions via the NASA equilibrium shock program.

*Data Reduction.* Two sets of scattering experiments were performed. In the first series of runs the scattered intensity and turbidity were monitored for 800 μs (particle time) after the arrival of the *incident* shock. A second series of experiments was run in which we investigated the initial growth period ($t \lesssim 200$ μs). Typical records of the "early" scattering and turbidity traces are shown in Figure 7. The shock arrival time is indicated by a schlieren spike (a) in the turbidity trace. Generally the turbidity signal departed from the zero line somewhat before the scattering trace did. However, after a very short time (≈10 μs, lab time) the limit of detection at the scattering phototube was reached and that signal rose rapidly.

The recorded output from the scattering phototube is *not* $I_{scat}$ of eq 6; corrections must be made for the attenuation of the laser beam before it reaches the scattering volume and for the attenuation of the scattered light as it traverses the gas to the exit window. However, the calibration signal is proportional to the unattenuated incident light, $I_0$. The net correction factor is simply ($I/I_0$), recorded as the turbidity. This results in an increase of the derived average radius of no more than 10%. The time recorded at the observation window, $t_{lab}$, under incident shock conditions is not the experimental particle time, $t_p$, because the shocked gas is flowing past the observation window; they are related by the ratio of the shocked to unshocked gas densities, $t_p = t_{lab}(\rho_2/\rho_1)$. A typical magnitude for $\rho_2/\rho_1$, also calculated in the NASA program, was ~3.6; $t_{lab} = 0$ was set when the incident shock arrived at the window.

Figure 8 reproduces very long time traces which encompass the entire incident shock regime, of about 3 ms.

The scattering channel shows large rapid fluctuations, beginning at ≈800 μs (particle time) after shock arrival. These fluctuations are probably due to large particles diffusing into the relatively narrow laser beam. When the slit width was narrowed, the sample concentration reduced, or the supersaturation decreased, the frequency of these fluctuations increased, consistent with the above explanation. Reduction of the slit width reduces the size of the observed scattering volume; reduction of the sample concentration decreases the density of scattering centers; and, decreasing the supersaturation ratio increases the average particle size and necessarily decreases the density of scattering centers. These fluctuations prevented us from utilizing data at times longer than 800 μs. Furthermore, in most runs, the incident light intensity was considerably reduced by extinction after 800 μs. Specifically, for $CHF_2Cl$ as a calibrating gas at λ 5682 Å, $l$ = 5.08 cm, $N'$ = 2.59 × $10^{19}$ mol $cm^{-3}$ (at 800 Torr), and $\alpha_p$ = 53 × $10^{-25}$ $cm^3$,[15] eq 8 reduces to

$$\ln (C_{sca}/C_{ext}) = \ln\left[\frac{-I_{sca}}{I_e \ln (I/I_0)} 5.53 \times 10^{-7}\right]$$

From the master plot of ln $(C_{sca}/C_{ext})$ vs. $\langle r \rangle$ (Figure 3), we read the average cluster size at the center of the bulk-KF envelope of curves, for each measurement. Given the average size as a function of time, one can determine the time dependence of the particle density by rearranging eq 1:

$$N(t) = \frac{\ln (I_0/I)}{l C_{ext}[r(t)]} \quad (1a)$$

There is less than 5% difference between the bulk $C_{ext}$ and the KF $C_{ext}$.

In deriving the above equations we assumed that $\langle v^2 \rangle^{1/2} \simeq \langle v \rangle$. This is equivalent to assuming that the distribution function, $P(v)$ [defined as the fraction of molecules with volumes between $v$ and $v + dv$], is a delta function, obviously unrealistic. To estimate the magnitude of the error introduced by this assumption, define

$$P(v) = f v^2 e^{-gv^2} \text{ normalized to } \int_0^\infty P(v)\, dv = 1 \quad (15)$$

Then, $f = 4g^{3/2}/\pi^{1/2}$. The mean volume is

$$\langle v \rangle = \int_0^\infty v P(v)\, dv = \frac{4g^{2/3}}{\pi^{1/2}} \int_0^\infty v^3 e^{-gv^2}\, dv = \frac{2}{\pi^{1/2} g^{1/2}} \quad (16)$$

and the mean square volume is

$$\langle v^2 \rangle = \int_0^\infty v^2 P(v)\, dv = {}^3/_2 g \quad (17)$$

So that, $\langle v^2 \rangle = (3\pi/8)\langle v \rangle^2$. It follows that for this functional form, the previously calculated values of ln $(C_{sca}/C_{ext})$ should be increased by ln $(3\pi/8) = 0.16$. In turn, this leads to an increase in the calculated $\langle r \rangle$ by about 3%. We neglected this correction and proceeded to use the average radii calculated previously to estimate the distribution function parameter $g = 4/\pi\langle v \rangle^2 = 9/4\pi^3\langle r \rangle^6$.

Several electron micrographs of lead particles scraped from the inside of the shock tube were scanned to estimate the distribution function of radii. Although the particles which were thus analyzed grew under condition in which they were subjected to both incident and reflected shocks, the final distribution should still be indicative of the early time distribution. In Figure 9 the results of the electron micrograph analysis are compared with the distribution based on eq 15. The electron micrograph distribution function is fairly symmetric, with an average radius of ≈200 Å, and reasonably close in shape and width to the predicted distribution.

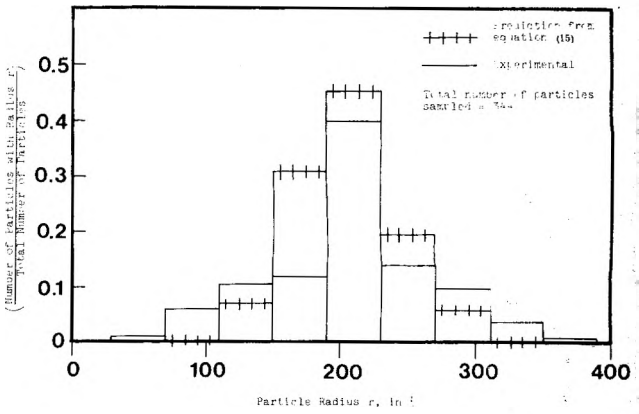


**Figure 9.** Distributions of particle radii, determined by electron microscope analysis, and predicted via eq 15.

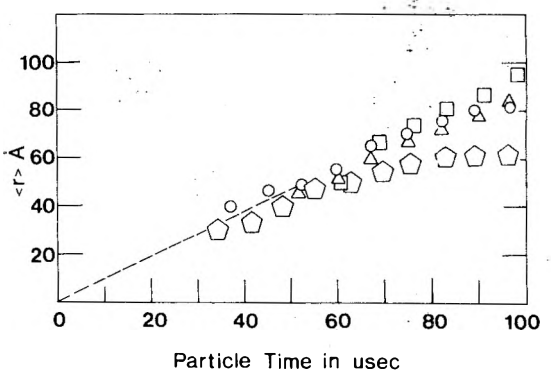


**Figure 10.** "Early time" growth rates at various supersaturation ratios (44–240). The dashed line is a "best fit" through the origin. The temperature span is 1050–1150 K.

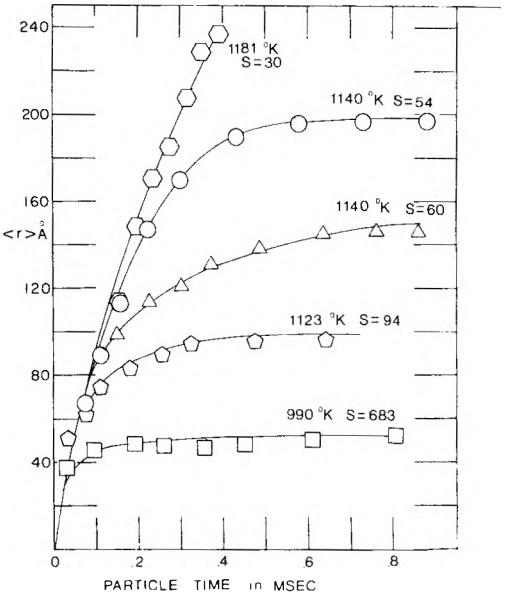


**Figure 11.** Experimental "long-time" growth curves at several supersaturations.

## Summary of Results and Analysis

Figures 10 and 11 are plots of the average cluster radii vs. particle time, for the early and long time experiments, respectively. The experimental conditions for these runs are summarized in Table I. Overall, the shock conditions encompassed the temperature range 990–1180 K, and supersaturation ratios 30–680. No scattering was observed in experiments in which the supersaturation was less than

TABLE I: Summary of Experimental Conditions

| Run no.[a] | $\langle r\rangle_{max}$, Å | $S = P/P_e$ | $T_{shock}$, K |
|---|---|---|---|
| | Long Time Runs | | |
| 1 | >250 | 30 | 1181 |
| 2 | 170 | 50 | 1152 |
| 3 | 225 | 54 | 1140 |
| 4 | 166 | 60 | 1141 |
| 5 | 120 | 84 | 1124 |
| 6 | 109 | 94 | 1123 |
| 7 | 122 | 96 | 1110 |
| 8 | 63 | 680 | 990 |
| 9 | 81 | 240 | 1066 |
| | Short Time Runs | | |
| 10 | | 44 | 1147 |
| 11 | | 56 | 1139 |
| 12 | | 88 | 1126 |
| 13 | | 65 | 1143 |
| 14 | | 240 | 1066 |

[a] In all runs $Pb(CH_3)_4$ was 1.0 or 2.0% in argon.

critical over the 700 μs (lab) observation time. In separate experiments[2] we measured $S_c(T)$, and found empirically that it is well represented by

$$\ln S_c = 69.4 \exp(-2.79 \times 10^{-3} T\ \mathrm{K}) \quad (18)$$

In some of the "long time" runs, fluctuations in the scattering trace prevented data reduction past 800 μs (particle time). As mentioned earlier, the scattering signal was not observed above the background noise until ≈25 μs (particle time) after shock arrival, so that no particle size data are available for earlier times. The minimum observable signal (above the background) was 0.2 mV.

Several general features appear. First, during early times the scattered intensity is essentially independent of the supersaturation ratio for all runs, despite the fact that this ratio ranged from 44 to 240. [The temperature range for these runs was relatively small: 1110 ± 40 K.] The growth rate, $d\langle r\rangle/dt$, is approximately linear in this region, and properly extrapolates to the origin. Thus, for $t \lesssim 80$ μs for Pb vapor

$$d\langle r\rangle/dt = \gamma = 9.4 \times 10^{-3}\ \mathrm{cm\ s^{-1}} \quad (19)$$

In terms of the average number of atoms per cluster, since $(4/3)\pi\langle r\rangle^3 = \langle v\rangle = \langle n\rangle/\rho_n$, where $\rho_n$ is the number of atoms per unit volume in an $n$mer

$$d\langle n\rangle/dt = \gamma\rho_n 4\pi\langle r\rangle^2 \quad (20)$$

i.e., the rate of addition of atoms onto a cluster of size $\langle n\rangle$ is directly proportional to the surface area of the cluster. Equation 20 follows from a simple kinetic model. During the early times in the growth process, monomer addition is the rate-controlling process.[16] The rate of bombardment of a spherical $n$mer by monomers is

$$Z_{n\leftarrow 1} = A_n N_1 \bar{c}_1/4$$

where $N_1$ is the monomer density and $\bar{c}_1$ is its mean molecular velocity. If one specifies that of all the monomers which impinge on a cluster only the fraction $\alpha$ stick, the growth rate is

$$d\langle n\rangle/dt = \alpha A_n N_1 \bar{c}_1/4 \quad (21)$$

Early in the growth process, the monomer concentration remains essentially at its initial level so that one may identify: $\gamma\rho_n \leftrightarrow (\alpha N_1^0 \bar{c}_1/4)$. To estimate $\rho_n$, use the bulk liquid density $\rho_\infty = 2.7 \times 10^{22}$ atoms $cm^{-3}$; then our data give for $\gamma\rho = 2.5 \times 10^{20}$. In turn, for $N_1^0 = 9 \times 10^{16}\ cm^{-3}$, so that at 1110 K, we deduce $\alpha = 1/3$. While this reasonable value strongly supports our experimental approach, we note that it is based on a simplistic hard-sphere-binary collision model; it is a *mean* value for the range of $n$mers generated during this time interval. Were we to use the ternary collision model introduced in ref 16, association rate constants with specific $n$ dependence (but no $\alpha$) would appear in eq 21.

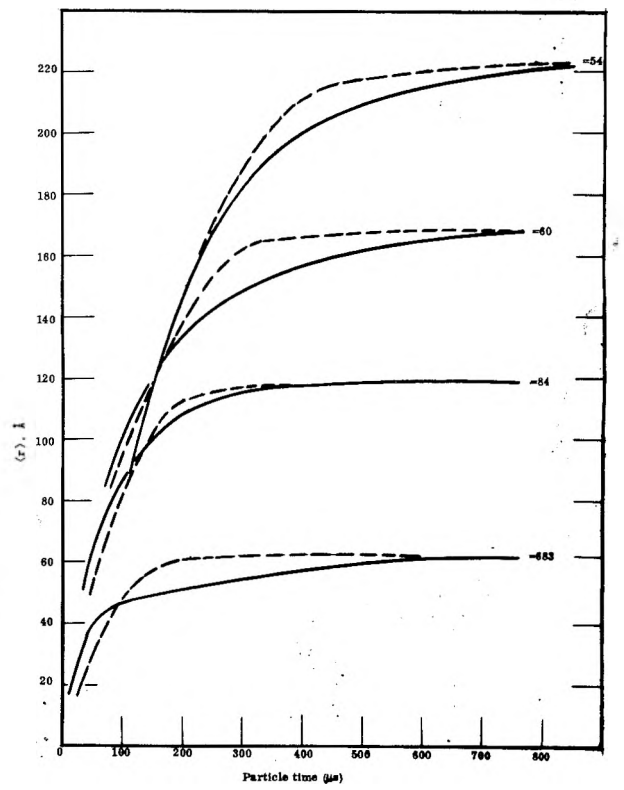


**Figure 12.** Growth curves at various supersaturation levels (full curves) compared with a simple kinetic theory model (dashed curves); $\alpha = 1/3$.

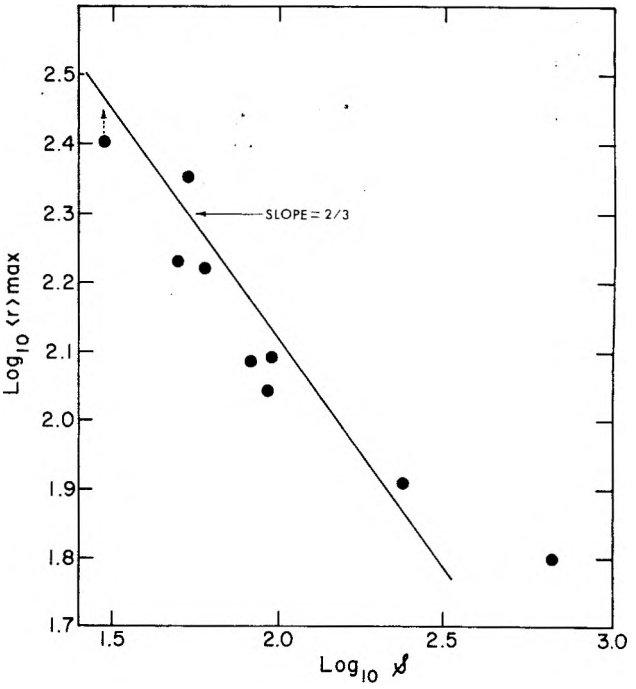


**Figure 13.** Correlation of $\langle r\rangle_{max}$ with $S$. Arrow (↑) on data point indicates that $\langle r\rangle$ had not leveled off at $\langle r\rangle_{max}$ during the observation time.

The longer time growth curves show two general features: (i) $d\langle n\rangle/dt$ decreases with increasing $t$, and (ii) after ≈500 μs the growth curves level off to $\langle r\rangle_{max}$, which varies inversely with the supersaturation ratio. Both are a

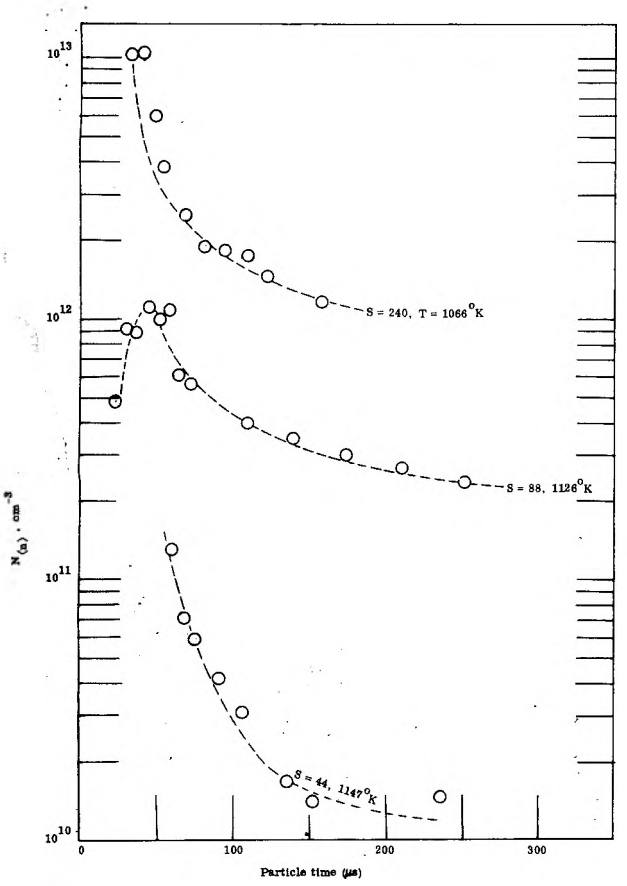


**Figure 14.** Time evolution of the cluster density (mean size) for three supersaturations.

consequence of depletion of the monomer concentration. Instead of assuming that the latter was constant, we set $N_1(t) = N_1^0 - N_n\langle n\rangle$. In terms of $\langle r\rangle$, $N_1(t) = N_1^0 - 4\pi\langle r\rangle^3\rho_n N_n/3$. The growth rate then assumes the form

$$d\langle r\rangle/dt = \varphi - \xi\langle r\rangle^3 \tag{22}$$

where $\varphi \equiv \alpha\bar{c}_1 N_1^0/4\rho_n$, and $\xi \equiv \pi\bar{c}_1 N_n\alpha/3$. If one assumes that, for the late times, the density of particles remains essentially constant, eq 22 can be integrated. [We shall show later that the density of particles does change, but not significantly after initial nucleation.]

$$\int_0^{\langle r\rangle} \frac{d\langle r\rangle}{\varphi - \xi\langle r\rangle^3} = t = \frac{\kappa}{3\varphi}\left[\frac{1}{2}\ln\frac{[\kappa + \langle r\rangle]^2}{(\kappa)^2 - \kappa\langle r\rangle + \langle r\rangle^2} + \sqrt{3}\tan^{-1}\left(\frac{2\langle r\rangle - \kappa}{\kappa\sqrt{3}}\right) - \sqrt{3}\tan^{-1}\left(-\frac{1}{\sqrt{3}}\right)\right] \tag{23}$$

where $\kappa \equiv (\varphi/\xi)^{1/3} = (3N_1^0/4\pi\rho_n N_n)^{1/3}$. Equation 23 has the correct limiting values; i.e. as $t \to 0$, $\langle r\rangle \to 0$; and as $t \to \infty$, $\langle r\rangle \to \kappa$. Hence identify $\kappa$ with $\langle r\rangle_{max}$. Using the experimentally estimated magnitudes for $\langle r\rangle_{max}$, the bulk value for $\rho$, $\alpha = 1/3$ and initial concentrations for the various runs, we calculated the right member of eq 23 for a range of values of $\langle r\rangle$, and plotted these against $\langle r\rangle$. In Figure 12, these curves are compared with the experimentally derived growth curves (Figure 11). There is a transient maximum difference of ≈20% between the simple model and the experimental rate. If the time dependence of $N_n$ were included, the rate equation would be difficult to integrate. More important, the ternary rate constant should be used in a refined model. At this stage we believe it is more significant to predict the magnitude of $\langle r\rangle_{max}$ from the experimental parameters.

The value of $\langle r\rangle_{max}$ varies approximately with the reciprocal of the supersaturation ratio. Qualitatively, this is expected. When $S$ is increased, $n^{transition}$ (defined in ref 16; it is analogous to the classical $n^{critical}$) decreases; i.e., the higher the supersaturation ratio the more critical size nuclei are generated, and the less material is available per nucleus. It is commonly known[17] that the average particle size of an aqueous precipitate is inversely proportional to its supersaturation level. Hence, at long times, the density of clusters ($N_\infty$) of size $\langle r\rangle_{max}$ is

$$N_\infty \to \frac{3N_1^0}{4\pi\langle r\rangle_{max}^3\rho_n} = \theta N^{ss} \tag{24}$$

where $N^{ss}$ is the density of critical size nuclei generated at the start of the steady state condition, and $\theta$ is a constant, always less than unity and generally about 1/10. Thus, $N^{ss}$ is also proportional to $1/\langle r\rangle_{max}^3$. Since the initial nucleation process occurs as a consequence of termolecular steps

$$Pb_1 + Pb_1 + Ar \to Pb_2 + Ar$$
$$\cdots\cdots\cdots\cdots\cdots\cdots$$
$$Pb_{(n-1)} + Pb_1 + Ar \to Pb_n + Ar$$

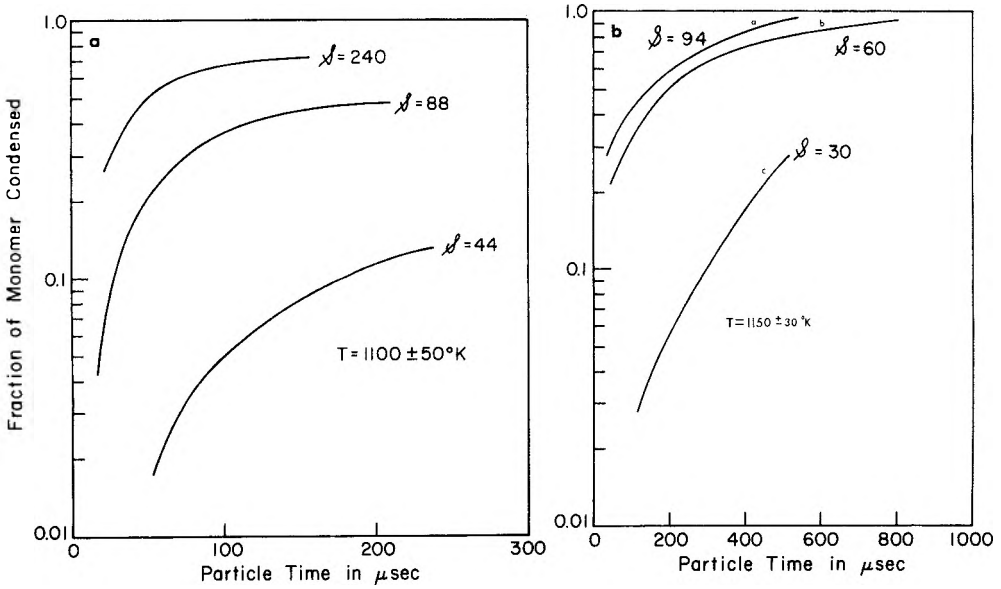


**Figure 15.** Fraction of monomer condensed X(t) vs. particle time for three runs: (a) early times; (b) long times.

in which all the species (except the monomer) rapidly approach steady state, the reaction rate, $d[Pb_n]/dt$, is proportional to the square of the monomer concentration. Hence $N^{ss} \propto (N_1^0)^2 \propto (S)^2$, and

$$1/\langle r\rangle_{max}{}^3 \propto S^2 \tag{25}$$

If this dimensional analysis is correct, a plot of log $\langle r\rangle_{max}$ vs. log $S$ should be linear with slope ($-^2/_3$). Figure 13 is a plot for the experimental values upon which a line of slope ($-^2/_3$) was superposed. Only the single point for the run in which the supersaturation was largest ($S$ = 680) deviates significantly from the prediction. Indeed one should anticipate that such a curve level off at large $S$ due to the finite amount of monomer available, and the rate at which the nuclei are produced. The "best fit" straight line is given by

$$\log\left[\frac{\langle r\rangle_{max}}{2.8\times 10^3\ \text{Å}}\right] = -\frac{2}{3}\log S \tag{26}$$

or in terms of the kinetic theory growth parameter for Pb vapor

$$\kappa \leftrightarrow \langle r\rangle_{max} = 2.8\times 10^3\ \text{Å}\ S^{-2/3}$$

Another aspect of the growth process follows from consideration of cluster densities. Figure 14 is a plot of mean particle density vs. time, calculated from eq 1a for three typical runs in which the temperature was near 1100 K and $S$ varied 44 → 240. In all cases, after ≈50 μs, the particle density decreased monotonically. In a few runs we were able to read the scattering traces at early times; for these the derived density peaked at about 40 μs. Of course, $N_{\langle n\rangle} = 0$ at $t = 0$. These observations emphasize the differences between two regimes in the condensation process: (1) the initial fast nucleation, when critical size clusters are generated from monomers, and the cluster density increases with time; (2) the subsequent growth and coagulation of clusters which causes their density to decrease. Note also the anticipated dramatic dependence of cluster density on the supersaturation ratio. Doubling $S$ increase $N_{\langle n\rangle}$ by approximately one order of magnitude.

Since the density curves must start at the origin, we can estimate the steady state nucleation rate. For supersaturation ratios of 240, 88, and 44, respectively, $\sim 10^{13}$, $10^{12}$, $10^{11}$ nuclei $s^{-1}$ $cm^{-3}$ are generated within ≈50 μs. Hence the nucleation current, $J$, is approximately $10^{17}$, $10^{16}$, and $10^{15}$ nuclei $s^{-1}$ $cm^{-3}$, respectively. Extrapolating these values to the critical supersaturation ratio at 1100 K, $S_c \sim 25$, we deduce a critical nucleation rate of $10^{12}$–$10^{14}$ $s^{-1}$ $cm^{-3}$. Parenthetically, the predicted classical steady state rate is $\sim 10^8$–$10^{10}$ $s^{-1}$ $cm^{-3}$.

One can now calculate the time dependence of the fraction of monomer which entered the condensed phase. Let $\chi(t)$ denote that fraction; then

$$\chi(t) = \frac{N_n\langle n\rangle}{N_1^0} = \left(\frac{N_n}{N_1^0}\right)\frac{4\pi\langle r\rangle^3}{3}\rho_n \tag{27}$$

From liquid density data at 1100 K, $\langle n\rangle = 0.11\langle r\rangle^3$ Å$^{-3}$. Figure 15a is a plot of $\chi$ vs. particle time, for the three runs shown in Figure 14. For times less than 50 μs, $\chi$ is less than 0.5, even when $S$ = 240. This confirms our analysis of the linear growth rate for early times, where we assumed that the monomer concentration remained nearly constant for $t \lesssim 60$ μs. Similar calculations for three typical longer time runs are shown in Figure 15b. When the supersaturation ratio is relatively high (curves a and b) essentially all the monomer enters the condensed phase when $t \gtrsim 600$ μs; however, for $S$ = 30, less than 30% of the monomer had condensed.

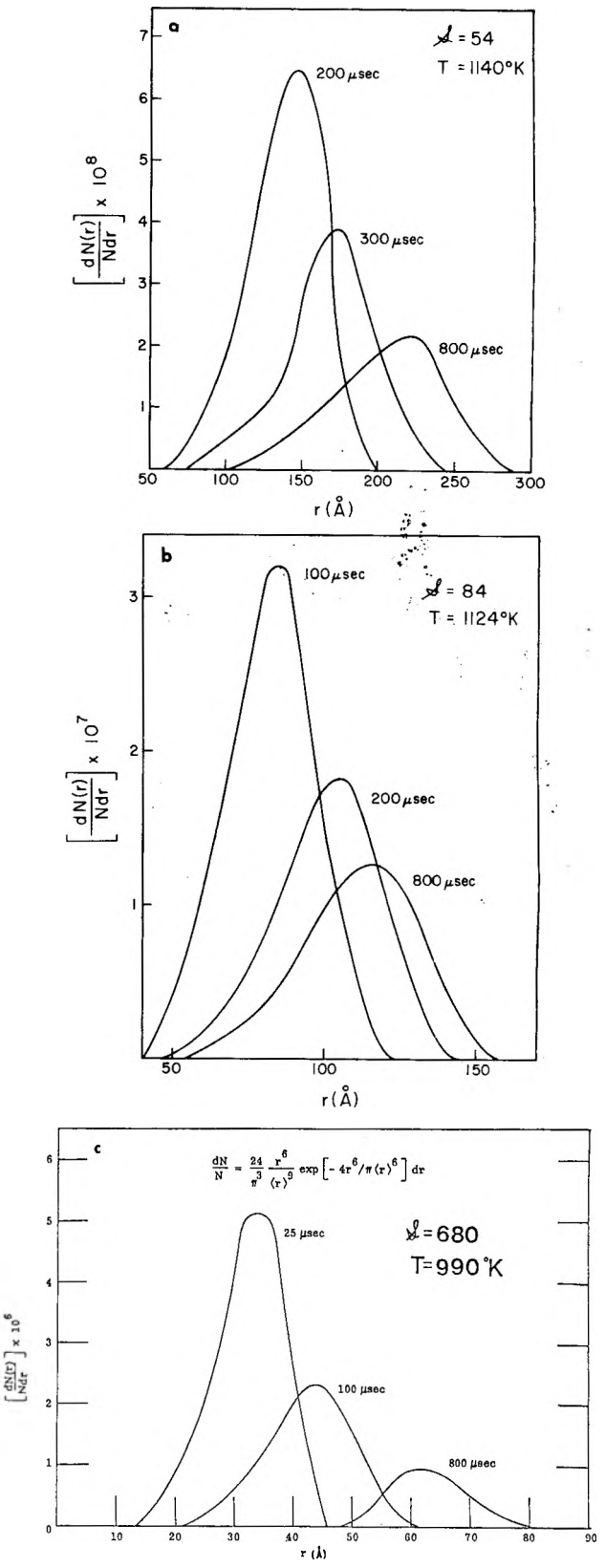


**Figure 16.** The distribution function for clusters, eq 15, with parameters given by eq 16 and the normalization condition: (a) $S$ = 54; (b) $S$ = 84; (c) $S$ = 680.

The calculated distribution functions (eq 15) for three runs are shown in Figure 16a–c. Although the specific form of the distribution function is arbitrary, it does have the expected features. At early times, the distribution is

relatively narrow and symmetric. Progressively the distribution becomes broader.

### Error Analysis and Comments

The uncertainty in the calculated mean radius depends on the uncertainty in the experimentally determined quantities $I_{scat}$, $I_c$, and ln $(I_0/I)$. Since

$$\delta\langle r\rangle = \left[\frac{\langle r\rangle}{3I_{scat}}\right]\delta I_{scat} - \left[\frac{\langle r\rangle}{3I_c}\right]\delta I_c - \left[\frac{\langle r\rangle}{3\ln(I_0/I)}\right]\delta \ln(I_0/I)$$

to calculate the maximum uncertainty in $\langle r\rangle$, sum the absolute values of the partial derivatives and rearrange ($\lambda$ are the estimated error limits):

$$\lambda\langle r\rangle = \frac{\langle r\rangle}{3}\left[\left|\frac{\lambda I_{scat}}{I_{scat}}\right| + \left|\frac{\lambda I_c}{I_c}\right| + \left|\frac{\lambda \ln(I_0/I)}{\ln(I_0/I)}\right|\right]$$

For typical runs, we found

$$|\lambda I_{scat}/I_{scat}| \lesssim 0.05,\ |\lambda I_c/I_c| \lesssim 0.10,$$
$$|\lambda \ln(I_0/I)/\ln(I_0/I)| \lesssim 0.02$$

The largest source of error is due to the relatively small signal to noise ratio in the calibration experiments. We conclude that $\lambda\langle r\rangle/\langle r\rangle \approx 0.05$. Since the largest $\langle r\rangle$ was $\approx$200 Å, the maximum uncertainty is ±10 Å. Note that the uncertainty in $\langle r\rangle$ is smaller at early times due to the lower $\langle r\rangle$. Thus the scattering-turbidity measurements constitute an appropriate diagnostic tool when applied to the growth of metal vapors in a shock tube.

During the early growth process (but still in the post-nucleation regime), a simple kinetic theory model (hard sphere, binary collisions) adequately accounts for our light scattering data, with $\alpha = 1/3$. The expected dramatic dependence on the supersaturation ratio of the particle number density, of the total amount of monomer which enters the condensed phase at any time, and the final particle size $\langle r\rangle_{max}$ are also derived. Of greater interest is the development of a technique for indirectly estimating flux rates at the critical supersaturation ratio for comparison with theoretical predictions.

*Acknowledgment.* This investigation was supported by the National Science Foundation through the Materials Science Center of Cornell University.

### References and Notes

(1) R. T. V. Kung and S. H. Bauer, "Shock Tube Research", 8th International Shock Tube Symposium, Chapman and Hall, London, 1971, Paper No. 61, (part I of this series).
(2) D. J. Frurip and S. H. Bauer, *J. Phys. Chem.*, **81**, 1001 (1977).
(3) H. J. Freund and S. H. Bauer, *J. Phys. Chem.*, **81**, 994 (1977).
(4) M. Kerker, "The Scattering of Light and Other Electromagnetic Radiation", Academic Press, New York, N.Y., 1969, Chapter 5.
(5) M. A. Vietti and B. G. Schuster, *J. Chem. Phys.*, **58**, 434 (1973).
(6) G. D. Stein, *J. Chem. Phys.*, **51**, 938 (1969).
(7) J. A. Clumpner, *J. Chem. Phys.*, **55**, 5042 (1971).
(8) S. C. Graham and J. B. Homer, *Faraday Symp. Chem. Soc.*, **7**, 85 (1973).
(9) H. C. van de Hulst, "Light Scattering by Small Particles", Wiley, New York, N.Y., 1957.
(10) C. Kittel, "Introduction to Solid State Physics", 4th ed, Wiley, New York, N.Y., 1971.
(11) J. N. Hodgson, *Phil. Mag.*, **6**, 509 (1961).
(12) R. H. Doremus, *J. Chem. Phys.*, **40**, 2389 (1964).
(13) U. Krelbig and C. V. Fragstein, *Z. Phys.*, **224**, 307 (1969).
(14) H. Carroll, Ph.D. Thesis, Cornell University, 1969.
(15) H. Sutter and R. H. Cole, *J. Chem. Phys.*, **54**, 4988 (1971).
(16) S. H. Bauer and D. J. Frurip, *J. Phys. Chem.*, **81**, 1015 (1977).
(17) D. Skoog and D. West, "Fundamentals of Analytical Chemistry", Holt, Reinhart and Winston, New York, N.Y., 1966, pp 157–174.

# Homogeneous Nucleation in Metal Vapors. 5. A Self-Consistent Kinetic Model

**S. H. Bauer* and D. J. Frurip**

*Department of Chemistry, Cornell University, Ithaca, New York 14853* *(Received July 19, 1976; Revised Manuscript Received March 7, 1977)*

The kinetic model developed for the condensation of metallic vapors is based on the solution of the master equation for $n$mer growth ($2 \le n \le 80$): $A_n + A_i + M \rightleftarrows A_{n+i} + M$. In these calculations the forward and reverse rate constants were related via $k_{n\to n+i}/k_{n+i\to n} = K^{(c)}_{n\to n+i} = \mathcal{R}T \exp[-(\Delta G°_{n+i} - \Delta G°_n - \Delta G°_i)/RT]$; $\Delta G°_1 \equiv 0$ where $\Delta G°_n$ is the *standard* Gibbs free energy increment for the association of $n$ monomers. The corresponding enthalpy and entropy increments were either measured or calculated. "Constrained equilibrium" $n$mer densities were defined; these proved to be identical with $N_n^{ss}$ (steady state densities) for $n < n^\dagger$, at which $N_n^{ss}$ has a minimum. A *kinetic* criterion for the onset of condensation emerged from this analysis. We demonstrated that the transition from the constrained equilibrium for $n < n^\dagger$ to avalanche cluster growth for $n > n^\dagger$ is not dependent on the presence of a maximum in the free-energy function, but is sensitive to the supersaturation ratio. The time to attain steady state was estimated, and we formulated an expression for the condensation flux at that condition.

## I. Introduction

In this report we present a self-consistent kinetic model for homogeneous nucleation and condensation of liquid droplets from a vapor. The specific example used to illustrate our procedure is the condensation of atomic iron generated under supersaturated conditions by shock heating $Fe(CO)_5$ highly diluted in argon.[1] While several kinetic models for homogeneous nucleation have been described,[2] in our opinion these are hybrids because they incorporated relations based on the liquid-drop model, and utilized undefinable quantities such as a surface free energy for clusters of the order of 10 monomer units. This obscured a significant feature of the approach to steady state. The self-consistent kinetic model (SCKM) will be contrasted with those previously published. As initially formulated, all models have many aspects of similarity.

Specifically we will demonstrate the following:

(i) The SCKM, free from ambiguities associated with the usual free energy function ($\Delta\Phi_n = 4\pi r_n^2\,\sigma_n - nkT \ln S$), predicts rapid approach to a steady state which is the start of avalanche condensation.

(ii) The thermodynamically defined *standard* free energy increment for $nA_g = A_{ng}$ [$\Delta G°_n = \Delta H°_n - T\Delta S°_n$] is needed *only* to provide the relation between the forward and reverse rate constants for the growth step: $A_{n-i} + A_i \rightleftarrows A_n$, and this is necessary only for small $n \leq n^\dagger$, as defined below.

(iii) SCKM naturally leads to an interesting interpretation for a condition which is designated as a "constrained equilibrium"; this has physical significance for values of $n < n^\dagger$ but none for $n > n^\dagger$.

(iv) SCKM also requires that a "critical" supersaturation level must be attained in order that condensation occur, but its basis is a low net flux through small *n*mers; it is *not* a consequence of the presence of a maximum in the *standard* free energy function; rather it is determined by how rapidly, with respect to *n*, the free energy function attains substantial negative values.

(v) The critical condition for the onset of condensation is formulated in *kinetic terms* (i.e., relative rates for specified reactions) rather than thermodynamic terms.

(vi) Tests of models based on the temperature dependence of the critical supersaturation ratio are not sufficiently sensitive to confirm or eliminate some of the proposed theories.

(vii) The fundamental unanswered question remains: how to calculate unambiguously and directly the standard enthalpy and entropy for a hypothetical gas of *n*mers, allowing for the wide range of structures such polymeric species could encompass.

In section II we formulated the kinetic model under the assumption that both $\Delta H°_n$ and $\Delta S°_n$ are known. We integrated the master equation, for several combinations of boundary conditions, for $1 \leq n \leq 80$. In section III we briefly outlined the basis for our assumed $\Delta S°_n$ function and estimated the consequences of allowing for reasonable changes in its magnitude. We utilize, without additional justification, the empirically determined *n* dependence of $\Delta H°_n$, based on extensive theoretical and experimental studies.[1] In section IV we introduced the concept of a "constrained equilibrium" and show how this is related to the kinetic model developed in section II. Section V is a brief summary wherein the basic assumptions of the classical[3] and modified models[4] are compared with those of SCKM.

## II. The Kinetic Model

The apparent difference between the previously reported kinetic models and the one described here is our insistence on consistency in formulating the rate equations for accretion and evaporation, subject to the usual thermochemical constraints, without introducing any aspects of the liquid drop model. As a consequence of solving for the time evolution of populations via the master equation, there emerged a characteristic $n^\dagger$, which has the features of a critical nucleus size, but is based on a *kinetic* criterion.

A. The growth of a cluster is a process of accretion, whereby an *n*mer collides with an *i*mer ($i = 1, 2, \ldots$) and the two adhere. Clearly, no bimolecular event can produce a permanently stable $(n + i)$mer, because the nascent unit incorporates sufficient energy for reevaporations. Some energy removing collisions must take place within the mean lifetime of the energized $(n + i)$mer. Since the lifetimes of the nascent clusters increase rapidly with the number of atoms[5] [extension of unimolecular reaction rate theory gives for the mean lifetime

$$\tau_{n+i}^{-1} = \nu^*\left(\frac{E^*_{n+i} - E^c_{n+i}}{E^*_{n+i}}\right)^{s-1}$$

where $E^*_{n+i}$ is the internal energy content of a nascent $(n+i)^{mer}$; $E^c_{n+i}$ is the minimum energy required for evaporation of *i* units, $\nu^*$ is a characteristic molecular frequency $\approx 10^{13}$ s$^{-1}$; and *s* is the number of effective oscillators in the $(n + i)$mer], there exists a transition region from small $(n + i)$mers when growth occurs only through termolecular events, to large $(n + i)$mers, when the applicable kinetics is bimolecular. Then the nascent adducts have a mean lifetime greater than the mean time between energy removing collisions with the ambient gas. It proves inconvenient and somewhat arbitrary to introduce such a deliberate switch-over in the kinetic formulation of cluster growth based on hard sphere kinetic theory. Indeed, rate constants for tertiary collisions as conventionally derived for hard spheres have the wrong temperature dependence, since they increase[6] as $T^{1/2}$ whereas both experiments[7] and trajectory calculations[8] clearly show that the ternary rate constant should be proportional to $T^{-p}$ ($0.5 \leq p \leq 2$).

A rational analysis which does provide for an inverse temperature dependence and automatically shifts from termolecular to bimolecular kinetics when the deexciting gas pressure rises is based on a transient-complex model; i.e.

$$A_n + A_i + Ar \underset{k_{n+i\rightarrow n}}{\overset{k_{n\rightarrow n+i}}{\rightleftharpoons}} A_{n+i} + Ar \qquad (1)$$

is replaced by

$$A_n + A_i \underset{\kappa_{n+i\rightarrow n}}{\overset{\kappa_{n\rightarrow n+i}}{\rightleftharpoons}} A_{n\ldots i} \quad \text{(unstable transient)} \qquad (2)$$

$$A_{n\ldots i} + Ar \xrightarrow[\kappa_s]{} A_{n+i} + Ar \quad \text{(stabilizing collision)} \qquad (2a)$$

On imposing the steady state condition on $A_{n\cdots i}$, one finds for the rate of production of stable $(n + i)$mers

$$\frac{d[A_{n+i}]}{dt} = \left\{\kappa_s \frac{\kappa_{n\rightarrow n+i}}{\kappa_{n+i\rightarrow n}}\right\} \frac{[A_n][A_i][Ar]}{1 + (\kappa_s/\kappa_{n+i\rightarrow n})[Ar]} \qquad (3)$$

This reduces to the bimolecular rate when $\kappa_s[Ar]/\kappa_{n+i\rightarrow n} \gg 1$; for the inverse conditions it reduces to the termolecular rate, with the constant equal to $\{\kappa_s(\kappa_{n\rightarrow n+i}/\kappa_{n+i\rightarrow n})\}$. Calculation of the latter is discussed in detail in many textbooks.[9] To estimate the steady state concentration of $A_{n\cdots i}$, refer to the pictorial representation in Figure 1; i.e., first express the equilibrium density of the transient pairs in terms of their interaction potential $U_{n,i}(r)$, and then estimate the rate of stabilization by treating the $A_{n\cdots i}$ species as well as the Ar atoms as hard sphere colliders. This leads to

$$k_{n\rightarrow n+i} = \left\{\kappa_s \frac{\kappa_{n\rightarrow n+i}}{\kappa_{n+i\rightarrow n}}\right\} = 4\pi^2\left(\eta_{n\ldots i} + \eta_{Ar}\right)^2 \left[\frac{8kT}{\pi\mu^\ddagger}\right]^{1/2} \times \int_{\tilde{\sigma}}^{1.5\tilde{\sigma}} dr\, r^2 \exp[-U_{n,i}(r)/kT] \qquad (4)$$

$\eta_{Ar}$ (= 1.77 Å) is the hard sphere radius of Ar, $\tilde{\sigma} \equiv \eta_n + \eta_i$; $\eta_n$ is the hard sphere radius of the *n*mer [for iron, $\eta_n = 2.95n^{1/3}$ Å]; $\eta_{n\cdots i}$ is the equivalent hard sphere radius of $(n\cdots i)$ species (= $1.5\tilde{\sigma}$; see Figure 1); and $\mu^\ddagger = M_{Ar}M_{n+i}/(M_{Ar} + M_{n+i})$. While the upper limit ($1.5\tilde{\sigma}$) incorporates all transient pairs which could be stabilized by an argon collision, direct integration shows that the result is trivially smaller than were the upper limit replaced by infinity. For

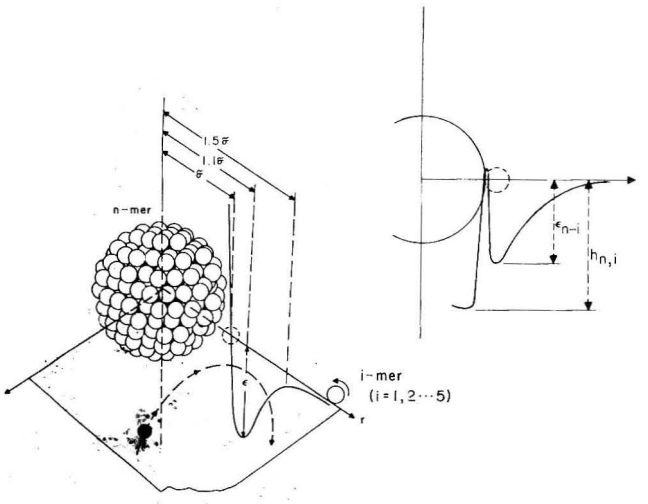


**Figure 1.** Representation of a three-body collision for stabilizing an $(n+i)$mer. The diagram on the right illustrates the difference between the initial attractive well depth and the final enthalpy increment.

$U_{n,i}(r)$ we assumed a Lennard-Jones potential

$$U_{n,i}(r) = 4\epsilon_{n,i}[(\tilde{\sigma}/r)^{12} - (\tilde{\sigma}/r)^{6}] \tag{5}$$

with

$$\epsilon_{n,i} \equiv \frac{|\Delta H^\circ_{n+i}| - |\Delta H^\circ_{n}| - |\Delta H^\circ_{i}|}{2i^{2/3}} \tag{6}$$

Very likely this underestimates the rate constants, but we later demonstrate that factors of 10 have no significant effect on our conclusions. The magnitude of $\epsilon_{n,i}$ is clearly less than $\{|\Delta H^\circ_{n+i}| - |\Delta H^\circ_{n}| - |\Delta H^\circ_{i}|\}$. The latter sum includes the stabilization energy gained by reorganizing the structures of the $n$mer and $i$mer into a stable $(n+i)$ cluster, whereas $\epsilon_{n,i}$ (Figure 1) is the depth of the potential function for the separate units, albeit distorted by their proximity. The transition from the $(n\cdots i)$ configuration to the integrated $(n+i)$mer, catalyzed by the Ar collision, probably involves a small activation energy. The denominator in (6) is arbitrary, and can be justified only a posteori. In addition, calculations show that contributions from events $i \geq 2$ are negligible.

To obtain the inverse rate constants, $k_{n+i\to n}$, start with the thermochemical relation for $n\mathrm{A} = \mathrm{A}_n$, applicable to an ideal gas, under standard conditions ($p^\circ_n = 1$ atm); then $\Delta G^\circ_n = \Delta H^\circ_n - T\Delta S^\circ_n$; $\Delta H^\circ_n = \Delta H^\circ_\infty(1 - n^{-0.25})$;[1] $\Delta S^\circ_n = \Delta S_n^{(\mathrm{r})} + \Delta S_n^{(\mathrm{c})}$ [section III]

$$\frac{k_{n\to n+i}}{k_{n+i\to n}} = \mathfrak{R}T \exp\left[-\frac{\Delta G^\circ_{n+i} - \Delta G^\circ_{n} - \Delta G^\circ_{i}}{RT}\right] \tag{7}$$

$$\Delta G^\circ_1 \equiv 0$$

$\mathfrak{R}$ (cm$^3$ atm cluster$^{-1}$ deg$^{-1}$); $k_{n\to n+i}$[Ar] (cluster$^{-1}$ cm$^3$ s$^{-1}$). Both the forward and reverse rate constants are plotted in Figure 2. These were calculated for iron vapor (in excess argon) at 1600 K; [Ar] = $1.88 \times 10^{18}$ cm$^{-3}$. The growth rate constants are large indeed even though the value of $\epsilon$ was reduced by dividing the net enthalpy increment for association by $(2i^{2/3})$. The constants have the expected dependence on $n$ and $i$; $k_{n\to n+i}$ increase due to the effect of cluster size (on the $\eta$'s), and the attractive potential (on $\epsilon$). The evaporation rates decrease with $n$ and $i$, as expected, due to the increase in stability with rising $n$. At this time we introduce (for later use) empirical expressions for the monomer growth rate constants

$$k_{n\to n+i} = 10^{-10}n^{1.8} \qquad 10 \leq n \leq 150$$
$$= 10^{-11}n^{2.6} \qquad 100 \leq n \leq 1500 \tag{8}$$

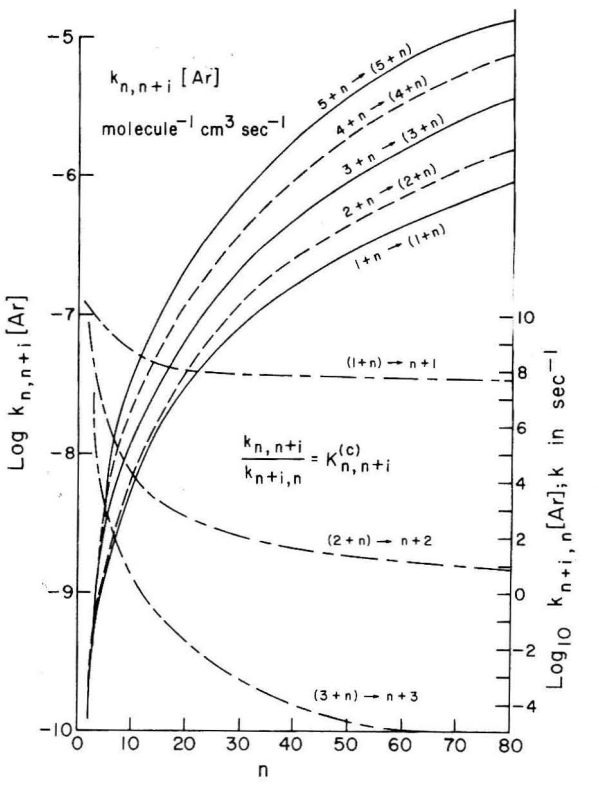


**Figure 2.** Rate constants for cluster growth and evaporation; dependence on cluster size.

*Our objective is to test the system dynamics for cluster growth.* Hence, we did not disect $k_{n\to n+i}$ into its component $\varkappa$'s. This could be done by estimating lifetimes of the transient species $\mathrm{A}_{n-i}$,[5] and the introduction of an arbitrary sticking coefficient for the forward bimolecular step. The general expression for the bimolecular rate constant[9a] is

$$k_{\mathrm{bi}} = \left(\frac{2}{\pi}\right)^{1/2}\left(\frac{\mu}{kT}\right)^{3/2} \times \int_0^\infty \mathrm{d}v_\mathrm{r} v_\mathrm{r}^3 S(v_\mathrm{r}) \exp[-\mu v_\mathrm{r}^2/2kT] \tag{9}$$

$\mu \equiv M_nM_i/(M_n + M_i)$; $v_\mathrm{r}$ is the relative velocity of $\mathrm{A}_n$ and $\mathrm{A}_i$; and $S(v_\mathrm{r})$ is the *reactive* collision cross section, which depends on $U_{n,i}(r)$ and the assumed sticking probability. Finally, a word regarding other cluster growth processes. These include

$$\mathrm{A}_n + \mathrm{A}_m \rightleftarrows \mathrm{A}_{n+m-i} + \mathrm{A}_i \quad \text{(coagulation)}$$
$$\mathrm{A}_n + \mathrm{A}_m \rightleftarrows \mathrm{A}_{n+i} + \mathrm{A}_{m-i} \quad \text{(abstraction)} \tag{10}$$

Obviously, there is no sharp distinction between these two steps; the classification is introduced purely for convenience, when $i$ is small while $n$ and $m$ are both large. It is our contention that such reactions do occur during later times in the condensation process,[10] and are of low probability during the onset of condensation.

B. The master equation for the system populations must be integrated starting with a specified initial monomer density, $N^\circ_1$, and $N_{n>1} = 0$ at $t = 0$; mass balance is maintained at all times.

$$\frac{1}{[\mathrm{Ar}]}\frac{\mathrm{d}N_n}{\mathrm{d}t} = \sum_{i=1}^{5}\{k_{n-i\to n}N_{n-i}N_i + k_{n+i\to n}N_{n+i} - k_{n\to n-i}N_n - k_{n\to n+i}N_nN_i\} \tag{11}$$

These coupled differential equations proved to be extremely "stiff", i.e., they involve both rapidly changing and slowly changing terms, with differences which nearly cancel. Solution was accomplished with a GEAR subrou-

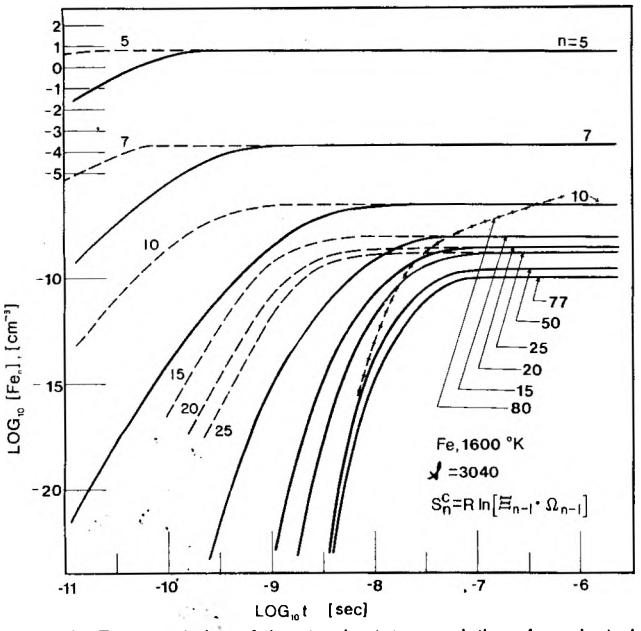


**Figure 3.** Time evolution of the steady state populations for selected *n*mers. The dotted curves were obtained when all the rate constants were multiplied by a factor of 10 [$S = 3040$]; $n^{ul} = 80$.

tine.[11] Nevertheless, computer time on the IBM-370 was quite long. Solutions were obtained at two supersaturations, in which we varied the number of coupled equations, from $n = 1 \rightarrow 20$ to $n = 1 \rightarrow 80$, and the types of reactions considered; i.e., monomer addition only ($i = 1$) to monomer $\rightarrow$ pentamer addition ($i = 1 \rightarrow 5$) inclusive. We found that the *n*mer concentrations vs. time were independent of the specified upper limit for $n(n^{ul})$ which is inserted in the program, for all $n \lesssim (n^{ul} - 3)$. The imposed limit on $n$ caused the distribution to "bottleneck" near $n^{ul}$ (i.e., values for $n^{ul} - 2$, $n^{ul} - 1$, and $n^{ul}$ were overvalued) while the concentration–time history of all the other species remained unaffected. This became apparent when the sequence $n^{ul} = 60, 70, 80$ were calculated in turn. It was found also that monomer addition was the most important process; $i = 2$ generally contributed less than 10%. Although dimer, trimer, etc. additions had only a small effect on the concentrations, they were included for the sake of completeness.

The monomer concentration decreased (from the initial value $[N_1^0]$) by less than 0.1% throughout the simulation time of ca. 250 $\mu$s. This can be used to check on the accuracy of the GEAR program. Were the monomer concentration to remain strictly constant the kinetics reduces to a sequence of unimolecular steps, and the consequent first-order rate equations can be solved in closed form. In practice this involves an $n^{ul} \times n^{ul}$ secular determinant for its eigenvalues. We discovered that to attain comparable accuracy this required as much computer time as the GEAR integration routine. We did obtain in closed form solutions for a run with $n^{ul} = 20$, and the results agreed exactly with the GEAR values.

Figure 3 consists of plots of *n*mer concentrations vs. time (GEAR integration) for $N_1^0 = 1.88 \times 10^{16}$ cm$^3$; $S = 3040$, $T = 1600$ K, and $n^{ul} = 80$. There is a rapid increase in the *n*mer concentrations between $10^{-11}$ and $10^{-7}$ s. By $t = 10^{-7}$ s the curves level off as the system attains steady state. For small $n$ the magnitudes of the steady state concentrations decrease rapidly with increasing $n$, but the difference is negligible for $n > 50$. During the final test period of $\sim$250 $\mu$s, the monomer concentration had decreased slightly. The dashed line shows the evolution of the 80-mer concentration; this illustrates the "bottleneck effect"; its rise above the $n = 77$ curve is an artifact of the upper limit. We call attention to the dotted curves; these were obtained when we arbitrarily multiplied all the rate constants by a factor of 10. As anticipated, the system approaches the *same steady state levels*, faster by about a factor of 10. Figure 4 shows the same data for selected times, plotted vs. $n$. This illustrates directly the effect of the upper limit ($n^{ul}$) on the computed concentrations. Figures 5 and 6 are analogous calculations for an excessively large $S = 30400$, to check on the two anticipated effects of high density: (i) increasing the supersaturation by a factor of 10 decreases the time for attainment of steady state by the same factor; and (ii) raises the steady state level of the large $n$ species by almost 10 orders of magnitude.

Since limitations on computer time, both practical and monetary, prevented us from extending the calculation significantly past $n^{ul} = 80$, we estimated the time to reach steady state for larger *n*mers as follows. We shall demonstrate below that for $n > n^{\dagger}$ the rate of evaporation is much less than the rate of accretion, and that for $n \geq 50$ it is entirely negligible. Hence the mean lifetime of an *n*mer, $\langle \tau_n \rangle$, is given approximately by

$$\langle \tau \rangle \simeq \{k_{n \rightarrow n+1}[\mathrm{Ar}]N_1\}^{-1} \tag{12}$$

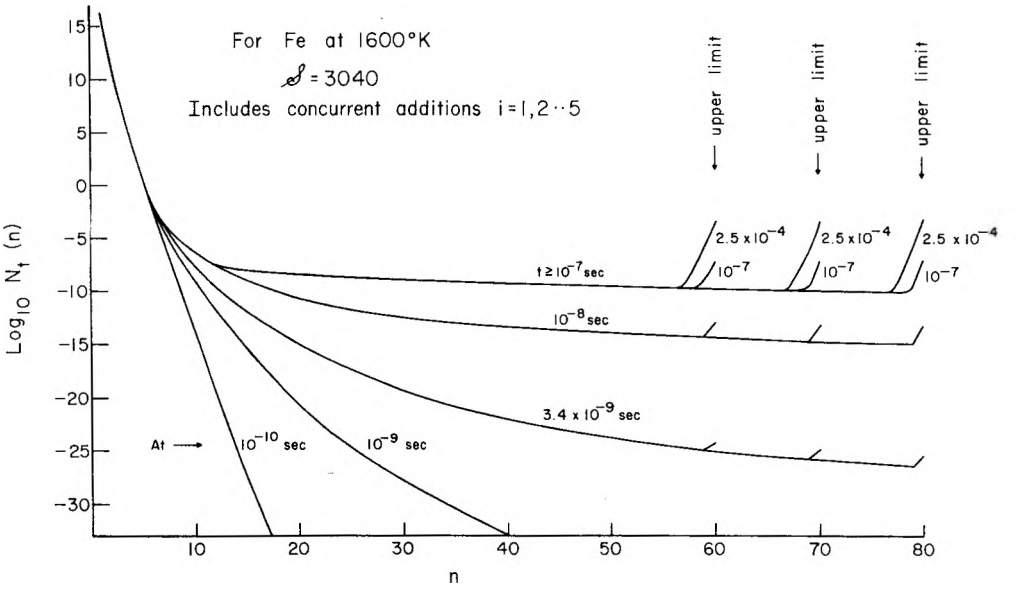


**Figure 4.** The distribution of populations at various times on the way toward a steady state [$S = 3040$].

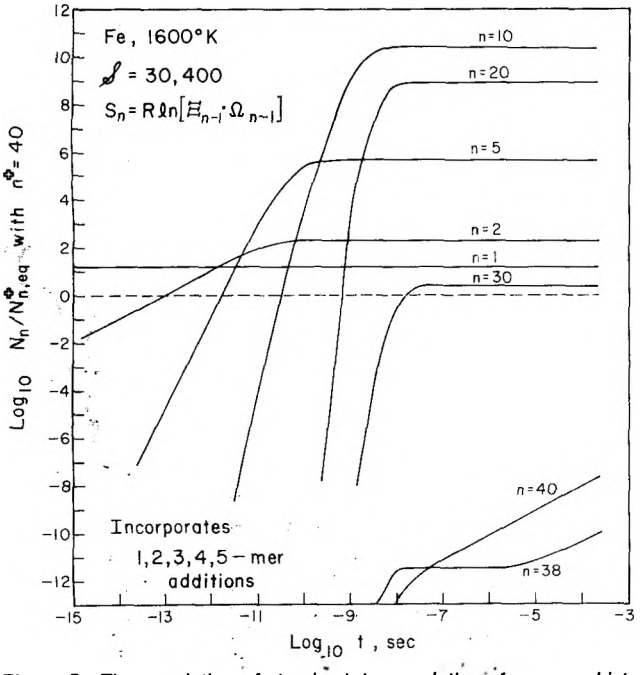


**Figure 5.** Time evolution of steady state populations for a very high supersaturation ratio [$S$ = 30400]; $n^{ul}$ = 40. Compare with Figure 3.

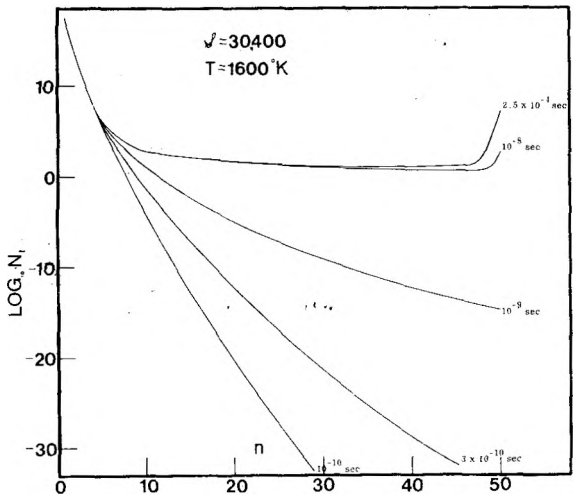


**Figure 6.** The distribution of populations for a very high supersaturation ratio [$S$ = 30400]; compare with Figure 4.

For $n \geq 50$

$$k_{n \rightarrow n+1} \approx 10^{-11} n^{2.6} \text{ cm}^3 \text{ s}^{-1} \quad (8')$$

when the argon concentration is $1.88 \times 10^{18}$ cm$^{-3}$, and the monomer concentration is $1.88 \times 10^{16}$ cm$^{-3}$ ($S$ = 3040). Hence $\langle \tau_n \rangle \approx 5.3 \times 10^{-6} n^{2.6}$. The approximate time for an $m$mer ($m > 50$) to reach steady state is then

$$\langle t \rangle_m^{ss} \approx \langle t \rangle_{50}^{ss} + \sum_{n=50}^{m-1} \langle \tau_n \rangle \quad (13)$$

Replacing the sum with an integral, and recognizing that the time for a 50-mer to reach steady state is ca. 0.1 $\mu$s

$$\langle t \rangle_m^{ss} = 0.10 + 5.3 \times 10^{-6} \int_{50}^{m-1} dn/n^{2.6} \quad (14)$$

$$\langle t \rangle_m^{ss} \approx \left[0.106 - \frac{3.32}{m^{1.6}}\right] \mu\text{s} \quad (15)$$

Hence, the time delay to reach steady state is indeed very short ($\sim 10^{-7}$ s), even for large $m$.[12]

C. The most interesting aspect of the steady state condition appears upon inspection of the relative magnitudes of the four terms which comprise the master eq 11. For small $n$, $N_n^{ss}$ remains at a steady state because the rate of production by accretion $\{\Delta n \equiv k_{n-i \rightarrow n} N_{n-i} N_i\}$ is very nearly balanced by the rate of evaporation loss $\{\nabla n \equiv k_{n \rightarrow n-i} N_n \approx \Delta n\}$; concurrently the magnitude of the upward flow is relatively small $\{\Delta(n+i) \equiv k_{n \rightarrow n+i} N_n N_i \ll \Delta n\}$, and this is nearly balanced by the downward flow $\{\nabla(n+i) \equiv k_{n+i \rightarrow n} N_{n+i} \approx \Delta(n+i)\}$ (Scheme I). In contrast, for large $n$ the steady state condition is maintained because $\Delta n \simeq \Delta(n+i) \gg \nabla n \simeq \nabla(n+i)$. Typical values are assembled in Table I. Comparison with Figure 4 shows that the *transition* $n$mer ($n^\dagger$) occurs at the rounded portion of the $t \geq 10^{-7}$ curve, where $\Delta n \approx \nabla n \approx \Delta(n+i) \approx \nabla(n+i)$. At higher supersaturations (Figure 6) the transition occurs at small $n^\dagger (\approx 7)$, as expected.

Scheme I

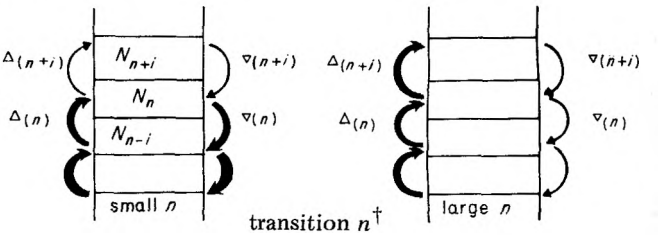


TABLE I: Unidirectional (Partial) Fluxes (cm$^{-3}$ s$^{-1}$) During Steady State Condition ($t = 5 \times 10^{-7}$ s)[a]

| | | | |
|---|---|---|---|
| 9 → 10 | $1.442 \times 10^2$ | 10 → 9 | $1.422 \times 10^2$ |
| 10 → 11 | $3.907 \times 10^1$ | 11 → 10 | $3.726 \times 10^1$ |
| 13 → 14 | 4.565 | 14 → 13 | 2.791 |
| 14 → 15 | 2.805 | 15 → 14 | 1.048 |
| 29 → 30 | 1.860 | 30 → 29 | $8.998 \times 10^{-2}$ |
| 30 → 31 | 1.843 | 31 → 30 | $7.918 \times 10^{-2}$ |
| 69 → 70 | 1.782 | 70 → 69 | $7.968 \times 10^{-3}$ |
| 70 → 71 | 1.773 | 71 → 70 | $7.754 \times 10^{-3}$ |

[a] Fe at 1600 K; $N_1^0 = 1.88 \times 10^{16}$ cm$^{-3}$; [Ar] = $1.88 \times 10^{18}$ cm$^{-3}$. Note: "Rounding-off" errors do accumulate after many integrations.

We propose the following *kinetic* criterion for the critical size cluster, and for the onset of catastrophic condensation: $n^\dagger$ is that cluster number for which the four unidirectional flows are nearly equal. At that juncture maintenance of the steady state condition on $N_n$ changes from that in which evaporation balances accretion to that when the growth rate is much larger than the decay rate. It is demonstrated below that this kinetic criterion is *not* dependent on the presence of a maximum in the free energy function. Catastrophic condensation sets in very soon after the attainment of the steady state, since $\langle t_m \rangle^{ss}$ is insignificantly longer for large $n$ than for small $n$.

This kinetic model also provides an estimate of the condensation flux during the steady state condition [i.e., the net flow from $n \rightarrow (n+1)$, cm$^{-3}$ s$^{-1}$]. Because only monomer accretion is an important contributor to the growth rate, *and* because early in the attainment of the steady state $N_1(t) \simeq N_1^0$, then

$$J^{ss} \cong k_{n \rightarrow n+1}[\text{Ar}] N_1^0 N_n - k_{n+1 \rightarrow n}[\text{Ar}] N_{n+1} \quad (16)$$

It will be demonstrated in section IV that this magnitude can be evaluated from thermochemical data and knowledge of $k_{n \rightarrow n+1}$. Note also that for $n > n^\dagger$, the condensation process is independent of the free energy function since the $(\nabla n)$ and $\nabla(n+i)$ terms are insignificant. However, the location of the bend in the $\langle t \rangle^{ss}$ curves [Figures 4 and 6] depends sensitively on the magnitude of $\Delta G^\circ_n$ for $2 < n < n^\dagger$. This portion of the free energy function determines

$N^{ss}$ at $n^{\dagger}$, which in turn controls $J^{ss}$. Obviously, changing the rate constants affects the magnitude of $J^{ss}$ as well as the time required to attain steady state.

## III. Estimation of the Entropy Function

The entropy change accompanying the formation of an $n$mer from a gas of monomers is $\Delta S^{\circ}_n = S^{\circ}_n - nS^{\circ}_1$. One of several approaches for estimating $S^{\circ}_n$ is to separate the standard entropy of an $n$mer into two parts

$$S^{\circ}_n = S^{r}_n + S^{c}_n \tag{17}$$

$S^{r}_n$ incorporates the translational, rotational, and vibrational terms for a "rigid" cluster, and $S^{c}_n$ is the configurational contribution, in essence, the isomer number for the $n$mer species, assuming that all distinguishable structures which have enthalpies about equal to that of the most stable configuration are counted. This molecular model for a cluster differs from, but is equivalent to, the representation of small clusters as liquid drops which possess excess entropy due to their relatively flabby structures. The molecular dynamics calculations by Burton[13] showed that the atoms in small clusters ($2 \leq n \lesssim 100$) have liquidlike mobility and are not constrained to rigid structures. This is the counterpart of the configurational entropy contribution, $S^{c}_n$, due to the multiplicity of equal energy configurations based on rigid structures. In $S^{c}_n = R \ln \Omega_n$, $\Omega_n$ is the number of possible configurations (isomers) of comparable energy for a cluster containing $n$ atoms. If every atom in the cluster were distinguishable from the rest, the upper limit for $\Omega_n$ would be $n!$. This is an overestimate, particularly for large $n$ since it has been shown[14] that

$$\lim_{n\to\infty} \Omega_n \propto (n^{2/3}) \tag{18}$$

Our estimates of $\Omega_n$ were made as follows.

$2 \leq n \leq 7$. In this range $\Omega_n$ was obtained by a direct count of the number of isomers for each $n$. For example, the trimer has two distinguishable configurations (linear; bent); the tetramer has four tetrahedral, etc.

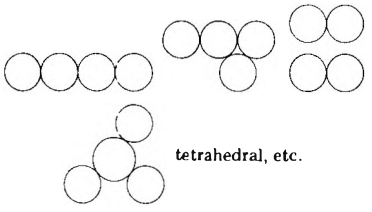


This approach is similar to that of Hoare and McInnes.[15]

$8 \leq n \lesssim 100$. In this size range we postulate that the number of isomers which can be generated from any type of $n$mer is $\Xi_{n-1}$ times the number of its antecedent $(n-1)$mers, where $\Xi_{n-1}$ is the number of surface atoms in the $(n-1)$mer [i.e., $\Omega_n = \Xi_{n-1}\Omega_{n-1}$]. For spherical clusters containing $(n-1)$ atoms ($n$ large)

$$\Xi_{n-1} = 2(n-1)^{2/3} \tag{19}$$

In the range $8 \leq n \leq 17$, a direct count was made of the number of surface atoms. For values of $n > 17$, eq 19 is adequate. A plot of configurational entropy (per atom) estimated in this manner is shown in Figure 7. Since $S^{c}_n/n$ must approach zero as $n$ approaches infinity, the above estimate is valid only for $n \leq 10^3$. The above analysis leads to

$$\frac{S^{c}_n}{nR} \approx \left(\frac{n-1}{n}\right)\ln 2 + \frac{2}{3n}\sum_{j=1}^{n-1} \ln j \tag{20}$$

which slowly diverges as $n \to \infty$. We may have overestimated $\Delta S^{c}_n$ and thus favored cluster formation; this counterbalances the effect of $(2i^{2/3})$ incorporated in denominator of eq 6.

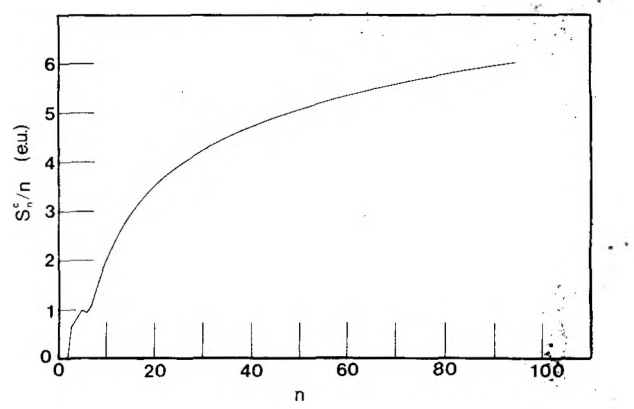


**Figure 7.** The configurational entropy based on our estimate of the total number of distinct structures which are energetically equivalent.

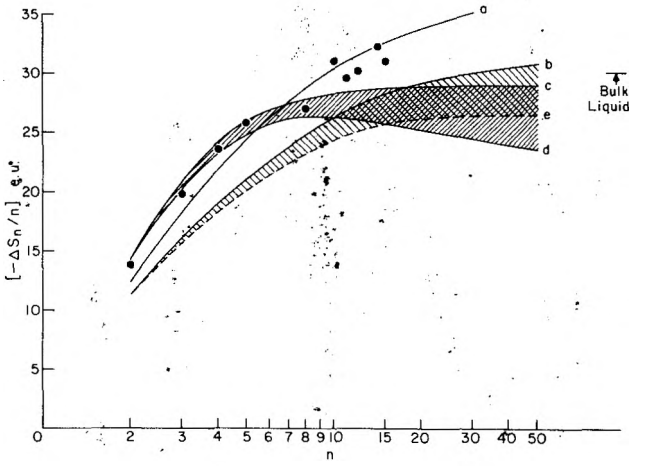


**Figure 8.** Estimated entropy increments for condensation [per $n$mer] vs. cluster size: (a) $\Delta S^{r}_n/n$, Fe crystal model, with $\nu_D = 2.3 \times 10^{13}$ s$^{-1}$; (b) $\Delta S^{r}_n/n$, Fe crystal model, with $\nu_D = 1.1 \times 10^{13}$ s$^{-1}$; (c) $\Delta S^{r}_n$ empirically fitted to entropy loss for $(2 \leq n \leq 8)$ [i.e., $29n^2/(3+n^2)$]; (d) $\Delta S^{r}_n$(c) + $\Delta S^{c}_n$ (Figure 7); (e) $\Delta S^{r}_n$(b) + $\Delta S^{c}_n$ (Figure 7). The shaded areas indicate the magnitude of the configurational entropy term. (●) Averaged values for $\Delta S_{(\text{recomb})}$ for $2 \leq n \leq 16$. Overall, these points are fitted by $[31n^2/(5+n^2)]$.

The increment in structural entropy, $\Delta S^{r}_n$, was obtained empirically by averaging many published values for gas phase polymerization reactions.[16] For each $n$, entropy decrements were tabulated for reactions such as

$$2K(g) \rightleftarrows K_2(g)$$
$$3C(g) \rightleftarrows C_3(g)$$
$$nX + mY \rightleftarrows X_nY_m$$

The mean values are plotted in Figure 8 (circles); a smooth curve through them has the form $\Delta S^{r}_n/n = 31n^2/(5+n^2)$. However, since this function does not extrapolate to the bulk liquid value ($n \to \infty$), we used curve c, Figure 8:

$$\Delta S^{r}_n/n = -29n^2/(3+n^2) \tag{21}$$

Hence an acceptable approximation for the standard entropy change for the association of $n$ monomers is

$$\Delta S^{\circ}_n = -\frac{29n^2}{3+n^2} + R \ln \Omega_{n-1}\Xi_{n-1} \tag{22}$$

The direct method for calculating the entropy is the statistical mechanics approach used by Hoare and Pal,[17] Hale and Plummer,[2c] and others in their studies of small clusters. We believe that the uncertainty introduced in any estimate of the partition functions which must include,

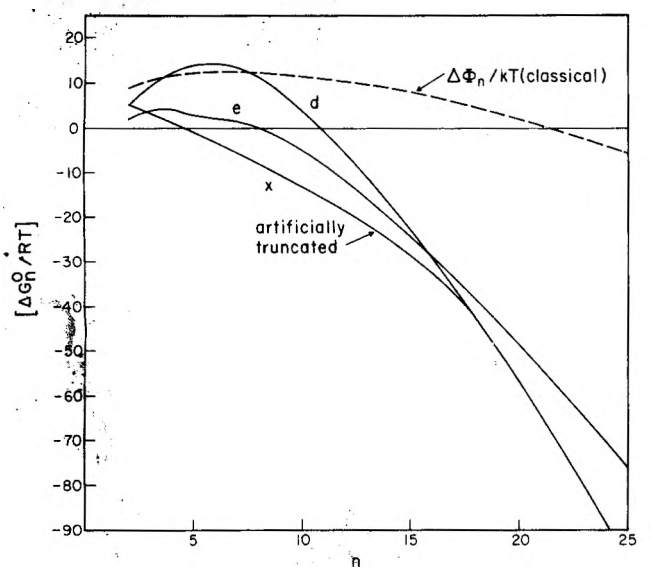


**Figure 9.** Reduced free energies for cluster formation vs. cluster size: (d) empirical $\Delta H^\circ_n$ combined with $T\Delta S^\circ_n$ (d) of Figure 8; (e) empirical $\Delta H^\circ_n$ combined with $T\Delta S^\circ_n$ (e) of Figure 8; (x) artificially truncated free energy function to test the effect of removing the maximum at $n = 6$. $\Delta\Phi_n/kT = (4\pi/k\bar{T})(3n/4\pi)^{2/3}(\sigma/\rho^{2/3})_{bulk} - n \ln \boldsymbol{S}_1$ for Fe at 1600 K; $\boldsymbol{S} = 3040$; $\sigma = 1800$ erg cm$^{-2}$.

besides estimated vibrational frequency distributions, allowance for symmetry factors and decisions on questions of equivalent configurations, etc., results in at least as much ambiguity in the final values as there is in our approach. However, we did calculate the translational, rotational, and vibrational contributions to the entropy of Fe $n$mers at 1 atm, at 1600 K via the standard statistical-mechanics equations, treating the clusters as spherical crystals. Specific structures were assumed for $2 \leq n \leq 5$; for $n > 5$ the rotational symmetry number was taken as unity, and the moments of inertia were calculated from the bulk density of atoms. For the vibrational contribution a single mean frequency was inserted and identified with $\nu_{Debye}$. From heat capacity data for solid iron at 1600 K ($C_v \simeq 5.8$ cal mol$^{-1}$ deg$^{-1}$), $\nu_D = 2.3 \times 10^{13}$ s$^{-1}$. Curve a in Figure 8 is $(\Delta S^r_n/n)$ for $\nu_D = 2.3 \times 10^{13}$ s$^{-1}$, and curve b corresponds to $\nu_D = 1.0 \times 10^{13}$ s$^{-1}$. Thus the empirical expression compares favorably with the statistical-mechanical calculation while the difference between curves a and b emphasizes the ambiguity of assigning a bulk value to small clusters.

On combining the enthalpy and entropy equations one obtains an expression for the *standard* Gibbs free energy change due to the formation of $n$mers from monomers

$$\Delta G^\circ_n = -n|\Delta H^\circ_\infty|(1 - n^{-0.25}) - T[\Delta S^r_n + R \ln (\Omega_{n-1}\Xi_{n-1})] \quad (23)$$

Graphs of $\Delta G^\circ_n/RT$ vs. $n$ for Fe at 1600 K are shown in Figure 9. For comparison, we also plotted the classical $\Delta\Phi_n$ function for Fe at 1600 K, $\boldsymbol{S} = 3040$, and $\sigma_{bulk} = 1800$ erg cm$^{-2}$.

## IV. The Constrained Equilibrium

A. For a system at a specified pressure, temperature, and initial composition one may calculate the equilibrium concentrations of all interrelated species if the corresponding *standard* free energy functions are known. Thus, for $nA \rightleftarrows A_n$

$$\frac{N_n^e}{(N_1^e)^n} = K^c_n = (\mathcal{R}T)^{n-1} \exp(-\Delta G^\circ_n/RT) \quad (24)$$

We also make use of the relation: $K^{(c)}_{n\rightarrow n+i} = K^{(c)}_{n+i}/K^{(c)}_n K^{(c)}_i$. With respect to the composition of any vapor which may incorporate polymers, eq 24 is precisely valid only for $\boldsymbol{S} \leq 1$.

We now define a "constrained" equilibrium, by postulating that eq 24 applies to a supersaturated vapor, as a transient state (or sequence of states through which the system passes on its way to the bulk state). Such a

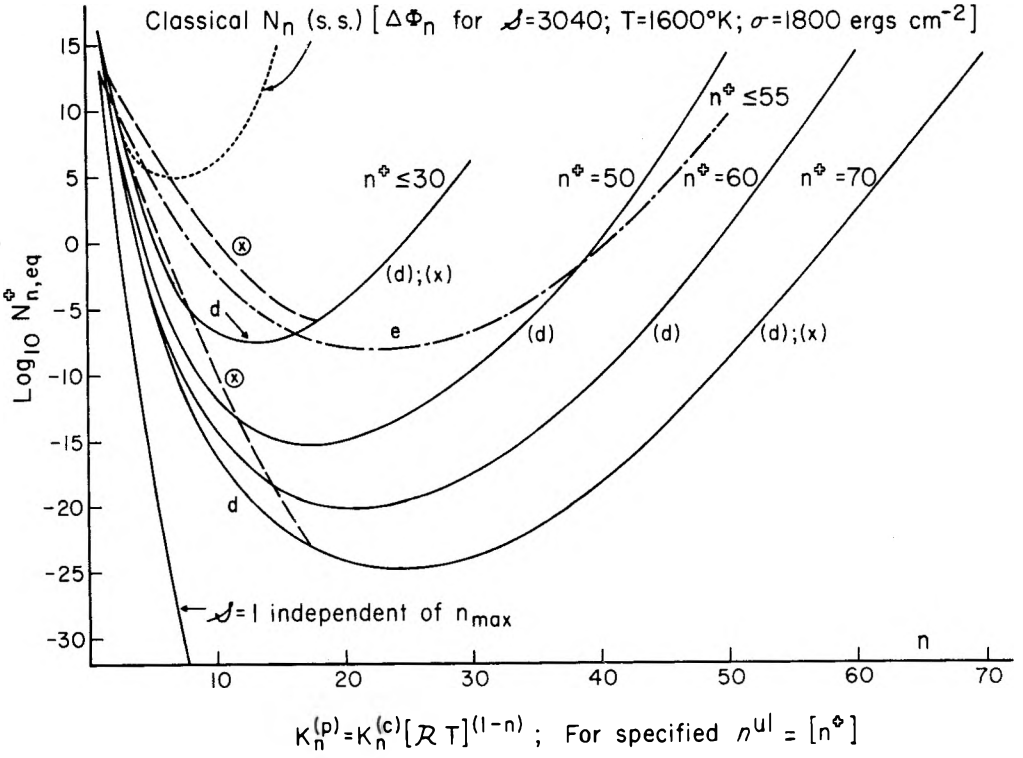


**Figure 10.** "Constrained equilibrium" $n$mer densities for specified upper cut-off ($n^{ul}$)mers [$\boldsymbol{S} = 3040$]. The full curves correspond to assigned entropy (d) in Figure 8. The dot-dash curve (e) corresponds to curve e in Figure 8. The dashed curves correspond to the truncated free energy function (x) in Figure 9. Contrast with the dotted curve for $N_n^{ss}$ (classical) based on $N_n = N_1 \exp(-\Delta\Phi_n/kT)$ with $\Delta\Phi_n = 4\pi r_n^2\sigma_n - nkT \ln \boldsymbol{S}$.

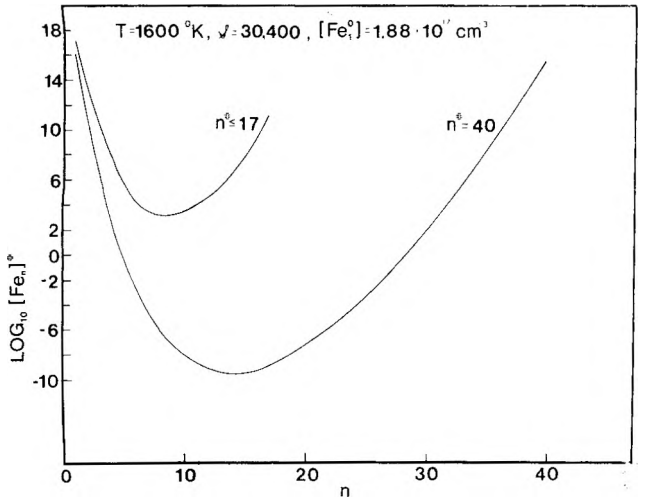


**Figure 11.** "Constrained equilibrium" *n*mer densities for a high supersaturation ratio [$S = 30400$]. The assigned entropy (d) was used for these calculations.

definition is meaningful *only* if concurrently one specifies *an upper bound to n*, the largest size cluster which is tolerated ($n^{ul}$). Then, to satisfy mass conservation

$$N_1^0 = N_1{}^{ul} + 2N_2{}^{ul} + 3N_3{}^{ul} + \ldots n^{ul}N^{ul}{}_{n^{ul}} \quad (25a)$$

$$= N_1{}^{ul} + 2K_2{}^{(c)}\{N_1{}^{ul}\}^2 + 3K_3{}^{(c)}\{N_1{}^{ul}\}^3 + \ldots n^{ul}K^{(c)}{}_{n^{ul}}\{N_1{}^{ul}\}^{n^{ul}} \quad (25b)$$

The results of calculations for Fe vapor at $S = 1$, and two levels of supersaturation 3040, and 30400 {$(Fe_1{}^0 = 6.2 \times 10^{12}$, $1.88 \times 10^{16}$, and $1.88 \times 10^{17}$ atoms/cm$^3$, respectively} are shown in Figures 10 and 11. For $S > 1$, note that the calculated values of the constrained equilibrium concentrations are essentially independent of $n^{ul}$ for small values of $n^{ul}$, i.e., for $n^{ul} \lesssim 30$ when $S = 3040$, and for $n^{ul} \lesssim 17$ when $S = 30400$. Only for $n^{ul}$ greater than these limits do the midportions of the curves get lowered, as the mass of the system shifts to larger *n*mers. Of greater interest, the minimum in the concentration curves *does not* correspond to the maximum in the standard free energy curve, Figure 9. In fact, the location of the minimum shifts to larger *n* as $n^{ul}$ is increased. To emphasize this aspect, contrary to classical formulation of condensation theory, the free energy curves for both supersaturations were artificially smoothed in the range $n \leq 18$ by truncating the maximum, as in curve x, Figure 9, and the constrained equilibrium concentrations were recalculated. The only effect of removing the free energy maximum was to increase the concentration of *n*mers over the range of values spanned by curve x, as anticipated in view of the more negative values for $\Delta G^\circ{}_n(x)$. All other *n*mer concentrations remained unchanged. Figure 12a,b shows the result of this calculation for $n^{ul} = 30$. For larger $n^{ul}$, the truncated free energy function has a smaller effect on the concentrations, and has no effect on the position of $N_n$ minimum. As a measure of the sensitivity of the $N_n$'s to the assumed entropy function, compare the $n^{ul} = 30$ curve in Figure 10, which is based on curve d of Figure 8 (and 9), with the corresponding curve based on curve e (Figures 8 and 9). $N_n(\min)$ remained essentially unchanged but the location of the minimum shifted from $n \simeq 13$ to $n \simeq 22$. The crucial role of the configurational entropy is evident. Were the shaded contributions in Figure 8 omitted, the $N_n$ distribution would not bottom-out until much large *n* values ($\sim 10^4$) are reached. We reemphasize: the magnitude of $n_{min}$ is determined primarily by how rapidly the $\Delta G^\circ{}_n$ function attains sufficiently negative values for $n \lesssim n_{min}$. Finally, note the dramatic effect of the supersaturation ratio on the magnitude of the minimum *n*mer concentration for a given $n^{ul}$. For example, a one order of magnitude increase in $S$ from 3040 to 30400 raises the concentration minimum, for the $n^{ul} = 30$ curve, from $\sim 10^{-8}$ to $10^{-4}$ cm$^{-3}$, while the value of *n* at the minimum decreases from $n \approx 14$ to $n \approx 11$. It is our contention that the classical $N_n$ curve (Figure 10) is too high, as anticipated by Courtney.[18]

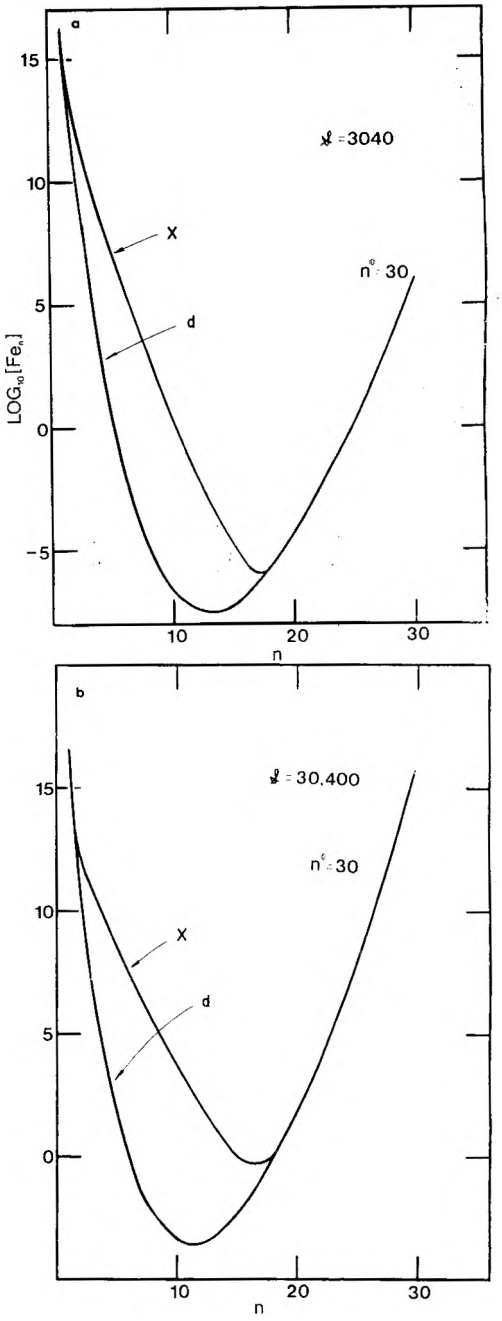


**Figure 12.** (a,b) Dependence of the "constrained equilibrium" densities on the presence of a maximum in the free energy function: curves (d) vs. (x) for two levels of supersaturation.

B. There is physical significance to the portion of the $n^{ul} \leq 30$ curve ($S = 3040$) and $n^{ul} \leq 17$ curve ($S = 30400$), for values of $2 < n < n_{min}$. If one superposes the steady state curve of Figure 4 onto the plot of the constrained equilibrium values, it becomes evident that (i) the kinetic model at steady state gives $N_n$ levels identical with the constrained equilibrium values for $n < n_{min}$, Figures 13 and 14. Furthermore, (ii) the minimum in the $n^{ul} \leq 30$ curve plays the same general role in our formulation as does the *critical cluster size* in classical theory, except that its

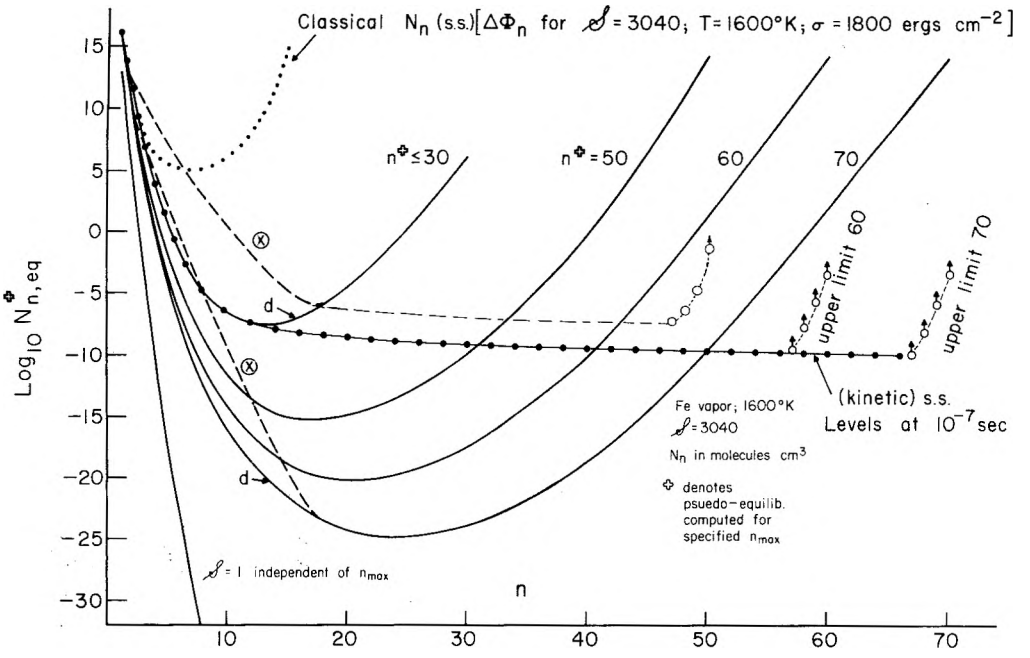


**Figure 13.** Superposition of steady state ($N_n^{ss}$) values upon the constrained equilibrium curves [$S = 3040$]. The two sets are essentially equal for all $n < n\dagger$.

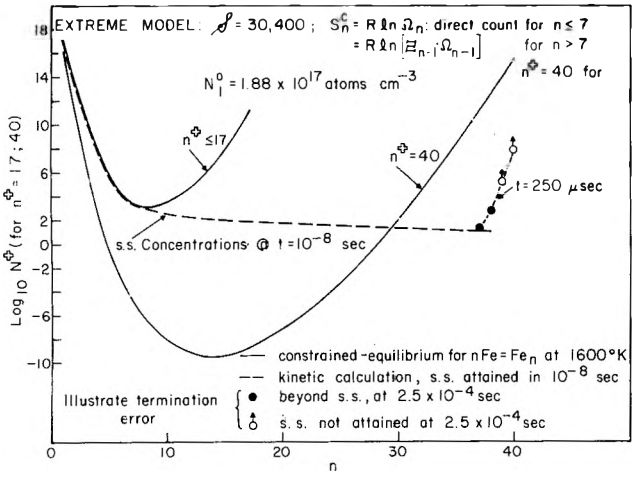


**Figure 14.** Similar to Figure 13, for $S = 30400$.

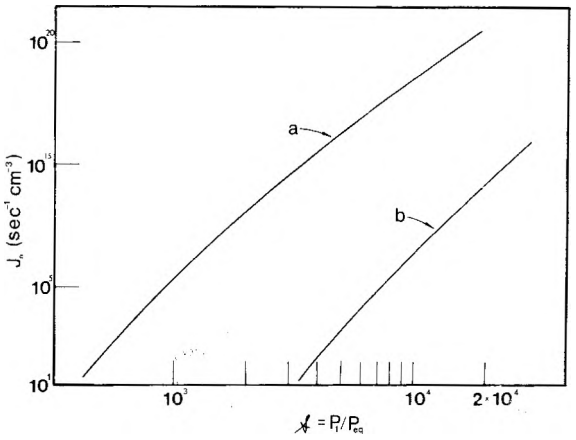


**Figure 15.** The dependence of $J^{ss}$ on $S$; comparison of the kinetic model (b) with classical theory (a).

location is not tied to a maximum in the free energy function. The "bottleneck" at the minimum of the limiting constrained equilibrium curve (smallest $n^{ul}$) is the *kinetic* switchover from a growth process in which reevaporation nearly balances accretion, to one in which loss by forward growth nearly balances the rate of production by accretion.

Study of the computer print-outs showed that for the limiting constrained equilibrium curve ($n^{ul} \leq 30$; $S = 3040$ and $n^{ul} \leq 17$; $S = 30400$) the monomer concentration $N_1^{ul}$ changed very little from its initial value, $N_1^0$, due to the low concentrations developed for all the $n$mers up to $n^{ul}$. Hence, to a good approximation, $N_n^{ul} \simeq (N_1^0)^n (\mathcal{R}T)^{n-1} \exp(-\Delta G^\circ_n/RT)$, for $n \leq n_{min}$. The *steady state* concentrations, attained *kinetically* after a very short time, $N^{ss}$ at $n^\dagger \simeq N^{ul}_{n(min)} = N^{ul}_{n+i(min)}$. However, the latter value can be computed from thermochemical data, by setting $(\partial N^{ul}_n/\partial n) = 0$ under the condition that $N^{ul}_1 = N_1^0$. Equation 16 can now be rewritten for $n = n_{min}$

$$J^{ss} \simeq k_{n\to n+1}[\text{Ar}] N^{ul}{}_{min} \left[ N_1^0 - (\mathcal{R}T)^{-1} \exp\left( + \frac{\Delta G^\circ_{n+1} - \Delta G^\circ_n}{RT} \right) \right] \qquad (16')$$

Thus, $J^{ss}$ is linear with $k_{n\to n+1}$, and through $N^{ul}{}_{min}$ is very sensitive to $S$. In Figure 15 the dependence of the flux on the supersaturation ratio, derived from eq 16′ is compared with that given by classical theory. The displacement of the curves is primarily due to the corresponding differences in $N^{ul}{}_{min}$ (see Figure 10).

## V. Comparison with Classical Nucleation Theory

The contrasts between SCKM and previous kinetic treatments appears at two levels. In the first place, all the latter accepted three relations with which we disagree:

$$\Delta\Phi_n = 4\pi r_n^2 \sigma_n - nkT \ln S_1 \qquad (26)$$

$$N_n{}^{\Phi} = N_1{}^0 \exp(-\Delta\Phi_n/kT) \qquad (27)$$

$$\frac{k^{\Phi}{}_{n\to n+1}}{k^{\Phi}{}_{n+1\to n}} = (N_1{}^0)^{-1} \exp\left( -\frac{\Delta\Phi_{n+1} - \Delta\Phi_n}{kT} \right) \qquad (28)$$

for *all* $n$

The first term of the right member of (26) is the surface free energy for spherical droplets, and is appropriate for large enough $n$ ($\gtrsim 10^3$), such that a meaningful surface layer can be identified [see Lee et al.[19]]. However, the usual substitution of $(\sigma_n/\rho_n{}^{2/3})$ by $(\sigma/\rho^{2/3})_{bulk}$ [$\rho_n$ is the density

of monomers in an $n$mer] is dubious for $n \lesssim 10^6$. This difficulty which has been discussed many times we avoided. The "Boltzmann like relation" indicated by eq 27 is inapplicable to a system wherein the total number of particles must change to achieve a condition which approximates statistical equilibrium.[20] Finally, the relation between the forward and reverse rate constants given by eq 28 is valid only at complete equilibrium, if applied to *all* $n$; at *steady state* it is valid only for $n \leq n^\dagger$; i.e., when that condition is a consequence of nearly equal rates of accretion and evaporation. We demonstrated that for $n > n^\dagger$

$$k_{n\to n+1} N_1{}^0 N_n{}^{ss} >> k_{n+1\to n} N^{ss}{}_{n+1}$$

Finally, use of a hard sphere model for binary collisions, with unit sticking coefficients, is highly arbitrary.

Secondly, even if one accepts the concept of a liquid-drop for clusters in the neighborhood of 10 units, eq 26 and 27 are mutually incompatible. One may consider eq 27 to be a *definition* of $\Delta\Phi_n$, and then evaluate it in terms of $\Delta G^\circ{}_n$, via (24) for a "constrained equilibrium", with $N_1{}^{ul} \equiv N_1{}^0$:

$$\Delta\Phi_n{}^{ul} = \frac{\Delta G^\circ{}_n}{\mathcal{L}} - (n-1)kT \ln p_1{}^\circ \qquad (29)$$

where $\mathcal{L}$ is Avagadro's number. At the same time, we can derive an expression for the increment in the Gibbs free energy for conversion of $n$ moles of monomer at $(p_1,T)$ to 1 mol of dimer at $(p_n, T)$. It is essential that the final state be specified.[18] The thermochemical cycle begins with expansion from $p_1$ to $p_1{}^e$, condensation to bulk liquid, cooling to 0 K, chopping to 1 mol of $n$mers, and heating to $(p_n, T)$ gives:

$$\Delta G_n(T)/\mathcal{L} = 4\pi r_n{}^2 \sigma_n(T) - nkT \ln S_1 - n(g_1 - g_n) + kT \ln (p_n/\psi_n) \qquad (30)$$

Here $-RT \ln \psi_n$ is the (translational) free energy of point masses $(n\mu)$ at 1 atm and $T$ K. Thus

$$\ln\psi_n \equiv 5/2 \ln T + 3/2 \ln (n\mu) - 3.665$$

$g_1$ and $g_n$ are the thermal free energy increments per monomer unit when in the bulk liquid and in an $n$mer, respectively. To obtain $\Delta G^\circ{}_n$, set $p_1$ and $p_n$ equal to unit atmosphere. We deduce

$$\Delta\Phi_n{}^{ul} = 4\pi r_n{}^2 \sigma_n{}^2(T) - nkT \ln S_1 - n(g_1 - g_n) + kT \ln (p_1{}^\circ/\psi_n) \qquad (31)$$

The last two terms in (31), which do not appear in (26), are not negligible, particularly when a large temperature range is covered in tests of the theory.

On viewing the immense literature on homogeneous nucleation it appears to us that the usually applied test for a model [comparison of predicted ln $S_c$ vs. $T$ curves with the experimentally determined dependence of the actual supersaturation ratio on the temperature] is exceptionally insensitive. A much sharper test would be to compare the predicted $J^{ss}$ with the observed flux for a range of supersaturations. Unfortunately, this is difficult to do. A procedure for determining flux magnitudes, within an order of magnitude, for condensing metal vapors was described in paper 4 of this series.

*Acknowledgment.* This investigation was supported by the National Science Foundation through the Materials Science Center of Cornell University. We are grateful to Professor John C. Wheeler (UCSD) for illuminating discussions of the statistical problems we encountered, and sincerely thank Professor B. Widom for his participation in these discussions.

## References and Notes

(1) H. J. Freund and S. H. Bauer, *J. Phys. Chem.*, **81**, 994 (1977).
(2) (a) W. G. Courtney, *J. Chem. Phys.*, **36**, 2009 (1962); (b) F. F. Abraham, *ibid.*, **51**, 1632 (1969); (c) B. N. Hale and P. L. M. Plummer, *ibid.*, **61**, 4012 (1974); (d) J. J. Burton in "Statistical Mechanics of Time Dependent Processes", B. J. Beine, Ed., 1976.
(3) Summarized by J. E. McDonald, *Am. J. Phys.*, **30**, 870 (1962); **31**, 31 (1963).
(4) Summarized by K. Nishioka and G. M. Pound in "Nucleation II", A. C. Zettlemoyer, Ed., Marcel Dekker, New York, N.Y., 1976.
(5) E. R. Buckle, *Trans. Faraday Soc.*, **65**, 1267 (1969).
(6) F. T. Smith, *Discuss. Faraday Soc.*, **33**, 183 (1962).
(7) L. P. Walkauskis and F. Kaufman, *Symp. (Int.) Combust., [Proc.], 15th*, **1**, 691 (1975).
(8) (a) P. A. Whitlock, J. T. Muckerman, and R. E. Roberts, *J. Chem. Phys.*, **60**, 3658 (1974); (b) G. Burns, et al., references to earlier publications: *Symp. (Int.) Combust., [Proc.], 15th*, 731 (1975).
(9) (a) I. Amdur and G. G. Hammes, "Chemical Kinetics", McGraw-Hill, New York, N.Y., 1966, pp 42, 43. (b) Use of a "soft sphere" formulation: W. G. Dorfeld and J. B. Hudson, *J. Chem. Phys.*, **59**, 1253 (1973).
(10) Electron micrographs of powders precipitated from highly supersaturated vapors of Fe, Bi, and Pb showed narrow bell-shaped distribution curves peaked at diameters ≈200 Å, but often with tails that extended to about 1000 Å. The latter are due to coagulation of large clusters generated during primary condensation.
(11) A. C. Hindmarsh, "GEAR: Ordinary Differential Equation System Solver", Lawrence Livermore Laboratory, UDID-30001 Rev-1, Computer Documentation, 1972.
(12) Professor J. C. Wheeler developed an elegant expression for the time required to reach steady state, in terms of the forward flux and the steady state densities:

$$\tau_{n_2} = \tau_{n_1} + \sum_{n_1+1}^{n_2} N_i^{ss}/J^{ss}$$

(13) J. J. Burton and C. L. Briant, *J. Chem. Phys.*, **63**, 2045 (1975).
(14) K. Binder, *J. Chem. Phys.*, **63**, 2265 (1975).
(15) M. R. Hoare and J. McInnes, *Chem. Soc., Faraday Discuss.*, **61** (1976).
(16) "JANAF Thermochemical Tables", The Dow Chemical Co., Midland, Mich.
(17) M. P. Hoare and P. Pal, *J. Crystal Growth*, **17**, 77 (1972).
(18) (a) W. G. Courtney, *J. Chem. Phys.*, **35**, 2249 (1961); (b) M. Blander and J. L. Katz, *J. Stat. Phys.*, **4**, 55 (1972).
(19) J. K. Lee, J. A. Barker, and F. F. Abraham, *J. Chem. Phys.*, **58**, 3166 (1973).
(20) H. Reiss, preprint of a review of nucleation theory.

# COMMUNICATIONS TO THE EDITOR

## Comment on Resonance Stabilization Energies from Cis–Trans Isomerization Studies

*Sir:* In a recent publication,[1] Marley and Jeffers reported single pulse shock tube relative rate measurements for the cis–trans isomerization of crotononitrile, 1,3-pentadiene, and 3-methyl-1,3-pentadiene. The results are log $k$ (crotononitrile) = $13.2 - 58.1/\theta$, log $k$ (1,3-pentadiene) = $13.6 - 53.0/\theta$, and log $k$ (3-methyl-1,3-pentadiene) = $14.0 - 55.0/\theta$, where $\theta = 2.303RT$ kcal/mol. On the assumption of a biradical mechanism for cis–trans isomerization the authors compared these findings with their previously established parameters for *cis*-2-butene,[2] log $k = 14.6 - 66.2/\theta$, to obtain resonance stabilization energies of ~8 kcal/mol for the cyano group, ~13 kcal/mol for allyl, and ~11 kcal/mol for methyl allyl. These values were concluded to be in good agreement with values of 6 kcal/mol for CN found by Sarner et al.,[3] 11.6 kcal/mol for methyl allyl deduced from the work of Walters[4] and Frey,[5] and 12.6 kcal/mol for allyl. The latter was quoted as being the "standard" accepted by Benson and O'Neal.[6] Recent measurements, however, have firmly established that the allyl stabilization energy is ~10 kcal/mol,[7,8] and that for methyl allyl should be ~13 kcal/mol.[9] Furthermore, the value for the cyano stabilization energy found by Sarner et al. from the pyrolysis of cyclobutyl cyanide is relative to a hydrogen atom. The definition of stabilization energy[10] requires that the comparison be made with respect to the corresponding alkyl substituent. Such a comparison is included in the value derived from cis–trans isomerizations. On this basis, a value of ~5 kcal/mol may be obtained from the kinetics of pyrolysis of several cyano-substituted small ring compounds.[3,11,13] This is strongly supported by a substantial body of recent data on the pyrolysis of alkyl cyanides.[12,13] Thus the agreement between stabilization energies derived from cis–trans isomerizations and values from other sources appears not to be as good as suggested by Marley and Jeffers.

The discrepancies may be due to the shock tube data although it is difficult to find any uncertainties. Nevertheless, it is noteworthy that a very recent study[14] of the cis–trans isomerization of 2-butene gave results in excellent agreement with early studies and not with the "high" parameters established by the shock tube technique.[2] Note also that the shock tube $A$ factor for *cis*-2-butene is about a power of ten higher than the transition-state estimate.[6] Also, the shock tube data yield a surprisingly large difference in $A$ factors ($10^{1.4}$ $s^{-1}$) between crotononitrile and 2-butene. The biradical mechanism for cis–trans isomerization proposed by Benson and co-workers[15,16] may be depicted as follows

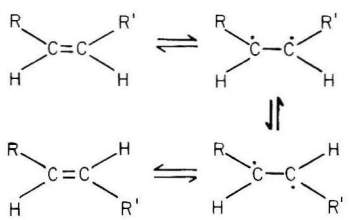

Rotation about the $sp^2$–$sp^2$ single bond in the biradical is rate determining. When a substituent can interact with the biradical, the $A$ factor will be lowered because of the stiffening of internal rotations accompanying this interaction[6,15,16] but this will not be the case with CN because of the cylindrical symmetry of the triple bond. Although increases in the frequencies of C–C≡N bends may make some contribution to a decreased $A$ factor[13] such changes are not likely to lead to a decrease of as much as $10^{1.4}$ $s^{-1}$.

According to the biradical mechanism the activation energy is the enthalpy of reaction to the biradical (which is equivalent to the $\pi$-bond energy in the olefin) plus the energy required to rotate about the single bond to the perpendicular conformation. Thus the use of cis–trans isomerizations to determine stabilization energies assumes that the barrier to rotation in the resonance stabilized biradical is the same as that in the nonstabilized species.[18] This may not be the case. For example, the difference in $\pi$-bond energies between *cis*-2-butene[18] and *cis*-crotononitrile[19] is ~6 kcal/mol whereas the difference in isomerization activation energies is ~8 kcal/mol.[1] This suggests a slightly higher barrier to rotation in the nonstabilized biradical. Note also that the difference in $\pi$-bond energies between ethylene[18] and *cis*-1,2-dichloroethylene[20] (2.1 kcal/mol) agrees with the radical stabilization energy of a Cl atom (relative to a H atom)[21] whereas the difference in isomerization activation energies (8.1 kcal/mol)[2,22] does not.

It is suggested that the use of cis–trans isomerization measurements for determining reliable resonance interaction energies should be viewed with caution.[23]

### References and Notes


(1) W. M. Marley and P. M. Jeffers, *J. Phys. Chem.*, **79**, 2085 (1975).
(2) P. M. Jeffers, *J. Phys. Chem.*, **78**, 1469 (1974).
(3) S. F. Sarner, D. M. Gale, H. K. Hall, Jr., and A. B. Richmond, *J. Phys. Chem.*, **76**, 2817 (1972).
(4) M. Zupan and W. D. Walters, *J. Phys. Chem.*, **67**, 1845 (1963).
(5) R. J. Ellis and H. M. Frey, *Trans. Faraday Soc.*, **59**, 2076 (1963).
(6) S. W. Benson and H. E. O'Neal, *Natl. Stand. Ref. Data Ser., Natl. Bur. Stand.*, **No. 21** (1970).
(7) D. M. Golden and S. W. Benson, *Chem. Rev.*, **69**, 125 (1969).
(8) D. M. Golden, N. A. Gac, and S. W. Benson, *J. Am. Chem. Soc.*, **91**, 2136 (1969).
(9) A. S. Rodgers and M. C. R. Wu, *J. Am. Chem. Soc.*, **95**, 6913 (1973).
(10) A. S. Rodgers, M. C. R. Wu, and L. Kuitu, *J. Phys. Chem.*, **76**, 3196 (1972).
(11) For references and a discussion, see ref 12.
(12) K. D. King and R. D. Goddard, *J. Phys. Chem.*, **80**, 546 (1976).
(13) K. D. King and R. D. Goddard, *J. Am. Chem. Soc.*, **97**, 4504 (1975); *Int. J. Chem. Kinet.*, **7**, 837 (1975).
(14) D. Masson, C. Richard, and R. Martin, *Int. J. Chem. Kinet.*, **8**, 37 (1976).
(15) S. W. Benson, K. W. Egger, and D. M. Golden, *J. Am. Chem. Soc.*, **87**, 468 (1965).
(16) S. W. Benson, "Thermochemical Kinetics", Wiley, New York, N.Y., 1968.
(17) Substituents that generate stabilization energies in one or both of the radical centers of the biradical have essentially the same effect on the $\pi$-bond energy as on $\sigma$ bonds and monoradicals.[18]
(18) K. W. Egger and A. T. Cocks, *Helv. Chim. Acta*, **56**, 1516 (1973).
(19) Assumed to be the same as that for $\alpha$-methacrylonitrile.[12]
(20) Estimated according to the procedure outlined in ref 18 using the data tabulated in J. A. Franklin and G. Huybrechts, *Int. J. Chem. Kinet.*, **1**, 3 (1969).

(21) E. N. Cain and R. K. Solly, *J. Am. Chem. Soc.*, **94**, 3830 (1972); *Aust. J. Chem.*, **28**, 2079 (1975).
(22) J. E. Douglas, B. S. Rabinovitch, and F. S. Looney, *J. Chem. Phys.*, **23**, 315 (1955).
(23) A referee has called attention to a paper by H. M. Frey, A. M. Lamont, and R. Walsh, *J. Chem. Soc. A*, 2642 (1971), which presents evidence to show that the cis–trans isomerization of 2,3-dimethyl-1,3-pentadiene almost certainly proceeds via the intermediate formation of 1,2,3-trimethylcyclobutane and not via a biradical mechanism. These workers also studied the cis–trans isomerization of 1,3-pentadiene. The situation was less clear but again intermediate formation of a cyclobutane seemed more likely than a biradical mechanism. A similar pathway for 3-methyl-1,3-pentadiene seems likely. This paper was overlooked by Marley and Jeffers.

*Department of Chemical Engineering* **Keith D. King**
*University of Adelaide*
*Adelaide, South Australia 5001*

*Received July 19, 1976*

## Reply to the Comment on Resonance Stabilization Energies from Cis–Trans Isomerization Studies

*Sir:* There is little we can challenge in Professor King's communication, except perhaps its tone. We feel that the differences in derived stabilization energies may well be within the stated experimental error limits, in most cases.

A discussion of the 2-butene rate constant was presented in *J. Phys. Chem.*, 78, 1469 (1974). However, since the stabilization energies under criticism are derived from relative rate measurements, the absolute value chosen for 2-butene isomerization seems irrelevant.

Most of the cis–trans isomerization results reported in our series of papers were based on about 10–20 shock experiments. Perhaps what is really needed is a more extensive (and perhaps more careful) set of experiments. Our studies appear to be the most complete and generally reliable set of results on the kinetics of systems which from all indications are difficult to study by other techniques. We would urge further experiments before challenging the shock tube relative rate techniques on the basis of existing cis–trans isomerization results.

*Department of Chemistry* **Peter M. Jeffers**
*State University of New York at Cortland*
*Cortland, New York 13045*

*Received September 15, 1976*

## Preliminary Report of a Spur Model Including Spur Overlap

*Sir:* Experimental results from picosecond pulse radiolysis studies[1] have prompted Kupperman[2] to introduce significant changes in certain parameters of the spur model in aqueous radiation chemistry.[3-5] Using the stroboscopic method, Wolff et al.[6] found there was very little, if any, decay of the hydrated electron concentration in pure water during the time period from 20 to 350 ps following the delivery of a short, high-energy electron pulse. Jonah et al.[7] have suggested the 3% decay in hydrated electron concentration, which they observe in their electron pulsed water from 100 to 350 ps, is probably within the experimental error of the measurements of Wolff et al.[6] However, both Wolff et al.[6] and Jonah et al.[7] state, for different reasons, that their hydrated electron decay (or lack thereof) differs by amounts greater than their estimated experimental error from the spur decay calculations based upon parameters used by Schwarz[5] and Kupperman,[2] respectively.

Most quantitative pulse radiolysis studies have concentrated on either one of two time periods following delivery of the pulse, either the period of "isolated spur decay" or a much later time period when all reactive intermediates are homogeneously distributed.

We have completed an experimental pulse radiolysis study of the effects of pulse dose on hydrated electron decay rates in pure water using 20-ns pulses of 14-MeV electrons.[8] In order to interpret the results of this study, we have postulated spur overlap as being responsible for the relatively abrupt alterations in the kinetics of electron decay observed as functions of pulse dose and of time following the pulse.

A simple model[9] for the relaxation of the concentration distribution in the spurs suggests that the critical length parameter is proportional to dose$^{1/3}$ and the critical (diffusional) time parameter should be scaled as time$^{1/2}$. The data were analyzed to yield an estimate of the time (in nanoseconds) of spur expansion following a 20-ns electron pulse to reach experimentally observable spur overlap ($t_0$):

$$t_0 \simeq \frac{1.2 \times 10^4}{[\text{dose(rads)}]^{2/3}} \text{ ns}$$

The time to reach observable spur overlap suggested by these relations is earlier than those predicted by Kenney and Walker.[9] Furthermore, these data suggest that spur overlap needs to be taken into account in spur modeling studies, *especially* when using large pulse doses and/or relatively low energy pulsed electrons as radiation sources.

As a result of the above experimental results, we have initiated a computer modeling study to attempt to fit a diffusion model incorporating spur overlap features to pulse radiolysis hydrated electron decay data between $\sim 10^{-11}$ and $10^{-7}$ s. In this relatively crude model we have included a smooth transition through the time regions of predominantly intraspur electron decay, spur overlap (with *spherical* symmetry), and, finally, homogeneous reactions of the hydrated electron. This model has given surprisingly good qualitative overall fits to these experimental data over this wide time region and especially good fits to very early electron decay data. We wish to report on these preliminary results at this time because the nature of the initial hydrated electron distribution employed differs qualitatively from those used heretofore.

Previously published computer modeling studies[3-5] have employed concentration probability distribution functions for intermediates created by the ionizing radiation centered about the spur origin with a maximum value at the origin for all intermediates contained in the spur. Such functions appeared to us to be inherently in conflict with at least some of the experimental data of picosecond pulse radiolysis experiments showing the lack of or very small amount of decay between $10^{-11}$ and $10^{-9}$ s. They also appeared to be in conflict with the basic ideas of Lea[10] and Platzman,[11] namely, that ejected electrons would be hydrated or thermalized at some distance from the parent positive ion. The Gaussian distribution for *hydrogen atoms* was originally chosen by Samuel and Magee[3a] (a) for mathematical tractability and (b) since the ejected "electron cannot go very far without suffering wide deflections resulting from scattering".[3a] We believe that electrons formed in the ionization event may very well be able to travel fairly large distances from their positive ion

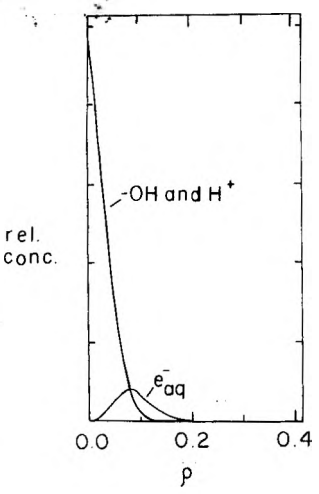


**Figure 1.** Probability density functions chosen for hydrated electron, hydroxyl radical, and hydrogen ion in the overlapping spur model. The ordinate represents the probability of finding the reactive species at the radial distance ($\rho = r/r_0$ where $r_0$ is half the average distance between nearest neighbor spur centers). These curves are constructed in the computer program to make the integrated concentration between $\rho = 0$ and $\rho = 1$ proportional to the initial $G$ values of the reactive species. $\rho = 1$ represents the radius of the sphere inside which the spur (whose center is located at $\rho = 0$) expands until overlapping with the spherically symmetrical average of all other spurs overlapping with that designated spur. Spur overlap in this figure occurs when the concentration of any reactive intermediate is a significantly nonzero value at $\rho = 1.0$. Parameters for these figures include the $G$ values: $G_{e_{aq}^-} = 4.6$, $G_{OH_2} = 4.6$, $G_{H^+} = 4.6$. The maximum in the hydrated electron distribution function illustrated is at 40 Å from the spur center, whereas the average interspur distance ($2r_0$) is approximately 900 Å (corresponding to a pulse dose of 2400 rads). The $1/e$ value for the ·OH and $H^+$ concentrations is 25 Å from the spur center. A value of 60 eV/spur is employed in these calculations

partner without significant scattering, perhaps by means of "conduction bands" formed from the transient water organization. As Samuel and Magee originally suggested[3a] their model is a classical picture and a quantum mechanical model is probably needed for a more accurate representation of very early electronic phenomena at times during and immediately following ionization. Some indirect evidence for separate distributions of electrons and positive ions or ·OH can be seen in the work of Raitsimring et al.[12] in their study of the detailed track structure of irradiated frozen aqueous acids.

In our model, we have assumed identical Gaussian initial distributions centered at the origin of the spur for both $H^+$ and ·OH and a skewed Gaussian for the hydrated electron distribution, with zero probability of finding the hydrated electron in the center of the spur. Plots of the distributions tested are shown in Figure 1. The forms are chosen to separate initially most of the hydrated electrons from other reactants and consequently produce a negligible initial rate of reaction for hydrated electrons.

The computer simulation used to model an overlapping spur is a straightforward application of diffusional processes coupled with chemical reaction. The simplest set of reactions which can be expected to represent hydrated electron decay at early times (less than 1 μs after the pulse) is comprised of the following reactions, using the rate constants quoted in ref 2:

$$e_{aq}^- + e_{aq}^- \rightarrow H_2 + 2OH^-$$
$$e_{aq}^- + OH\cdot \rightarrow OH^-$$
$$e_{aq}^- + H_{aq}^+ \rightarrow H\cdot$$
$$OH\cdot + OH\cdot \rightarrow H_2O_2$$

The model is the numerical solution to three partial differential equations of the form

$$\partial C_i/\partial t = D_i \nabla^2 C_i - r_i \qquad (1)$$

where $C_i$ is the concentration of $e_{aq}^-$, $H^+$, or OH·; $D_i$ is the translational diffusivity of the species (values were taken from ref 2); and $r_i$ is the rate of consumption of the ith species.

Equation 1 is formulated in spherical coordinates; the two boundary conditions are:

$\partial C_i(t, 0)/\partial r = 0$ bounded concentration at spur center

$\partial C_i(t, r_0)/\partial r = 0$ no *net* diffusion out of the spherical volume of radius $r_0$ (where $r_0 = (3/4\pi N)^{1/3}$; $N$ = no. spurs/unit vol)

The first boundary condition is conventional; the concentration at the center of the sphere cannot have a singularity. The second boundary condition is less conventional in aqueous radiation chemistry. The spur at the center of the coordinate system is viewed as being surrounded by a smooth smear of nearest neighbor spurs. Since all the neighbors are identical, there is no net diffusional transport out of the spherical volume whose radius ($r_0$) is one-half the average distance between nearest neighbor spur centers. The centers for nearest neighbors are assumed to be distributed in a random fashion throughout the field, and at first glance the spherical symmetry does not seem appropriate. However, the distribution function of nearest neighbor interspur distances, ($dP/d\rho$), in a random distribution in three-dimensional space is fairly sharply peaked, [$dP/d\rho = 3\rho^2 e^{-\rho^3}$; $\rho = (r/r_0)$][8] and, therefore, the symmetrical sphere is an adequate first approximation.

Thus a plot of concentration probability density[2] for any spur transient vs. $r$ between $r = 0$ and $r = 2r_0$ is a mirror image reflected around the line at the value $r = r_0$. Spur overlap in this model occurs when the value of the probability density of any one of the spur transients is deemed to be a value significantly different from zero at $r = r_0$. The second boundary condition represents a departure from the models of Kupperman[2] and Schwarz.[5]

The initial concentration distributions are adjustable features of this simulation. The concentrations of OH· and $H_{aq}^+$ are Gaussian about the center; the maximum concentration at the center increases as the distribution sharpens. The initial concentration distribution for hydrated electrons is skewed Gaussian. Mathematically the two forms have been chosen as

$$OH\cdot,\ H_{aq}^+ \quad C_i(r, 0) = m_i e^{-(n_i r/r_0)^2}$$
$$e_{aq}^- \quad C_i(r, 0) = m_i (r/r_0)^3 e^{-(n_i r/r_0)^2}$$

These functions are folded at $r_0$, the radius of the spherical spur-containing volume to ensure that the second boundary condition is satisfied at the beginning of the simulation. However, the initial concentration at the edge of the spur is very low, and the folding is not particularly important at low pulse doses. The form of these approximations is shown in Figure 1.

The set of equations are put in dimensionless form in which $\rho$ ($= r/r_0$) is the fractional radial position within the

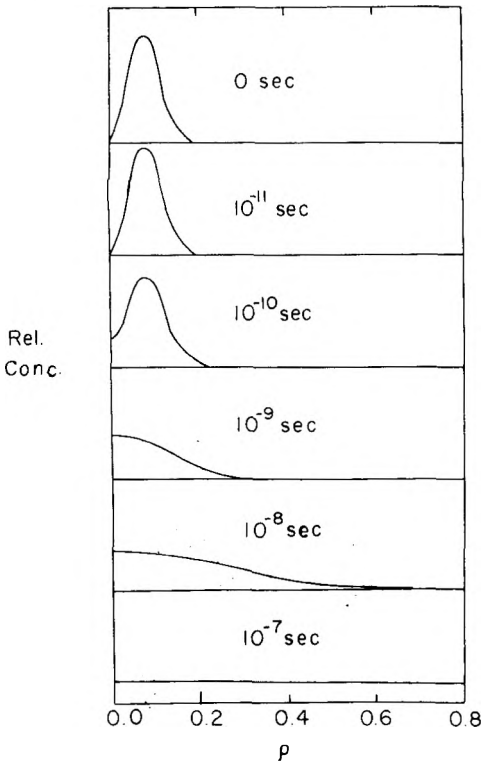


**Figure 2.** Calculated hydrated electron concentration profiles as a function of time following a 2400-rad pulse. Parameters are same as indicated in Figure 1. Initial $G$ values for $e_{aq}^-$, $H^+$, and ·OH are equal to 4.6. Diffusion coefficients and rate constants are those quoted in ref 4 for the following reactions: $e_{aq}^- + e_{aq}^- \rightarrow 2OH^- + H_2$; ·OH + ·OH $\rightarrow H_2O_2$; $e_{aq}^- + H^+ \rightarrow H\cdot$; and $e_{aq}^- +$ ·OH $\rightarrow OH^-$ used in the computer calculations. Relative concentrations are scaled by values which increase with time.

spherical volume containing the spur. The equations are solved by an iterative form of the Crank–Nicholson method. The solution starts with a predicted value for first-order approximation of the kinetic rate expression and then revises the estimated terms in the kinetic expression as the solution progresses.

The concentration profiles relax to radially homogeneous values in $10^{-7}$ to $10^{-6}$ s. This relation is shown by the radial concentration profiles for $e_{aq}^-$ at a series of times in Figure 2. Secondary chemical reactions in the spur have not been included yet in these preliminary calculations, and, consequently, the model currently is quantitatively inadequate for times greater than $10^{-8}$ to $10^{-7}$ s. The time limit decreases with increasing radiation dose.

Experimentally, only the average concentration in the spur can be followed. The average concentration in our calculations is defined by the relation

$$\bar{C}_i(t) = \int_0^1 3\rho^2 C_i(\rho, t)\, d\rho$$

The calculated average concentration is plotted as a function of time in Figure 3 and is compared with experimental data taken from ref 7 and 8.

A very good correlation is found in Figure 3 between calculation and experiment in the time region from $10^{-11}$ to $10^{-8}$ s. Beyond this latter time there is qualitative but not quantitative agreement between the decay curves. Since the chemical equations employed up to the present time in these computations are only the primary chemical reactions, it is predicted from comparisons with the other homogeneous kinetic calculations that, as secondary reactions between hydrated electrons and primary products

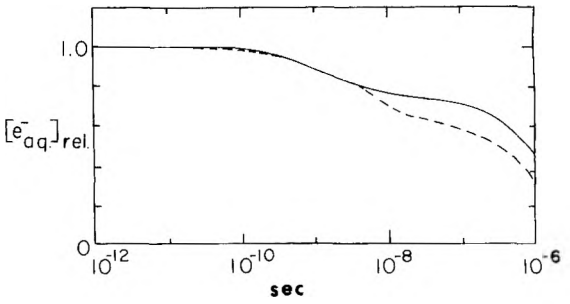


**Figure 3.** Plot of calculated vs. experimental integrated hydrated electron concentration vs. time following pulse. Assumptions are identical with those indicated in the legends of Figures 1 and 2. Experimental data (dashed line) are taken from Jonah et al.[7] and Fanning[18] normalized at $10^{-7}$ s. Secondary reactions have not been included yet in the computations and will tend to improve agreement between experimental and computed concentrations beyond $10^{-8}$ s as will the inclusion of an additional scavenging of hydrated electrons by a residual oxygen concentration of $\sim 1$ $\mu$M

(especially $e_{aq}^- + H_2O_2$) are incorporated into the program, the predicted hydrated electron decay rate at later times will be larger and therefore in closer agreement with experimental results. However, at this preliminary stage of the calculations, the agreement between calculated and experimental hydrated electron concentrations at very early times where spur decay is essentially *independent* of secondary chemical reactions is excellent and encourages us to explore further the concept of a hydrated electron distribution of the type shown in Figure 1.

Since literature values for rate and diffusion constants and $G$ values are fixed, the variable parameters in our computations are the nature of the concentration distributions and the average number of electron volts deposited per spur. We have found excellent early time matches between experiment and computer calculations using the aforementioned skewed Gaussian for the hydrated electron and values of less than 100 eV/spur. The Lea–Platzman type charge separation[10,11] has been neglected, despite its use by Platzman in successfully predicting the existence of the hydrated electron.[13] This neglect is primarily because in its original form the theory tended to make hydrated electrons nearly homogeneously distributed upon hydration.[14] Magee has favored a much tighter clustering of positive ions and hydrated electrons such that almost all electrons recombine to give neutral species,[15] but more recently Mozumder and Magee have stated[16] that the assumptions regarding initial spatial distributions in spurs require further investigation. Our results tend to favor a compromise between the Lea–Platzman and the tight Gaussian distributions. The values we have used of less than 100 eV deposited per average spur are more in agreement with those estimated by Mozumder and Magee who state that "low energy spurs are greatly favored statistically".[17] Their calculated most probable spur energy for 1 MeV electrons is 20 eV. We feel that our model is qualitatively in agreement with these calculations.

Further refinements of the above computer calculation are in progress and both published and unpublished data,[18] including reaction with added solutes (e.g., $O_2$), are currently being included as further tests of the proposed model. We believe the preliminary calculations demonstrate the promise of our approach and lend further weight to the interpretation of our pulse radiolysis study using variable pulse dose.[8]

*Acknowledgment.* This research was supported in part by the U.S. Atomic Energy Commission.

## References and Notes


(1) J. W. Hunt, R. K. Wolff, M. J. Bronskill, C. D. Jonah, E. J. Hart, and M. S. Matheson, *J. Phys. Chem.*, **77**, 425 (1973).
(2) A. Kupperman in "Physical Mechanisms in Radiation Biology", Technical Information Center, Office of Information Services, U.S. Atomic Energy Commision, Washington. D.C., 1974, p 155.
(3) (a) A. H. Samuel and J. L. Magee, *J. Chem. Phys.*, **21**, 1080 (1953); (b) A. K. Ganguly and J. L. Magee, *ibid.*, **25**, 129 (1956).
(4) A. Kupperman, "Radiation Research", G. Silini, Ed., North Holland Publishing Co., Amsterdam, 1967 (see references therein to earlier computations by Kupperman and others).
(5) H. A. Schwarz, *J. Phys. Chem.*, **73**, 1928 (1969).
(6) R. K. Wolff, M. J. Bronskill, J. E. Aldrich, and J. W. Hunt, *J. Phys. Chem.*, **77**, 1350 (1973).
(7) C. D. Jonah, M. S. Matheson, J. R. Miller, and E. J. Hart, *J. Phys. Chem.*, **80**, 1276 (1976).
(8) J. E. Fanning, C. N. Trumbore, P. G. Barkley, and J. Olson, to be published.
(9) G. A. Kenney and D. C. Walker, *J. Chem. Phys.*, **50**, 4047 (1969).
(10) D. E. Lea, *Proc. Cambridge Phil. Soc.*, **30**, 80 (1934).
(11) R. L. Platzman in "Radiation Biology and Medicine", W. D. Claus, Ed., Addison Wesley, Reading, Mass., 1958, pp 15–72 (see earlier references therein).
(12) A. M. Raitsimring, V. M. Moralev, and Yu. D. Tsvetkov, *Khim. Vys. Energ.*, **9**, 517 (1975) (translation by Plenum Press).
(13) R. L. Platzman, *Natl. Acad. Sci. Res. Counc., Publ.* **No. 305**, 34 (1953).
(14) J. K. Thomas, *Adv. Radiat. Chem.*, **1**, 111 (1969).
(15) J. L. Magee, *Radiat. Res. Suppl.*, **4**, 20 (1963).
(16) A. Mozumder and J. L. Magee, *Int. J. Radiat. Phys. Chem.*, **7**, 83 (1975).
(17) A. Mozumder and J. L. Magee, *J. Chem. Phys.*, **45**, 3332 (1966); see figures on p 67 of *Adv. Radiat. Chem.*, **1**, (1969).
(18) J. E. Fanning, Jr., Ph.D. Thesis, 1975, University of Delaware, Newark, Del.
(19) (a) Department of Chemistry. (b) Department of Chemical Engineering.



*Departments of Chemistry and Chemical Engineering*
*University of Delaware*
*Newark, Delaware 19711*

**James E. Fanning, Jr.*[19a]**
**Conrad N. Trumbore[19a]**
**P. Glenn Barkley[19a]**
**David R. Short[19a]**
**Jon H. Olson[19b]**


*Received May 17, 1976; Revised Manuscript Received January 27, 1977*

## Absorption Rate of Hydrogen by Cold-Worked Palladium

*Sir:* The problem of absorption of $H_2$ by palladium has been under consideration for many years. It is well known that the elementary steps occurring during absorption from the gas phase are (a) surface processes and (b) internal diffusion. It has been pointed out that at low temperatures (<100 °C) the overall rate of absorption is very sensitive to the way in which the surfaces are pretreated.[1] This result suggests that the steps on the surface may be responsible for the absorption process. In most recent studies, argon ion bombardment or an oxidation–reduction has been used as a method for producing active surfaces.[1,2] On the other hand, many studies have shown that the catalytic activities of metals for various reactions are greatly influenced by pretreatments such as cold-working and annealing, and that these changes in activity are ascribed to the presence of lattice defects as active sites which can be generated or removed during the treatments.[3,4] It seems probable that a similar situation exists in the case of the absorption of $H_2$ by cold-worked Pd. The purpose of this study was to clarify the effect of lattice defects on the absorption process. An attempt devoted to this problem was already made by Smith and Derge in 1934.[5] Recently Flanagan et al.[6] have demonstrated that the solubility of $H_2$ is enhanced by cold-working. It has been confirmed by different investigators[7,8] that the electrical resistance in the $\alpha$ phase of the Pd–$H_2$ system is proportional to the hydrogen concentration. All experiments were carried out by observing the resistance within the range of this phase to avoid introducing additional complexity to the system.

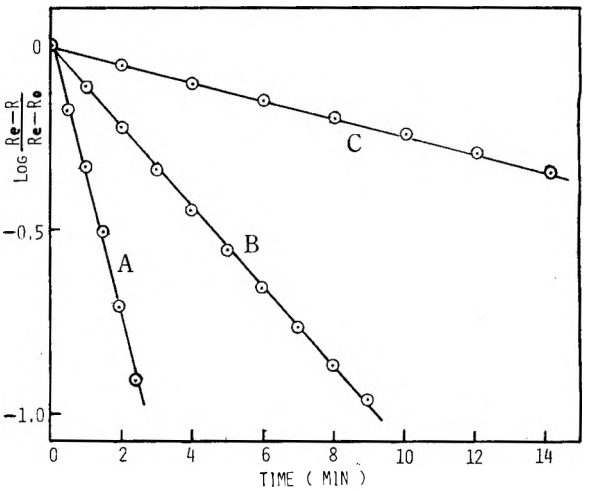


**Figure 1.** Plots of log $(R_e - R)/(R_e - R_0)$ vs. time (min), where $R_0$ is the hydrogen free resistance and $R_e$ is the value at equilibrium, at an absorption temperature of 55.6 °C for the specimens annealed at: (A) 200, (B) 300, (C) 500 °C.

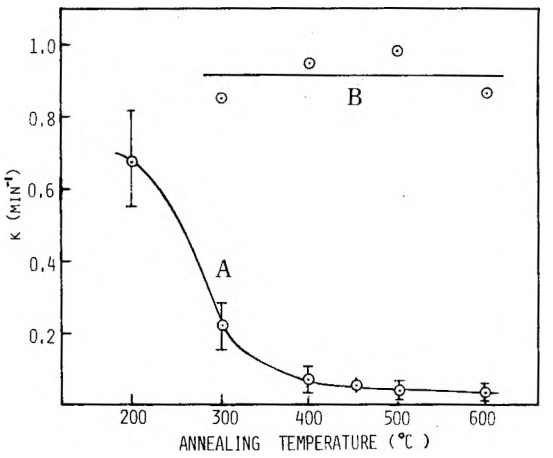


**Figure 2.** (A) Dependence of rate constant ($k$) on annealing temperature (absorption temperature 55.6 °C). (B) Effect of surface treatment (oxidation-reduction) on $k$ for annealed specimens.

Pd (>99.9% purity) for the experiment was in the form of wire cold-worked by stretching (0.02 cm diameter). Specimens 25 cm in length were cut from this wire in the cold-worked state. The annealing experiments were carried out in an absorption vessel in vacuo for 1 h at different temperatures in the range 200–600 °C. The resistance changes were measured using a bridge technique (accuracy $\pm 10^{-4}$ Ω) at temperatures between 55 and 90 °C and in a constant pressure of $H_2$ below 30 Torr.

Figure 1 shows some typical results on specimens annealed at different temperatures. This result indicates that within the limits of this experiment the absorption rate is expressed by a first-order reaction (rate = $k(C_e - C)$, where $C$ is the concentration of absorbed hydrogen and $C_e$ is the value at equilibrium) in agreement with the result of Wagner.[9] Figure 2A shows the change in the rate constant, $k(\text{min}^{-1})$, as a function of the annealing temperature at an absorption temperature of 55.6 °C. The decrease in $k$ is considerable in the range 200–400 °C. According to the previous results,[10,11] this range approximately corresponds to the recovery temperature range involving the annihilation of lattice defects produced by cold-working. If we estimate the diffusion coefficient ($D$) by the approximate equation[12]

$k \doteqdot (2.405)^2 D/r^2$

(where $r$ is the radius of wire) values $2.3 \times 10^{-7} \sim 1.4 \times 10^{-8}$ $cm^2\ s^{-1}$ are obtained from the data in Figure 2A. Compared with ($6 \sim 7 \times 10^{-7}$ $cm^2\ s^{-1}$) literature values,[13,14] the values for annealed specimens are very small. In addition, activation energies for absorption were 11.0 ± 0.5 kcal over the absorption temperature range 55–90 °C regardless of the annealing temperature. The well-known value for the activation energy of bulk diffusion is 5.7 ± 0.3 kcal.[14] This difference is difficult to explain but it may suggest that under the conditions of the present experiments the surface process plays an important role in the absorption. At any rate, it is reasonable to conclude that the concentration of defects in Pd may be responsible for governing the overall rate of absorption. However, it is uncertain at present whether the presence of defects is effective in the surface process or in the internal diffusion process. An attempt was also made to clarify this question. It was noticed that the formation of a very thin oxide occurs if this metal is heated in $O_2$ at temperatures above 200 °C.[15] Fresh specimens annealed at 300–600 °C in vacuo were pretreated in $O_2$ (10 Torr) for 1 h at temperatures above 200 °C followed by reduction in $H_2$ (10 Torr) at 300 °C. The results obtained with these specimens are given in Figure 2B. The rates are greatly increased by this treatment, however, these values are independent of the prior annealing temperatures. These findings lead to the conclusion that the rate of internal diffusion is not sensitive to the presence of defects in the crystal. On the other hand, these enhanced rates decreased by subsequent treatments at higher temperatures in vacuo. We have found similar phenomena in the case of Pd and Pt for some catalytic reactions.[16,17] Consequently, it seems probable that the oxidation–reduction treatment of the Pd surface is a method for producing the active sites (possibly a kind of surface defects) for the surface processes. Furthermore, solubility enhancement following cold-working was observed; the ratio H-to-Pd (cold-worked)/H-to-Pd (annealed above 400 °C) was 1.2. This result agrees qualitatively with that of Flanagan et al.[6]

## References and Notes


(1) F. A. Lewis, "The Palladium/Hydrogen System", Academic Press, New York, N.Y., 1967, Chapter 7.
(2) D. N. Jewett and A. C. Makrides, *Trans. Faraday Soc.*, **61**, 932 (1965).
(3) J. M. Thomas and W. J. Thomas, "Introduction to the Principles of Heterogeneous Catalysis", Academic Press, New York, N.Y., 1967, Chapter 5.
(4) A. J. B. Robertson, "Catalysis of Gas Reactions by Metals", Logos Press Limited, 1970, Chapter 10.
(5) D. P. Smith and G. J. Derge, *J. Am. Chem. Soc.*, **56**, 2513 (1934).
(6) T. B. Flanagan, J. F. Lynch, and J. D. Clewley, *Scr. Metall.*, **9**, 1063 (1975).
(7) J. W. Simons and T. B. Flanagan, *J. Chem. Phys.*, **44**, 3486 (1966).
(8) W. Auer and H. J. Grabke, *Ber. Bunsenges. Phys. Chem.*, **78**, 58 (1974).
(9) C. Wagner, *Z. Phys. Chem. A*, **159**, 459 (1932).
(10) Y. Inoue and I. Yasumori, *J. Phys. Chem.*, **75**, 880 (1971); **78**, 583 (1974).
(11) S. Kishimoto, *Rev. Phys. Chem. Jpn.*, **44**, 89 (1974).
(12) W. Jost, "Diffusion", Academic Press, New York, N.Y., 1952, p 45.
(13) J. W. Simons and T. B. Flanagan, *J. Phys. Chem.*, **69**, 3581 (1965).
(14) H. K. Birnbaum and C. A. Wert, *Ber. Bunsenges. Phys. Chem.*, **76**, 806 (1972).
(15) S. Kishimoto, to be submitted for publication.
(16) S. Kishimoto, *Rev. Phys. Chem. Jpn.*, **45**, 88 (1975).
(17) S. Kishimoto and A. Norimatsu, *J. Chem. Soc. Jpn.*, 565 (1976).



*Department of Chemistry*
*Faculty of Science*
*Kobe University*
*Nada, Kobe, Japan 657*

**Shozo Kishimoto***
**Yuji Hirai**


*Received October 12, 1976*

# New Tape Recordings on ENERGY

☐ **FUELS FOR THE NEXT 50 YEARS**
A Panel Discussion
Length: 178 minutes
7 Speakers—15 Figures
Price: $18.00

**The Panel:**
**G. R. Hill**—Direct Utilization of Coal
**L. G. Massey**—Gaseous Fuels from Coal and Petroleum
**E. Gorin**—Liquid Fuels from Coal
**R. J. Cameron**—Liquid Fuels from Petroleum and Oil Shale
**T. J. Joyce**—Natural Gas and LNG
**D. P. Gregory**—Hydrogen, Methanol, and Other Nonconventional Fuels
**I. Wender**—Fuels from Plant and Waste Materials
Each speaker briefly discusses his subject; the panel then engages in a freewheeling, give-and-take discussion of the energy problem and suggested solutions.

☐ **COAL—NATURE'S BLACK DIAMOND**
Length: 136 minutes
4 Speakers—61 Figures
Price: $18.00

**The Speakers:**
**R. T. Eddinger**—Coal—Nature's Black Diamond
**R. F. Moran**—Genesis of a Formed-Coke Process
**J. F. Jones**—Clean Fuels for Power Generation from High-Sulfur Coals
**L. Seglin**—The COGAS Process for Pipeline Gas
This symposium presents a incisive look at coal as a source for synthetic fuels and includes general economic and process details of the COED and COGAS processes.

☐ **LOW SULFUR LIQUID FUELS FROM COAL**
Length: 148 minutes
5 Speakers—66 Figures
Price: $18.00

**The Speakers:**
**J. G. Guin**—Photomicrographic Studies of Coal Dissolution
**H. E. Lebowitz**—Deashing of Coal Liquefaction Products via Partial Deasphalting-Hydrogen Donor Extraction Effluents
**C. J. Kulik**—Deashing of Coal Liquefaction Products via Partial Deasphalting-Hydrogenation and Hydroextraction Effluents
**H. P. Malone**—Characterization and Upgrading of Coal Liquids to High Value Fuels and Chemicals
Processes for upgrading liquids extracted from coal are described and first details of a new coal liquefaction process from Gulf Oil are revealed.

☐ **THE ROLE OF TECHNOLOGY IN THE ENERGY CRISIS**
Length: 128 minutes
4 Speakers—60 Figures
Price: $18.00

**The Speakers:**
**H. H. Hasiba**—Contribution of Enhanced Recovery Technology to Domestic Crude Oil
**R. N. Quade**—Process Applications of Nuclear Heat
**L. W. Russman**—Engineering Perspective of a Hydrogen Economy
**A. Decora**—Oil Shale Development and its Environmental Considerations
In-depth examination of the gains—and problems—which state-of-the art technology will bring if brought to bear on our energy problems.

☐ **UNUSUAL FUELS PRODUCTION**
Length: 138 minutes
5 Speakers—91 Figures
Price: $18.00

**The Speakers:**
**D. L. Klass**—Long-Range Approach to the Natural Gas Shortage Utilizing Nonfossil Renewable Carbon
**R. G. Sheehan**—Methanol or Ammonia Production from Solid Waste by the City of Seattle
**W. A. Scheller**—Production of Ethanol and Vegetable Protein by Grain Fermentation
**P. E. Cassady**—Use of Methanol as a Motor Fuel
**W. A. Scheller**—Performance of an Ethanol-Gasoline Blend in Automobiles and Light Trucks
An up-to-date rundown of results achieved in programs to use methanol and ethanol as additives in motor fuel, and details of advanced projects to use solid waste and biomass as sources of fuels.

**AVAILABLE ON TAPE CASSETTES ONLY**
**PRICES:** $18.00 per Title (Postpaid)
$45.00 Any THREE Titles (Postpaid)

**ORDER FROM:**
American Chemical Society
1155 Sixteenth Street, N.W.
Washington, D.C. 20036
Dept. AP

NAME:_____

ADDRESS:_____

City_____ State_____ Zip_____

(Allow 4 to 6 weeks for delivery)

# PHYSICAL PHENOMENA

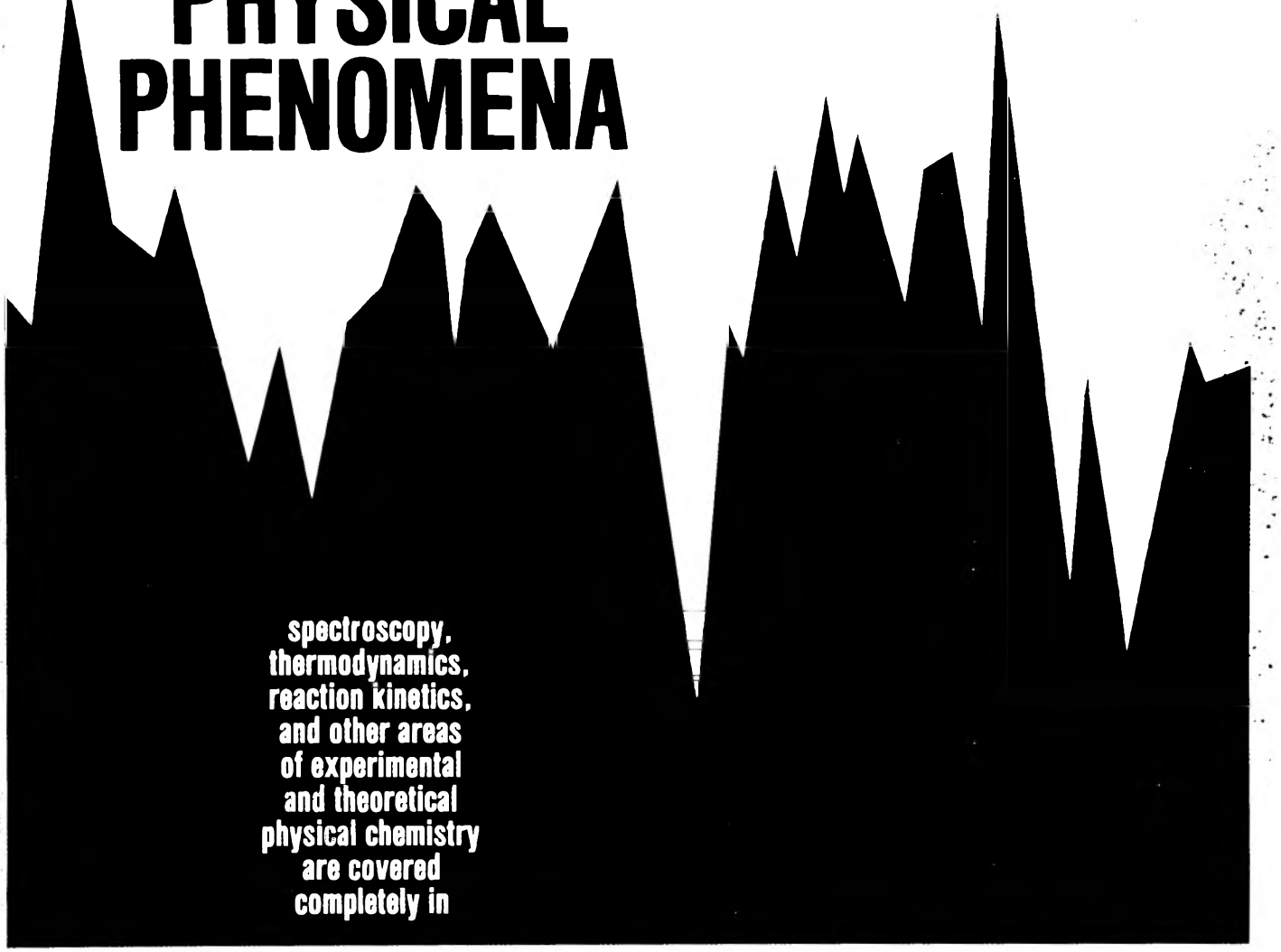


# THE JOURNAL OF PHYSICAL CHEMISTRY

The biweekly JOURNAL OF PHYSICAL CHEMISTRY includes over 25 papers an issue of original research by many of the world's leading physical chemists. Articles, communications, and symposia cover new concepts, techniques, and interpretations. A "must" for those working in the field or interested in it, the JOURNAL OF PHYSICAL CHEMISTRY is essential for keeping current on this fast moving discipline. Complete and mail the coupon now to start your subscription to this important publication.

AVAILABLE IN HARD COPY OR MICROFICHE.

**The Journal of Physical Chemistry**
**American Chemical Society** **1977**
1155 Sixteenth Street, N.W.
Washington, D.C. 20036

Yes, I would like to receive the JOURNAL OF PHYSICAL CHEMISTRY at the one-year rate checked below:

| | U.S. | Foreign and Canada | Latin America |
|---|---|---|---|
| ACS Member* | ☐ $24.00 | ☐ $34.00 | ☐ $33.00 |
| Nonmember | ☐ $96.00 | ☐ $106.00 | ☐ $105.00 |

Bill me ☐ Bill company ☐ Payment enclosed ☐

*Air freight rates available on request.*

Name _____

Street _____ Home ☐ Business ☐

City _____ State _____ Zip _____

**Journal subscriptions start in January '77.**
Allow 60 days for your first copy to be mailed.
*NOTE: Subscriptions at ACS member rates are for personal use only.